

TRANSITION METAL- BASED CATALYSTS FOR ELECTROCHEMICAL WATER SPLITTING

by Zhijie Chen

Thesis submitted in fulfilment of the
requirements for the degree of

Doctor of Philosophy

under the supervision of Prof. Bruce Ni

University of Technology Sydney
Faculty of Engineering and Information
Technology

February 2022

CERTIFICATION OF ORIGINAL AUTHORSHIP

I, Zhijie Chen declare that this thesis, is submitted in fulfilment of the requirements for the award of Doctor of Philosophy, in the Faculty of Engineering and Information Technology at the University of Technology Sydney. This thesis is wholly my own work unless otherwise referenced or acknowledged.

In addition, I certify that all information sources and literature used are indicated in the thesis. This document has not been submitted for qualifications at any other academic institution. This research is supported by the Australian Government Research Training Program.

SIGNATURE OF STUDENT:

Production Note:

Signature removed prior to publication.

DATE: 01/02/2022

ACKNOWLEDGEMENTS

I acknowledge and thank all those who guided, supported, and encouraged me throughout my Ph.D. study. First and foremost, my sincere gratitude to my supervisor, Professor Bruce Ni, whose insight, formidable wisdom, and expertise make me complete this thesis. Without his endless guidance and constant encouragement, I cannot finish my research under the influence of the COVID-19. Also, deep thanks are extended to my co-supervisor Dr. Yiwen Liu, who gave me a lot of guidance.

Special thanks to Prof. Hong Chen and all the group members at Southern University of Science and Technology for their assistance. Their contributions to my research are deeply appreciated. I feel very lucky to have the chance to study with such creative and energetic young people.

I am thankful to all the researchers I have worked with on this journey. I would like to thank Dr. Dawei Su from the School of Mathematical and Physical Sciences at UTS; Prof. Shaobin Wang and Dr. Xiaoguang Duan from the University of Adelaide; Prof. Hong Chen, Dr. Renji Zheng, Dr. Wenfei Wei, Ranhao Wang, Jing Li, and Wensong Zou at Southern University of Science and Technology; Yinhong Song at Wuhan Textile University; Prof. Grzegorz Lota and Dr. Małgorzata Graś at Poznan University of Technology for their strong support for my doctoral research.

I would like to thank my colleagues and friends in UTS, Dr. Derek Hao, Lan Wu, Xiaoqing Liu, Dr. Wei Wei, Dr. Teng Bao, Huan Liu, Zehao Zhang, Chen Wang, Dr. Jiantao Li, Dr. Lei Zheng, Dr. Wenkui Dong, Dr. Yuanyao Ye, Dr. Jiawei Ren, Dr. Dongle Cheng, Dr. Huan Li, Dr. Bentuo Xu, Haoding Xu, Fulin Qu, Yayong Li, Bing Zhang, and Irdis Ibrahim, we had a happy time in Sydney. I would like to thank Dr. Md Johir and Dr. Nirenkumar Pathak, their kind help and support are essential to my laboratory work. Moreover, I want to acknowledge the support from administrative and academic staff from the School of Civil and Environmental Engineering and Graduate Research School.

My deepest love and thanks to my family. I appreciate my father Xinchun Chen, my mother Meihua Lv, my brother Yaoyong Chen, my sister-in-law Rihong Chen, my lovely niece Yanqi Chen and nephew Yuqi Chen for their unconditional support and love. My deepest love and thanks to my wife Duo Zhang for her companionship and love. Without their continuing support and encouragement, I would not achieve my goals during my Ph.D. study.

Finally, financial supports provided by UTS, China Scholarship Council, and the Australian Research Council are gratefully acknowledged.

RESEARCH PUBLICATIONS

Publications included in this thesis

1. **Chen, Z.**, Wei, W., & Ni, B. J. (2021). Cost-effective catalysts for renewable hydrogen production via electrochemical water splitting: Recent advances. *Current Opinion in Green and Sustainable Chemistry*, 27, 100398. (Chapter 2)
2. **Chen, Z.**, Duan, X., Wei, W., Wang, S., & Ni, B. J. (2019). Recent advances in transition metal-based electrocatalysts for alkaline hydrogen evolution. *Journal of Materials Chemistry A*, 7(25), 14971-15005. (Chapter 2)
3. **Chen, Z.**, Duan, X., Wei, W., Wang, S., Zhang, Z., & Ni, B. J. (2020). Boride-based electrocatalysts: Emerging candidates for water splitting. *Nano Research*, 13(2), 293-314. (Chapter 2)
4. **Chen, Z.**, Zheng, R., Graś, M., Wei, W., Lota, G., Chen, H., & Ni, B. J. (2021). Tuning electronic property and surface reconstruction of amorphous iron borides via W, P co-doping for highly efficient oxygen evolution. *Applied Catalysis B: Environmental*, 288, 120037. (Chapter 4)
5. **Chen, Z.**, Ibrahim, I., Hao, D., Liu, X., Wu, L., Wei, W., Su, D., & Ni, B. J. (2020). Controllable design of nanoworm-like nickel sulfides for efficient electrochemical water splitting in alkaline media. *Materials Today Energy*, 18, 100573. (Chapter 5)
6. **Chen, Z.**, Zheng, R., Zou, W., Wei, W., Li, J., Wei, W., Ni, B. J., & Chen, H. (2021). Integrating high-efficiency oxygen evolution catalysts featuring accelerated surface reconstruction from waste printed circuit boards via a boriding recycling strategy. *Applied Catalysis B: Environmental*, 298, 120583. (Chapter 6)
7. **Chen, Z.**, Zheng, R., Wei, W., Wei, W., Zou, W., Li, J., Ni, B. J., & Chen, H. (2022). Recycling spent water treatment adsorbents for efficient electrocatalytic water oxidation reaction. *Resources, Conservation & Recycling*, 178, 106037. (Chapter 7)

Other publications during candidature

1. **Chen, Z.**, Zheng, R., Wei, W., Wei, W., Ni, B. J., & Chen, H. (2022).

- Unlocking the electrocatalytic activity of natural chalcopyrite using mechanochemistry. *Journal of Energy Chemistry*, 68, 275-283.
2. **Chen, Z.**, Zheng, R., Li, S., Wang, R., Wei, W., Wei, W., Ni, B. J., & Chen, H. (2022). Dual-anion etching induced in situ interfacial engineering for high-efficiency oxygen evolution. *Chemical Engineering Journal*, 431, 134304.
 3. **Chen, Z.**, Zou, W., Zheng, R., Wei, W., Wei, W., Ni, B. J., & Chen, H. (2021). Synergistic recycling and conversion of spent Li-ion battery leachate into highly efficient oxygen evolution catalysts. *Green Chemistry*, 23, 6538-6547.
 4. **Chen, Z.**, Zheng, R., Deng, S., Wei, W., Wei W., Ni, B. J., & Chen, H. (2021). Modular design of efficient heterostructural FeS₂/TiO₂ oxygen evolution electrocatalyst via sulfidation of natural ilmenites. *Journal of Materials Chemistry A*, 9, 25032-25041.
 5. **Chen, Z.**, Duan, X., Wei, W., Wang, S., & Ni, B. J. (2020). Electrocatalysts for acidic oxygen evolution reaction: Achievements and perspectives. *Nano Energy*, 78, 105392.
 6. **Chen, Z.**, Liu, Y., Wei, W., & Ni, B. J. (2019). Recent advances in electrocatalysts for halogenated organic pollutants degradation. *Environmental Science: Nano*, 6(8), 2332-2366.
 7. Zou, W., Li, J., Wang, R., Ma, J., **Chen, Z.**, Duan, L., Mi, H., & Chen, H. (2022). Hydroxylamine Mediated Fenton-like Interfacial Reaction Dynamics on Sea Urchin-like Catalyst Derived from Spent LiFePO₄ Battery. *Journal of Hazardous Materials*, 128590.
 8. Liu, X., **Chen, Z.**, Tian, K., Zhu, F., Hao, D., Cheng, D., Wei, W., Zhang, L., & Ni, B. J. (2021). Fe³⁺ Promoted the Photocatalytic Defluorination of Perfluorooctanoic Acid (PFOA) over In₂O₃. *ACS ES&T Water*, 1, 2431-2439.
 9. Graś, M., Kolanowski, Ł., **Chen, Z.**, Lota, K., Jurak, K., Ryl, J., Ni, B.-J., Lota, G. (2021). Partial inhibition of borohydride hydrolysis using porous activated carbon as an effective method to improve the electrocatalytic activity of the DBFC anode. *Sustainable Energy & Fuels*, 5, 4401-4413.
 10. Hao, D., Liu, C., Xu, X., Kianinia, M., Aharonovich, I., Bai, X., Liu, X., **Chen, Z.**, Wei, W., Jia, G., & Ni, B. J. (2020). Surface defect-abundant one-dimensional graphitic carbon nitride nanorods boost photocatalytic nitrogen fixation. *New Journal of Chemistry*, 44(47), 20651-20658.
 11. Wei, W., Hao, Q., **Chen, Z.**, Bao, T., & Ni, B. J. (2020). Polystyrene

- nanoplastics reshape the anaerobic granular sludge for recovering methane from wastewater. *Water Research*, 182, 116041.
12. Bao, T., Damtie, M. M., Hosseinzadeh, A., Wei, W., Jin, J., Vo, H. N. P., Ye, J., Liu, Y., Wang, X., Yu, Z., **Chen, Z.**, Wu, K., Frost, R., & Ni, B. J. (2020). Bentonite-supported nano zero-valent iron composite as a green catalyst for bisphenol A degradation: Preparation, performance, and mechanism of action. *Journal of Environmental Management*, 260, 110105.

TABLE OF CONTENTS

TITLE PAGE	
CERTIFICATION OF ORIGINAL AUTHORSHIP	i
ACKNOWLEDGEMENTS	ii
RESEARCH PUBLICATIONS	iv
TABLE OF CONTENTS	vii
LIST OF ABBREVIATIONS/SYMBOLS	xi
LIST OF TABLES	xii
LIST OF FIGURES	xiii
ABSTRACT	xx
CHAPTER 1 Introduction	1
1.1. Research background	2
1.2. Objectives and scope of the research	3
1.3. Research significance	4
1.4. Organization of the thesis	4
CHAPTER 2 Literature review	8
2.1. Hydrogen energy and electrochemistry of water splitting	9
2.2. Key parameters for catalyst evaluation	10
2.3. Transition metal-based electrocatalysts for water splitting.....	12
2.3.1. Transition metal sulfides	13
2.3.2. Transition metal borides	18
2.4. Conclusions	39
CHAPTER 3 Experimental methods	40
3.1. Introduction	41

3.2.Experimental materials.....	41
3.3.Catalyst preparation	41
3.4.Materials characterization	42
3.4.1. X-ray diffraction	42
3.4.2. Scanning electron microscopy	43
3.4.3. X-ray photoelectron spectroscopy	43
3.4.4. Transmission electron microscopy	43
3.4.5. Inductively coupled plasma spectroscopy	43
3.4.6. Raman spectroscopy	44
3.4.7. Fourier-transform infrared spectroscopy	44
3.4.8. N ₂ sorption/desorption measurement.....	45
3.4.9. Vibrating sample magnetometer measurement.....	45
3.5.Electrochemical techniques.....	45
3.5.1. Electrode preparation	45
3.5.2. Cyclic voltammetry.....	45
3.5.3. Linear sweep voltammetry.....	46
3.5.4. Electrochemical impedance spectroscopy	46
3.5.5. Chronopotentiometry and chronoamperometry test	46
3.6.Computational methods	46
CHAPTER 4 Tuning electronic property and surface reconstruction of amorphous iron borides via W-P co-doping for highly efficient oxygen evolution	48
4.1 Introduction	49
4.2.Experimental section.....	51
4.2.1.Catalyst synthesis.....	51
4.2.2.Material characterization	52
4.2.3.Electrochemical tests	53

4.2.4. Computational methods	53
4.3. Results and discussion.....	53
4.3.1. Synthesis and characterization	53
4.3.2. Electrochemical performance	57
4.3.3. Understanding the enhanced OER activity of W, P-FeB.....	63
4.4. Conclusions	71

CHAPTER 5 Controllable design of nanoworm-like nickel sulfides for efficient electrochemical water splitting in alkaline media

5.1. Introduction	74
5.2. Experimental section	75
5.2.1. Material synthesis	75
5.2.2. Structural characterization	76
5.2.3. Electrochemical tests	76
5.3. Results and discussion.....	76
5.3.1. Material characterizations	76
5.3.2. Electrocatalytic performance	80
5.4. Conclusions	85

CHAPTER 6 Integrating high-efficiency oxygen evolution catalysts featuring accelerated surface reconstruction from waste printed circuit boards via a boriding recycling strategy

6.1. Introduction	87
6.2. Experimental Methods	90
6.2.1. Catalyst synthesis.....	90
6.2.2. Physical and chemical characterization	91
6.2.3. Electrochemical tests	91
6.3. Results and Discussion.....	91

6.3.1.Catalyst synthesis and structural characterizations.....	91
6.3.2.Electrocatalytic performance of FNCSBs.....	98
6.3.3.Elucidation of the structure-activity correlations.....	106
6.4.Conclusions	110
CHAPTER 7 Recycling spent water treatment adsorbents for efficient electrocatalytic water oxidation reaction	112
7.1.Introduction	113
7.2.Experimental section.....	115
7.2.1.Conversion of spent adsorbents to electrocatalysts	115
7.2.2.Physical and chemical characterization	117
7.2.3.Electrochemical tests	117
7.3.Results and discussion.....	117
7.3.1.Conversion of spent adsorbents into borides/SA.....	117
7.3.2.Characterizations of synthesized borides/SA.....	121
7.3.3.Electrochemical properties of borides/SA	127
7.4.Conclusions	134
CHAPTER 8 Conclusions and recommendations.....	136
8.1. Conclusions	137
8.2. Recommendations	139
REFERENCES.....	141
APPENDIX	163

LIST OF ABBREVIATIONS/SYMBOLS

Abbreviations /Symbols	Description
CA	Chronoamperometry
C_{dl}	Double-layer capacitance
CP	Chronopotentiometry
CV	Cyclic voltammetry
j	Current density
DFT	Density functional theory
ECSA	Electrochemical surface area
EDS	Energy-dispersive X-ray spectroscopy
EIS	Electrochemical impedance spectroscopy
EWS	Electrochemical water splitting
FTIR	Fourier-transform infrared spectroscopy
HRTEM	High-resolution transmission electron microscopy
HER	Hydrogen evolution reaction
ICP-MS	Inductively coupled plasma mass spectrometry
ICP-OES	Inductively coupled plasma optical emission spectroscopy
LSV	Linear sweep voltammetry
NF	Nickel foam
OER	Oxygen evolution reaction
OWS	Overall water splitting
η	Overpotential
SAED	Selected area electron diffraction
TEM	Transmission electron microscopy
TMB	Transition metal borides
TMS	Transition metal sulfides
VSM	Vibrating sample magnetometer
WPCBs	Waste printed circuit boards
XRD	X-ray diffraction
XPS	X-ray photoelectron spectroscopy

LIST OF TABLES

Table 4.1	A summary of the property of OER for recently reported electrocatalysts supported on nickel foam.....	58
Table 4.2	Calculated charge transfer resistance (R_{ct}) and solution resistance (R_s) (in Ohm, Ω) of the materials deposited on NF obtained from the Nyquist plot during the EIS experiments.....	62
Table 6.1	The metal ion concentrations in leachate precursors.....	93
Table 6.2	A summary of base metal recovery from WPCBs with state-of-the-art techniques.....	94
Table 6.3	A summary of the OER properties of FNCSB-4 and the recently documented waste-derived OER catalysts.....	100
Table 6.4	A summary of the OER properties of the recently documented TM-based nanocatalysts, as well as a group of noble metal catalysts.....	102
Table 6.5	Calculated charge transfer resistance (R_{ct}) and solution resistance (R_s) (in Ohm, Ω) of the materials deposited on NF obtained from the Nyquist plot during the EIS experiments.....	104
Table 7.1	Characters of industrial wastewater.....	116
Table 7.2	Elemental composition of the biochar.....	124
Table 7.3	A summary of the recently documented TM-based and biochar-bearing OER catalysts.....	129
Table 7.4	Calculated charge transfer resistance (R_{ct}) and solution resistance (R_s) (in Ohm, Ω) of the materials deposited on NF obtained from the Nyquist plot during the EIS experiments.....	132

LIST OF FIGURES

- Figure 2.1** A sustainable pathway for the circulation of the hydrogen economy by combining renewable energy and water splitting.....9
- Figure 2.2** Scheme of water electrolyzers and the possible reaction pathways in basic and acidic solutions.....10
- Figure 2.3** (a) Schematic of the preparation of Ni₃S₂/NF and N-doped Ni₃S₂/NF. (b) HER polarization curves of the pristine (black) and N-doped Ni₃S₂/NF (red). (c) Tafel plots of the pristine and N-doped Ni₃S₂/NF. (d) Reaction energy of H adsorption, ΔG_{H^*} , displayed for sites present before (black lines) and after treatment (red lines). (e) Scheme for the preparation of Co₃S₄ PNS_{vac}. (f) EPR spectra of Co₃S₄ PNS_{vac} and Co₃S₄ NS. (g) The mass activity of different samples as a function of η . (h) The adsorption energies (ΔE_{ads}) and (i) the activation energy barriers of an H₂O molecule on three models surfaces.....16
- Figure 2.4** (a) Schematic illustration of the microstructure of Cu NDs/Ni₃S₂ NTs-CFs. (b) HRTEM image of Cu/Ni₃S₂ border. (c) LSV curves and (d) Tafel plots of Cu NDs/Ni₃S₂ NTs-CFs, Ni₃S₂ NTs-CFs, Cu NDs-CFs, and CFs. (e) The calculated adsorption free energy changes of H₂O on Cu/Ni₃S₂, Ni₃S₂, and Cu. (f) H adsorption free energy profiles of Cu NDs/Ni₃S₂ hybrid, Ni₃S₂, and Cu. (g) Schematic of hydrogen evolution process on Cu/Ni₃S₂. (h) HRTEM images of NiCo₂S₄/Ni₃S₂/NF. (i) Schematic illustration of 3D NiCo₂S₄/Ni₃S₂/NF. (j) Polarization curves and (k) the corresponding Tafel slopes of NiCo₂S₄/Ni₃S₂/NF, NiCo-LDH/NF, NiCo₂S₄/NF, Ni₃S₂/NF, and bare Ni foam.....18
- Figure 2.5** (a) Schematic illustration of the synthesis of VCNB via self-templated ion exchange method combined with atomic layer deposition. (b) TEM image of VCNB. The inset shows an enlarged image of the marked region. (c) EDX images for Co, V, Ni, and B in VCNB. Partial DOS (PDOS) plots for (d) VCNB and (e) possible charge transfer procedure in VCNB.....21

Figure 2.6	(a) XRD patterns of amorphous metal borides annealed at different temperatures. (b) Polarization curves of CNBO-NS and their annealed samples at different temperatures. (c) Influence of annealing temperature on the crystal structure of Co ₂ B. (d) HRTEM image of Co ₂ B-500. The inset shows the SAED pattern of the square marked region. (e) HRTEM image of Co ₂ B-500. The inset shows the unit cell structure of Co ₂ B. (f) LSVs of Co ₂ B and Co ₂ B annealed at 500 °C and 1000 °C. (g) Effect of annealing temperature on the OER activity. (h) XANES and (i) EXAFS spectra of Co ₂ B, Co ₂ B-500 and references of CoO and Co foils.....29
Figure 2.7	XPS analysis: (a) Ni 2p and (b) B 1s core-level spectra of Ni _x B minimally exposed to air (i) and after prolonged air exposure (ii). (c) O 1s spectra of Ni _x B-300 before and after the electrochemical activation. (d) XPS spectra of B 1s of the NiB _{0.45} /Cu before and after OER process. (e) HRTEM image of a NiB _{0.45} NP after used for OER electrolysis. (f) surface sensitive TEY XAS spectra at the Ni L-edge for the NiB _{0.45} film before and after OER electrolysis. (g) TEM image and (h) HRTEM image of the post-HER CoB catalyst, and the inset in (h) shows the SAED pattern. (i) XPS spectra of Co 2p of the CoB/NF, annealed CoB/NF, post-OER and post-HER CoB/NF catalysts.....33
Figure 4.1	Schematic illustration for the synthesis of W, P-FeB by a facile NaBH ₄ chemical reduction process.....53
Figure 4.2	Microscopic measurements of W, P-FeB. (a) SEM image of W, P-FeB. (b) High-resolution SEM image of W, P-FeB. (c) EDS mapping of W, P-FeB. (d) TEM image of W, P-FeB. (e) HRTEM image of W, P-FeB (the inset shows the corresponding SAED pattern).....54
Figure 4.3	XRD patterns of FeB, P-FeB, W-FeB, and W, P-FeB.....55
Figure 4.4	(a) XPS survey spectrum, (b) Fe 2p, (c) W 4f, (d) B 1s, (e) P 2p, and (f) O 1s XPS spectra of W, P-FeB. M in (d) and (f) means metal.....57

- Figure 4.5** (a) LSV curves of as-prepared catalysts in 1.0 M KOH. (b) Comparison of η_{10} , η_{50} , and η_{100} of as-prepared catalysts. (c) The effect of Fe/W feeds ratio on the η . (d) The effect of B/P feed ratio on the η . (e) Tafel plots of as-prepared catalysts. (f) Comparison of η and Tafel slope of OER between W, P-FeB and reported iron boride-based catalysts.....60
- Figure 4.6** (a) Cyclic voltammograms of W, P-FeB at different scan rates. (b) Scan rate dependence of j for as-prepared catalysts and the IrO₂ catalyst at 1.15 V vs. RHE. (c) Nyquist plots of as-prepared catalysts and the IrO₂ catalyst at 1.5 V vs. RHE. (d) Chronoamperometric curve of W, P-FeB at 1.458 V vs. RHE.....61
- Figure 4.7** (a) LSV curves of W, P-FeB before and after the CA test in 1 M KOH. (b) Chronoamperometric curve of the IrO₂ catalyst at 1.498 V vs. RHE.....63
- Figure 4.8** (a) ECSA values of W, P-FeB, W-FeB, P-FeB, FeB, and the IrO₂ catalyst. (b) LSV curves normalized with respect to ECSA for W, P-FeB, W -FeB, P-FeB, FeB, and the IrO₂ catalyst. (c-g) High-resolution XPS scans of W, P-FeB in the (c) Fe 2p, (d) W 4f, (e) O 1s, (f) B 1s, and (g) P 2p regions before and after the OER test. (h) The dissolved ion concentrations in electrolytes during the 25 h OER test. (i) HRTEM image of W, P-FeB after the OER test.....66
- Figure 4.9** (a) XRD patterns of the post-OER W, P-FeB sample and bare NF. (b) Raman spectra of W, P-FeB before and after the OER test....68
- Figure 4.10** The structural diagrams of FeOOH (a) and W-doped FeOOH (b). The charge population of FeOOH (c) and W-doped FeOOH (d)...69
- Figure 4.11** DFT simulations of OER. (a) Calculated electron density differences of FeOOH and W-doped FeOOH (red and blue colors denote electron accumulation and depletion, respectively; the labelled Fe atom is the selected active site for the free-energy calculation). (b) Computed DOS for FeOOH and W-doped FeOOH (the E_F is set to be zero). (c) Reaction free-energy diagrams for OER on FeOOH and W-doped FeOOH at zero potential ($U = 0$); the potential limiting steps and the η are also given. (d) Calculated free-

	energy landscapes for OER on W-doped FeOOH in alkaline solution at various potentials.....	70
Figure 4.12	Illustration of the proposed mechanism for OER activity enhancement.....	71
Figure 5.1	Schematic of the formation of NiS-NW/NF and NiS-NP/NF.....	77
Figure 5.2	(a) SEM image of NiS-NW/NF, (b) SEM image of NiS-NP/NF, (c) SEM-EDS mapping of NiS-NW/NF, (d) XRD patterns of NiS-NW/NF, NiS-NP/NF and bare Nickel foam, (e) HRTEM image of NiS-NW/NF.....	78
Figure 5.3	(a) XPS survey spectrum, (b) Ni 2p, and (c) S 2p XPS spectra of NiS-NW/NF.....	79
Figure 5.4	(a) LSV curves of the OER performance of Ni foam, NiS-NW/NF, NiS-NP/NF, and IrO ₂ /NF in 1.0 M KOH. (b) Comparison of η_{100} , η_{200} , and η_{400} of NiS-NW/NF, NiS-NP/NF, and IrO ₂ /NF. (c) Tafel plots of Ni foam, NiS-NW/NF, NiS-NP/NF, and IrO ₂ /NF. (d) Comparison of η and Tafel slope of OER between the NiS-NW/NF and reported nickel sulfide-based catalysts.....	81
Figure 5.5	(a-c) Cyclic voltammograms of NiS-NW/NF, NiS-NW/NF, and nickel foam at different scan rates. (d) Scan rate dependence of j for NiS-NW/NF, NiS-NW/NF, and nickel foam at 1.15 V vs. RHE, (e) Nyquist plots at the open circuit potential, (f) Amperometric i-t curve of NiS-NW/NF at 1.5 V versus RHE.....	82
Figure 5.6	XPS spectra of (a) Ni 2P and (b) S 2p in NiS-NW/NF before and after OER tests.....	83
Figure 5.7	(a) LSV curves of the HER performance of NiS-NW/NF, NiS-NW/NF, nickel foam, and 20 wt % Pt/C, (b) corresponding Tafel plots. (c) Amperometric i-t curve of NiS-NW/NF for HER at an η of 190 mV. (d) LSV curve of water electrolysis using NiS-NW/NF or NiS-NW/NF as both HER and OER electrocatalysts in a two-electrode configuration, (e) Amperometric i-t curve of NiS-NW/NF for water splitting at an applied potential of 1.563 V.....	84
Figure 6.1	Schematic illustration of the boriding recycling process. (a) Schematic illustration showing the synthesis of electrocatalysts for	

	OER from the waste leachates of WPCBs via a facile boriding recycling process. (b) Photographs of the WPCB leachates before and after the boriding reaction. (c) Recovery rates of Fe, Cu, Ni, and Sn via the boriding recycling process for FNCSB-4.....91
Figure 6.2	Microscopic characterization of FNCSB-4. (a, b) SEM images. (c) TEM bright-field image. (d) HRTEM image and (e) corresponding SAED pattern. (f) TEM EDS mapping.....96
Figure 6.3	XRD and XPS characterizations of FNCSB-4. (a) XRD pattern. (b) XPS survey of FNCSB-4. (c-h) High-resolution XPS spectra of B 1s, Sn 3d, Cu 2p, Ni 2p, Fe 2p, and O 1s for FNCSB-4.....98
Figure 6.4	OER performance of FNCSBs. (a) LSV curves of FNCSBs, the RuO ₂ catalyst, and bare NF. (b) η_{10} , and the current densities at 1.50 V vs. RHE of FNCSBs and the RuO ₂ catalyst. (c) Tafel plots of FNCSBs and the RuO ₂ catalyst. (d) OER activity comparison graph showing the Tafel slope with η_{10} for FNCSB-4 and reported state-of-the-art TM-based electrocatalysts, as well as noble metal-containing catalysts (listed in Table 6.3).....99
Figure 6.5	(a) Nyquist plots of FNCSBs and NF at 1.5 V vs. RHE, and the inset shows an enlarged part of the Nyquist plots. (b) ECSA normalized LSV curves for FNCSBs, and ECSA values of FNCSBs (inset). (c) Linear relationship between the η at the ECSA normalized current density of 3 mA cm ⁻² and the (Fe + Ni) ratio in FNCSBs of all FNCSBs. (d) Chronopotentiometry curve of FNCSB-4 at the j_{10} for 24 h.....105
Figure 6.6	Post-OER characterizations of FNCSB-4. (a) TEM and (b) HRTEM images of FNCSB-4 after the OER test. High-resolution XPS scans in the (c) Ni 2p, (d) Fe 2p, (e) Cu 2p, (f) O 1s, (g) B1s, and (h) Sn 3d regions of FNCSB-4 before and after the OER stability test...108
Figure 6.7	Surface evolution process of FNCSB-4 during OER. (a) B and Sn leaching in electrolytes during the 12 h OER test. (b) LSV curves of pristine FNCSB-4, CV activated FNCSB-4, and post-OER FNCSB-4 in 1.0 M KOH. (c) Difference in current density ($\Delta j = (j_a - j_c)/2$) plots against scan rate of FNCSB-4 before and after OER test, and

	the inset shows the ECSA values. (d) Illustration of the proposed surface evolution process and the mechanism for the enhanced OER activity of FNCSB-4.....	110
Figure 7.1	Schematic of the design of heterostructured OER electrocatalysts from spent biochar adsorbents.....	117
Figure 7.2	(a) Industrial process of spent adsorbents treatment. (b) General strategy of converting biochar based heavy metal contaminated spent adsorbents into OER electrocatalysts, and the multiple merits of multimetal borides/SA as electrocatalysts for OER.....	119
Figure 7.3	(a) An image of magnetic separation of metal boride/biochar heterostructures from reaction solution. (b) conversion efficiency of NiCuB/SA and NiCuFeB/SA reaction system.....	120
Figure 7.4	XPS spectra of (a) C 1s, (b) N1s and (c) O 1s for biochar before and after metal ions adsorption, (d) Fe 2p, (e) Ni 2p, and (f) Cu 2p spectra for post-adsorption biochar.....	122
Figure 7.5	(a) N ₂ adsorption-desorption isotherms of the biochar, (b) corresponding pore distribution of the biochar based on a method of Barrett-Joyner-Halenda (BJH).....	123
Figure 7.6	Microscopic characterization of the as-converted NiCuFeB/SA. (a) TEM image. (b) HRTEM image, and the inset is the corresponding SAED pattern. (c) EDS mapping.....	123
Figure 7.7	(a) XRD patterns of NiCuFeB/SA, NiCuB/SA, and SA. XPS spectra of NiCuFeB/SA: (b) survey (c) B 1s, (d) C 1s, (e) N 1s, (f) O 1s, (g) Ni 2p, (h) Fe 2p, and (i) Cu 2p.....	125
Figure 7.8	FTIR spectrum of SA.....	127
Figure 7.9	OER performance of catalysts. (a) LSV curves and (b) Tafel plots of the catalysts in 1.0 M KOH. (c) Comparison of η_{100} , η_{10} , and Tafel slopes of NiCuB/SA, NiCuFeB/SA, and the RuO ₂ catalyst. (d) LSV curves real wastewater-based NiCuFeB/SA and simulated wastewater-based NiCuFeB/SA. (e) OER activity comparison graph showing the Tafel slope with η_{10} for NiCuFeB/SA and reported the state-of-the-art TM-based electrocatalysts, as well as biochar-based heterostructured catalysts.....	127

Figure 7.10	(a) Nyquist plots of NiCuB/SA, NiCuFeB/SA, and NF at 1.5 V vs. RHE, and the inset shows an enlarged part of the Nyquist plots. (b) The difference in current density ($\Delta j = (j_a - j_c)/2$) plots against scan rate of as-prepared catalysts. (c) LSV curves normalized with ECSA of NiCuB/SA, NiCuFeB/SA, and NF, and the inset shows ECSA values. (d) LSV curves of NiCuFeB/SA before and after the OER test, and the inset shows the chronoamperometric curve of NiCuFeB/SA at 1.485 V vs. RHE.....	131
Figure 7.11	(a) TEM and (b) HRTEM images of NiCuFeB/SA after the OER test.....	133
Figure 7.12	High-resolution XPS scans of NiCuFeB/SA in (a) Fe 2p, (b) Cu 2p, (c) Ni 2p, and (d) B 1s regions after the OER test.....	134

ABSTRACT

Electrocatalytic water splitting (EWS) is a promising route to produce green hydrogen, which is centrally hindered by the anodic oxygen evolution reaction (OER) due to its sluggish kinetics. To advance the OER process, substantial efforts have been put into exploring high-performance catalysts. Recently, transition metal-based sulfide (TMS) and boride (TMB) catalysts have attracted enormous attention, while the design of novel TMSs/TMBs with high cost-effectiveness is an ongoing challenge. Hence, in this thesis, useful catalyst design strategies are developed for the construction of cost-effective TMS/TMB electrocatalysts.

The P and W dual-doping strategy was first used to design OER electrocatalysts from FeB with accelerated surface reconstruction and regulated intrinsic activity of evolved FeOOH. The obtained catalyst demonstrates an excellent OER activity (an overpotential of 209 mV to achieve 10 mA cm^{-2}), surpassing most boride-based catalysts. Specifically, anion etching facilitates surface reconstruction and W doping enhances intrinsic catalytic activity. Moreover, the hierarchical structure and amorphous features also benefit OER. This study provides a powerful strategy to construct efficient OER catalysts.

A morphology control strategy was then performed to construct nickel sulfides for overall water splitting (OWS). By taking advantage of small size, large electrochemical surface area, and good conductivity, the nanoworm-like nickel sulfides exhibit better performance for OWS than the nanoplate-like analogues. This study provides a facile strategy to design sulfide-based electrocatalysts for diverse applications.

Designing catalysts from wastes can further enhance catalysts' cost-effectiveness. Herein, a boriding method is developed to turn waste printed circuit boards into OER catalysts (FeNiCuSnBs). High metal recovery rates ($> 99\%$) are attained, and the optimal FNCSB-4 attains 10 mA cm^{-2} at an overpotential of 199 mV. The in-depth study suggests that the superior OER performance arises from accelerated surface self-reconstruction by B/Sn co-etching, and the newly formed multimetal (oxy)hydroxides are OER active species.

The boriding strategy was further implemented to convert spent adsorbents into heterostructural OER catalysts (NiCuFeB/SA) which outperforms many state-of-the-art catalysts. Comprehensive analyses suggest the high catalytic efficiency mainly attributed to the porous biochar confined well-dispersed metallic borides and the *in situ* evolved metal (oxy)hydroxides.

This thesis has realized the design of cost-effective TMS and TMB-based electrocatalysts for EWS, which provides guidelines for further design of novel catalysts for advanced electrochemical applications from earth abundant resources. In addition, the boriding strategy presented here may open up a new avenue to design functional materials from wastes.

CHAPTER 1

Introduction

1.1. Research background

The ever-growing demands in energy and the alerts for global environment deterioration and climate change have impelled researchers to develop green and advanced strategies to secure renewable energy supplies. Currently, hydrogen energy is recognized as an appealing alternative to exhaustible fossil fuels because of its earth abundance, high gravimetric energy density, and zero carbon footprints (Ding et al., 2021; Huang et al., 2017). However, a key challenge in the development of hydrogen energy is the sustainable and clean production of hydrogen gas (Yang et al., 2018). Compared with other conventional methods to produce hydrogen, electrocatalytic water splitting (EWS) is regarded as an efficient strategy to obtain hydrogen gas with high purity. The EWS comprises two half-reactions, including the OER at the anode and the hydrogen evolution reaction (HER) at the cathode. Compared with the 2e HER process, the anodic 4e OER is a more sluggish process, which is the main obstacle to fulfil efficient water electrolysis systems. To advance the OER efficiency, substantial efforts have been put into exploring cost-effective catalysts.

The efficiency of EWS is greatly governed by the electrochemical properties of catalysts. Nevertheless, noble metal (e.g., Ir, Pd, Ru, Pt) and oxides (e.g., IrO₂, RuO₂) exhibit high performances for HER and OER separately, the applications are severely limited by their low abundance and high cost as well as poor stability in long-term operation. Alternatively, numerous metal-based catalysts, especially transition metals (TMs), have achieved great success in the EWS process. To our delight, many TM-based catalysts even outperform the noble metal-based catalysts (Guo et al., 2019b; Lu et al., 2019; Sun et al., 2019a; Xin et al., 2019; Zhu et al., 2019b). Among various TM-based catalysts, TM sulfides (TMSs) and TM borides (TMBs) have attracted great interest owing to their good electroactivity, high

conductivity, tunable physical and chemical properties, and low price (Nsanzimana et al., 2019; Wu et al., 2021). Although remarkable progress has been achieved in the design of TMS and TMB-based catalysts for EWS, the development of novel cost-effective electrocatalysts is still an ongoing challenge. Typically, how to develop efficient catalyst design strategies to transform the mediocre materials into a high-performance catalyst through increasing the number of electroactive sites and enhancing the conductivity, intrinsic activity, and durability needs further investigations.

Apart from adopting efficient catalyst design strategies to develop favourable electrocatalysts, another vital factor that governs the cost-effectiveness of catalysts is the cost of catalytic materials. Recently, the synthesis of functional materials (e.g., adsorbents, catalysts, and electrode materials) from waste, which has environmental and economic benefits, has attracted growing attention (Assefi et al., 2019; Natarajan and Aravindan, 2018; Niu and Xu, 2019). Inspired by the concept of "waste-to-treasure" strategy and industrial ecology, considerable attention has been arisen to recycle and reuse urban mines solid wastes, including the ever-increasing electrical and electronic wastes. Recycling critical TMs (e.g., Fe, Ni, Cu, Sn, Mn) from the massive amount of wastes are particularly interesting, not only for their high economic potential but also ascribing to its potential environmental risks (Sun et al., 2020). To this end, developing novel methods to convert the wastes into efficient catalysts would significantly reduce the cost of electrocatalysts and eventually enhance the cost-effectiveness of the electrolyzer systems.

1.2.Objectives and scope of the research

This thesis focuses on developing TM-based electrocatalysts with high cost-effectiveness for EWS. Different TMS and TMB-based electrocatalysts

are designed and synthesized, and their applications in EWS (especially in OER) are explored. The specific objectives of the present study are as follows:

(1) To develop an efficient strategy to upgrade the electrocatalytic performance of iron borides for OER and investigate the catalytic mechanism with experimental and computational tools.

(2) To develop a useful approach to enhance the electrocatalytic activity of nickel sulfides for OWS and uncover the structure-performance relationship of nickel sulfides.

(3) To develop a method to turn electronic wastes into efficient electrocatalysts for OER and correlate the structure-performance relationship of the waste-derived catalysts.

(4) To develop efficient OER electrocatalysts from spent adsorbents and correlate the structure-performance relationship of the spent adsorbents-derived catalysts.

1.3. Research significance

This research mainly focuses on two main issues in the design of cost-effective electrocatalysts for water electrolysis. First, this research provides powerful strategies for the design of high-performance catalysts. Second, this research can offer efficient methods for the design of high-performance electrocatalysts from wastes, which is of great economic and environmental significance. Accordingly, the results presented in this thesis would provide enlightenment for the future design of cost-effective TM-based electrocatalysts for water splitting and other electrochemistry-driven advanced energy processes.

1.4. Organization of the thesis

This thesis contains eight chapters and the main content of each chapter are listed as follows:

Chapter 1 introduces the research background of developing TM-based electrocatalysts for water splitting, together with the objectives and scope of the research. The research significance is highlighted afterward.

Chapter 2 reviews the recent advances in the design of TMSs and TMBs for EWS, and an emphasis is put on illustrating the catalyst design strategies.

Chapter 3 introduces the detailed materials and experimental methods used in the study. It mainly includes experimental materials, catalyst preparation methods, materials characterization methods, and electrochemical techniques.

Chapter 4 demonstrates a rational design of tungsten and phosphorus co-doped amorphous FeB (W, P-FeB). It is found that the catalytic performance of *in situ* formed FeOOH can be improved via accelerating surface reconstruction by anion (P and B species) leaching and regulating intrinsic activity by evolved W incorporated-FeOOH. The results show that efficient pre-catalysts can be designed using a rational strategy through component regulation with P and W doping in amorphous FeB. Anion etching during the OER process can not only accelerate the mass/charge transfer but also facilitate surface self-reconstruction. Density functional theory (DFT) calculations further confirm that the W doping efficiently enhances intrinsic electrocatalytic activity by enhancing conductivity and optimizing the adsorption free energy of reaction intermediates. This study provides a fundamental insight into the correlation between surface structure- catalytic activity and an effectual strategy to design pre-catalysts for high OER performance.

Chapter 5 shows a one-step solvothermal method to construct nickel sulfides as efficient water splitting catalysts. By taking advantage of the small

size, abundant active sites, large electrochemical surface area, and good conductivity, the nanoworm-like nickel sulfides (NiS-NW/NF) exhibit better OER performance than the nanoplate-like analogues. Additionally, the NiS-NW/NF directly used as bifunctional electrodes for OWS requires a low voltage of 1.563 V to attain j_{10} with good long-term durability. This work provides a facile strategy for the design of efficient nickel sulfide-based electrocatalysts for energy conversion applications.

Chapter 6 demonstrates a facile boriding strategy to directly convert the multimetal cations contained leachates of waste printed circuit boards in multimetal borides (FeNiCuSnBs) for efficient OER. Fe, Ni, Cu, and Sn have been efficiently recovered from the leachate via the novel boriding process. The as-obtained mixed metal boride catalysts have exhibited excellent OER performance with low OER catalyst manufacturing costs. Additionally, it is unveiled that the accelerated surface reconstruction induced by B/Sn etching significantly promotes the OER process. Moreover, the efficient mass/charge transfer and multiple active sites (Ni/Fe/Cu (oxy)hydroxides) and the amorphous hierarchical structure also benefit the OER performance. Considerably, the proposed facile and efficient boriding strategy can be applied to regenerate efficient catalysts from WPCBs and be extended to the high-efficiency waste metal recovery and reutilization of critical metals from other electrical and electronic wastes.

Chapter 7 introduces a facile boriding route to directly convert the multiple metal ions contaminated biochar adsorbents into heterostructured electrocatalysts. Via this one-step boriding strategy, the converted spent biochar adsorbent shows high efficiency in electrocatalytic OER. With a low manufacturing cost, the optimized heterostructured catalyst exhibits excellent OER performance. Furthermore, comprehensive analyses suggest the high catalytic efficiency mainly attributed to the porous biochar confined well-

dispersed nano-sized metallic borides. The boriding method developed in this report can not only be applied to regenerate efficient catalysts from biochar-based spent carbon-based adsorbents, but can be further broadened to other types of spent heavy metal removal products, like membranes, metal oxides/sulfides adsorbents, metal-organic frameworks, and polymeric nanocomposites, for other types of advanced applications.

Chapter 8 concludes the main results of the four studies in Chapters 4 – 7 and outlines future research challenges and perspectives in this field.

CHAPTER 2

Literature review

This chapter has been published as *Current Opinion in Green and Sustainable Chemistry*, 2021, 27, 100398, *Journal of Materials Chemistry A*, 2019, 7(25), 14971-15005, and *Nano Research*, 2020, 13(2), 293-314 with modifications.

2.1. Hydrogen energy and electrochemistry of water splitting

Rapidly increased utilization of traditional fossil fuels and the negative environmental consequences have motivated researchers to develop advanced strategies to secure renewable and affordable energy supplies (Chen et al., 2020d; Lyu et al., 2019). Due to the earth-abundance, high gravimetric energy density, and carbon-free emission, hydrogen energy is a promising candidate to replace exhaustible fossil fuels (Shan et al., 2019). Currently, most of the hydrogen gas (over 95%) is produced from fossil fuels, however, such a process induces severe environmental problems. Alternatively, water electrolysis powered by renewable energy sources (e.g., solar, wind) can produce high-purity eco-friendly hydrogen, which is recognized as a green and sustainable technology to fulfill the hydrogen economy (Fig. 2.1) (Dastafkan and Zhao, 2020; Jiang et al., 2020; Zhang et al., 2020a).

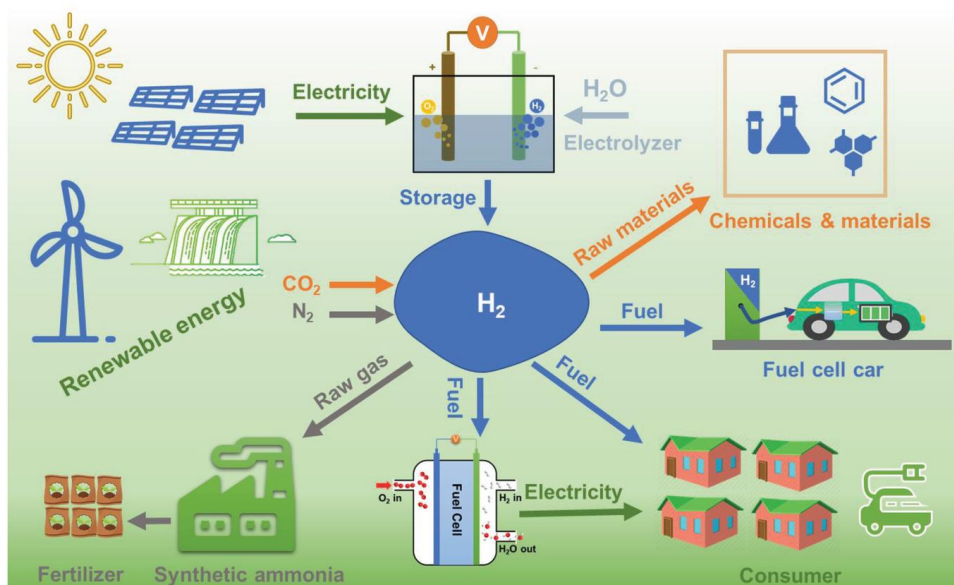


Figure 2.1. A sustainable pathway for the circulation of the hydrogen economy by combining renewable energy and water splitting (adapted from (Zhang et al., 2020a)).

Electrochemical water splitting (EWS) can produce high-purity oxygen and hydrogen gases in water electrolyzers at the anode and the cathode, respectively. The possible reaction pathways are listed in Fig. 2.2 (Guo et al.,

2019d; Varun Vij, 2017). Theoretically, EWS just needs a potential of 1.23 V (25 °C, 1 atm) to initiate the reactions (Chaudhari et al., 2017; Han et al., 2016). However, a higher potential is required due to the intrinsic reaction activation barriers and other factors (e.g., contact and solution resistances) (Han et al., 2016). Hence, it is sensible to design cost-effective electrocatalysts for EWS. Especially, compared with the two-electron HER, the anodic four-electron OER is a more sluggish process, which is the main obstacle to fulfil efficient water electrolysis systems. To improve the OER efficiency, great efforts have been made to explore high-performance and cost-effective electrocatalysts.

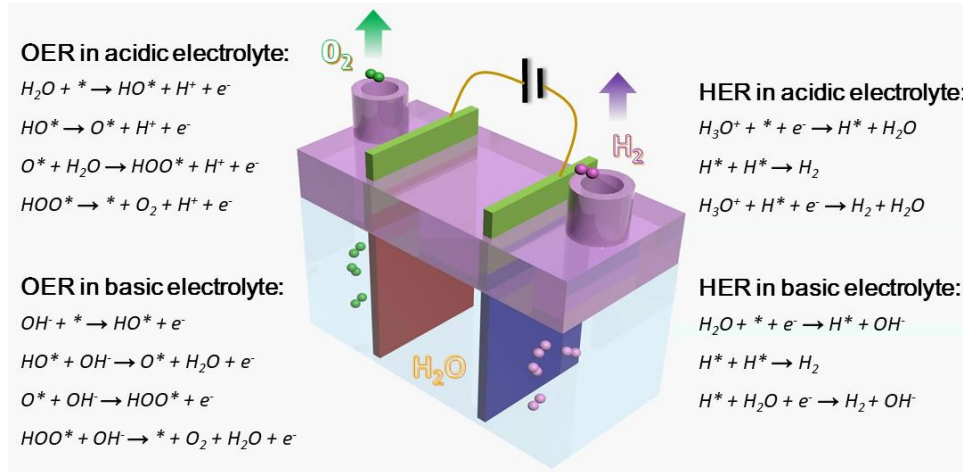


Figure 2.2. Scheme of water electrolyzers and the possible reaction pathways in basic and acidic solutions.

2.2. Key parameters for catalyst evaluation

To guide the design of novel catalysts, it is of great significance to assess and compare the catalytic activities of different catalysts. Currently, some crucial parameters have been measured, including the overpotential (η), turnover frequency (TOF), Tafel plots, Faradaic efficiency, and durability, which can be used to evaluate the performance of the catalysts. In this part, these parameters will be briefly introduced, and more discussions can be obtained from an informative review by S. Anantharaj et al. (2018). η is the

extra potential that is required to overcome the reaction barriers and initiate the electrochemical reactions. Commonly, the η at a fixed current density (j) (e.g., 10 mA cm^{-2} , denoted as j_{10}) is calculated to estimate the activity of the catalyst; a lower η value illuminates a better electrocatalytic activity. Tafel plot can be obtained from the linear sweep voltammetry (LSV) curves. It discloses the electrochemical reaction kinetics by correlating the electrochemical reaction rate to η . The linear regions of the Tafel plot can be fitted by the Tafel equation ($\eta = a + b \log j$, where b means the Tafel slope). When $\eta = 0$, the acquired j obtained from the Tafel equation is defined as the exchange current density (j_0). Normally, j_0 indicates the intrinsic activity of electrocatalysts in the equilibrium state. For a good electrocatalyst, a low b and a large j_0 are required.

The Faradaic efficiency presents the utilization efficiency of the electron involved in the electrochemical reaction (i.e., OER or HER). It can be obtained by comparing the amount of the produced gas from the electrodes to the theoretical value. Usually, the amount of produced gas(es) can be determined via the internal water displacement method or measured by gas chromatography (GC). Additionally, the rotating ring disc electrode (RRDE) voltammetry (Guo et al., 2019d) or the fluorescence-based oxygen sensor (Han et al., 2016) can be used to measure oxygen.

TOF is interpreted as the number of reactants (H_2O) that an electrocatalyst can convert to the desired product (H_2 or O_2) per catalytic site per time unit. Therefore, TOF represents the intrinsic electrocatalytic activity of every catalytic site. Typically, the value of TOF can be measured by the following equation, $\text{TOF} = (jA)/(\alpha Fn)$, where A is the surface area of the working electrode; α represents the electron numbers of the catalyst; F means the Faraday's constant, and n is the number of moles of the active materials. It should be noticed that not all of the sites/atoms of the material are equally accessible or catalytically active, and thus it seems unrealistic to receive a precise TOF value for electrocatalysts. Nonetheless, it is still meaningful for comparing similar electrocatalytic materials.

Durability is another crucial parameter that determines the practicability of an electrocatalyst in commercial applications. Generally, there are two routes to measure the stability of the electrocatalysts. The first one is to record the chronoamperometry curves or chronopotentiometry curves in a long-term operation. The second one is the accelerated degradation test, which records the LSV or cyclic voltammetry (CV) curves for thousands of cycles. A durable catalyst is expected to show a negligible shift of current density or potential after the stability test.

2.3. Transition metal-based electrocatalysts for water splitting

Both HER and OER involve several critical reaction intermediates including H*, O*, HO*, and HOO*. The generation of these intermediates is a prerequisite for EWS, which is governed by the properties of electrode materials (electrocatalysts). Therefore, nanomaterials that can effectually form these surface species with appropriate bonding energies are thus considered favorable electrocatalysts (Joo et al., 2019). In this context, noble-metal (NM, e.g., Ir, Ru, Pt, Pd)-based electrocatalysts are excellent candidatures for EWS. However, the prohibitive cost and limited reserves of NMs considerably hamper their large-scale applications (Wan et al., 2019a). Therefore, it is of great significance to develop low-cost, electroactive, and robust electrocatalysts for EWS (Kong et al., 2020; Xing et al., 2019).

Transition metals have significantly contributed to the development of advanced electrocatalysts because of their high abundance, impressive activities, and easy accessibility. Lately, researchers perform intensive and extensive studies on the design and application of TM-based catalysts for EWS. To our delight, grand progress on both catalyst synthesis and mechanism explorations rapidly pushes the boundary of the field to a high level. Part of these TM-catalysts are promising alternatives to the NM-based materials and provide new concepts to design cost-effective electrocatalysts for EWS.

Notably, TMs, TM alloys, and TMXs (X = O, S, Se, N, P, C, and B) exhibit good catalytic activities. Among these categories, TMS and TMB are well studied because of their high conductivity, high electroactivity, and low-cost (Nsanzimana et al., 2019; Wu et al., 2021). In this section, the recent achievements of TMS and TMB-based catalysts will be showcased and classified by the catalyst design strategies.

2.3.1. Transition metal sulfides

TMSs are outstanding catalysts for alkaline HER and OER owing to their high catalytic activity and low price (Anantharaj et al., 2016). Researchers hold different opinions on the role of S atoms in TMSs in their excellent catalytic activities. On one hand, catalytic activities were determined by the electronic properties of S atoms. With high electronegativity, S atoms in TMSs could withdraw electrons from TMs, and then sulfur acts as the electroactive sites to regulate the adsorption/desorption of reaction intermediates (Joo et al., 2019). On the other hand, S atoms may play an indirect role in alkaline HER by creating S vacancy to modify the electron density of TMs or improving water dissociation via the $S^{\delta-}-TM^{n+}-H_2O$ network (Joo et al., 2019; Staszak-Jirkovský et al., 2016). Currently, MoS_2 , Ni_xS_y , and Co_xS_y are the most reported TMSs, and the fabrication and catalysis of MoS_2 have been extensively studied and reviewed (Wang et al., 2018b; Wei et al., 2018). Therefore, in this part, we emphasize the design strategy of high-performance TMSs.

2.3.1.1. Anion doping

Ni_xS_y (NiS , NiS_2 , Ni_3S_2 , etc.) manifests good structural stabilities and appealing catalytic activities which exhibits great potentials for alkaline HER, especially the Ni_3S_2 . To further elevate the catalytic performance of Ni_3S_2 , doping appears as an attractive method. Take nitrogen as an example, Kou et al. (2018) prepared an N-doped Ni_3S_2/NF through hydrothermal reaction and

ammonia treatment (Fig. 2.3a). Compared to the pristine Ni₃S₂, the modified one exhibited a better alkaline HER ability with a lower η and Tafel slope (Fig. 2.3b-c). In addition, theoretical analysis implied that the outstanding catalytic activity of N-doped Ni₃S₂ could be attributed to the enriched electroactive sites and the favourable ΔG_{H^*} (Fig. 2.3d). Interestingly, it was unveiled that the activity of Ni₃S₂ particularly relied on the coordination number of the surface S atoms, as well as the charge depletion of the neighboring Ni atoms. Yu et al. (2018) also suggested that N-doping could significantly improve the electrocatalytic activity of Ni₂S₃. The N-doped Ni₂S₃ possessed a high surface area, and the great differences in electronegativity between H and N facilitated the adsorption of H. These features significantly upgraded the catalytic performance of N-doped Ni₂S₃, with a lower η compared to Ni₂S₃ ($\eta_{10} = 105$ vs. 228 mV). Similarly, Zhong and co-workers (2018b) investigated the electrocatalytic performance of N-doped Ni₃S₂/VS₂. Compared with bare Ni₃S₂/VS₂, the N-doped sample exhibited improved conductivity and a larger catalytically active area. Consequently, the N-doped Ni₃S₂/VS₂ exhibited a HER activity than other samples (e.g., Ni₃S₂/VS₂, N-doped Ni₃S₂, and Ni₃S₂). Briefly, the N-doping method can enrich the catalytic active sites, improve the conductivity and optimize the adsorption energy of reaction intermediates.

2.3.1.2. Cation doping

Other than anion-doping, introducing metal atoms into Ni₃S₂ frameworks also can improve electrocatalytic performance. Jian et al. (2018) fabricated Sn-doped Ni₃S₂ nanosheets by a facile hydrothermal process. Impressively, the Sn-Ni₃S₂/NF only took a very low potential of 1.46V at 10 mA cm⁻² for OWS. The Sn doping changed the morphology of pristine Ni₃S₂ and improved the intrinsic catalytic performance. Apart from Sn, other metals (e.g., Fe (Zhang et al., 2018b), V (Qu et al., 2017), Mn (Du et al., 2018)) also act as effective dopants that can improve the alkaline HER activity of Ni₃S₂. For example,

Zhang et al. (2018b) disclosed the mechanism for the enhanced electrocatalytic performance of Fe-Ni₃S₂/NF by systematic experiments and DFT calculations. The Fe-doping could enlarge the active surface area, improve the electronic conductivity, boost the water adsorption ability, and optimize the H adsorption energy of Ni₃S₂. These advantages cooperatively benefit the overall electrocatalytic performance of Fe_{17.5%}-Ni₃S₂/NF.

2.3.1.3. Defect engineering

Defect engineering by constructing S vacancies can further tailor the catalytic performance of TMSs. Theoretically, the presence of vacancies can modify the physicochemical properties and the electronic configuration of TMSs (Zhang and Lv, 2018), thus refining the intrinsic activity of catalysts. Zhang and co-workers (2018a) fabricated a non-layered structure of Co₃S₄ ultrathin porous nanosheets with plentiful S vacancies (Co₃S₄ PNS_{vac}) by Ar plasma-induced dry exfoliation (Fig. 2.3e). The obvious electron paramagnetic resonance (EPR) signal with $g = 2.003$ implied the abundant S vacancies (Fig. 2.3f). Electrochemical experiments indicated that the mass activity of Co₃S₄ PNS_{vac} was higher than that of pristine Co₃S₄ samples. As a result, the modified Co₃S₄ owned an extraordinarily large mass activity of 1056.6 A g⁻¹ at an η of 200 mV, surpassing the Pt/C (20 wt.%) electrode (Fig. 2.3g). In addition, Co₃S₄ PNS_{vac} possessed a lower water adsorption energy than Co₃S₄, so S vacancies could efficiently expedite the initial step of alkaline HER (Fig. 2.3h). The activation energy barrier of the water dissociation process for Co₃S₄ PNS_{vac} was also the lowest, which could benefit the formation of catalyst-H_{ads} (Fig. 2.3i). Altogether, the kinetics of alkaline HER can be impressively boosted. Moreover, Wu et al. (2017b) suggested that the rich S vacancies/defect sites in CoMoS layers could enhance the reactive sites for alkaline HER because the catalytic active sites are located at the basal edges of catalysts. More relevant

information on this topic can be found in the previous reviews by Jia et al. (2018).

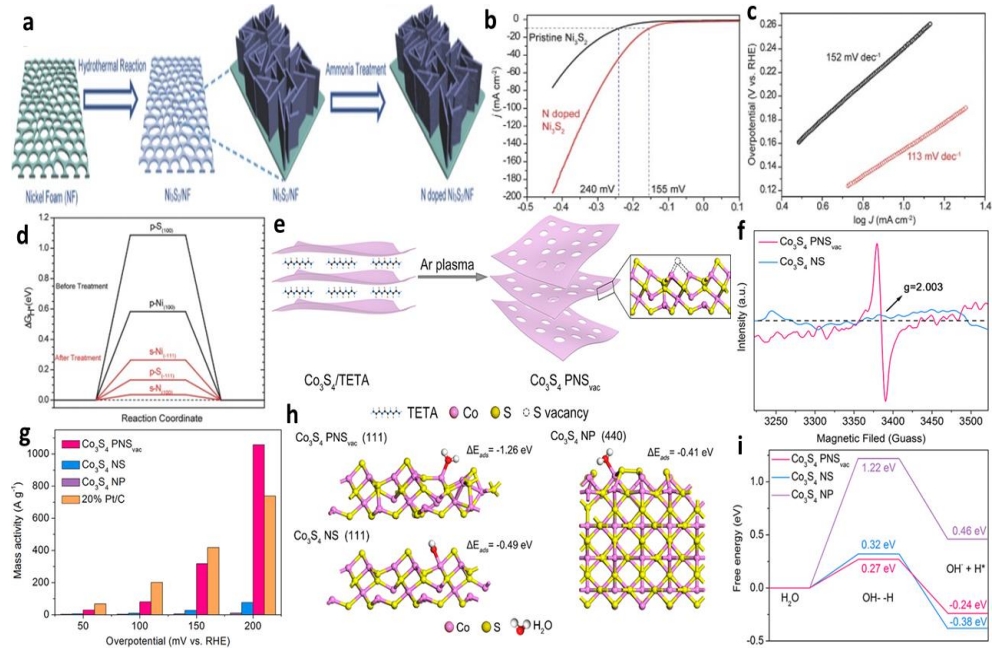


Figure 2.3. (a) Schematic of the preparation of Ni₃S₂/NF and N-doped Ni₃S₂/NF. (b) HER polarization curves of the pristine (black) and N-doped Ni₃S₂/NF (red). (c) Tafel plots of the pristine and N-doped Ni₃S₂/NF. (d) Reaction energy of H adsorption, ΔG_{H*}, displayed for sites present before (black lines) and after treatment (red lines) (adapted from (Kou et al., 2018)). (e) Scheme for the preparation of Co₃S₄ PNS_{vac}. (f) EPR spectra of Co₃S₄ PNS_{vac} and Co₃S₄ NS. (g) The mass activity of different samples as a function of η. (h) The adsorption energies (ΔE_{ads}) and (i) the activation energy barriers of an H₂O molecule on three models surfaces (adapted from (Zhang et al., 2018a)).

2.3.1.4. Constructing heterostructures

Recently, a growing number of high-performance TMSs are fabricated as hybrids. These composites commonly consist of two or more active components. Strong interactions between the different compounds can induce electron transfer which will significantly optimize the intrinsic catalytic

activity of the metallic sites in TMSs (Feng et al., 2018). Recently, Feng et al. (2018) reported a Cu-Ni₃S₂ hybrid for alkaline HER (Fig. 2.4a-b). Compared with the single Ni₃S₂ and Cu-based samples, the metal/metal sulfide hybrids manifested a better electrochemical activity (Fig. 2.4c-d). The DFT calculations indicated that the electron density of Cu increased while the electron density of Ni₃S₂ decreased. The positively charged Cu could adsorb and activate H₂O molecules by capturing O atoms of water. As a result, the Cu/Ni₃S₂ hybrids owned a lower water adsorption energy and could promote H₂O adsorption for alkaline HER (Fig. 2.4e). In addition, the Cu/Ni₃S₂ hybrids attained appropriate adsorption energy of H (Fig. 2.4f), which was beneficial to H desorption. In short, the hybridization of Cu with Ni₃S₂ can facilitate the entire process of alkaline HER process (Fig. 2.4g).

In addition, the mixed TMSs possess more active sites and the electron tunneling effects between different TMSs also benefit the alkaline HER. For instance, Liu et al. (2018b) fabricated a 3D heteromorphous NiCo₂S₄/Ni₃S₂/NF network with NiCo-LDH as the precursor (Fig. 2.4i). The HRTEM image elucidated the interfacial heterostructure between NiCo₂S₄ and Ni₃S₂ terminations (Fig. 2.4h). The electrochemical tests indicated that NiCo₂S₄/Ni₃S₂/NF manifested a better catalytic activity towards HER with the lowest η_{10} (119 mV) and smallest Tafel slope (105.2 mV dec⁻¹) compared to other samples in Fig. 2.4j-k. Moreover, recently documented hybrids, like NiCo₂S₄/Co₉S₈ (Basu, 2018) also exhibit distinguished catalytic performance in alkaline HER.

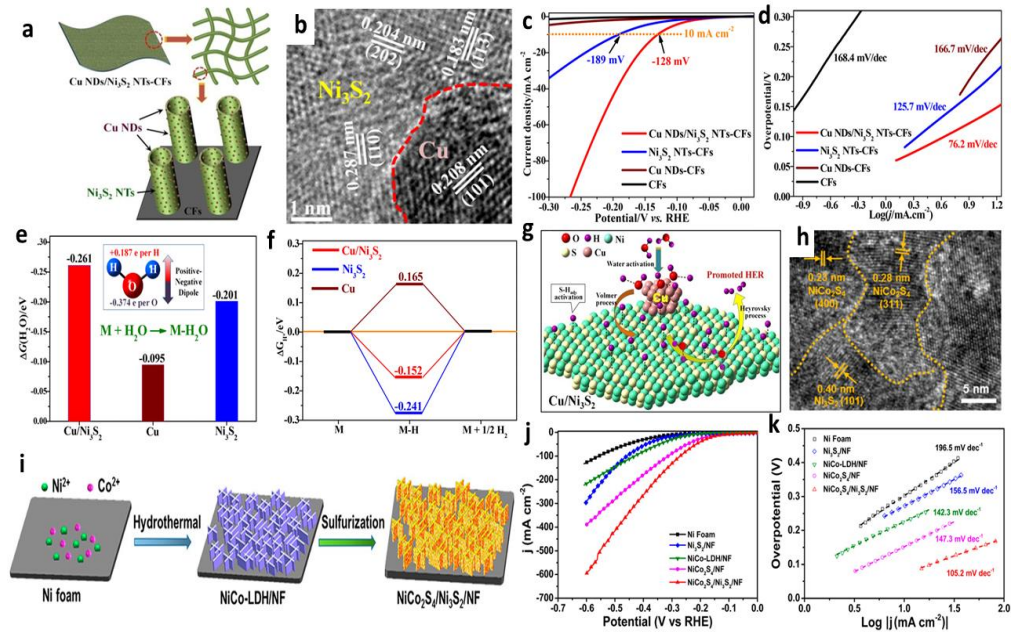


Figure 2.4. (a) Schematic illustration of the microstructure of Cu NDs/Ni₃S₂ NTs-CFs. (b) HRTEM image of Cu/Ni₃S₂ border. (c) LSV curves and (d) Tafel plots of Cu NDs/Ni₃S₂ NTs-CFs, Ni₃S₂ NTs-CFs, Cu NDs-CFs, and CFs. (e) The calculated adsorption free energy changes of H₂O on Cu/Ni₃S₂, Ni₃S₂, and Cu. (f) H adsorption free energy profiles of Cu NDs/Ni₃S₂ hybrid, Ni₃S₂, and Cu. (g) Schematic of hydrogen evolution process on Cu/Ni₃S₂ (adapted from (Feng et al., 2018)). (h) HRTEM images of NiCo₂S₄/Ni₃S₂/NF. (i) Schematic illustration of 3D NiCo₂S₄/Ni₃S₂/NF. (j) Polarization curves and (k) the corresponding Tafel slopes of NiCo₂S₄/Ni₃S₂/NF, NiCo-LDH/NF, NiCo₂S₄/NF, Ni₃S₂/NF, and bare Ni foam (adapted from (Liu et al., 2018b)).

2.3.2. Transition metal borides

Boride-based electrocatalysts are emerging as promising candidates for HER and/or OER catalysts due to their good catalytic activity, earth abundance, wide accessibility, and environmental benignity (Hao et al., 2018). Nevertheless, the promotable electroactivity, and low exposure of the surface-active site, of TMBs hampered their electrocatalytic performances severely (Chen et al., 2019a). To tackle these issues, a series of advanced strategies are advocated to tailor the property of TMBs by morphology, component, structure, or surface engineering.

2.3.2.1. Morphology control

The morphology of catalysts has profound effects on the electrocatalytic performance by determining the population of the exposed active sites and governing the adsorption/desorption behaviors of the intermediates and reactants (Wang et al., 2018c). For TMBs, the large particle size and thick aggregates/films severely constrain the exposure of catalytic active sites and remarkably inhibit the catalytic performance of TMBs for EWS. To disperse the catalyst particles and increase the exposure of the active centres, the morphology of TMB can be shaped by downsizing or building nanostructures such as nanochains, nanosheets, nanospheres, and hierarchical nanostructures.

TMB catalysts present as large particle sizes with low active surface areas due to the agglomeration in the synthesis, which dramatically affects the catalytic activity (Wu et al., 2019c). Downsizing TMBs into nanoparticles is a feasible and efficient strategy, which can enlarge the specific surface area and populate accessible active sites; the process further facilitates the interactions between electrolytes and catalysts, and eventually upgrades the electrocatalytic performances in EWS. For example, Zhang et al. (2018c) designed the Co-10Ni-B and the Co-10Ni-B-sp catalysts by chemical reduction and water-in-oil micro-emulsion strategy, respectively. The mesoporous Co-10Ni-B-sp exhibited a smaller average particle size (10 ± 3 nm) and a higher Brunauer-Emmett-Teller (BET) surface area ($118.85 \text{ m}^2 \text{ g}^{-1}$) than the Co-10Ni-B (20 ± 5 nm and $46.89 \text{ m}^2 \text{ g}^{-1}$). These characteristics drastically increased the density of active sites. As a result, the Co-10Ni-B-sp exhibited better electrocatalytic performance for OER than Co-10Ni-B, with a lower η ($\eta_{10} = 310$ vs. 330 mV of Co-10Ni-B) and a lower Tafel slope (66 vs. 73.3 mV dec^{-1} of Co-10Ni-B).

Nanosizing also has significant impacts on the electroactivity of TMB catalysts (Jothi et al., 2018; Wang et al., 2019b; Zeng et al., 2016). Wang et al. (2019b) found that the bipolar electrochemistry (BP) treatment could reduce the size of commercial Mo_2B_5 and W_2B_5 from the micrometer to nanometer; meanwhile, the thickness of bulk materials was significantly decreased. The BP-treated borides possessed a higher electrocatalytic performance for HER

than the bulk counterparts, and the BP-treated W_2B_5 exhibited the best activity ($\eta_{10} = 210$ mV, Tafel slope 62.2 mV dec^{-1}). In addition, the downsized samples showed lower charge transfer resistance (R_{ct}) compared to their counterparts. Hence, the abundant active sites, fast electron transfer, and less oxidized surface contaminants induced by the BP treatment resulted in better HER performance.

2.3.2.2. Nanostructure control

The shape-dependent properties of TMB catalysts also attract enormous interest. To avoid the aggregation of TMB particles, unique nanostructures have been designed. Nanostructure control not only facilitates the enhancement of electroactive sites but promotes the penetration/diffusion of electrolytes in electrocatalytic processes (Chaudhari et al., 2017). Hence, the control of nanostructure demonstrates a favourable strategy to upgrade the ultimate electrocatalytic performance of the TMBs.

Recently, TMBs with diverse nanostructures (nanochains, nanosheets, nanoparticles, etc.) have exhibited impressive electroactivity for water splitting. For example, Nsanzimana and co-workers (2019) found that metal precursors have a vital influence on the morphology of TMBs. Four Co-B samples prepared with different cobalt salts (chloride (Cl), nitrate (N), acetate (Ac), and sulfate (S)) exhibited distinct nanostructures. Nanosheets and nanoparticles were fabricated using cobalt nitrate and chloride accordingly. Not surprisingly, the Co-B (N) nanosheets with the highest surface area exhibited the best electrocatalytic activity for OER than the peer catalysts. These results provide a facile tactic to control the morphology of resulting TMBs by selecting appropriate precursors. In this framework, nanochains also have been designed and exhibited appealing catalytic performance for EWS (Li et al., 2019d; Wu et al., 2019c). Li et al. (2019d) synthesized the NiCoFeB nanochains with the addition of polyvinyl pyrrolidone (PVP) in the chemical reduction process. Elements of Fe, Co, and Ni were evenly dispersed in the amorphous NiCoFeB nanochains with a width of ~ 20 nm. Benefited from the nanochain structure and composition of multi-metals, NiCoFeB exhibited great potential for both HER ($\eta_{10} = 64$ mV, Tafel slope 80.9 mV dec^{-1}) and OER ($\eta_{10} = 264$ mV, Tafel

slope 126.2 mV dec⁻¹).

Constructing hierarchical nanostructures emerges as an efficient strategy to develop high-performance electrocatalysts. A hierarchical nanostructure is composed of different nanoscale subunits, including nanoparticles/quantum dots (zero dimension, 0D), nanotubes/nanobelts/nanochains/nanowires (1D), and nanosheets (2D) (Wang et al., 2018c). Hierarchical nanostructures can take full advantage of the edges of each subunit and offer more chances to modify the physical and chemical characteristics for various applications. Furthermore, the hierarchical nanostructures can avoid particle aggregation, facilitate the exposure of electroactive sites, and accelerate the electrolyte penetration and diffusion, in addition to the rapid release of gaseous products in the electrocatalytic process (Wang et al., 2018c).

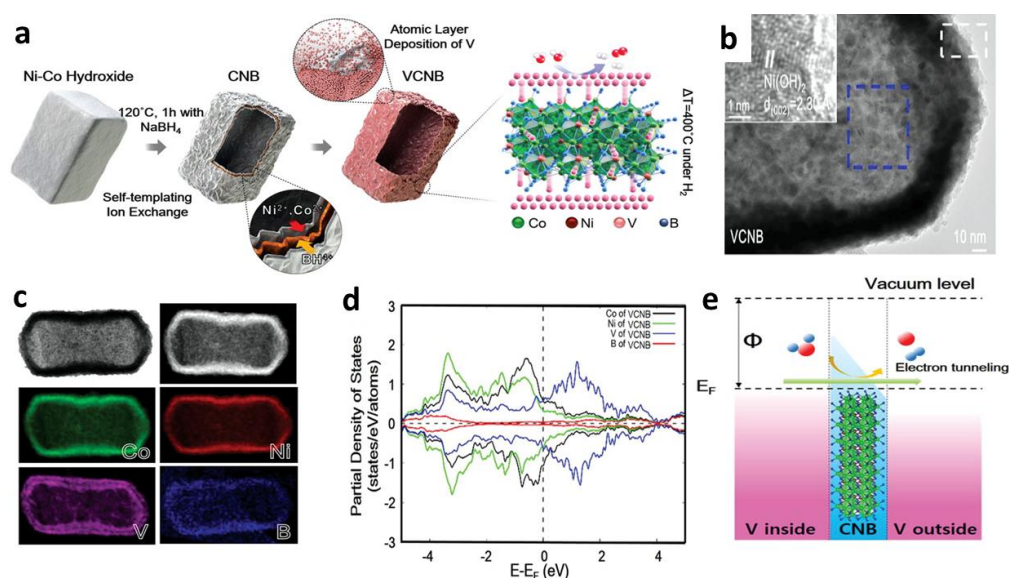


Figure 2.5. (a) Schematic illustration of the synthesis of VCNB via self-templated ion exchange method combined with atomic layer deposition. (b) TEM image of VCNB. The inset shows an enlarged image of the marked region. (c) EDX images for Co, V, Ni, and B in VCNB. Partial DOS (PDOS) plots for (d) VCNB and (e) possible charge transfer procedure in VCNB (adapted from (Han et al., 2019b)).

Han and co-authors (2019b) reported a vanadium-doped cobalt nickel boride (VCNB) via a self-templating route combined with the atomic layer

deposition (Fig. 2.5a). The VCNB hierarchical nanostructures consisted of boride nanosheets anchored on the hollow nanoprism (Fig. 2.5b). Surprisingly, V was well scattered over the hierarchical nanosheets, and a double-layered structure (V-CNB-V) was successfully constructed (Fig. 2.5c). The as-prepared VCNB exhibited a high catalytic performance for OER ($\eta_{10} = 340$ mV, Tafel slope = 58 mV dec^{-1}). The intriguing V-CNB-V double-layered structure played a key role in maintaining the great OER activity and durability. DFT calculation unveiled that the V atoms in the vicinity of Co and Ni served as charge carrier suppliers enhancing charge transfer (Fig. 2.5d-e). Additionally, the induced electronic double layers of V could effectively inhibit the dissolution of the surface active sites. Therefore, the advantages of VCNB hierarchical nanostructure can be summarized in the following aspects. First, the hierarchical structure results in populated electroactive sites and efficient release of generated oxygen bubbles. Second, the V-CNB-V double-layer structure improves the charge transfer and stability. Third, the Ni atoms lower the energy barriers of the adsorption/desorption of intermediates, while Co and B atoms act as active sites for water oxidation. Currently, only a few TMB hierarchical nanostructures were reported, and more efforts are encouraged to explore high-performance TMB nanostructures for EWS.

2.3.2.3. Component tailoring

The wide selection of TMB precursors provides massive opportunities for constructing high-performance TMB electrocatalysts with desired chemical compositions. For TMBs, the category and composition of the elements can significantly modulate the morphology, electronic structures, and robustness of the electrocatalysts, and ultimately the electrochemical performance (Liu et al., 2017). In this part, the implications of boron/metal ratios and hetero-atom dopants are detailed.

The B/TM atomic ratio can influence the morphology and intrinsic electrochemical activity of TMBs. Park and co-workers (2017a) discovered the boron-dependent electroactivity of Mo_xB_y for HER in acidic solutions. The boron-rich MoB_2 exhibited the highest electrocatalytic activity, followed by β -

MoB, α -MoB, and Mo₂B. The electrochemical surface area (ECSA) results indicated that the HER activity was promoted with increased B content from Mo₂B to MoB₂. Similar phenomena were reported by Zhang et al. (2016b), who found that Ni-B_{0.54} possessed a better electrocatalytic activity than its counterparts for HER in the wide pH range, following the order of Ni-B_{0.54} > Ni-B_{0.48} > Ni-B_{0.36} > Ni-B_{0.27}. It is intriguing to notice that the average particle size of Ni-B_x decreased from 2.27 to 0.55 μ m when the B/Ni atomic ratio increased from 0.27 to 0.54. Additionally, NiB_x with a richer content of B exhibited a higher ECSA than other borides. More active sites (metallic Ni nanocrystals) would be exposed on the NiB_{0.54} surface to electrolytes which enhanced the HER performance. Apart from MoB_x and NiB_x, FeB_x also presented a similar tendency. However, Ma et al. (2017b) reported the contradictory results that there was no direct correlation between OER performance of Co_xB and Co/B ratios. Compared with CoB and Co₃B, Co₂B exhibited higher electrochemical activities for OER (Co₂B > Co₃B > CoB). Further investigations suggested that the ECSA values of Co_xB catalysts were in line with their trend in OER performance, and Co₂B exhibited a higher effective active area. Additionally, the R_{ct} of Co₂B was smaller than the analogues, indicating a faster charge transport during the electrochemical processes. Therefore, the higher performance of Co₂B was attributed to its better conductivity and larger active areas.

Based on the above results, it may not be accurate to predict the electrochemical activity of TMBs just based on the B/TM atomic ratio. The reason may be that other characteristics/factors (e.g., particle size, morphology, surface area, structure, nature of active sites) can profoundly affect the electrocatalytic performance, and the variation of B/TM atomic ratios would partially tailor these features. As a result, these factors should be critically evaluated in the catalytic system to unveil the intrinsic role of TMBs in electrocatalytic reactions (Park et al., 2017a).

The synergic effect can be induced by incorporating other metal elements to enhance the catalytic performance of TMB. The hetero-metal dopants can enlarge the surface area by diminishing the agglomeration, providing more

electroactive sites, regulating the crystal structure, and modulating the electronic structures (Guo et al., 2019a; Nsanzimana et al., 2018b). Therefore, cationic doping is a favourable strategy to develop mixed metal borides.

The influence of alien-metal dopants on the regulation of the electronic structure of TMBs has been extensively researched. The modified electronic configuration of TMBs can directly alter the intrinsic electrocatalytic activity of the surface active sites (Nsanzimana et al., 2018a; S. Gupta, 2016). For example, Li et al. (2019d) investigated the EWS performance of TMBs with different metal compositions. The multimetal borides nanochains were prepared with a one-pot chemical reduction. As a result, the OER and HER activities of TMBs highly depend on the category of metal dopants. Specifically, with more metal species involved, the catalytic activities are more favourable. The theoretical calculation witnessed the changes in electronic structure from CoB to NiCoFeB, as well as their different reaction energy barriers for OER. First, the Co-3d band in NiCoFeB had a higher electronegativity than that in CoB, which was ascribed to the electron transfer from Ni and Fe sites, especially the Fe-3d band. This was verified by the 3d orbital behaviors of Fe sites on the surface of NiCoFeB. The Fe-3d- t_{2g} had been broadened into multiple peaks compared with the Fe-site from the bulk metal, indicating the mixed-valence states for Fe (e.g., Fe^{2+} and Fe^{3+}) from NiCoFeB system. Second, the significant charge transfer between Co and B was experienced in NiCoFeB due to the better band-overlapping of Co-3d and B-2p orbitals. Besides, the stronger spin-polarization induced by the Fe-3d band in NiCoFeB benefited the dissociation of H_2O molecules over the strong polarized Co-surface-sites. Further, the NiCoFeB had a lower energy barrier in water splitting than the CoB (1.60 vs. 2.53 eV). The cationic doping improves the electrocatalytic activities of CoB by enhancing the electronegativity of Co, boosting the surface charge transfer, and facilitating water dissociation and mediation of the intermediates.

Chen et al. (2017) also probed the synergistic effect of Co and Fe in CoFeB for OER. Compared with FeB and CoB, the Co_xFeB showed a better activity toward OER. The co-occurrence of Co and Fe not only increased the

proportion of high-oxidation-state Co-OOH species but also promoted the conductivity. Interestingly, the atomic ratio of Co/Fe could affect the electrochemical performance, and Co₂-Fe-B (2 was the molar ratio of Co/Fe) performed better than its analogues. The highest Co²⁺/Co^{3+/4+} transformation amount (73.03 mC cm⁻²) and the high-valence Co species (Co^{3+/4+}) account for the superior activity of Co sites in OER.

Apart from improving the intrinsic catalytic activities and conductivity of TMBs, previous results demonstrated that metal doping could effectively shape the morphology by preventing TMBs from agglomeration (Chattopadhyay and Srivastava, 2017; S. Gupta, 2017). Therefore, the electrocatalytic properties can be enhanced by exposing more active sites. For example, Gupta and co-authors (2017) found that Mo-doping in Co-B led to lower agglomeration and a smaller average size than the bare Co-B (18 ± 6 vs. 30 nm). Moreover, The BET and ECSA results further confirmed the morphology change: the mesoporous Co-3Mo-B showed higher surface area (38.8 ± 0.5 m² g⁻¹) and ECSA (C_{dl}: 0.380 mF cm⁻²) than Co-B (20.3 ± 0.3 m² g⁻¹, 0.240 mF cm⁻²). Consequently, the Mo insertion increased the number of surface active sites. Furthermore, the higher TOF value of the Mo-doped sample indicated that Mo-doping also enhanced the intrinsic activity of the per catalytic site. As a result, the Co-3Mo-B exhibited a more satisfactory reactivity than Co-B in HER (η_{10} : 96 (Co-3Mo-B) vs. 197 (Co-B) mV, pH = 7).

Notably, the insertion of metals into TMBs can have diverse effects on the properties of catalysts, including the morphology, conductivity, and electronic configuration of the surface atoms. Hence, further research is expected to figure out the overall influence of cationic doping on the catalysts; more precise information can be provided for the principle of developing high-performance boride-based electrocatalysts.

Anionic doping is another strategy to regulate the electronic structure of TMBs, stemming from the different electronegativity between B and other anions (Kim et al., 2018; Sun et al., 2018). Phosphorus, with rich electrons, has been intensively investigated as a dopant to improve the electrochemical

activities of TMBs. Kim and co-workers (2018) found that $\text{Co}_{59}\text{B}_{20}\text{P}_{21}$ exhibited a better electrocatalytic activity for HER than Co-P and Co-B ($\eta_{10} = 172$ mV, Tafel slope = 68 mV dec^{-1}). Although the B/P atomic ratio had a marginal effect on the morphology of catalysts, the $\text{Co}_{59}\text{B}_{20}\text{P}_{21}$ (B/P ≈ 1) exhibited higher electrocatalytic properties than the analogues. Intriguingly, the HER intrinsic activity exhibited a volcano relationship when plotted as a function of the B/P ratio in the Co-P-B system. In-depth XPS results implied that the competitive electron transfer between Co-P and Co-B was operative in the ternary Co-P-B system and was maximized in $\text{Co}_{59}\text{P}_{20}\text{B}_{21}$ due to the favourable electronic structure of Co modulated by both P and B.

Importantly, the DFT results can further uncover the effects of anionic doping on the electronic structures of TMs. Hu and co-authors (2019a) investigated the influence of P and B co-doping on the electrocatalytic activities of an amorphous NiFe-based electrocatalyst. As expected, the P, B co-doping resulted in higher electrocatalytic performance of a-NiFePB for OER than the counterparts. DFT results suggested that the d electrons of both Ni and Fe were delocalized at the Fermi level to some extent, improved by the incorporation of P atoms, and further boosted by co-doping with P and B atoms. The off-domain effect of electrons not only promoted the electron transfer and conductivity but upgraded the intrinsic activity of the catalytic sites. Additionally, the narrowed d-band centre induced by B and P doping enhanced the interactions between the reactants and active site, ultimately improving the catalytic performances. Sun et al. (2018) also reported the advantages of Co-B-P over binary Co-P or Co-B for HER. Apart from the contribution of electronic regulation, the high superhydrophilicity of Co-B-P also facilitated the HER, because the hydrophilic and aerophobic surface accelerated the hydrogen gas released from the electrode surface.

The integration of dual-doping with metal and metal-free elements is an emerging schedule to further ameliorate the electrochemical performance of TMBs. Wu et al. (2019c) found that both Co and P doping could increase the OER and HER performance of Fe-B. The as-prepared chain-like $\text{Co}_1\text{-Fe}_1\text{-B-P}$ quaternary electrocatalyst showed higher catalytic performances for HER (η_{10}

= 173 mV, Tafel slope = 96 mV dec⁻¹) and OER (η_{10} = 225 mV, Tafel slope = 40 mV dec⁻¹) than its counterparts (e.g., Fe-B and Co₁-Fe₁-B). The satisfactory electrocatalytic activities mainly derive from the following aspects: (i) the coupling effects among B, P, Fe, and Co, which accelerates the electrocatalytic process by reducing the energy barrier; (ii) the 1D chain-like structure facilitates the exposure of active sites, mass transport, as well as the gas evolution. Currently, anionic doping has yet received enough attention, and more efforts are encouraged to explore the underlying mechanisms and design high-performance anionic-doped TMBs for water splitting.

2.3.2.4. Phase engineering

Crystalline phases of solid materials have remarkable impacts on their physical and chemical properties because of the differences in packing density, surface energy, reactivity, and durability. Moreover, it is highly ascertained that the electrocatalytic properties of materials considerably rely on the crystalline phase; thus, phase engineering can be an appealing strategy to manipulate the intrinsic electrocatalytic activity of TMBs.

Researchers recently found that the variation of B substructures in crystalline TMBs has a phenomenal effect on electrocatalytic activities. Typically, the boron layers in MB₂-type crystalline borides have four basic arrangements, including AlB₂-type diborides (M = Ta, Cr, Hf, Ti, Zr, Mo, V, Mn, and Nb), WB₂-type diboride (M = W), ReB₂-type diboride (M = Re), and RuB₂-type diboride (M = Ru) (Guo et al., 2019a). The boron atoms are covalently bonded into graphene-like boron layers in AlB₂-type diborides, while WB₂ possesses both puckered (phosphorene-like) and graphene-like boron layers; these boron layers feature "chair" and "boat" configurations in ReB₂ and RuB₂ diborides, respectively. For a typical transition metal, the boride with the flat graphene-like boron layer shows a higher electrocatalytic activity for HER than the counterparts (Jothi et al., 2018; Park et al., 2019). Park et al. (2017b) investigated the HER performance of Mo₂B₄, which consists of both flat and puckered boron layers. Surprisingly, the Mo₂B₄ exhibited similar catalytic performance to α -MoB₂ ($\eta_{3.5}$: 270 vs. 260 mV, Tafel

slope: 80 vs. 75 mV dec⁻¹), although Mo₂B₄ possessed a five-time larger surface area and a higher ECSA than α -MoB₂ (C_{dl} : 156 vs. 101 μ F cm⁻²). These results suggested that Mo₂B₄ possessed fewer active sites than α -MoB₂, and DFT calculations unveiled the mystery. The computation of ΔG_H for H adsorption on different surfaces showed that H bonded much stronger on the phosphorene-like boron layer than on the graphene-like boron layer, and ΔG_H of flat B layers is closed to the benchmark Pt. Therefore, the puckered phosphorene-like B layers perform unsatisfactorily for the HER, while graphene-like B layers exhibit magnificent catalytic activities.

Inspired by this, Park and co-authors (2019) designed the α -Mo_{0.7}W_{0.3}B₂ with flat B layers, by partially substituting Mo with W. Although α -WB₂ and β -WB₂ contain both graphene-like and phosphorene-like boron layers, the introduction of 30% W did not change the B layers in α -MoB₂, and only flat B layers were presented in the as-prepared α -Mo_{0.7}W_{0.3}B₂. Electrochemical results demonstrated that the HER performances of different catalysts were closely related to the structure of B layers in an order of β -MoB₂ < β -WB₂ < α -MoB₂ < α -Mo_{0.7}W_{0.3}B₂. Compared with the α -MoB₂, the better catalytic activities of α -Mo_{0.7}W_{0.3}B₂ were mainly due to the synergistic effects between Mo and W. In-depth DFT calculations also uncovered the importance of flat B layers to the HER process due to the favourable ΔG_H on graphene-like B layers. Therefore, crystalline borides with flat B layers are supposed to be more favourable for HER. Currently, the effects of B layer structures on the OER performance have not been explored, which deserves more attention.

The existence of amorphous phases is another feature of the TMBs. Compared with the crystalline analogues, amorphous phases have a higher proportion of under-coordinative and unsaturated sites. This eases the adsorption of intermediates/reactants in the EWS processes (Chattopadhyay and Srivastava, 2017; Han et al., 2019a). Additionally, the isotropic structure and chemical stability of amorphous TMBs also improve their overall performance for electrocatalytic reactions. Recently, a great number of amorphous TMBs have shown excellent performances for HER and/or OER. Intriguingly, some reports suggest that amorphous phases outperform the

crystalline counterparts for HER/OER. For example, Sun et al. (2018) regulated the crystallinity of the amorphous Co-B-P by heating the sample at 500 °C, and a mixture of Co₂B and Co was obtained. Compared with the amorphous Co-B-P, the crystalline phase showed inferior catalytic performance for the HER. Similarly, the crystallinity of the Co-Ni-B-O sample was found to be positively correlated with the annealing temperature (Fig. 2.6a), while the electrocatalytic activity of the amorphous Co-Ni-B-O for OER declined gradually with the increase in crystallinity (Fig. 2.6b) (He et al., 2018b). These results highly advocate the advantages of amorphous TMBs over their crystalline counterparts.

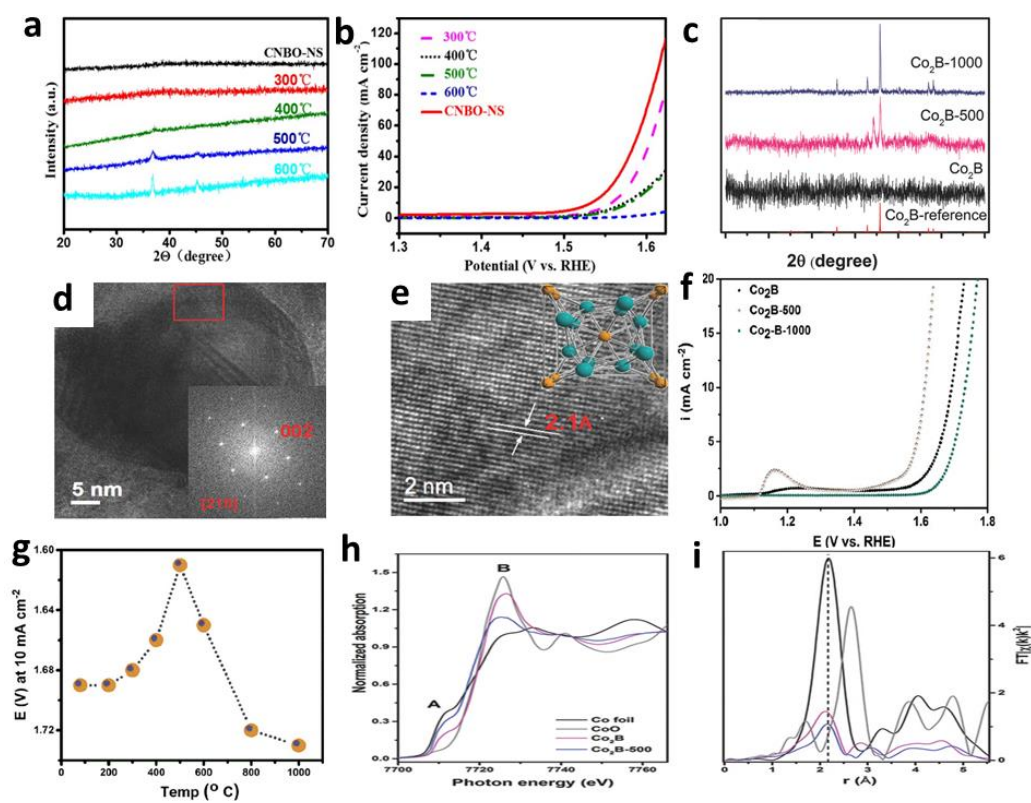


Figure 2.6. (a) XRD patterns of amorphous metal borides annealed at different temperatures. (b) Polarization curves of CNBO-NS and their annealed samples at different temperatures (adapted from (He et al., 2018b)). (c) Influence of annealing temperature on the crystal structure of Co₂B. (d) HRTEM image of Co₂B-500. The inset shows the SAED pattern of the square marked region. (e) HRTEM image of Co₂B-500. The inset shows the unit cell structure of Co₂B. (f) LSVs of Co₂B and Co₂B annealed at 500 °C and 1000 °C. (g) Effect of annealing temperature on the OER activity. (h) XANES and (i) EXAFS spectra

of Co₂B, Co₂B-500 and references of CoO and Co foils (adapted from (Masa et al., 2016)).

However, many contradictory results imply that the moderate improvement in crystallinity can profoundly upgrade the electrocatalytic performance (Cao et al., 2017; Jiang et al., 2017a; Jiang et al., 2017b; Masa et al., 2017; Masa et al., 2016; Xu et al., 2017). For instance, Masa et al. (2016) investigated the electrocatalytic properties of Co₂B annealed at different temperatures. The crystallinity of Co₂B samples increased with the elevated annealing temperature (Fig. 2.6c) and enlarged particle size. The HRTEM images indicated that discrete nanocrystallites of Co₂B in the extensive amorphous layer (Fig. 2.6d-e). Surprisingly, the Co₂B-500 exhibited the best catalytic performance for OER than the counterparts (Fig. 2.6f-g). Apart from the increased electrical conductivity and modified electronic structures, the authors claimed that the enhanced activity of Co₂B in OER at higher annealing temperatures (up to 500°C) was also associated with the lattice strain of cobalt crystal induced by boron (Fig. 2.6h-i). The lattice strain in Co potentially diminished the thermodynamic and kinetic barriers for the formation of key intermediates (e.g., OOH*), and thus facilitating the OER process. Nevertheless, the decrease in activity at much higher annealing temperatures was certainly due to the reduced surface area because of the growth in particle size.

Combining the individual advantages of amorphous and crystalline phases, Han and co-authors (2019a) investigated the role of crystalline-amorphous interfaces of F-doped Co₂B in the OER process. The as-prepared F-Co₂B exhibited high-density crystalline-amorphous interfaces (c-a interfaces). Compared with Co₂B and RuO₂, the F-Co₂B showed a higher performance for OER with a small η_{10} (320 mV) and a low Tafel slope (32 mV dec⁻¹). The ECSA of F-Co₂B was about 80 times greater than that for Co₂B because the c-a interfaces in F-Co₂B offered numerous active sites for the OER. Furthermore, the TOF values of Co₂B and F-Co₂B were 0.005 and 0.22 s⁻¹, respectively at an η of 320 mV. Therefore, the c-a interfaces also drastically upgraded the intrinsic OER activities. DFT calculation further uncovered the

role of c-a interfaces in the OER process. The energy barrier for the rate-determining step (III) (< 2 eV) was greatly reduced at the c-a interface, compared with those of the crystalline phase (5.18 eV) or the amorphous phase (4.0 eV). Interestingly, the HRTEM image of the post-OER sample illustrated the emergence of cobalt (oxy)hydroxide phases at the c-a interfaces. The energy landscapes illustrated that the CoOOH and Co(OH)₂ species are favourable active species for the generation of O₂ and OOH, respectively. As a result, the c-a interfaces with the cobalt (oxy)hydroxide phases led to magnificent OER performance.

It should be noticed that characterizations beyond XRD are required to monitor the phase change during the heating treatment. Thermal annealing at a relatively low temperature has a negligible effect on the XRD patterns, but many nanocrystalline and crystalline-amorphous phases may occur in this process (Han et al., 2019a; Masa et al., 2017). Although phase engineering can regulate the electrocatalytic performance of TMBs via tuning the electronic structures, improving the conductivity, and/or offering more active sites, only a few reports concentrate on phase engineering which deserves further exploration.

2.3.2.5. Surface oxidation

The surface oxidation of TMBs is an inevitable process when the catalysts are exposed to air/water (Nsanziimana et al., 2019; S. Gupta, 2017; Sun et al., 2019b). The oxidized TMBs surface can be composed of the TM oxides/(oxy)hydroxides, as well as the boron oxides/borates (Masa et al., 2019; Nsanziimana et al., 2019). More importantly, the formed oxygen-containing species and core@shell (TMB@TM oxide/(oxy)hydroxide) structure play a vital role in the electrochemical reactions. Many interesting studies have explored the effect of surface oxidation on the HER/OER performance of TMBs, which offers valuable information for the construction of high-performance TMB electrocatalysts for EWS, especially OER.

The origins of surface oxidation are diverse. Exposure to air/water, electrochemical activation, and electrochemical reaction (e.g., OER) can all

facilitate the evolution of oxidized surfaces over TMBs. Masa et al. (2017) investigated the effect of air exposure and electrochemical activation on the chemical state of Ni_xB . The air exposure of Ni_xB for several hours resulted in a high proportion of $\text{Ni}(\text{OH})_2$ while the proportion of surface Ni-B decreased profoundly (Fig. 2.7a). Correspondingly, the boron oxide species also increased while the content of $\text{B}^{(0)}$ almost disappeared (Fig. 2.7b). Meanwhile, the electrochemical activation process (50 cycles of potential cycling in 1.0 M KOH between 0.95-1.65 V vs. RHE) could convert the $\text{Ni}(\text{OH})_2$ into NiOOH ($\text{Ni}^{2+} \rightarrow \text{Ni}^{3+}$) in Fig. 2.7c. These pre-treatments can remarkably tune the chemical states of TMBs. The evolved boron-oxo species and the TM-oxide/(oxy)hydroxide species would benefit the following OER process. The OER can also promote the generation of other oxygen-containing species on the surface of TMBs (Jiang et al., 2017a; Xu et al., 2017). Jiang and co-authors (2017a) compared the XPS spectra of $\text{NiB}_{0.45}$ before and after OER. After OER electrolysis, the $\text{B}^{(0)}$ peak reduced significantly, and more BO_x was produced (Fig. 2.7d). In addition, the peaks of NiO_x also increased, which was further verified by electron microscopic and spectroscopic evidence. The HRTEM image suggested a thin layer of nickel oxides/hydroxides with a thickness of 6-8 nm was formed on the $\text{NiB}_{0.45}$ surface after the OER test (Fig. 2.7e). The bands centered at 480 and 560 cm^{-1} in the Raman spectra were assigned to NiOOH. Further, the XAS spectra found that the surface coordination environment around Ni in $\text{NiB}_{0.45}$ was modified from metal Ni-alike to NiO-alike, and the valence state of Ni is increased from 0 to +2 after the OER electrolysis (Fig. 2.7f). The scenarios in the HER process seem more complex. In the acidic HER process, the formed oxides on TMBs will be dissolved during the initial operation cycles (Park et al., 2017b). In contrast, mixed results were observed in the alkaline HER process. On the one hand, Li et al. (2017) found that the HER process had little effect on the chemical states of the FeB_2 catalyst, supported by XPS and ICP-OES analysis. On the other hand, Chen and co-workers (2018) found that the crystalline $\text{Co}(\text{OH})_2$ hexagonal nanoplates emerged after the HER test (Fig. 2.7g-i). So more in-depth investigations are necessary to uncover the variations of surface structure and chemistry during the HER processes.

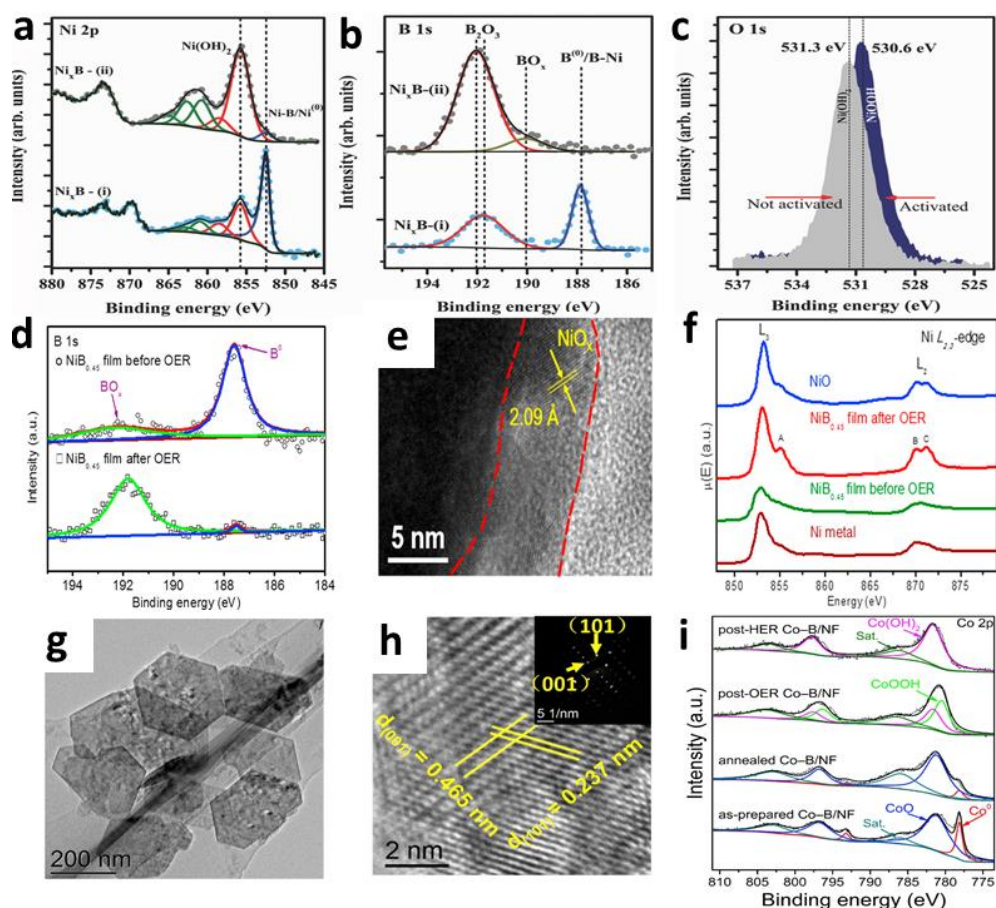


Figure 2.7. XPS analysis: (a) Ni 2p and (b) B 1s core-level spectra of Ni_xB minimally exposed to air (i) and after prolonged air exposure (ii). (c) O 1s spectra of Ni_xB -300 before and after the electrochemical activation (adapted from (Masa et al., 2017)). (d) High-resolution XPS spectra of B 1s of the $\text{NiB}_{0.45}/\text{Cu}$ before and after OER process. (e) HRTEM image of a $\text{NiB}_{0.45}$ NP after used for OER electrolysis. (f) surface sensitive TEY XAS spectra at the Ni L-edge for the $\text{NiB}_{0.45}$ film before and after OER electrolysis (adapted from (Jiang et al., 2017a)). (g) TEM image and (h) HRTEM image of the post-HER CoB catalyst. The inset in (h) shows the SAED pattern. (i) XPS spectra of Co 2p of the CoB/NF, annealed CoB/NF, post-OER and post-HER CoB/NF catalysts (adapted from (Chen et al., 2018)).

Taking the great advantages of TM oxides/(oxy)hydroxides in water dissociation processes (Anantharaj et al., 2017; Dionigi and Strasser, 2016), TMB@TM oxide/(oxy)hydroxide structures are promising candidates for EWS. Wang et al. (2019a) employed a facile approach of air exposure to oxidize the Fe_2B and FeB_2 samples. The surface-activated Fe_xB (Fe-B-

O@Fe_xB) was covered by an amorphous oxide/hydroxide layer due to the strong peaks of Fe³⁺ and B-O, as well as the negligible intensity of Fe_xB in the spectra of Fe 2p and B 1s. Surprisingly, the Fe-B-O@Fe_xB showed comparable OER performance to the IrO₂ catalyst. Further investigations revealed that the Fe oxide/hydroxides and borates on the surface of the completely oxidized Fe-B-O@Fe_xB promoted the OER performance. However, surface oxidation leads to poor HER performance. Guo and co-workers (2019e) functionalized the Ni_xB surface with similar oxidation treatment. The surface oxidized Ni_xB also possessed a Ni-B-O@Ni_xB structure. The increasing B content resulted in more Ni oxide/hydroxide and B_xO_y species and less Ni_xB. Hence, the boron-rich Ni-B-O@NiB₂ with the highest Ni oxide/hydroxide and B_xO_y species exhibited the most favourable OER activities than their counterparts. Nevertheless, the HER performance of Ni-B-O@Ni_xB was in the opposite order. Namely, the less surface oxidation, the better HER activity. Herein, a high reductivity of Ni_xB is expected for functioning as the HER catalysts.

As aforementioned, the oxide-rich surface can be *in situ* generated during the OER process, which offers a facile route to obtain high-performance TMB catalysts for EWS. For example, Li et al. (2019b) found that the boronized Ni was further oxidized after the electrochemical process. Intriguingly, the Ni(OH)₂ was transformed into γ -NiOOH as the active catalytic phase in the OER process. In this study, the importance of B/borates was also highlighted. The borates formed in the OER process could modify the electronic structure and increase the electron density around the Ni atoms because of the negative shift of the Ni 2p_{3/2} peak. Moreover, the presence of borates accelerated the electrochemical reaction rate, whereas the reaction pathways remained the same. As a result, the activated and boronized Ni exhibited a higher OER activity than the bare Ni.

Therefore, the surface activation via the facile oxidation can profoundly tailor the surface chemical characteristics of TMBs. Generally, TM components will convert to TM oxides/(oxy)hydroxides, and the B will be presented as boron oxides/borates. The types and ratios of different oxygen-containing species are highly dependent on the selected treatment process.

Currently, the role of generated TM oxides/(oxy)hydroxides has been emphasized, and these species can improve the OER activities. However, the evolved boron oxides/borates are rarely investigated, although they have exhibited great potentials as OER catalysts (Bediako et al., 2012; Chen et al., 2016; Hu et al., 2019b; Ma et al., 2017a). Accordingly, more in-depth discussions and surface characterizations are encouraged to explore the effect of boron-containing species on the evolution of TM-containing species, as well as on the OER activities. Another issue that should be taken into consideration is the influence of oxidation on the HER performance. As discussed above, many studies evidenced that the oxidized layer on TMBs is unfavourable for HER (Guo et al., 2019e; Park et al., 2017a; S. Gupta, 2016; Vrabel and Hu, 2012; Wang et al., 2019a; Wang et al., 2019b), while several reports indicated that the oxidation can facilitate the alkaline HER through the formation of TM hydroxides (Chen et al., 2019a). More *in situ* characterizations and experimental analysis are suggested to elucidate the relationship between the evolution of surface chemistry as well as the HER process.

2.3.2.6. Hybridization

It is well known that hybridization is a universal strategy to construct high-performance catalysts. The hybrids harmonically inherit the individual merits (e.g., good conductivity, abundant active sites, high electroactivity, great durability) of different components, and thus leading to upgraded performance (Long et al., 2019; Wang et al., 2018c). To improve the overall catalytic performance of TMBs for EWS, it is vital to decrease the agglomeration, improve the conductivity, and enhance the intrinsic electroactivity by compositing TMBs with other promising nanomaterials. Currently, functional materials, including conductive materials and electroactive materials, have been employed to hybridize with TMB for EWS.

To improve the electrocatalytic activities for EWS, TMBs can be supported over diverse porous materials, such as Ni foam (NF)/foil, Cu foam, carbon, and titanium, acquire both high conductivity and large surface area (Arivu et al., 2018; Hao et al., 2018). Due to their porous structure, these supports can efficiently disperse the electroactive catalysts and reduce

nanoparticles agglomeration; therefore, the composites can provide high surface area and abundant active sites (Chattopadhyay and Srivastava, 2017). Meanwhile, the porous scaffold also facilitates reactant diffusion through the pores to accelerate the EWS process.

Ni foam is frequently served as a support to construct binder-free TMB-based electrocatalysts because of its high conductivity, porous 3D structure, and low price. These features can improve the conductivity and stability, improve the dispersion of electroactive particles to attain a more electroactive surface area, increase the contact between the catalysts and electrolytes, and accelerate the release of generated gaseous products (Wang et al., 2018c). For example, Sun and co-workers (2018) designed a Co-B-P/NF electrode by electroless deposition under strong ultrasonication. Due to the firm adhesion between NF and Co-B-P and the strong hydrophilicity, the Co-B-P/NF electrode possessed a low interface resistance, high structural durability, and abundant active sites, as well as accelerated mass transfer. Together with other favourable properties toward HER, the as-prepared Co-B-P/NF showed great HER performance, with a low η_{10} (12 mV) and Tafel slope (42.1 mV dec⁻¹).

Apart from NF, other conductive substrates also exhibit great potentials in the synthesis of TMB-based hybrids. Lately, Hao et al. (2018) deposited a group of TMBs on different conductive substrates (CC, Ti foil, and Ni foil). The FESEM images elucidated a rather uniform coating of the TMBs on the conductive substrates, regardless of the chemical components of catalysts and the materials of substrates. The as-prepared 3D networks showed intimate interactions between the electroactive TMBs and the substrates, which facilitated the charge transfer and enhanced the stability. Surprisingly, a variety of supported TMBs exhibited impressive activities for HER and/or OER.

Carbon-based materials (carbon cloth/paper (Hao et al., 2019b; Kim et al., 2018; Sheng et al., 2018), porous carbon (Li et al., 2018b), graphene (An et al., 2018; Arivu et al., 2018; Masa et al., 2016; Nsanzimana et al., 2018a; Sun et al., 2019b), CNTs (Chen et al., 2019a; Elumeeva et al., 2017), etc.) have been frequently employed as TMB supports in EWS. Such hybrids would benefit

from the physical and chemical features of carbonaceous materials, such as the good electronic conductivity, large surface area, remarkable thermal stability, and great mechanical strength. Recently, Nsanzimana et al. (2018a) prepared a Fe-doped NiB coupled to reduced graphene oxide (GO) sheets by one-step chemical reduction. The abundant carboxyl and hydroxyl groups on the 2D GO could attract metal ions by electrostatic interaction; the introduction of NaBH₄ simultaneously reduced the metal ions and GO to rGO. Compared to the unsupported sample, the presence of rGO significantly boosted the OER performance, and 30% rGO was then revealed to be optimal. As the supported and unsupported catalysts with similar compositions shared a similar OER catalytic mechanism, the rGO support significantly enhanced the electrical conductivity rather than acting at the active compounds. Other studies also verified the rGO in the TMB-based hybrids improved the conductivity and promoted the formation of nanostructures (Arivu et al., 2018; Masa et al., 2016; Sun et al., 2019b).

Metal-organic framework (MOF)-based catalysts have shown great potentials in EWS due to their fascinating functionalities and diversities (Shi et al., 2019; Yan et al., 2018; Zhu et al., 2018a). Inheriting the merits of pure MOFs (e.g., tunable porosity, high surface area, and facile functionalization with other heteroatoms), MOF derivatives also attract enormous attention for the construction of nano-catalysts (Yan et al., 2018). For the first time, Li et al. (2018b) synthesized Co-B nanoparticles incorporated in porous carbon using a MOF (ZIF-67) as the precursor. The as-prepared Co-B/C exhibited a large surface area of 119 m² g⁻¹ because of the presence of porous carbon substrate derived from the ZIF-67. Compared to the analogues, Co-B/C showed better electrocatalytic performances in OER. The ZIF-67 derived porous carbon not only decreased the charge transfer resistance but also offered large ECAS. Benefiting from the high electrocatalytic activity of the Co-B species and the high conductivity and surface area of porous carbon, the synthesized Co-B/C thus displayed excellent OER activity. Based on this result, more MOFs can be employed as precursors to developing high-performance TMBs for EWS.

Preparing heterostructures with different electroactive materials is an

effective scheme to achieve higher electrocatalytic performance than the corresponding single part. The additional electroactive materials can not only increase the electroactive area but also manipulate the intrinsic activity of host materials through chemical coupling effects. For TMBs, several studies show that hybridizing TMBs with TM-based electroactive materials (e.g., TMSe (Guo et al., 2017), TMO (Lu et al., 2017), $\text{TM}(\text{OH})_2$ (Liang et al., 2018)) can dramatically upgrade the catalytic performance of TMBs for EWS.

Lately, Liang et al. (2018) developed a porous hierarchical structure $\text{NiB}@\text{Ni}(\text{OH})_2@\text{NF}$ via a facile dip-coating scheme. In this case, the $\text{Ni}(\text{OH})_2$ facilitated the generation of NiOOH , which accounted for OH^- adsorption in the OER process. Besides, NiB could provide an abundant catalytic site for OER. The synergistic effect between $\text{Ni}(\text{OH})_2$ and NiB also resulted in a low charge transfer resistance. Consequently, the $\text{NiB}@\text{Ni}(\text{OH})_2@\text{NF}$ exhibited a higher OER performance than the counterparts, even surpassing the benchmark RuO_2 . Similarly, Guo and co-authors (2017) found that the coupled effects between Co_2B and CoSe_2 nanosheets also lead to higher electrocatalytic activities for HER and OER than Co_2B and CoSe_2 . The hybrid was prepared via a chemical reduction process. The homogeneously distributed amino groups on the $\text{CoSe}_2/\text{DETA}$ surface-induced Co_2B nucleate, disperse and reduce the size, thus exposing more electroactive sites. Accordingly, the $\text{Co}_2\text{B}/\text{CoSe}_2$ hybrid exhibited better electrocatalytic performances for EWS than $\text{CoSe}_2/\text{DETA}$ and Co_2B , as well as good durability. In another study, She et al. (2019) found that the addition of $\text{Sr}_3\text{B}_2\text{O}_6$ into $\text{Sr}_{0.8}\text{Co}_{0.8}\text{Fe}_{0.2}\text{O}_{3-\delta}$ ($\text{S}_{0.8}\text{CF}$) perovskite could significantly improve the OER performance of $\text{S}_{0.8}\text{CF}$ perovskite. The $\text{Sr}_3\text{B}_2\text{O}_6$ served as a proton acceptor and enhanced the interfacial proton transfer, and thus facilitating the deprotonation of surface-bound intermediates. The hybrid exhibited a high OER activity with a low η of 240 mV in 1M KOH required for 10 mA cm^{-2} . Compositing TMBs with other electroactive materials is promising to construct high-performance catalysts for EWS, while there are limited relevant studies. Accordingly, more low-price electrocatalysts can be candidates to form TMB-based hybrids for EWS, which needs further investigations.

2.4. Conclusions

Developing advanced low-cost electrocatalysts for water splitting is of great scientific and industrial significance. Herein, recently reported efficient TM-based catalysts (TMS and TMB) for EWS are discussed. For TMS/TMB-based catalysts, strategies that aim at regulating the internal and external characteristics of nanomaterials are recommended, such as heteroatom-doping, hybridization, defect engineering, phase control, and nanostructure construction. To realize the commercial application of low-cost catalysts in water electrolyzers, some issues deserve further consideration. First, developing simple and scalable catalyst synthetic routes to enable mass production is a prerequisite for large-scale applications. Furthermore, it is favourable to construct efficient catalysts from wastes, which would significantly reduce the fabrication cost of catalysts. Second, in-depth study of the fundamental principles is required to gain full knowledge of the origin of activity improvement, which would guide the engineering of next-generation catalysts. Last, developing bifunctional catalysts is highly desirable given simplification, cost reduction, and practical application of water electrolyzers.

CHAPTER 3

Experimental methods

3.1. Introduction

This chapter presents detailed information about the experimental materials, catalyst preparation methods, materials characterization methods, and methods for catalyst performance assessment involved in Chapters 4 – 7.

3.2. Experimental materials

Iron(II) chloride ($\text{FeCl}_2 \cdot 4\text{H}_2\text{O}$), Hydrochloric acid (HCl), potassium sodium tartrate tetrahydrate ($\text{KNaC}_4\text{H}_4\text{O}_6 \cdot 4\text{H}_2\text{O}$), nitric acid (HNO_3), sodium tungstate dihydrate ($\text{Na}_2\text{WO}_4 \cdot 2\text{H}_2\text{O}$), sodium hypophosphite (NaH_2PO_2), 5 wt% Nafion solution, acetone ($\geq 99.5\%$), sulfuric acid (H_2SO_4), thiourea ($\geq 99.0\%$), sodium hydroxide (NaOH), isopropanol alcohol ($\geq 99.5\%$), potassium hydroxide (KOH), nickel foam (NF), zinc chloride (ZnCl_2), glycerol ($\geq 99.5\%$), sodium borohydride (NaBH_4), and ethanol were all purchased from Sigma-Aldrich and were used without further purification. Deionized (DI) water from a Millipore Milli-Q water system was used. The graphite rod and Hg/HgO electrode were purchased from Tianjin Aida Hengsheng Technology Development Co., Ltd. The waste printed circuit boards leachates used in Chapter 6 were obtained from a recourse recycling company in Changsha, China. The waste rice husk used in Chapter 7 was purchased from a rice processing plant in Guangdong, China.

3.3. Catalyst preparation

The catalyst preparation methods in Chapters 4–7 mainly contain solvothermal synthesis and boriding process.

For the synthesis of nickel sulfides (Chapter 5), a solvothermal method was introduced. Typically, a piece of NF was ultrasonically treated with 1 M HCl, followed by acetone and distilled water to remove the oxide layer. The

growth solution was prepared by dissolving 2 mmol of thiourea (TU) as a sulfur source into 27 mL of isopropanol alcohol (IA) under vigorous stirring at room temperature for 1 hour. After TU completely dissolved, 3 mL of glycerol was added to the solution and continued stirring for another 30 min. Afterward, the mixed solution was transferred into a 50 mL autoclave followed by immersing a piece of NF ($2 \times 2 \text{ cm}^2$) and placed in a conventional oven at 180 °C for 3 hours. After the reaction is completed, the autoclave was allowed to be cooled naturally. Then, the as-obtained materials were washed with ethanol and water several times and finally dried in a vacuum oven at 60 °C for 4 h. Via changing the dosages of IA and glycerol, a series of NiS samples were prepared.

For the synthesis of metal borides, a facile boriding process was employed. Since the precursors used in Chapters 4, 6, and 7 are quite different, a general boriding process is presented here and detailed catalyst synthesis of various metal borides can be found in corresponding chapters. Typically, a certain amount of metal salts and $\text{KNaC}_4\text{H}_4\text{O}_6 \cdot 4\text{H}_2\text{O}$ were dissolved in DI water in a three-necked round-bottom flask and stirred vigorously under N_2 . After about 30 min, an aqueous solution containing sufficient NaBH_4 was added into the flask dropwise in an ice-water bath. The solution was then stirred for another 30 min to ensure the complete reaction. After that, the precipitate in the solution was centrifuged and well washed with ethanol and water. At last, the metal boride products were dried at 60 °C, in a vacuum oven.

3.4. Materials characterization

3.4.1. X-ray diffraction

The crystal structure of as-synthesized catalysts was analyzed by X-ray diffraction (XRD) in this study. The crystal structure of synthesized materials can be identified after comparing the collected XRD pattern to the standard

one in the Joint Committee on Powder Diffraction Standards (JCPDS) database. The employed XRD equipment is the Rigaku Smart-Lab 9 kW diffractometer with the X-ray tube operated at 45 kV and 20 mA.

3.4.2. Scanning electron microscopy

Scanning electron microscopes (SEM) are frequently used tools to check the nanostructure/morphology and element percentages (Furnished with energy dispersive X-ray spectroscopy, EDS) of synthesized catalysts. In this study, scanning electron microscopy (Zeiss Sigma 500 , Germany) was used.

3.4.3. X-ray photoelectron spectroscopy

X-ray photoelectron spectroscopy (XPS) is used to analyze the surface chemistry of catalysts, which can provide relative quantification of different elements and the valence of elements also can be obtained via XPS spectra. By examining the binding energies of elements, the chemical states can be achieved. In this study, the X-ray photoelectron spectroscopy (Thermo K-Alpha+, Thermo Fisher Scientific, USA) with the Al (K_{α}) radiation was used for XPS analysis.

3.4.4. Transmission electron microscopy

Transmission electron microscopy (TEM) is generally used to get nanostructure information of prepared catalysts at a much higher resolution than SEM. Lattice images can be seen with the high-resolution TEM (HRTEM, JEOL JEM-2100F, Japan). In addition, the selected area electron diffraction (SAED) can be used to investigate the phase characteristics of catalysts (crystalline or amorphous).

3.4.5. Inductively coupled plasma spectroscopy

Inductively coupled plasma (ICP) spectroscopy is a widely used analytical technique to determine and identify elements within a typical sample based on the ionization of elements. Two ICP systems are widely used, namely the ICP optical emission spectroscopy (ICP-OES) and the ICP mass spectrometry (ICP-MS). ICP-OES measurement is based on the quantification of excited atoms and ions at the wavelength characteristics of the typical elements. However, ICP-MS measures the atom's mass by mass spectrometry. Because of the difference in element detection, ICP-MS possesses a lower detection limit which can extend to parts per trillion (ppt). In this study, both ICP-OES (Varian 720, Varian Inc., Santa Clara, CA, USA) and ICP-MS (Agilent 7700s, Agilent Technologies, Tokyo, Japan) were used to analyze the chemical compositions of catalysts and the ion concentrations in the wastewater, leachates, and electrolytes.

3.4.6. Raman spectroscopy

Raman spectroscopy can provide specific vibrational information which is specific to a compound's chemical bonds and symmetry. Generally, it is used for the identification of inorganic substances. Herein, Raman spectroscopy was used to identify the surface reconstruction process of catalysts during electrochemical reactions. In this study, Raman spectra were collected on the Horiba Jobin Yvon LabRAM HR-Evolution Raman microscope (HORIBA Jobin Yvon, France).

3.4.7. Fourier-transform infrared spectroscopy

Similar to Raman spectroscopy, Fourier-transform infrared spectroscopy (FTIR) is a technique to identify organic substances based on the specific vibrational information of a compound's chemical bonds and symmetry. In this work, the FTIR spectrum of biochar was tested on a Bruker V80 machine (Germany) at room temperature.

3.4.8. N₂ sorption/desorption measurement

Brunauer-Emmer-Teller (BET) method is used to test the physical adsorption/desorption of N₂ on the surface of the biochar (Chapter 7). Critical parameters (e.g., pore size, surface area, pore volume) can be obtained via conducting N₂ sorption/desorption measurements by a physical adsorption apparatus (ASAP2460, Micromeritics, USA) at the temperature of 77 K. The Barret-Joyner-Halenda (BJH) method was used to obtain the pore volume and pore size of materials, while the biochar's surface area was determined with the Langmuir Isotherm Method.

3.4.9. Vibrating sample magnetometer measurement

A vibrating sample magnetometer (VSM) is used to measure the magnetic properties of materials based on Faraday's Law of Induction. In this study, the magnetic properties of catalysts were studied by a vibrating sample magnetometer (LakeShore 7404, LakeShore, USA).

3.5. Electrochemical techniques

3.5.1. Preparation of working electrode

To prepare a working electrode, 5 mg of catalyst powder was first dispersed in 1 mL of mixed solution (0.05 mL of 5 wt% Nafion solution, 0.5 mL of water, and 0.45 mL of ethanol). After sonication for 30 min, a homogeneous ink was obtained. 0.10 mL of the ink was deposited onto a piece of acid-treated nickel foam (NF).

3.5.2. Cyclic voltammetry

Cyclic voltammetry (CV) is a commonly used electrochemical technique, and the potential is changed as a linear function of time. CV can provide

meaningful information regarding the redox voltage and the electrochemical reaction rates of a typical catalyst. Additionally, performing CV measurements in a non-faradic region at different scan rates can be used to calculate the double-layer capacitance (C_{dl}). In this study, CV was performed on the CHI660 electrochemical station (CH Instrument, USA).

3.5.3. Linear sweep voltammetry

Linear sweep voltammetry (LSV) is a simple electrochemical technique, which is similar to CV. Rather than cycling over the potential range linearly in both directions of CV measurements, LSV involves only a single linear sweep from the lower potential limit to the upper potential limit. In this study, LSV curves were recorded to compare the electrochemical activities of catalysts.

3.5.4. Electrochemical impedance spectroscopy

Electrochemical impedance spectroscopy (EIS) is a widely used electrochemical technique to measure the impedance of an electrochemical system in dependence on the AC potentials frequency. In this work, EIS was measured by using the CHI660, the AC voltage of 5 mV in amplitude was chosen with a frequency of $10^5 - 10^{-2}$ Hz.

3.5.5. Chronopotentiometry and chronoamperometry test

Chronopotentiometry (CP) and chronoamperometry (CA) tests are two popular methods to evaluate the long-term durability of catalysts. In the CP measurement, the current densities are fixed and the rise/decrease of the potential in a long operation is recorded. In the CA measurement, the potential of the working electrode is fixed, and the resulting current is recorded over a long period. The less variation of j (CA) or the η (CP) marks better longevity.

3.6. Computational methods

All spin-polarized DFT calculations were carried out with the generalized gradient approximation (GGA) (Yu et al., 2020), and the Perdew–Burke–Ernzerhof (PBE) functional was used to model the exchange and correlation interactions. Considering the strong correlation effect of transition metals, the DFT + U method was employed. In this study (Chapter 4), the value of $U_{\text{eff}} = 5$ eV was applied on Fe atoms based on previous studies on goethite (α -FeOOH) (Zhou et al., 2017). A vacuum space of 15 Å was constructed to avoid the interaction between adjacent slabs. The kinetic energy cutoff was set to 500 eV for the plane-wave basis set. Brillouin zone integration was sampled with the $3 \times 1 \times 5$ and $2 \times 2 \times 1$ Monkhorst-Pack mesh k-point for bulk and surface calculations, respectively. The convergence tolerances were set to 1×10^{-5} eV per atom for energy, 1×10^{-3} Å for maximum displacement, and 0.03 eV Å⁻¹ for maximum force. During the geometry optimizations step, the three bottom layers were constrained at the bulk position and other atoms were relaxed.

CHAPTER 4

**Tuning electronic property and
surface reconstruction of
amorphous iron borides via W-P
co-doping for highly efficient
oxygen evolution**

This chapter has been derived from the published paper of *Applied Catalysis B: Environmental*, 2021, 288, 120037.

4.1. Introduction

Water electrolysis is a green and sustainable strategy to generate hydrogen with zero carbon emission. In principle, water splitting contains OER and HER. Compared with the two-electron HER, the four-electron OER with inherent sluggish kinetics is recognized as the main obstacle to advance water electrolysis systems (Liang et al., 2020). To address this issue, many efforts have been made to improve the OER efficiency by developing high-performance catalysts. Noble metal (e.g., Ir, Ru)-based materials are extensively employed for the OER because of their excellent activity and good stability. Despite their superior catalytic performance, the high price and low reserve seriously hinder their large-scale industrial applications (Chen et al., 2021b). To this end, it is necessary to develop low-cost and high-performance catalysts for OER.

Recently, low-cost electrocatalysts for OER based on 3d transition metals have attracted enormous attention, including phosphides (Zhang et al., 2020a), sulfides (Xu et al., 2020), oxides (Heard et al., 2019), hydroxides (Fan et al., 2016), borides (Chen et al., 2020d; Chunduri et al., 2019), nitrides (Han et al., 2018), alloys (Zhang et al., 2019e), and carbides (Dinh et al., 2019). Among them, transition metal borides (TMBs, e.g., Co_xB_y , Ni_xB_y , Fe_xB_y , and Mo_xB_y) are emerging as promising catalysts for water splitting owing to their great conductivity, high intrinsic catalytic activity, compositional flexibility, and easy accessibility. To further improve the catalytic performance of TMBs, strategies that focus on enlarging the surface area, improving the conductivity, regulating the electron structure, and enhancing the durability have been advocated. For example, Gupta et al. (2019a) found that the CoB film showed better OER performance than the CoB powder sample because of its lower particle aggregation degree. This feature can benefit the electrochemical reactions by providing more electroactive active sites. In another study,

Nsanzimana and co-authors (2019) also suggested that the morphology of CoB could affect the OER performance, and the CoB nanosheet performed better than the CoB nanoparticles. Their further investigation suggested that the doping of Fe could significantly enhance the catalytic activity via the synergistic effect of transition metals in ternary CoFeB. Apart from cationic doping, anionic doping also alters the electronic structures of TMBs and thus influences catalytic performance. For instance, Li et al. (2014) found the synergistic effects of P and B of CoBP could improve the catalytic performance toward both HER and OER. Although anionic or cationic doping is an effective method to upgrade the electrochemical performance of nanomaterials (Chen et al., 2020b), optimizing the catalytic performance of TMBs through anion-cation dual doping is still rarely reported, especially the amorphous FeB. More importantly, previous studies suggest that the real active center of iron-based catalysts is strongly associated with the iron oxyhydroxide (FeOOH), which is generally generated on the surface of the pre-catalyst under the oxidizing potential applied during the OER process. Unfortunately, the commonly synthesized pure FeOOH phase is not a highly active OER catalyst due to its low conductivity and mediocre catalytic activity. Accordingly, a fundamental understanding of the pre-catalysts design would enable the exposure of abundant active oxyhydroxides and would significantly advance efficient OER electrocatalysts with low-cost iron-based materials.

In this study, we demonstrate a rational design of a pre-catalyst, W, P-FeB (tungsten and phosphorus co-doped amorphous FeB) that can upgrade the catalytic performance of *in situ* formed FeOOH via accelerating surface reconstruction by anion (P and B species) leaching and regulating intrinsic activity by evolved W incorporated-FeOOH. The W, P co-doped FeB-evolved anode only takes a low η of 209 mV to achieve j_{10} with good stability in alkaline electrolyte. Overall, these results show that efficient pre-catalysts can be designed using a rational strategy through component regulation with P and

W doping in amorphous FeB. Anion etching during the OER process can not only accelerate the mass/charge transfer but also facilitate surface self-reconstruction. DFT calculations further confirm that the W doping efficiently enhances intrinsic electrocatalytic activity by enhancing conductivity and optimizing the adsorption free energy of reaction intermediates. Last, but not least, the hierarchical structure and amorphous feature benefit the overall OER process. By this general approach, we can get a fundamental insight into the correlation between surface structure-catalytic activity and an effectual strategy to design pre-catalysts for high OER performance.

4.2. Experimental section

4.2.1. Catalyst synthesis

Synthesis of FeB. The FeB nanoparticles were prepared by a chemical reduction method. In a typical process, 5 mmol of $\text{FeCl}_2 \cdot 4\text{H}_2\text{O}$ and 5 mmol $\text{KNaC}_4\text{H}_4\text{O}_6 \cdot 4\text{H}_2\text{O}$ were dissolved in 70 mL of DI water in a three-necked round-bottom flask (250 mL) and stirred vigorously under N_2 . After 30 min, 30 mL of an aqueous solution with 15 mmol NaBH_4 was added dropwise in an ice-water bath. The solution was then stirred for another half an hour to ensure the complete reaction. Then, the precipitate in the solution was centrifuged and washed with ethanol and water. Finally, the products were dried overnight in a vacuum oven at 60 °C.

Synthesis of W-FeB. The synthesis of W-doped FeB is similar to that of FeB except for using the mixture of sodium tungstate dihydrate ($\text{Na}_2\text{WO}_4 \cdot 2\text{H}_2\text{O}$) and $\text{FeCl}_2 \cdot 4\text{H}_2\text{O}$ as metal salts, and the total amount of Fe^{2+} and W^{6+} was controlled at 5 mmol. The Fe/W molar ratios of the samples were modified by adjusting the amounts of the corresponding precursors. The optimal consumption of $\text{Na}_2\text{WO}_4 \cdot 2\text{H}_2\text{O}$ was determined by the electrocatalytic activity.

Synthesis of P-FeB. The synthesis of P-doped FeB is similar to that of FeB except for using the mixture of sodium hypophosphite (NaH_2PO_2) and NaBH_4 to replace the NaBH_4 in the preparation of FeB, and the total amount of H_2PO_2^- and BH_4^- was controlled at 15 mmol. The NaH_2PO_2 was mixed with metal ions and $\text{KNaC}_4\text{H}_4\text{O}_6 \cdot 4\text{H}_2\text{O}$ before stirring. The B/P molar ratios of the samples were modified by adjusting the amounts of the corresponding precursors, and the optimal consumption of $\text{NaH}_2\text{PO}_2 \cdot \text{H}_2\text{O}$ was determined by the electrocatalytic activity.

Synthesis of W, P-FeB. The synthesis of W, P co-doped FeB is similar to that of FeB. The amounts of chemicals were chosen based on the electroactivity results of W-FeB and P-FeB, 1 mmol $\text{Na}_2\text{WO}_4 \cdot 2\text{H}_2\text{O}$ and 4 mmol $\text{FeCl}_2 \cdot 4\text{H}_2\text{O}$ were used as metal salts, and 7.5 mmol NaH_2PO_2 and 7.5 mmol NaBH_4 were used.

4.2.2. Material characterization

The structural morphology of the samples was analyzed using SEM (Zeiss Sigma 500). EDS mapping measurements were carried out utilizing a SEM which is equipped with an EDS. The crystal structure of the samples was obtained by XRD measurements on a Rigaku Smart-Lab 9 kW diffractometer with the X-ray tube operated at 45 kV and 20 mA. HRTEM images were obtained on a TEM instrument (FEI Tecnai G2 F20 S-TWIN) with an acceleration voltage of 200 kV. The element composition of the material was analyzed by XPS (Thermo K-Alpha+, Thermo Fisher Scientific, USA) with the Al ($\text{K}\alpha$) radiation. The Raman spectra were recorded on a Horiba Jobin Yvon LabRAM HR-Evolution Raman microscope. The chemical composition of the catalyst was determined by an ICP-OES instrument (Varian 720), and the dissolved ion concentrations in electrolytes were measured with an ICP-MS instrument (Agilent 7700s).

4.2.3. Electrochemical tests

Electrochemical measurements were carried out with a CHI 660E electrochemical workstation. OER activities were recorded in a three-electrode system. A graphite rod acted as the counter electrode and a Hg/HgO electrode was used as the reference electrode in O₂-saturated 1.0 M KOH electrolyte. LSV was performed at a scan rate of 5 mV s⁻¹, and the polarization curves were calibrated with 90% iR compensation to eliminate the solution resistance. All potentials measured were converted to a reversible hydrogen electrode (RHE) using the following equation: $E_{\text{vs. RHE}} = E_{\text{vs. Hg/HgO}} + 0.098 \text{ V} + 0.059 \text{ pH}$. EIS was recorded at 1.5 V vs. RHE over a frequency range of 10⁵ to 10⁻² Hz, an AC signal amplitude of 5 mV was applied. The C_{dl} was calculated through CV at different scan rates in 1.0 M KOH. The value of ECSA was calculated by the equation: $\text{ECSA} = S * C_{\text{dl}} / C_{\text{s}}$, where C_s is the general specific capacitance, the value is about 0.04 mF cm⁻² in 1.0 M KOH, and S means the actual area of the working electrode. The chronoamperometric i-t curves were recorded to evaluate the stability of catalysts.

4.2.4. Computational methods

Methods for DFT calculations are described in Chapter 3, Section 3.6.

4.3. Results and discussion

4.3.1. Synthesis and characterization

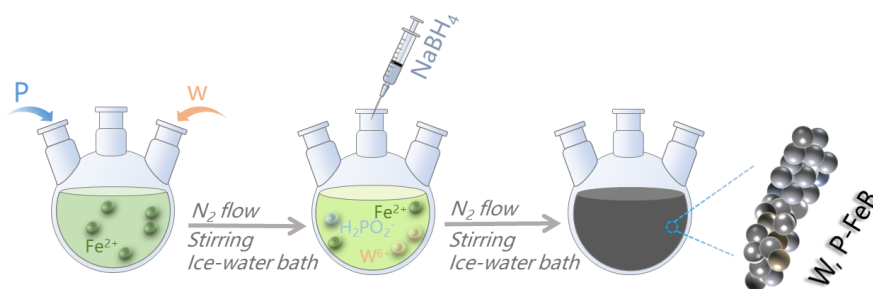


Figure 4.1. Schematic of the synthesis of W, P-FeB by a facile NaBH₄ chemical reduction process.

The Fe-based boride nanostructures were synthesized by a facile and effective chemical reduction process, as shown in Fig. 4.1. For the preparation of pure iron boride (FeB), the Fe^{2+} was chemically reduced in the presence of potassium sodium tartrate tetrahydrate ($\text{KNaC}_4\text{H}_4\text{O}_6 \cdot 4\text{H}_2\text{O}$) using NaBH_4 as the reductant under a continuous flowing N_2 atmosphere in an ice-water bath. In this study, $\text{KNaC}_4\text{H}_4\text{O}_6 \cdot 4\text{H}_2\text{O}$ is functionalized as a chelating agent to ease the aggregation of nanoparticles. Sodium hypophosphite (NaH_2PO_2) and/or sodium tungstate dihydrate ($\text{Na}_2\text{WO}_4 \cdot 2\text{H}_2\text{O}$) were added to the vessel to prepare doped FeB. The doping levels of P and W were investigated, and the optimized W, P-FeB was obtained with a Fe/W/B/P feed ratio of 8:2:15:15. The ICP-OES results reveal the composition of the best sample to be $\text{Fe}_{18.8}\text{W}_{3.9}\text{B}_{8.2}\text{P}_{3.8}\text{O}_{65.3}$.

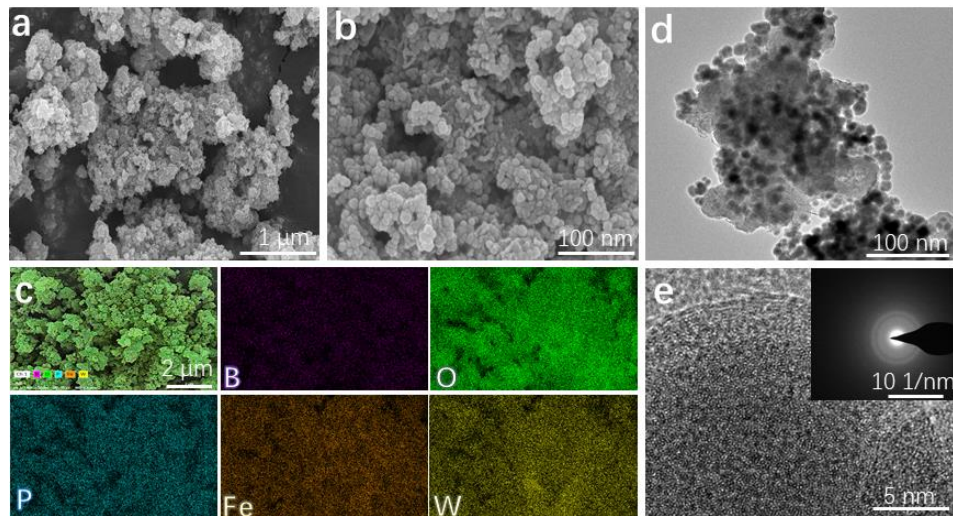


Figure 4.2. Microscopic measurements of W, P-FeB. (a) SEM image of W, P-FeB. (b) High-resolution SEM image of W, P-FeB. (c) EDS mapping of W, P-FeB. (d) TEM image of W, P-FeB. (e) HRTEM image of W, P-FeB (the inset shows the corresponding SAED pattern).

The as-obtained W, P-FeB were first characterized by SEM. Figure 4.2a-b shows that the W, P-FeB nanoparticles exhibit uniformly granular morphology with a small particle size of $\sim 10\text{-}20$ nm. Interestingly, the nanoparticle aggregates self-assembled into a 3D nano-forest structure, with

abundant nanopores. In addition to the stacked nanoparticles, nanochains and nanoplates are also observed. The as-formed porous hierarchical structure may contribute to the exposure of electroactive sites, and accelerate electrolyte penetration and diffusion, in addition to the rapid release of gaseous products in the catalytic process (Chen et al., 2020d). The EDS analysis was carried out to probe the elemental composition of W, P-FeB (Fig. 4.2c). It is determined that the existence of B, O, P, Fe, W elements in the catalysts, and these elements are evenly distributed on the catalyst surface. It should be noticed that the presence of oxygen is mainly due to the inevitable surface oxidation when borides are exposed to air (Wang et al., 2019a). In addition, the results of TEM analysis revealed that the nanoparticles are well dispersed with a size of about 10-20 nm, in line with the SEM observations (Fig. 4.2d). Furthermore, the HRTEM image (Fig. 4.2e) and SAED (inset of Fig. 2e) image suggest that W, P-FeB exhibits an amorphous structure, which is also proved by the XRD pattern. As depicted in Fig. 4.3, there is no distinct diffraction peak in the XRD spectrum of W, P-FeB, and other analogues also present a similar amorphous phase.

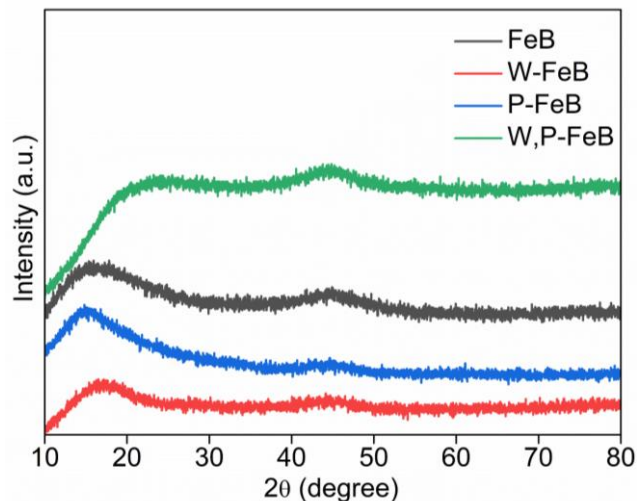


Figure 4.3. XRD patterns of FeB, P-FeB, W-FeB, and W, P-FeB.

The surface composition and the chemical state of W, P-FeB were further scrutinized by XPS. The whole spectrum survey demonstrates the presence of

B, P, O, Fe, and W elements in W, P-FeB (Fig. 4.4a), which is in line with the EDS mapping results. For the Fe 2p spectrum (Fig. 4.4b), an obvious peak at 706.5 eV can be attributed to metallic Fe bonding with B/P. Additionally, the spectrum in the Fe 2p region also exhibits two spin-orbit doublets with one doublet at 709.6 and 722.7 eV assigned to Fe²⁺ and another one located at 711.1 and 724.2 eV derived from Fe³⁺, since iron borides are easily oxidized when exposed to air (Li et al., 2019d). Similar to the Fe 2p spectrum, the W 4f spectrum exhibits two peaks at 31.3 eV, and 33.5 eV are characteristic of W 4f_{7/2} and W 4f_{5/2} of metallic W, mainly due to the formation of W-P and W-B (Fig. 4.4c). While two peaks are found at higher binding energy (35.5 eV and 37.7 eV), corresponding to the W 4f_{7/2} and W 4f_{5/2} peaks of WO₃, which might be because of the oxidation of W, P-FeB under ambient conditions. In addition, a small peak located at 41.3 eV is the WO₃ loss feature. In Fig. 4.4d, both metalloid boron (187.5 eV) and oxidized boron (191.7 eV, borate) are present in the B 1s spectrum. It is noticed that the binding energy of B (zero valence) in W, P-FeB is positively shifted in comparison with that of pure B (187.0 eV), implying that B atoms can contribute electrons to Fe/W (Masa et al., 2019). This is further evidenced by the negative shifts of Fe⁰ and W⁰ by 0.2 eV and 0.3 eV respectively, compared to those of pure metals. Hence, the existence of boron/borate can alter the electronic structure of Fe/W in W, P-FeB. The P 2p spectrum in Fig. 4.4e exhibits three peaks at 128.1, 128.9, and 133.3 eV, respectively. A peak at 133.3 eV is attributed to the oxidized phosphorus (phosphate). The peaks at 128.1 (2p_{3/2}) and 128.9 eV (2p_{1/2}) are from phosphorus, which are lower than that of elemental P (130.2 eV) (Sun et al., 2018). The lower P 2p binding energy may be attributed to the bonding to Fe/W metals which are not fully oxidized. The generated phosphorus species (i.e., metal phosphides and phosphates) are also claimed as great OER (pre-)catalysts by previous studies (Guo et al., 2018; Hu et al., 2019c; Ni et al., 2019b; Wang et al., 2017b), and the co-existence of electroactive metal borides/phosphides and borates/phosphates densifies the active sites and thus

benefits the OER process. Furthermore, the XPS spectrum of O 1s showcases further evidence for the existence of multiple oxidation states in W, P-FeB (Fig. 4.4f). Three peaks located at 529.3, 530.9, and 532.5 eV can be indexed to lattice oxygen, a substituted hydroxyl group, and surface physic-/chemisorbed H₂O, successively. These results further verify the surface oxidation of the as-prepared boride, and the hydrophilic oxide-rich surface would benefit the water oxidation process (Chen et al., 2020d; Wang et al., 2019a).

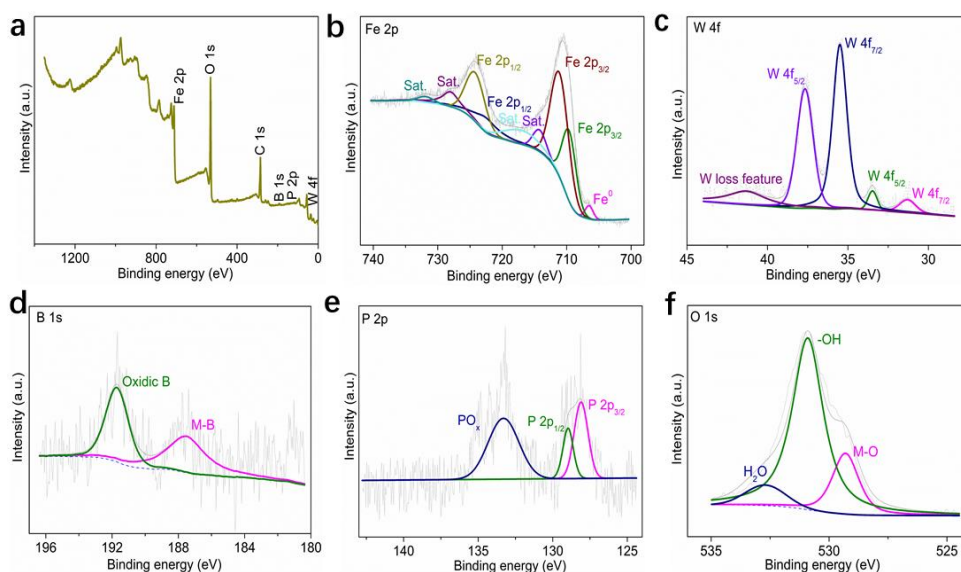


Figure 4.4. (a) XPS survey spectrum, (b) Fe 2p, (c) W 4f, (d) B 1s, (e) P 2p, and (f) O 1s XPS spectra of W, P-FeB. M in (d) and (f) means metal.

4.3.2. Electrochemical performance

The electrocatalytic OER performance of as-prepared catalysts (FeB, W-FeB, P-FeB, W, P-FeB) was evaluated in an alkaline solution. In this study, the activity of nickel foam and the IrO₂ catalyst was also tested, and the noticeable peaks range from 1.3 to 1.4 V vs. RHE can be ascribed to the oxidation of Ni species from the nickel foam substrate (Fig. 4.5a) (Chen et al., 2020e). The LSV curves suggest that both W and P single doping can improve the OER performance, and the W, P dual doping can further enhance the catalytic activity. Remarkably, W, P co-doped FeB needs a low η of 209

mV to realize j_{10} ($\eta_{10} = 209$ mV), which is smaller than most of recently reported catalysts supported on nickel foam (Table 4.1). In addition, the W, P co-doped FeB displays the lowest η of 246 mV at 50 mA cm^{-2} , in comparison to that of P-FeB (256 mV), W-FeB (270 mV), and FeB (284 mV). It is worth noting that all of the iron boride-based samples show higher catalytic activity than the commercial IrO_2 catalyst ($\eta_{50} = 301$ mV) (Fig. 4.5b).

Table 4.1. A summary of the property of OER for recently reported electrocatalysts supported on nickel foam.^a

Catalyst	η_{10} (mV)	Reference
Fe-Ni MOF NSs/NF	258@50 ^b	<i>Appl. Surf. Sci.</i> , 2020, 529, 147201
Fe-doped Ni_3Se_2 /NF	225	<i>Sustain. Energy Fuels</i> , 2020,4, 1150-1156
$\text{NiCo}_2\text{O}_4/\text{AgO}/\text{NF}$	232	<i>Nanoscale</i> , 2020,12, 7180-7187
$\text{Ni}_x\text{Fe}_{(1-x)}@\text{Ni}_x\text{Fe}_{(1-x)}\text{O}/\text{NF}$	215	<i>Nano Res.</i> , 2020, 13, 461-466
Ni-ZIF/Ni-B@NF	234	<i>Adv. Energy Mater.</i> , 2020, 10, 1902714
$\text{NiSe}_2/\text{CoSe}/\text{NF}$	270@100 ^c	<i>Mater. Today Energy</i> , 2020, 17, 100468
(P, W)- MoO_2/NF	308@40 ^d	<i>Appl. Surf. Sci.</i> , 2020, 529, 146987.
Ni/NiFeMoO _x /NF	255	<i>Adv. Sci.</i> , 2020, 7, 1902034.
Ru-NiCoP/NF	265@50 ^b	<i>Appl. Catal. B: Environ.</i> , 2020, 279, 119396.
CoFe-PBA NS@NF	256	<i>Nano Energy</i> , 2020, 68, 104371.

W, P-FeB/NF

209

This study

246@50^b

259@100^c

^a *Electrolyte: 1 M KOH.*

^b *the η of 258 mV at j_{50} .*

^c *the η of 270 mV at j_{100} .*

^d *the η of 308 mV at j_{40} .*

The effect of doping level was studied to optimize the chemical composition of catalysts, and the electrochemical activity of samples with different W and P doping concentrations are presented in Fig. 4.5c-d, respectively. For W-doped FeB, the presence of W can improve the OER activity of FeB, regardless of the concentration of W. The sample with a Fe/W molar ratio of 4/1 exhibits the highest activity, which only requires 247 mV to obtain j_{20} . A lower or a higher W concentration will decrease the electrocatalytic performance. For P-doped FeB, the sample with a P/B molar ratio of 1/1 shows the highest activity, which only requires 241 mV to obtain j_{20} . The η_{20} are 258, 250, 248, and 252 mV for P-FeB with the P/B molar ratio of 4:1, 2:1, 1:2, and 1:4, respectively. Based on the optimized concentration of different precursors, the W, P co-doped FeB with a Fe/W/B/P feed ratio of 8:2:15:15 and with a chemical component of $\text{Fe}_{18.8}\text{W}_{3.9}\text{B}_{8.2}\text{P}_{3.8}\text{O}_{65.3}$ displays a better OER performance than the bare FeB, W-doped FeB, and P-doped FeB.

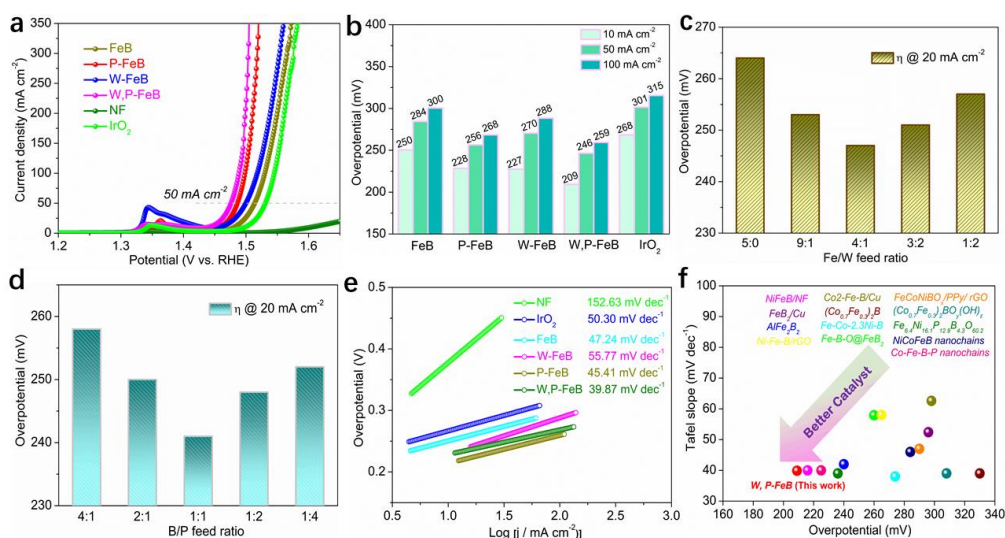


Figure 4.5. (a) LSV curves of as-prepared catalysts in 1.0 M KOH. (b) Comparison of η_{10} , η_{50} , and η_{100} of as-prepared catalysts. (c) The effect of Fe/W feeds ratio on the η . (d) The effect of B/P feed ratio on the η . (e) Tafel plots of as-prepared catalysts. (f) Comparison of η and Tafel slope of OER between W, P-FeB and reported iron boride-based catalysts.

The OER kinetics of the above catalysts are investigated by corresponding Tafel plots. Compared to NF ($152.63 \text{ mV dec}^{-1}$), W-FeB ($55.77 \text{ mV dec}^{-1}$), IrO_2 ($50.30 \text{ mV dec}^{-1}$), FeB ($47.24 \text{ mV dec}^{-1}$), and P-FeB ($45.41 \text{ mV dec}^{-1}$), W, P-FeB has a lower Tafel slope of $39.87 \text{ mV dec}^{-1}$ (Fig. 4.5e). The smallest Tafel slope suggests that W, P-FeB is the most efficient catalyst among the studied materials. These results also indicate that the W, P co-doping can lead to better OER kinetics. In addition, to our knowledge, the OER activity (η_{10} , Tafel slope) of W, P-FeB is better than most of the recently documented iron boride-based nanocatalysts (Fig. 4.5f) (An et al., 2018; Chen et al., 2017; Klemenz et al., 2018; Li et al., 2017; Li et al., 2019d; Liu et al., 2018a; Mann et al., 2019; Mao et al., 2020; Nsanzimana et al., 2018b; Ren et al., 2019; Wang et al., 2019a; Wu et al., 2019c; Xue et al., 2018), such as Fe-Co-2.3Ni-B (274 mV , 38 mV dec^{-1}) (Nsanzimana et al., 2018b), Ni-Fe-B/rGO (265 mV , 58 mV dec^{-1}) (An et al., 2018), FeB_2 (296 mV , 52.4 mV dec^{-1}) (Li

et al., 2017), $\text{Fe}_{6.4}\text{Ni}_{16.1}\text{P}_{12.9}\text{B}_{4.3}\text{O}_{60.2}$ (236 mV, 39 mV dec^{-1}) (Ren et al., 2019), $(\text{Co}_{0.7}\text{Fe}_{0.3})_2\text{BO}_y(\text{OH})_z$ (308 mV, 39 mV dec^{-1}) (Xue et al., 2018).

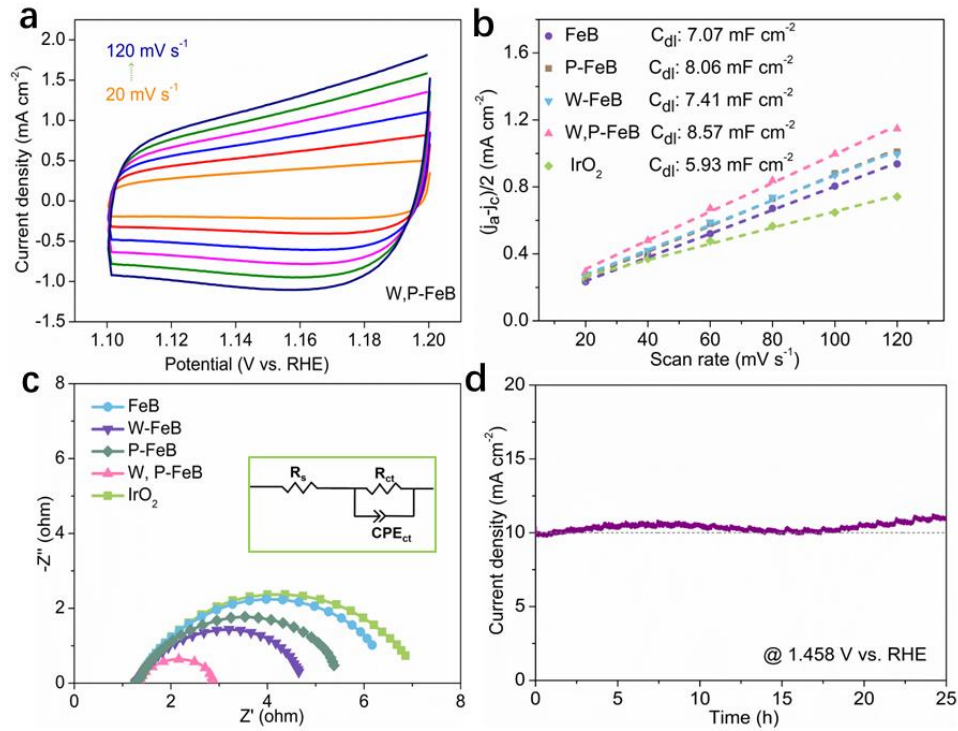


Figure 4.6. (a) Cyclic voltammograms of W, P-FeB at different scan rates. (b) Scan rate dependence of j for as-prepared catalysts and the IrO_2 catalyst at 1.15 V vs. RHE. (c) Nyquist plots of as-prepared catalysts and the IrO_2 catalyst at 1.5 V vs. RHE. (d) Chronoamperometric curve of W, P-FeB at 1.458 V vs. RHE.

The ECSA of the catalysts was compared by testing the C_{dl} at the solid/liquid interface, as C_{dl} is positively proportional to ECSA. The C_{dl} is calculated via performing CV measurements in a non-faradic region 1.10 -1.20 V vs. RHE at different scan rates (Fig. 4.6a). The C_{dl} of W, P-FeB is 8.57 mF cm^{-2} , which is larger than that of the P-doped FeB (8.06 mF cm^{-2}), W-doped FeB (7.41 mF cm^{-2}), FeB (7.07 mF cm^{-2}), and the IrO_2 catalyst (5.93 mF cm^{-2}) (Fig. 4.6b). The doping of W or P increases the number of electroactive sites on the FeB catalyst, and the co-doping of W and P has a synergistic effect on boosting the population of accessible electroactive sites for OER.

To further investigate the electrocatalytic kinetic characteristics of catalysts, EIS analyses were conducted. The Nyquist plots are plotted in Fig. 4.6c and fitted with an equivalent circuit model to quantify the key kinetic parameter, the charge transfer resistance (R_{ct}). According to the fitting results (Table 4.2), the R_{ct} of W, P-FeB catalysts is only 1.62 Ω , much smaller than that of W-FeB (3.54 Ω), P-FeB (4.32 Ω), FeB (5.31 Ω), and the IrO₂ catalyst (5.92 Ω), confirming the highly efficient electron transfer at the W, P-FeB electrode and electrolyte interface occurring during the water oxidation reaction. In addition, it can be convinced that both W and P doping indeed improves the charge transfer kinetics during the OER.

Table 4.2. Calculated charge transfer resistance (R_{ct}) and solution resistance (R_s) (in Ohm, Ω) of the materials deposited on NF obtained from the Nyquist plot during the EIS experiments.

Catalyst	R_s	R_{ct}
IrO ₂	1.33	5.92
FeB	1.34	5.31
W-FeB	1.33	3.54
P-FeB	1.36	4.32
W, P-FeB	1.32	1.62

Apart from the electrocatalytic activity, the performance stability of catalysts is another important issue. In this study, the chronoamperometry (CA) measurement was conducted at 1.458 V vs. RHE to evaluate the durability of W, P-FeB toward OER. As depicted in Fig. 4.6d, the j remains stable after 25 h running, with a small range of fluctuations above the 10 mA cm⁻². The variation of current densities may be due to the evolution of surface chemistry. In addition, the LSV plot was recorded after the long-term test (Fig. 4.7a). Compared with the initial one, the post-OER LSV curve shows ignorable variations, and the η even decreased by 5 mV at 10 mA cm⁻², in line with the

CA measurement. In contrast, for the benchmark IrO₂ catalyst, significant degradation of OER activity is exhibited in Fig. 4.7b, and the current density decreased by 32% over the 25 h CA test. This result indicates that W, P-FeB exhibits better activity and stability than the IrO₂ catalyst under alkaline conditions.

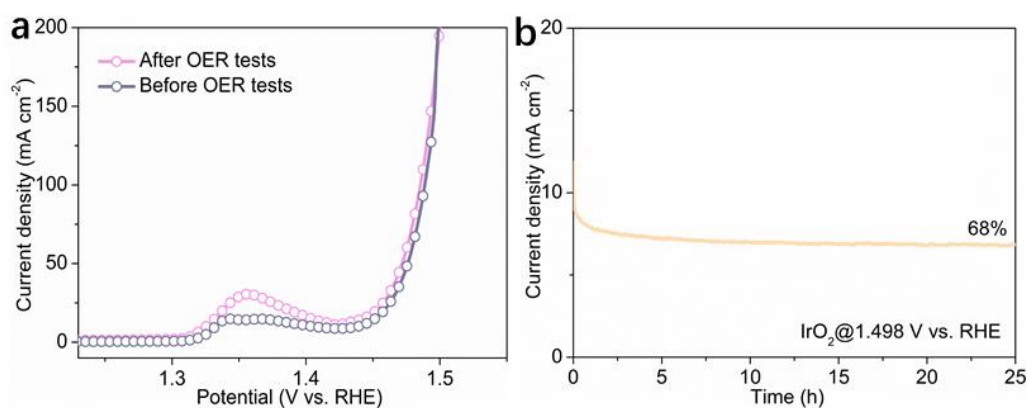


Figure 4.7. (a) LSV curves of W, P-FeB before and after the CA test in 1 M KOH. (b) Chronoamperometric curve of the IrO₂ catalyst at 1.498 V vs. RHE.

4.3.3. Understanding the enhanced OER activity of W, P-FeB

The outstanding catalytic activity of W and P co-doped FeB can be attributed to the harmonized elemental synergy and the unique amorphous structure. It is known that the activity of an electrocatalyst is governed by several key factors, including the nanostructure, charge transfer efficiency (conductivity), active surface area, and intrinsic catalytic activity (Chen et al., 2019b; Chen et al., 2020d). Firstly, the hierarchical structure of W, P-FeB can ease the exposure of abundant electroactive sites, and accelerate electrolyte penetration/diffusion, in addition to the rapid release of molecular oxygen products during the OER process (Fang et al., 2017). Secondly, W, P-FeB possesses an excellent electrical conductivity and a lower charge transfer resistance than its counterparts (Fig. 4.6c), indicating efficient electron transfer between the collector and active catalytic sites and less resistance in between

and at catalyst interfaces (Hu et al., 2019a). Thirdly, ECSA values of W, P-FeB (214.25 cm²), W-FeB (201.50 cm²), P-FeB (185.25 cm²), FeB (176.75 cm²), and the IrO₂ catalyst (148.25 cm²) suggest that W, P-FeB exhibits a higher electrocatalytic surface area for OER (Fig. 4.8a). To understand the intrinsic activity of each active site, we further normalized the OER current against ECSA (j_{ECSA}), instead of the geometric surface area, to exclude the effect of enlarged surface area. As shown in Fig. 4.8b, the η required for the IrO₂ catalyst, FeB, P-FeB, W-FeB, and W, P-FeB to deliver a j_1 are 324, 316, 281, 306, and 270 mV, respectively. The W, P-FeB shows the highest intrinsic catalytic activity among all electrocatalysts, which is followed by P-FeB, W-FeB, and bare FeB. Therefore, P or W doping can improve the intrinsic catalytic property of FeB which is further enhanced via the P and W co-doping. The above results suggest that the extraordinary OER activity of W, P-FeB is not only resulted from the improved electrical conductivity and enlarged ECSA, but also from the enhanced intrinsic activity of each active site after P and/or W doping.

The amorphous feature of W, P-FeB is another critical factor that contributes to its great OER activity. In this study, the amorphous W, P-FeB catalyst with a large ECSA and a high proportion of under coordinative and unsaturated sites ease the adsorption of intermediates/reactants in the OER process, which also facilitate surface and volume reconstruction of active sites (Anantharaj and Noda, 2019; Chen et al., 2020d). As depicted in Fig. 4.2, the surface of as-prepared boride particles is functionalized with amorphous oxygen-containing species, mainly referred to as borates, phosphates, and metal oxides. The formation of such amorphous oxidative layers benefits from the amorphous nature of the W, P-FeB bulk phase and provides optimal catalytically active sites (Hu et al., 2019a), resulting in boosted OER kinetics and thus the excellent intrinsic activity.

To further identify the active catalytic sites during the OER process, surface chemistry and structure evolution of the post-OER catalyst were checked by TEM, XPS, and XRD analysis. In contrast to the XPS spectrum of Fe 2p before OER, no signals corresponding to metallic and bivalent Fe are present in the spectrum of W, P-FeB after OER. This suggests substantial changes have occurred at the catalyst surface during the OER process. The metallic and bivalent Fe atoms are entirely replaced by the trivalent oxidation states of Fe and two peaks corresponding to the FeOOH appear at 710.9 and 724.0 eV (Fig. 4.8c) (Liu et al., 2020). In the XPS spectrum of W 4f (Fig. 4.8d), the peaks assigned to the W-B bond (31.3 and 33.5 eV) and the peaks (35.5 and 37.7 eV) assigned to W-O bonds are absent (Chen et al., 2020a; Zhao et al., 2019a), while the peaks (33.1 and 35.3 eV) assigned to W^{4+} emerge and maintain during the long-term OER process, indicating the effective doping of tungsten into iron oxyhydroxide (Chen et al., 2020a). The presence of electron-rich and low-valence-state W species might be a consequence of the electro-oxidation and the electron transfer from other elements (i.e., O and Fe) to W. In the O 1s spectrum (Fig. 4.8e), the lattice oxygen species of the post-OER catalyst (529.7 eV) increase considerably than the as-prepared catalyst, which further verifies the formation of metal oxyhydroxides on the catalyst surface (Zhang et al., 2019b; Zhang et al., 2019d). In addition, the signals of B and P elements are almost not detected in the XPS spectrum of W, P-FeB after the long-term OER test (Fig. 4.8f-g), suggesting that the surface of W, P-FeB has wholly converted to polyphase complexes containing high-valent metal (oxy)hydroxides, which is in line with results reported in the literature (Zhang et al., 2020b). A further investigation by ICP-MS suggests that B, P, W, and Fe on the surface area are progressively dissolved during the 25 h OER test (Fig. 4.8h). The prominent anion (B and P) etching/dissolution leads to more vacancies and continuously regulated surface electron properties, which not only accelerates the mass/charge transfer and facilitates the surface self-reconstruction but also benefits the adsorption of OH^- on the catalyst surface

to accelerate the OER. Moreover, the dissolved phosphates (PO_4^{3-}) and borates (BO_3^{3-}) may also promote the OER process, which has been proved in the TM selenides/sulfides-based OER catalysts system (Shi et al., 2020). Such speculation deserves further investigation. The dissolution of W mainly refers to the etching of WO_3 on the surface because no W^{6+} signal is detected in the XPS spectrum of W 4f of the post-OER sample. In addition, Fe exhibits a minor dissolution during the long-term OER test, indicating the good structure stability of the catalyst.

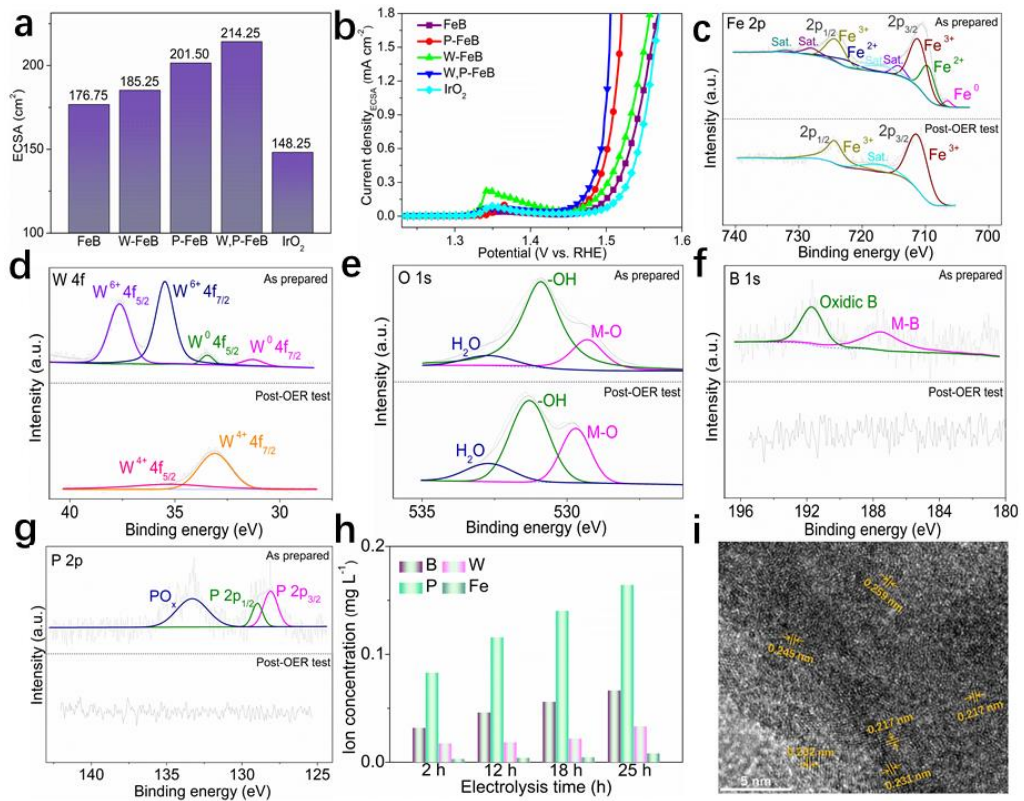


Figure 4.8. (a) ECSA values of W, P-FeB, W-FeB, P-FeB, FeB, and the IrO_2 catalyst. (b) LSV curves normalized with respect to ECSA for W, P-FeB, W-FeB, P-FeB, FeB, and the IrO_2 catalyst. (c-g) High-resolution XPS scans of W, P-FeB in the (c) Fe 2p, (d) W 4f, (e) O 1s, (f) B 1s, and (g) P 2p regions before and after the OER test. (h) The dissolved ion concentrations in electrolytes during the 25 h OER test. (i) HRTEM image of W, P-FeB after the OER test.

Besides, the TEM image verifies the surface structure evolution during the OER process. Different from the TEM images of the original amorphous catalyst, the HRTEM image of the post-OER catalyst shows a mixed amorphous and crystalline structure (Fig. 4.8i). Many lattice fringes are presented in the HRTEM image of the post-OER catalyst, indicating the formation of stable species under alkaline and oxidative conditions. In addition, the XRD pattern of the post-OER sample indicates the generation of α -FeOOH (Fig. 4.9a). Notably, although NF is used as the substrate of W, P-FeB, the new peaks that appear on the XRD pattern do not belong to NiOOH, but FeOOH. Raman spectroscopy was further performed to uncover the surface reconstruction during OER. The as-prepared W, P-FeB powder did not show any distinguishable features indicating that W, P-FeB does not possess any Raman bands (Fig. 4.9b). After the OER test, obvious Raman bands at 248, 299, 389, 421, 475, and 559 cm^{-1} were noticed, which are in agreement with the reported vibrations of pure phase goethite, α -FeOOH (Chakraborty et al., 2020). Combined with the above XPS, XRD, and Raman results, the lattice fringe spacings of 0.202, 0.217, 0.231, 0.245, and 0.259 nm can be indexed to the (131), (140), (200), (111), (021) crystallographic planes of FeOOH (JCPDS card no. 29-0713), respectively. Furthermore, we suppose the formation of W-doped FeOOH on the catalyst surface and W atoms are protected by the FeOOH from being further oxidation since W atoms keep an intermediate valence (+ 4) during the long-term OER test (Chen et al., 2020a; Zhang et al., 2016a). Overall, the XPS, XRD, and TEM results suggest that the surface of the as-prepared W, P-FeB has been evolved into W doped iron (oxy)hydroxides (FeOOH), which is promoted by the etching of B and P-containing components from the catalyst surface. The as-prepared W, P-FeB works as a pre-catalyst which converts into core-shell W-FeOOH@W, P-FeB during the OER process, with the evolved W-FeOOH acts as the catalytically active sites for OER. It is worth noting that the internal boron and phosphorus of the evolved W-FeOOH@W, P-FeB still play a critical role in modifying the

electronic structure of metals and boosting charge transfer efficiency, and thereby improving the catalytic performance of W, P-FeB (Hausmann et al., 2021; Selvam et al., 2020).

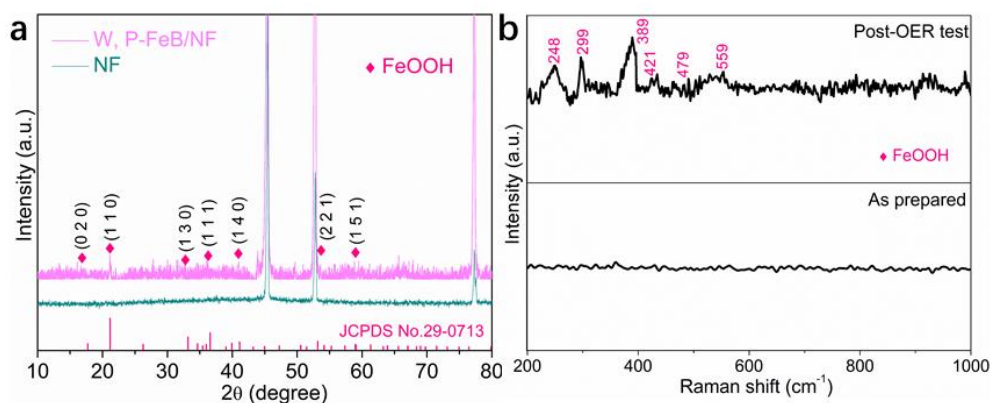


Figure 4.9. (a) XRD patterns of the post-OER W, P-FeB sample and bare NF. (b) Raman spectra of W, P-FeB before and after the OER test.

To gain more mechanistic insights, DFT calculations were performed to simulate the OER process. In this study, the W-FeOOH and bare FeOOH models are established and computed (Fig. 4.10a-b), which represent the true active phases of W, P co-doped FeB and bare FeB, respectively. In this study, the (010) surface of α -FeOOH was selected for DFT computations based on the XRD results and the high stability of this surface (Zhang et al., 2019a). Firstly, the effect of W doping on the electronic properties was investigated by calculating the electron density differences. The introduction of W can profoundly regulate the electronic structure of FeOOH (Fig. 4.11a). It can be seen that the W atom is the electron depletion center due to its highest electronegativity among the involved elements. The strong interaction between W and the nearest O atom is also suggested by the charge population analysis (Fig. 4.10c-d), from which it can be found that the charge of the O atom not increased but decreased by 0.1 e, as compared with the O atom in the pure FeOOH system. This phenomenon indicates the O atoms near the W atom may

inhibit the electron depletion process of the W atom, and it may account for the formation intermediate valence state of W.

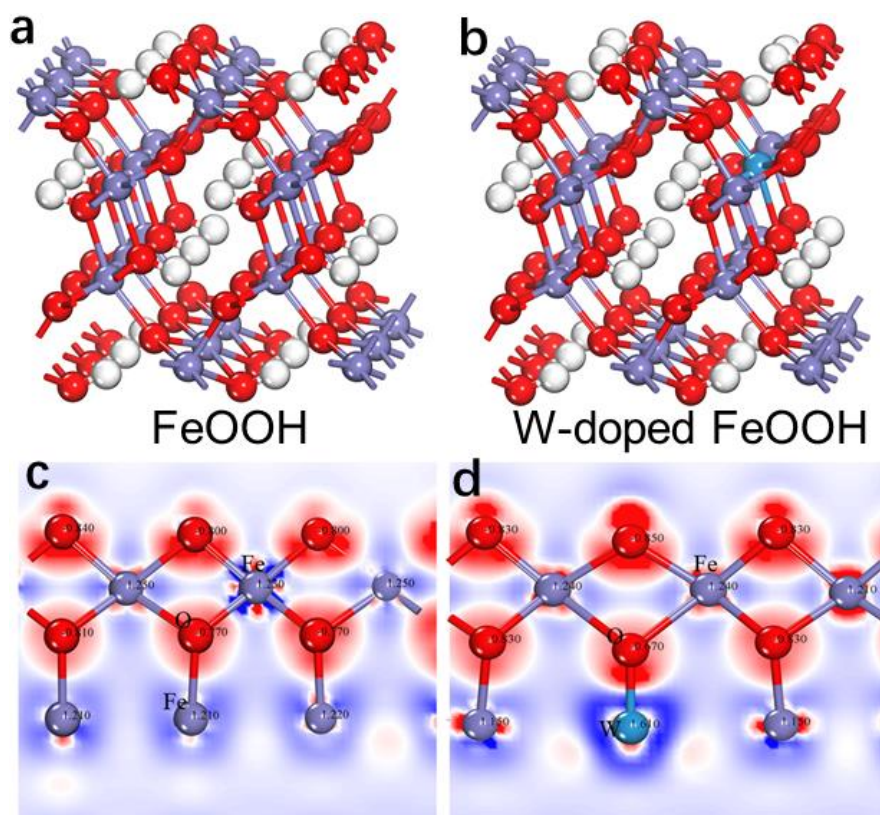


Figure 4.10. The structural diagrams of FeOOH (a) and W-doped FeOOH (b). The charge population of FeOOH (c) and W-doped FeOOH (d).

In addition, the density of state (DOS) of W-doped FeOOH and pristine FeOOH models was also calculated to deeply illustrate the inner W effect in the catalyst. As shown in Fig. 4.11b, the bandgap between the valence and conduction bands of FeOOH is about 0.7 eV. However, the doping of W results in a metallic nature, implying a significantly enhanced conductivity and electron transport rate, which would benefit the OER kinetics. In addition, W dopants delocalize the electron density in the Fe 3d orbital near the Fermi level, improving the reactivity of Fe atoms and accelerating the OER process.

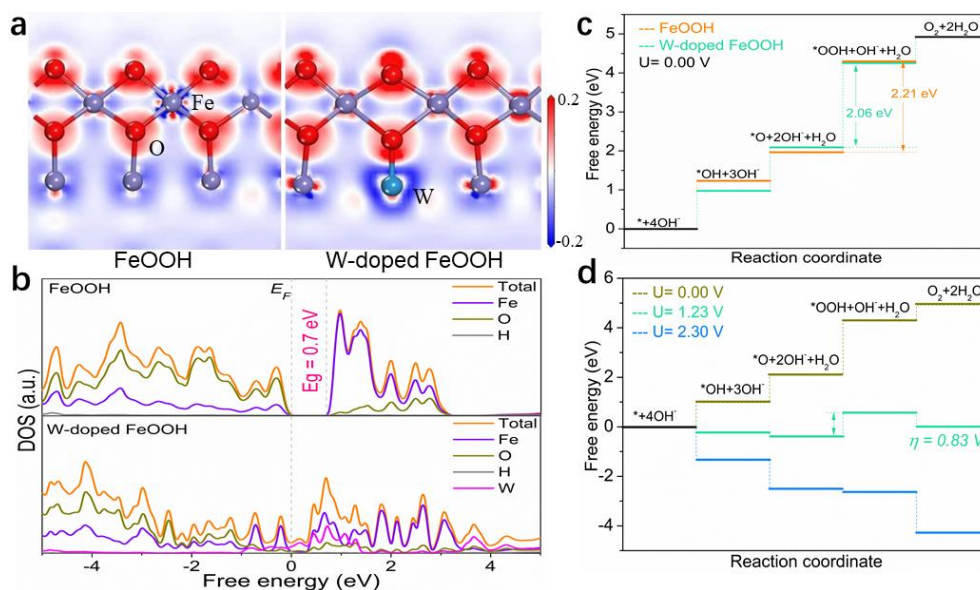


Figure 4.11. DFT simulations of OER. (a) Calculated electron density differences of FeOOH and W-doped FeOOH (red and blue colors denote electron accumulation and depletion, respectively; the labelled Fe atom is the selected active site for the free-energy calculation). (b) Computed DOS for FeOOH and W-doped FeOOH (the E_F is set to be zero). (c) Reaction free-energy diagrams for OER on FeOOH and W-doped FeOOH at zero potential ($U = 0$); the potential limiting steps and the η are also given. (d) Calculated free-energy landscapes for OER on W-doped FeOOH in alkaline solution at various potentials.

To better understand the doping effect of the W atom on the OER process, we have computed the reaction free-energy diagrams based on the four-electron transfer pathway. As displayed in Fig. 4.11c, the third elementary reaction step ($O^* + OH^- \rightarrow OOH^* + e^-$) is the potential determining step (PDS) for both W-doped FeOOH and bare FeOOH. The largest free energy change of the PDS in FeOOH is 2.21 eV, corresponding to a 0.98 V theoretical η . After W doping, W-doped FeOOH possesses a lower free energy change (2.06 eV) of the RDS than that of FeOOH, indicating that W-doped FeOOH needs an η lower than that of undoped FeOOH by 0.15 V to drive the OER. Hence, the W dopants can regulate the adsorption free energy of reaction intermediates

and reduce the energy barrier for OER. For W-doped FeOOH, as the applied potential increases to the equilibrium potential (1.23 V), some elementary reactions (e.g., OH* and O* formation) become energetically downhill (exothermic), and only the formation of OOH* is still an uphill step, with an η of 0.83 V (Fig. 4.11d). To ensure each step goes downhill, a higher bias is required. When the potential is further increased to 2.30 V, every step of W-doped FeOOH goes downhill, indicating the spontaneous OER process.

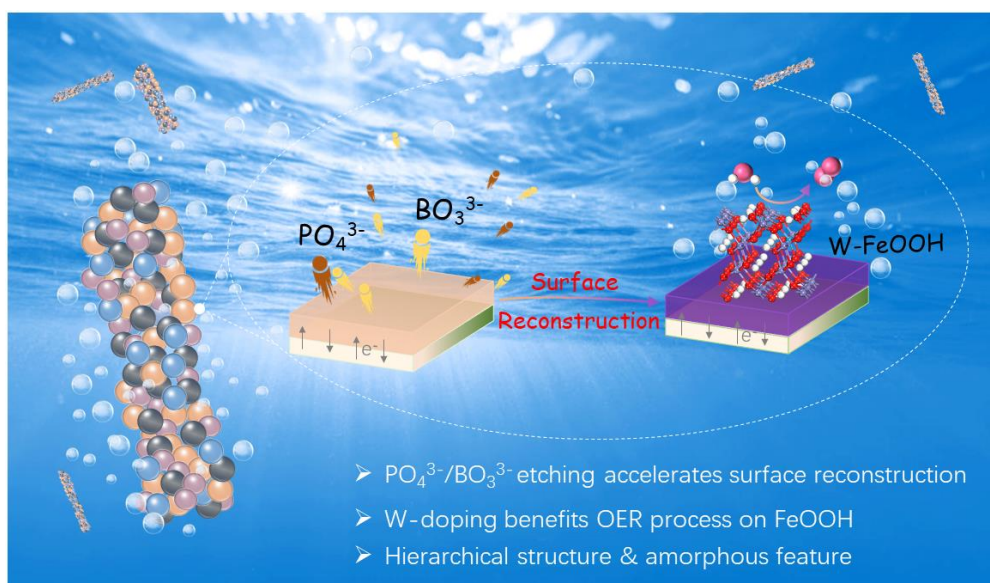


Figure 4.12. Illustration of the proposed mechanism for OER activity enhancement.

Overall, the excellent OER activity of W, P-FeB mainly derives from the accelerated surface reconstruction and the mass/charge transfer by anion (borate and phosphate) etching, enhanced intrinsic catalytic activity via W doping, in addition to the amorphous feature and hierarchical structure, as schematized in Fig. 4.12.

4.4. Conclusions

In this study, a FeB-based OER pre-catalyst with accelerated surface reconstruction and upgraded intrinsic activity of evolved FeOOH by W and P

co-doping has been developed. The amorphous W and P co-doped FeB exhibits great OER activity in alkaline media ($\eta_{10} = 209$ mV, Tafel slope = 39.87 mV dec⁻¹), as well as excellent long-term durability. Furthermore, the anion (borate and phosphate) etching during the OER process facilitates the surface reconstruction and accelerates the mass/charge transfer. Density functional theory calculations suggest W doping can enhance intrinsic catalytic activity by optimizing the adsorption free energy of reaction intermediates. What is more, the hierarchical structure and amorphous feature of W, P co-doped FeB also benefit the overall OER process. This study provides a general strategy to optimize metal borides (e.g., CoB_x, MoB_x, NiB_x) for OER pre-catalysts.

CHAPTER 5

**Controllable design of
nanoworm-like nickel sulfides for
efficient electrochemical water
splitting in alkaline media**

This chapter has been derived from the published paper of *Materials Today Energy*, 2020, 18, 100573.

5.1. Introduction

Developing renewable energy technologies is an urgent issue to mitigate the impending energy crisis and the alarming environmental degradation. Water splitting is an efficient and clean way to produce hydrogen which is considered a green energy carrier (Wan et al., 2019a; You and Sun, 2018). The efficiency of the EWS is highly dependent on the electrode materials, namely the catalysts. Noble metal (e.g., Pt, Ir, Pd, and Ru)-based catalysts have exhibited great performance for EWS, however, the low reserve and high price of these materials significantly limit their commercial applications (Chen et al., 2020d; Shi et al., 2019). As a result, it is imperative to design cost-effective catalysts for EWS. To our delight, numerous earth-abundant materials have shown good catalytic performance for EWS (Chen et al., 2021b), including transition metal-based materials (Li and Zheng, 2017; Lv et al., 2019; Yang et al., 2018; Yu et al., 2019; Zhao et al., 2016; Zhu et al., 2018a) and metal-free materials (Hu and Dai, 2019; Liu et al., 2019; Liu and Dai, 2016; Zhao et al., 2019b; Zhao et al., 2019c). Typically, transition metal sulfides (TMSs) have attracted enormous attention as OER and HER catalysts among these low-cost candidates, due to their high intrinsic catalytic activity, good electrical conductivity, and structural stability.

Nanoscale TMSs have been widely studied for EWS, but their catalytic performance is still inferior to that of precious metal-based materials. To further improve the catalytic properties of TMSs, various efficient strategies have been employed, including chemical component regulation (Wan et al., 2019a), morphology control (Hou et al., 2019; Joo et al., 2019), defect engineering (Sun et al., 2019c; Zhang et al., 2018e), and hybridization (Shifa et al., 2018; Tang et al., 2019), etc. Recent studies show that the morphology of nanocatalysts has a prominent effect on the catalytic performance of TMSs (Chen et al., 2020c). For example, Wu et al. (2017a) compared the catalytic

performance of three zinc cobalt mixed sulfide nanostructures with different morphologies, including nanosheets, nanoplates, and nanoneedles. The one-dimensional Zn-Co-S nanoneedles exhibited higher catalytic activities toward both HER and OER than the analogues. This is because the integrated Zn-Co-S nanoneedle/CFP nanostructure can provide enhanced electrochemical active area, facilitate ion transfer, and gas evolution. Similarly, You and co-workers (2016) investigated the correlation between morphology and HER activity of a series of CoS with different nanostructures. The CoS nanoparticle shows the largest surface area and ECSA, and such merits contribute to populated electroactive sites and enhanced mass/charge transport, rendering its best HER performance. As a result, it is of great significance to tune the morphology of catalysts, and thus improve the surface active sites and the structural stability (Chen et al., 2019c). Although TMSs with different morphologies for EWS have been documented, the morphology-control synthesis of efficient NiS catalysts with facile methods is still challenging. Additionally, the relationship between the morphology-controlled catalysts and their catalytic properties needs further exploration.

Herein, we have developed a one-step solvothermal strategy to construct nickel sulfides as efficient water splitting catalysts. The morphology-dependent electrochemical performance is uncovered, and the nanoworm-like nickel sulfides (NiS-NW/NF) outperform the nanoplate-like counterpart. Benefiting from the small size, abundant active sites, large electrochemical surface area, and good conductivity, the NiS-NW/NF exhibits great OER performance (e.g., $\eta_{100} = 279$ mV, Tafel slope = 38.44 mV dec⁻¹) and good HER activity. When fabricated in a two-electrode cell, only a voltage as low as 1.563 V was required to achieve j_{10} .

5.2. Experimental section

5.2.1. Material synthesis

The NiS nanoworms (NW) were prepared using a solvothermal method. Briefly, NF with a thickness of 1 mm was ultrasonically treated with 1M HCl, followed by acetone and distilled water to remove the oxide layer. The growth solution was prepared by dissolving 2 mmol of thiourea (TU) as a sulfur source into 27 mL of isopropanol alcohol (IA) under vigorous stirring at room temperature for 1 hour. After TU completely dissolved, 3 mL of glycerol was added to the solution and continued stirring for another 30 min. Then, the mixed solution was transferred into a 50 mL autoclave followed by immersing NF ($2 \times 2 \text{ cm}^2$) and placed in a conventional oven at 180 °C for 3 hours. After the reaction is completed it is allowed to be cooled naturally. Finally, the as-obtained materials were well washed with ethanol and water and then dried at the vacuum oven at 60 °C for 4 h. Similarly, the NiS nanoplates (NP) were synthesized when 30 mL of IA was used, without the addition of glycerol. A series of NiS samples were prepared by changing the dosages of IA and glycerol, and the total amount of IA and glycerol was controlled at 30 mL.

5.2.2. Structural characterization

Methods for XRD, SEM, TEM, and XPS measurements are described in Chapter 4, Section 4.2.2.

5.2.3. Electrochemical tests

Methods for electrochemical measurements are described in Chapter 4, Section 4.2.3.

5.3. Results and discussion

5.3.1. Material characterizations

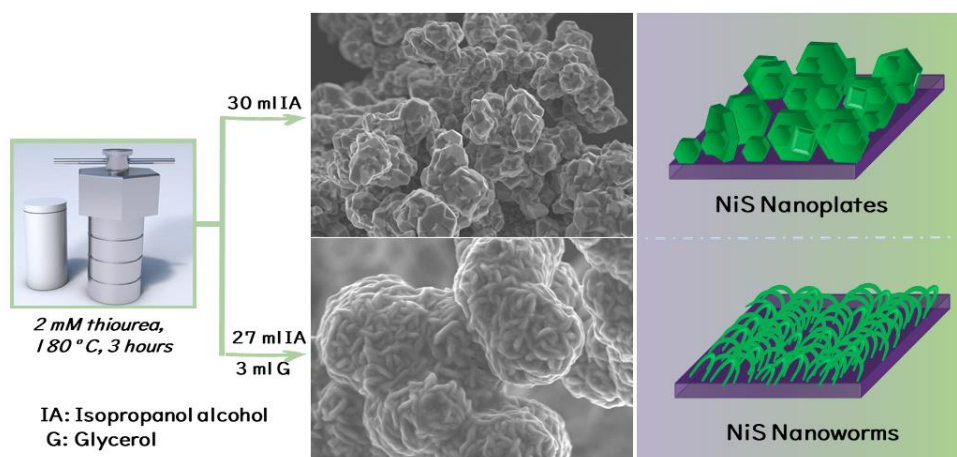


Figure 5.1. Schematic of the formation of NiS-NW/NF and NiS-NP/NF.

Figure 5.1 illustrates the synthesis procedure of the nickel sulfide samples, which only comprises a solvothermal sulfidation of direct growth of nickel sulfides on nickel foam. The appropriate addition of glycerol and IA as surfactants is the key for tuning the morphology of nickel sulfides. The nanoworm-like nickel sulfide sample (NiS-NW/NF) is obtained when a small amount (3 mL) of glycerol and 27 mL of IA are added as the solvent, while the nanoplate-like nickel sulfide sample (NiS-NP/NF) is formed by adding 30 mL of IA only. Compared with the NiS-NP/NF, the NiS-NW/NF possesses a smaller average size (~100 vs. ~200 nm) and higher surface area (Fig. 5.2a-b). These features suggest that the NiS NWs may be more favorable for electrochemical reactions than their counterpart. In addition, the energy-dispersive spectroscopy (EDS) elemental mapping images of the NiS NWs (Fig. 5.2c) show the uniform distribution of Ni and S.

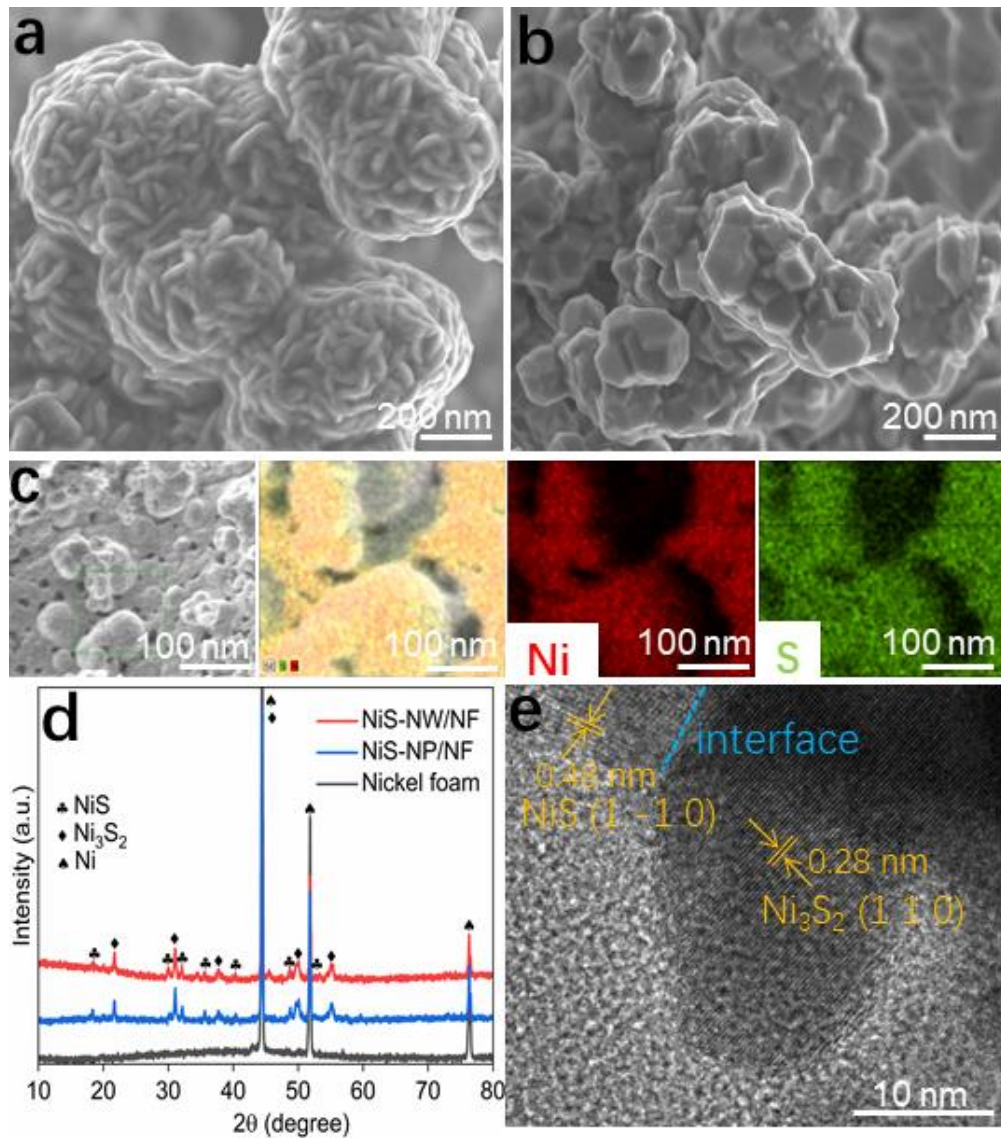


Figure 5.2. (a) SEM image of NiS-NW/NF, (b) SEM image of NiS-NP/NF, (c) SEM-EDS mapping of NiS-NW/NF, (d) XRD patterns of NiS-NW/NF, NiS-NP/NF and bare Nickel foam, (e) HRTEM image of NiS-NW/NF.

The crystal structures of the as-prepared nickel sulfides were investigated with XRD. As depicted in Fig. 5.2d, most of the strong peaks in the XRD patterns of NiS-NW/NF and NiS-NP/NF are matched to Ni₃S₂ (JCPDS No. 71-1682) and NiS (JCPDS No. 86-2280), indicating that the two nickel sulfide samples are mainly composed of Ni₃S₂ and NiS. The diffraction peaks at 21.7°, 31.0°, 37.7°, 38.2°, 44.3°, 49.6°, 50.0°, and 55.2° can be assigned to (101), (110), (003), (021), (202), (113), (211), and (122) reflection planes of Ni₃S₂,

respectively; whereas those at 18.3°, 30.2°, 32.1°, 35.7°, 40.4°, 48.8°, 50.1°, 52.6°, and 57.3° can be indexed to (1-10), (101), (300), (021), (211), (131), (410), (401), and (330) reflection planes of NiS, respectively. Apart from Ni₃S₂ and NiS, the strong peaks of metallic Ni are still observed on the patterns of nickel sulfide samples, suggesting that the nickel foam is partially sulfurized. Further insights into the nanostructure of NiS NWs are provided by the TEM analysis. Figure 5.2e presents a typical high magnification TEM image of NiS NWs, the crystal lattices of NiS NWs can be indexed to Ni₃S₂ and NiS with a clear interface. The lattice distances of 0.28 and 0.48 nm correspond to the (110) and (1-10) crystal planes of Ni₃S₂ and NiS, respectively. The results from the TEM image are in line with the XRD analysis.

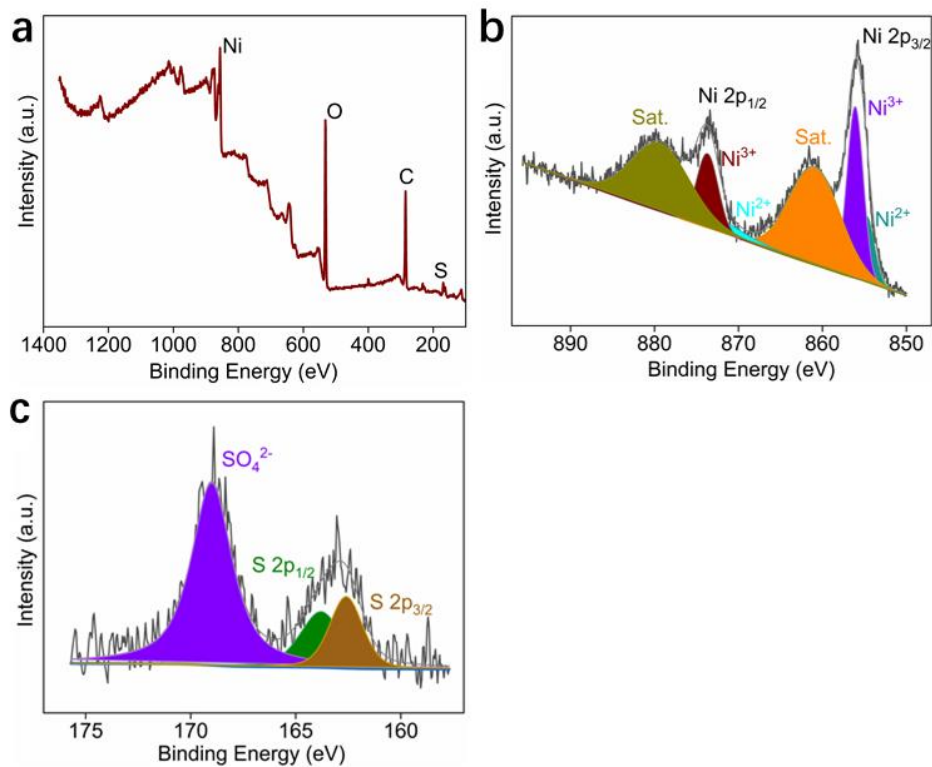


Figure 5.3. (a) XPS survey spectrum, (b) Ni 2p, and (c) S 2p XPS spectra of NiS-NW/NF.

XPS analysis was employed to ascertain the elemental composition and the electronic structure of the NiS-NW/NF. The obtained survey spectrum in

Fig. 5.3a suggests the co-presence of S and Ni elements. The appreciable peaks at 854.7 and 872.1 eV in Fig. 5.3b can be attributed to the Ni²⁺ state, and the distinct peaks at 856.1 and 873.7 eV correspond to the Ni³⁺ state. These results suggest the co-existence of NiS and Ni₃S₂ in NiS-NW/NF (Guan et al., 2019). Meanwhile, the high-resolution spectrum of S 2p in Fig. 5.3c displays three fitting peaks at 169.1 eV, 163.8 eV and 162.6 eV, which can be assigned to SO₄²⁻, S 2p_{1/2} and S 2p_{3/2} in NiS-NW/NF, respectively, and the presence of SO₄²⁻ is mainly due to surface oxidation.

5.3.2. Electrocatalytic performance

The OER activity of the as-prepared nickel sulfide samples was examined in the oxygen-saturated 1.0 M KOH solution. The OER performances of acid-treated bare NF and IrO₂/NF were also tested. As shown in Fig. 5.4a, NiS-NW/NF requires a substantially lower η of 279 mV to obtain 100 mA cm⁻² compared to NiS-NP/NF (300 mV), and IrO₂/NF (315 mV). The peaks ranging from 1.3 to 1.4 V vs. RHE for the LSV curves are ascribed to the oxidation of Ni²⁺ to Ni³⁺. Furthermore, at the anodic current densities of 200 and 400 mA cm⁻², the applied η of NiS-NW/NF are 334 and 398 mV respectively, significantly lower than those of NiS-NP/NF (450 and 652 mV) (Fig. 5.4b). Figure 5.4c shows that NiS-NW/NF delivers a lower Tafel slope (38.44 mV dec⁻¹) than NiS-NP/NF (88.03 mV dec⁻¹) and NF (89.51 mV dec⁻¹), suggesting the OER kinetics of NiS-NW/NF is superior to that of NiS-NP/NF and NF. These results of η and Tafel slopes reveal that NiS-NW/NF indeed exhibits efficient OER performances ($\eta_{100} = 279$ mV, Tafel slope = 38.44 mV dec⁻¹), which are much better than NiS-NP/NF ($\eta_{100} = 300$ mV, Tafel slope = 88.03 mV dec⁻¹). In addition, the OER activities (η_{100} , Tafel slope) of NiS-NW/NF outperform most of the recently documented nickel sulfide-based OER catalysts (Fig. 5.4d) (Ding et al., 2018; Guan et al., 2019; He et al., 2020; Li et al., 2019a; Lin et al., 2018; Qin et al., 2020; Shit et al., 2018; Wan et al., 2019b;

Wu et al., 2019a; Yan et al., 2017; Zhao et al., 2019d; Zhou et al., 2019; Zhu et al., 2019a), such as NiCoS/NF (370 mV, 145 mV dec⁻¹) (Yan et al., 2017), Ni₃N-Ni₃S₂ (404 mV, 112 mV dec⁻¹) (Zhao et al., 2019d), CoS_x/Ni₃S₂@NF (373 mV, 105 mV dec⁻¹) (Shit et al., 2018), P-doped Ni₃S₂/NF (306 mV, 99 mV dec⁻¹) (Ding et al., 2018), Ni₃S₄ (340 mV, 67 mV dec⁻¹) (Wan et al., 2019b).

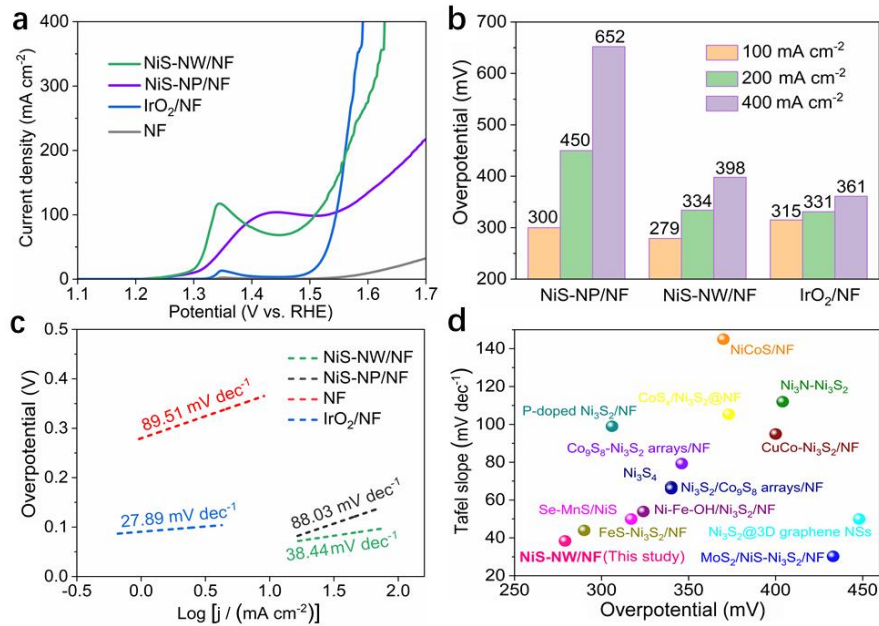


Figure 5.4. (a) LSV curves of the OER performance of Ni foam, NiS-NW/NF, NiS-NP/NF, and IrO₂/NF in 1.0 M KOH. (b) Comparison of η_{100} , η_{200} , and η_{400} of NiS-NW/NF, NiS-NP/NF, and IrO₂/NF. (c) Tafel plots of Ni foam, NiS-NW/NF, NiS-NP/NF, and IrO₂/NF. (d) Comparison of η_{100} and Tafel slope of OER between the NiS-NW/NF and reported nickel sulfide-based catalysts.

To probe the charge-transfer kinetics and the ECSA of catalysts, C_{dl} and EIS were measured. C_{dl} is a convincing parameter for the estimation of accessible active sites of electrocatalysts, as the C_{dl} is positively proportional to ECSA. The C_{dl} was measured via CV scans in a non-faradic potential region (1.1 - 1.2 V vs. RHE) at various scan rates (40 - 120 mV s⁻¹) (Fig. 5.5a-c). The

capacitive current density differences ($\Delta j = (j_a - j_c)/2$) at 1.15 V vs. RHE as a function of scan rate display the C_{dl} values of catalysts (Fig. 5.5d). The calculated C_{dl} values of NiS-NW/NF, NiS-NP/NF, and NF are 39.42, 10.36, and 2.88 mF cm^{-2} , respectively. The high C_{dl} value means NiS-NW/NF possesses a much higher ECSA in comparison to that of NiS-NP/NF and NF, suggesting that NiS-NW/NF exposes more electroactive sites for the electrocatalytic water oxidation reaction. To further investigate the OER kinetics, EIS was also measured. Fig. 5.5e presents the Nyquist plots of NiS-NW/NF, NiS-NP/NF, and NF. The Nyquist plot of NiS-NW/NF shows a smaller semicircle than that of NiS-NP/NF and NF in the high-frequency region. The fitting results suggest that NiS-NW/NF exhibits a smaller R_{ct} (4.84 Ω) than that of NiS-NP/NF (21.11 Ω) and NF (67.11 Ω), revealing a faster charge transfer and the smaller charge transfer resistance of the NiS-NW/NF during the OER process.

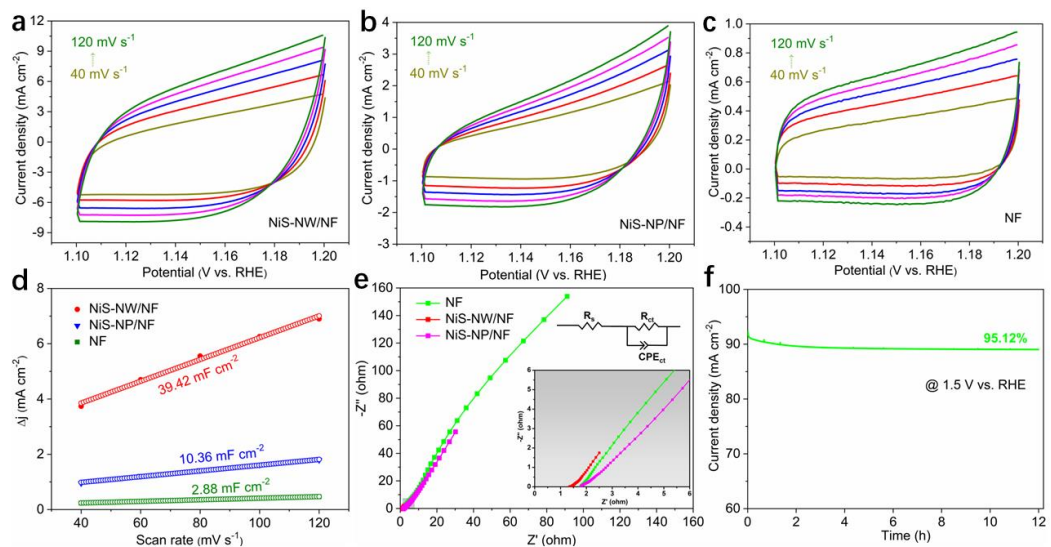


Figure 5.5. (a-c) Cyclic voltammograms of NiS-NW/NF, NiS-NW/NF, and nickel foam at different scan rates. (d) Scan rate dependence of j for NiS-NW/NF, NiS-NW/NF, and nickel foam at 1.15 V vs. RHE, (e) Nyquist plots at the open circuit potential, (f) Amperometric $i-t$ curve of NiS-NW/NF at 1.5 V versus RHE.

In this study, the chronoamperometry (CA) measurement was conducted at 1.5 V vs. RHE to evaluate the durability of NiS-NW/NF toward OER. As depicted in Fig. 5.5f, the j remains stable after 12 h running, and only about 5% j loss happened on the NiS-NW/NF electrode. This result indicates that the NiS-NW/NF exhibits good stability under alkaline conditions. In addition, the XPS test was performed to examine the chemical state of the pre-catalytic and post-OER NiS-NW/NF. There is no obvious change observed for signals for the Ni species (Fig. 5.6a) for the catalyst after the OER electrocatalysis. However, the S 2p spectra show that the intensity of S peaks decreases significantly after the long-term OER test (Fig. 5.6b), indicating the surface oxidation of NiS-NW/NF.

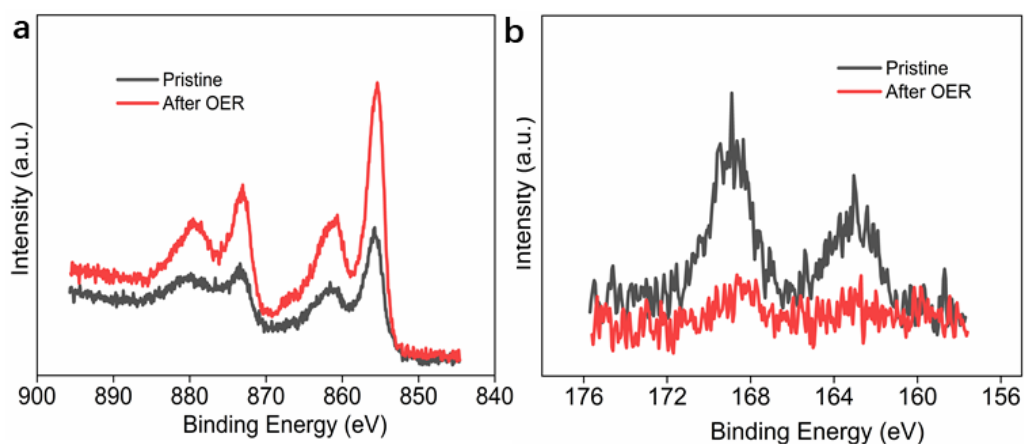


Figure 5.6. XPS spectra of (a) Ni 2P and (b) S 2p in NiS-NW/NF before and after OER tests.

Moreover, the HER activity of NiS-NW/NF, NiS-NP/NF, and NF was also measured in N_2 -saturated 1.0 M KOH. The η required to reach 20 mA cm^{-2} are determined to be 224, 228, and 415 mV for NiS-NW/NF, NiS-NP/NF, and NF, respectively (Fig. 5.7a). This comparison clearly shows that NiS-NW/NF exhibits a lower η than NiS-NP/NF. However, the HER performances of NiS catalysts in this study are inferior to those of the 20 wt % Pt/C benchmark catalyst which only takes 92.6 mV to achieve j_{20} . Although the 20

wt % Pt/C catalyst exhibits the smallest Tafel slope ($72.35 \text{ mV dec}^{-1}$) (Fig. 5.7b), NiS-NW/NF ($116.24 \text{ mV dec}^{-1}$) shows a lower Tafel slope than that of NiS-NP/NF ($122.37 \text{ mV dec}^{-1}$) and NF ($163.94 \text{ mV dec}^{-1}$). These results suggest that NiS-NW/NF exhibits improved HER activity compared to NiS-NP/NF, demonstrating the advantage of the dimensionally constructed heterogeneous nanoworm structure with multi-level interfaces. Moreover, the excellent HER performance of NiS-NW/NF is also attributed to abundant exposure of electroactive sites owing to the high surface area. Apart from the favorable HER activity, NiS-NW/NF also shows good durability in 1 M KOH. The results displayed in Fig. 5.7c suggest the electrocatalytic activity of HER decreases very little after 12 h electrocatalysis.

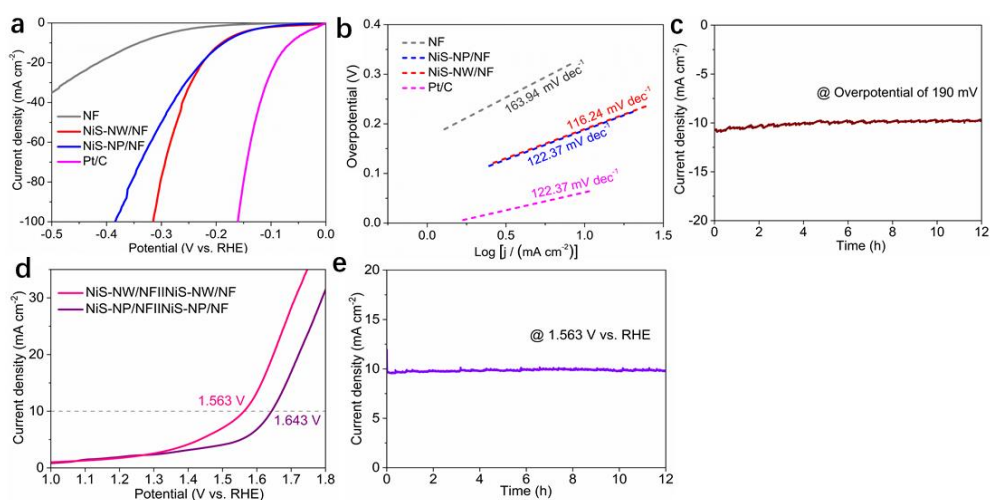


Figure 5.7. (a) LSV curves of the HER performance of NiS-NW/NF, NiS-NW/NF, nickel foam, and 20 wt % Pt/C, (b) corresponding Tafel plots. (c) Amperometric i-t curve of NiS-NW/NF for HER at an η of 190 mV. (d) LSV curve of water electrolysis using NiS-NW/NF or NiS-NW/NF as both HER and OER electrocatalysts in a two-electrode configuration, (e) Amperometric i-t curve of NiS-NW/NF for water splitting at an applied potential of 1.563 V.

As the synthesized catalyst showcases good electrocatalytic activities toward both OER and HER in the alkaline solution, a two-electrode single-cell system was constructed using NiS-NW/NF as both cathode and anode to

investigate its OWS competency. For comparison, the performance of NiS-NP/NF was also tested. Impressively, the j_{10} is achieved obtained at a low cell voltage of 1.563 V over the NiS-NW/NF||NiS-NW/NF, which is smaller than that of 1.643 V over the NiS-NP/NF||NiS-NP/NF (Fig. 5.7d). At a constant potential of 1.563 V, NiS-NW/NF shows a negligible change of j after continuous operation for 12 h (Fig. 5.7e), which indicates its great durability. As a catalyst for OWS, the NiS-NW/NF shows favorable catalytic activity and structural stability, directing an efficient and large-scale synthetic strategy for binder-free catalysts in renewable energy conversion.

5.4. Conclusions

In summary, we have synthesized a nanoworm-like nickel sulfide nanostructure via a one-step solvothermal method. With a smaller size, larger electrochemical surface area, and lower charge transfer resistance, the as-prepared nanoworm-like nickel sulfides (NiS-NW/NF) perform better than the nanoplate-like counterpart as well as most of reported nickel sulfide-based catalysts. In addition, when used as a bifunctional catalyst for OWS, the NiS-NW/NF achieves j_{10} at only 1.563 V with good long-term durability. This study provides a facile and effective strategy for the design and development of cost-effective catalysts for water splitting.

CHAPTER 6

Integrating high-efficiency oxygen evolution catalysts featuring accelerated surface reconstruction from waste printed circuit boards via a boriding recycling strategy

This chapter has been derived from the published paper of *Applied Catalysis B: Environmental*, 2021, 298, 120583.

6.1. Introduction

Energy safety and environmental sustainability gain top priority in our community in the current era. The depletion of fossil fuels, environmental degradation, and climate changes has attracted extensive research interest in advancing sustainable technologies (Chen et al., 2019b; Seh et al., 2017; Zhang et al., 2021). Energy conversion from renewable sources is a great solution to meet the growing energy demands and tackle the associated environmental issues (Tiwari et al., 2020; Zhang et al., 2019c). Among different energy techniques governed by electrochemistry, water splitting, fuel cells, and metal-air batteries are the most efficient ones. It is noted that the OER acts as a central reaction for these important schemes (Fang and Liu, 2010; Seitz et al., 2016; Suen et al., 2017; Zhong et al., 2018a). Developing high-performance catalysts to overcome the sluggish kinetics of OER is thus highly glamorous.

Noble metal (e.g., Ru and Ir)-based materials are the state-of-the-art OER catalysts due to their high catalytic activity and broad pH durability (Chen et al., 2020b). Nevertheless, the high-cost and low reservoir of Ir and Ru gravely hamper their large-scale applications (Wang et al., 2013; Yuan et al., 2020). Therefore, designing low-cost and efficient catalysts for OER remains an ongoing challenge. Recently, many transition metal (TM, e.g., Fe, Co, Ni, Cu, Mn, Mo)-based nanomaterials such as alloys, oxides, hydroxides, sulfides, selenides, borides, and phosphides are emerging as excellent catalysts for OER, attributing to their low-cost, good catalytic performance (Chen et al., 2021b; Hausmann et al., 2020; Zhang et al., 2019c; Zhang et al., 2018d). Among the different catalysts, multimetal-based materials gain growing interest as they generally outperform the mono-metal counterparts due to the populated active sites and tunable electronic structure (Yu and Lou, 2018), especially Fe/Co/Ni-bearing catalysts (Jiang et al., 2018; Zhang et al., 2016a). Intriguingly, most TM-based OER electrocatalysts (e.g., pnictides and chalcogenides) are

reported to undergo surface reconstruction into metal (oxy)hydroxides as the active phase during the catalytic process (Christopher et al., 2021; Sivanantham et al., 2020). However, the surface evolution of multimetal-based catalysts has yet to be identified, and the structure-property relationship needs to be further elucidated.

Generally, cations in TM-based compounds act as active sites for OER, because the electronic structure of cations significantly governs the OER activity. Nevertheless, anions, mainly refer to nonmetals and metalloids (e.g., P, B, Sn, S, Se), also play a crucial role in ruling the OER properties. On one side, anions can modulate their neighbouring cationic active sites' electronic structure, regulate the adsorption/desorption of reaction intermediates, and eventually contribute to the OER activity (Chen et al., 2020b). On the other side, the dissolution/etching of anions can induce abundant defective sites on the catalyst surface and accelerate the surface reconstruction under oxidative working conditions (Wang et al., 2020). Under this circumstance, amorphous materials with flexible structures and abundant defects are more favourable for the surface evolution process (Anantharaj and Noda, 2019). Thus, it is of great interest to achieve an excellent catalytic activity by regulating anions and cations of TM-based amorphous electrocatalysts.

The synthesis of functional materials (e.g., adsorbents, catalysts, and electrode materials) from waste, which has environmental and economic benefits, has attracted growing attention over the past few years (Assefi et al., 2019; Natarajan and Aravindan, 2018; Niu and Xu, 2019). Inspired by the concept of "waste-to-treasure" strategy and industrial ecology, considerable attention has been arisen to recycle and reuse urban mines solid wastes, including the ever-increasing electrical and electronic wastes. Recycling critical metals (e.g., Au, Ag, Pt, Fe, Ni, Cu) from the massive amount of waste printed circuit boards (WPCBs) are particularly interesting, not only for their

high economic potential but also ascribing to its potential environmental risks (Sun et al., 2020). Currently, the recovery of precious metals from WPCBs is the most critical issue due to their higher economic value. However, efficient recovery/reuse of waste metals has not received sufficient attention, leading to substantial economic loss, severe environmental impacts, and human health issues. To this end, designing efficient recycling processes is a highly emergency for WPCBs management. At present, the dominated hydrometallurgical process relies on a step-by-step separation of TMs with similar physical and chemical properties (e.g., Ni, Cu, Fe, and Sn) from their mixed leachates of WPCBs, which requires complex flowsheets, large volumes of chemicals, and a portion of metal loss. On the other hand, supposing the mixed metals can be used as a composite material, there is no need to separate Ni, Cu, Fe, or Sn from their mixed leachates during the recovery process (Yang et al., 2016). In this context, the metals' recycling flowsheet is supposed to be significantly simplified and cost-effective.

Keeping these in mind, herein, we have extended the "waste-to-treasure" principle via employing a facile boriding strategy to directly convert the multimetal cations contained leachates of various of WPCBs in multimetal borides (FeNiCuSnBs) for efficient OER. Fe, Ni, Cu, and Sn have been efficiently recovered from the leachate via the novel boriding process. The as-obtained mixed metal boride catalysts have exhibited excellent OER performance (the j_{10} is achieved with a low η of 199 mV) with low OER catalyst manufacturing cost. Additionally, the catalyst structure-activity relationship has been elucidated with the aid of *ex-situ* characterization techniques. It is unveiled that the accelerated surface reconstruction induced by B/Sn etching significantly promotes the OER process. Moreover, the efficient mass/charge transfer and multiple active sites (Ni/Fe/Cu (oxy)hydroxides) and the amorphous hierarchical structure also benefit the OER performance. Considerably, the proposed facile and efficient boriding

strategy can be applied to regenerate efficient catalysts from WPCBs and be extended to the high-efficiency waste metal recovery and reutilization of critical metals from other electrical and electronic wastes.

6.2. Experimental section

6.2.1. Catalyst synthesis

The FeNiCuSnB catalysts (FNCSBs) derived from the leachates of WPCBs were prepared via a simple and low-cost boriding route. The pretreatment processes, such as crushing, sampling, and physical separation, were finished in a recourse recycling company in Changsha, China, as well as the hydrometallurgical recovery of noble metals (e.g., Pd, Au, Pt, Ag). Later, the resulting noble metal-free leachates were taken as the precursor in our study. Four leachates with various ion concentrations were employed to verify the universality of the proposed "waste-to-treasure" strategy.

In a typical boriding process, a certain amount of as-obtained leachates was added in a 500 mL three-necked round-bottom flask, which was diluted to a fixed volume of 100 mL with pure water. A small volume of solution was collected to calculate the ion concentrations before the reaction. Then the solution was stirred vigorously under an Ar flow for about 30 min. Afterward, 30 mL of 0.1 M NaOH aqueous solution containing excess sodium borohydride (NaBH_4) was slowly added to the solution using a syringe under constant stirring, in an ice-water bath. The solution was then stirred for 20 min to ensure the complete reaction. After that, the vessel was kept still for 12 h, and a small volume of solution was collected with a syringe to test the ion concentrations after the reaction. Subsequently, the precipitate in the solution was separated with a magnet and well washed with ethanol and water. At last, the products were dried at 50 °C, in a vacuum oven. Four borides were prepared via the same procedures, with different leachate precursors.

6.2.2. Physical and chemical characterization

Methods for XRD, SEM, TEM, XPS, ICP-OES, and ICP-MS measurements are described in Chapter 4, Section 4.2.2.

6.2.3. Electrochemical tests

Methods for electrochemical measurements are described in Chapter 4, Section 4.2.3.

6.3. Results and discussion

6.3.1. Catalyst synthesis and structural characterizations

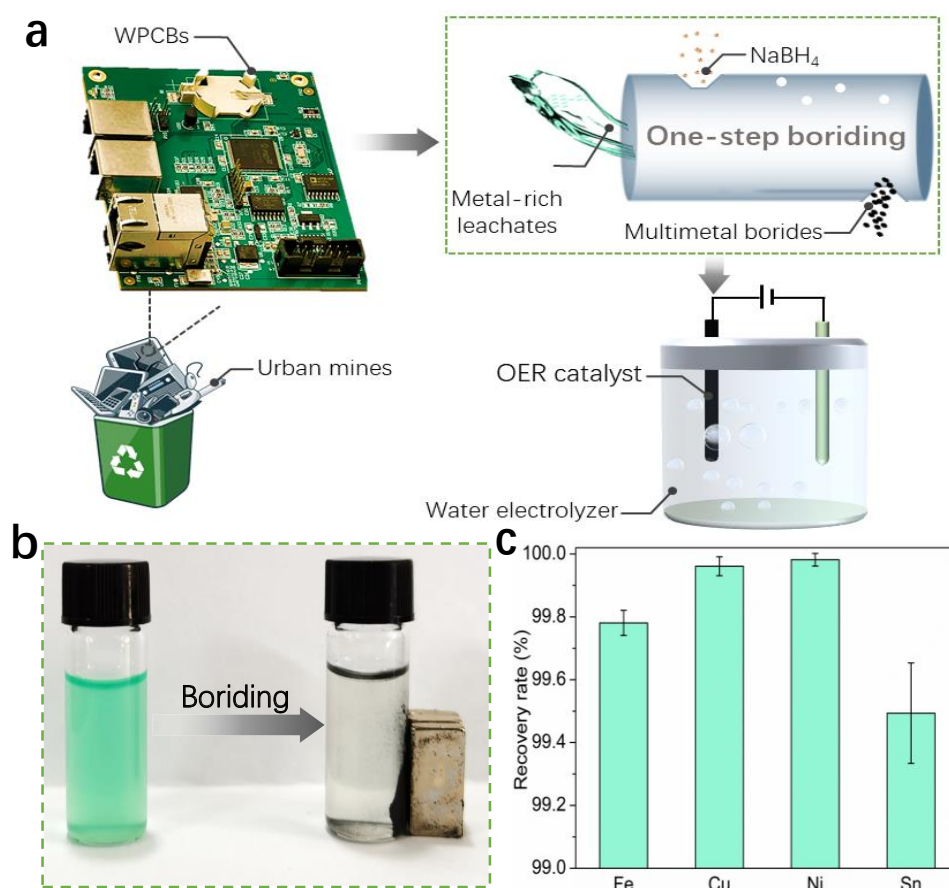


Figure 6.1. Schematic illustration of the boriding recycling process. (a) Schematic illustration showing the synthesis of electrocatalysts for OER from the waste leachates of WPCBs via a facile boriding recycling process. (b)

Photographs of the WPCB leachates before and after the boriding reaction. (c) Recovery rates of Fe, Cu, Ni, and Sn via the boriding recycling process for FNCSB-4.

The multimetal borides, denoted as FeNiCuSnBs (FNCSBs), were obtained from the leachates of WPCBs via a facile boriding strategy as shown in Fig. 6.1a. In brief, the collected WPCBs were subjected to a series of physical and chemical treatments processes (e.g., crushing, separation, and leaching) to obtain the leachates, which were substantially chemically reduced in an ice-water bath by NaBH₄ under the Ar atmosphere. To further verify the universal of the proposed "waste-to-treasure" strategy, four samples (FNCSB-1 to FNCSB-4) originated from four PCB precursors with various metal ratios (Table 6.1) were prepared via the boriding chemical reduction process. In addition, the boriding process could be visually tracked by the color changes of the solution, as shown in Fig. 6.1b. Compared to the initial WPCB leachates (green), the solution turns to be colorless and transparent after about 10 min, possibly as a result of the significantly decreased concentration of metal ions. The chemical components of the obtained FNCSBs were further studied with ICP-OES. Compared with FNCSB-1 (Fe_{15.6}Ni_{8.7}Cu_{2.3}Sn_{1.3}B_{6.2}O_{65.9}), FNCSB-2 (Fe_{9.5}Ni_{15.6}Cu_{0.7}Sn_{1.2}B_{9.2}O_{63.8}), and FNCSB-3 (Fe_{16.1}Ni_{18.1}Cu_{1.1}Sn_{1.7}B_{14.5}O_{48.5}), FNCSB-4 (Fe_{4.8}Ni_{36.4}Cu_{0.9}Sn_{1.3}B_{28.1}O_{28.5}) contains a summation of 41.2 % Ni and Fe concentration, which is higher than the other three multimetal borides.

Table 6.1. The metal ion concentrations in leachate precursors.

Sample	Concentration (mg L ⁻¹)					
	Fe	Cr	Cu	Mn	Ni	Sn
Precursor of FNCSB-1	10530.70	28.8	5044.7	78.30	5364.80	2817.45
Precursor of FNCSB-2	9524.48	27.35	4572.50	88.65	5499.65	2809.45
Precursor of FNCSB-3	13217.52	16.25	8537.53	81.95	5736.88	1326.36
Precursor of FNCSB-4	7326.88	30.85	5614.45	67.42	12830.44	1821.51

During the boriding process, Fe, Ni, Cu, and Sn's recovery efficiencies were calculated via characterizing the ion concentrations before and after the reaction. As shown in Fig. 6.1c, the recovery rates of Fe, Ni, Cu, and Sn attain 99.78%, 99.98%, 99.96%, and 99.49%, respectively. Compared with the prominent (bio)hydrometallurgical processes (Table 6.2) in metal recovery for WPCBs, here the one-step boriding process is facile with fewer chemicals consumption, fast recovery dynamics, and higher metals recovery rates than the state-of-the-art selective (bio)leaching/extraction routes. The high recovery rate achieved during the boriding process for Fe, Ni, Cu, and Sn is mainly due to the strong reducing capability of NaBH₄. The Fe³⁺, Ni²⁺, Cu²⁺, and Sn⁴⁺ cations in the leachate can be unselectively and rapidly (within several minutes) reduced and precipitated in the solution via the following chemical equation: Fe³⁺ + Ni²⁺ + Cu²⁺ + Sn⁴⁺ + 11BH₄⁻ + 30H₂O → FeNiCuSnB + 37H₂ + 10B(OH)₃ (Carenco et al., 2013). Interestingly, the generated multimetallic borides can be easily separated from the solution by using a magnet (Fig. 6.1b), which could be facile for further large-scale separation processes under a magnetic field. After the separation of the FNCSB-4 solid, the Fe³⁺, Ni²⁺, Cu²⁺,

and Sn⁴⁺ concentrations in the solution have been reduced to 0.9735, 0.5334, 0.2289, and 0.4295 mg L⁻¹. The remaining concentrations of Ni²⁺ and Cu²⁺ are close to the emission limits (0.5 mg L⁻¹ for Ni, 0.5 mg L⁻¹ for Cu) of the Discharge Standard of Water Pollutants for Electronic Industry in China (GB 39731-2020). Thus, the highly efficient boriding process can facilitate the subsequent wastewater treatment process.

Table 6.2. A summary of base metal recovery from WPCBs with state-of-the-art techniques.

WPCB type	Recovery method	Recovery rate (%)				Reference
		Ni	Cu	Fe	Sn	
LCD modules WPCBs*	Two-stage leaching, selective extraction	97.4	99.99	-	-	<i>Green Chem.</i> 2020, 22, 7080-7092.
Mixed WPCBs	Ball milling, leaching, recrystallization	-	99.8	-	-	<i>Environ. Sci. Technol.</i> 2019, 53, 2748-2757.
Computers WPCBs*	Selective leaching	12.6	96.5	-	9.3	<i>Resourc. Conserv. Recycl.</i> 2020, 154, 104624.
Mixed WPCBs	Biobleaching, cementation	-	99	-	-	<i>Hydrometallurgy</i> 2020, 191, 105170.
Mixed WPCBs*	Selective leaching, cyclone electrowinning	-	95.72	92.59	92.75	<i>J. Hazard. Mater.</i> 2020, 384, 121355.

						ACS
						<i>Sustainable</i>
Mixed WPCBs*	Supergravity separation	-	97.80	-	97.69	<i>Chem. Eng. 2018, 6, 186-192.</i>
mobile phones WPCBs*	Ionic liquid-assisted leaching	-	92.65	-	-	<i>J. Clean. Prod. 2020, 256, 120368.</i>
Mixed WPCBs*	Bioleaching (12 days)	82	90	-	-	<i>Hydrometallurgy 2013, 131-132, 138-143.</i>
Computers WPCBs	Bioleaching (8 days)	-	85	-	-	<i>Waste Manage. 2015, 41, 148-158.</i>
Mixed WPCBs	One-step boronizing	99.98	99.96	99.78	99.49	This study

* *Note: In these studies, the metal recovery refers to the leaching ratio of metals from the PCBs, and these studies did not recycle metals from the solution.*

The morphology of FNCSB-4 was firstly probed by SEM. Figure 6.2a-b reveals that FNCSB-4 exhibits a coral-like interconnected structure that consists of hierarchical aggregates of nanocolumn-like particles with abundant pores. These creamy pores are capable of providing abundant transportation channels for electrolytes and gaseous products (Chen et al., 2020d). Besides, the as-formed multicomponent hierarchical nanostructure not only provides sufficient electroactive sites but also facilitates the mass/charge transfer during OER (Dang et al., 2017; Guo et al., 2019c). The size of FNCSB-4 nanoparticles varies in the range of 50-100 nm, as observed in the TEM image (Fig. 6.2c).

An extension of the amorphous layer, as revealed in Fig. 6.2d, is attributed to the development of a thin metal oxide/borate layer on metal boride particles (Nsanziimana et al., 2018b). Besides, the SAED pattern in Fig. 6.2e discloses a local disordered structure of FNCSB-4 as no diffraction spots or sharp diffraction rings are observed. The EDS analysis implies the co-existence of B, O, Sn, Fe, Cu, and Ni elements in FNCSB-4, and these six elements are homogeneously distributed (Fig. 6.2f). It should be mentioned that oxygen in the borides mainly stems from the inescapable surface oxidation during the catalyst synthesis process, which is also validated by the previous TEM image.

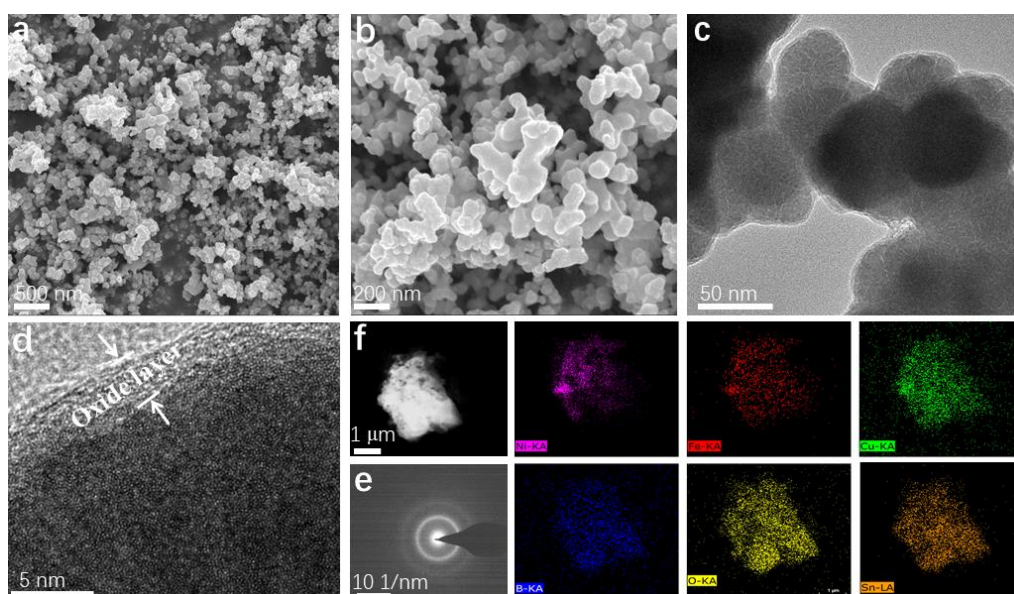


Figure 6.2. Microscopic characterization of FNCSB-4. (a, b) SEM images. (c) TEM bright-field image. (d) HRTEM image and (e) corresponding SAED pattern. (f) TEM EDS mapping.

The crystallinity of FNCSB-4 was further investigated via the powder XRD technique. As depicted in Fig. 6.3a, there are no pronounced crystalline diffraction peaks observed, and only a broad hump within the 2θ range of $40 - 50^\circ$ is observed. The XRD result tells the amorphous feature of FNCSB-4 and supports the HRTEM and SAED observations, being in line with earlier reports on amorphous borides (Chen et al., 2021c; Li et al., 2019d; Nsanziimana et al.,

2019). XPS was employed to uncover the surface chemistry of FNCSB-4. As expected, the survey spectrum of FNCSB-4 identifies the co-presence of Sn, Fe, Cu, Ni, B, and O elements (Fig. 6.3b). In the B 1s spectrum (Fig. 6.3c), two peaks at 187.7 and 192.2 eV can be assigned to metalloid boron and oxidized boron, respectively. Additionally, the binding energy of metalloid B in FNCSB-4 is higher than that of pure B (187.0 eV), hinting B atoms in FNCSB-4 can donate electrons to the bonded metals (Masa et al., 2019). Thus, the existence of boron can regulate the electronic structure of Ni/Fe/Cu/Sn in FNCSB-4. The Sn 3d spectrum shows two peaks at 485.2 and 486.4 eV, respectively (Fig. 6.3d). The former one at 485.2 eV is attributed to the metallic Sn, and the latter one at 486.4 eV is from Sn^{4+/2+} (Li et al., 2018a), arising from the oxidation of FNCSB-4 under ambient conditions. There are two separate peaks in the Cu 2p core-line spectrum (Fig. 6.3e). The binding energy at 931.9 eV can be indexed to the Cu 2p_{3/2} of metallic Cu or Cu⁺, and the higher binding energy at 951.9 eV can be assigned to Cu^{0/1+} 2p_{1/2} (Ling et al., 2018). The Ni 2p spectrum can be deconvoluted into six peaks in Fig. 6.3f, which is attributed to four spin-orbit doublets and two shakeup satellite peaks. The two peaks with lower binding energies of 851.8 and 869.1 eV can be ascribed to Ni⁰ 2p_{3/2} and Ni⁰ 2p_{1/2}, respectively, indicating the generation of Ni-B/Ni-based alloys in FNCSB-4. Moreover, the binding energies at 855.6 and 873.6 eV can be indexed to Ni²⁺ 2p_{3/2} and Ni²⁺ 2p_{1/2} with two satellite peaks at 860.8 and 880.1 eV accordingly. For the Fe 2p core-line spectrum in Fig. 6.3g, the peak located at 706.1 eV is assigned to Fe⁰. The other two spin-orbit doublets are stemmed from Fe³⁺ (711.5 and 724.6 eV) and Fe²⁺ (709.1 and 722.2 eV). In the O 1s spectrum (Fig. 6.3h), three peaks located at 529.5, 531.6, and 532.8 eV can be attributed to the lattice oxygen, substituted hydroxyl groups, and surface physic-/chemisorbed H₂O, respectively. The rich oxidation states of surface metals could be ascribed to that transition metal borides can be oxidized readily when exposed to water/air (Li et al., 2019d), and the formed highly oxidized

surface would escalate the subsequent electrocatalytic reaction (Chen et al., 2020d; Wang et al., 2019a).

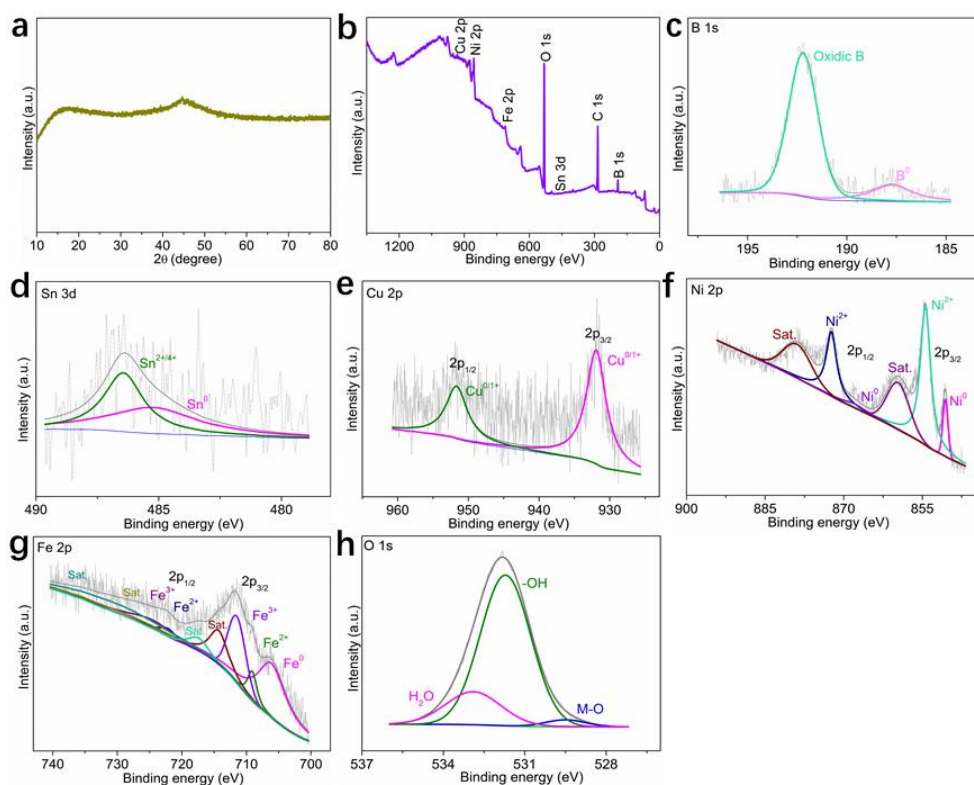


Figure 6.3. XRD and XPS characterizations of FNCSB-4. (a) XRD pattern. (b) XPS survey of FNCSB-4. (c-h) High-resolution XPS spectra of B 1s, Sn 3d, Cu 2p, Ni 2p, Fe 2p, and O 1s for FNCSB-4.

6.3.2. Electrocatalytic performance of FNCSBs

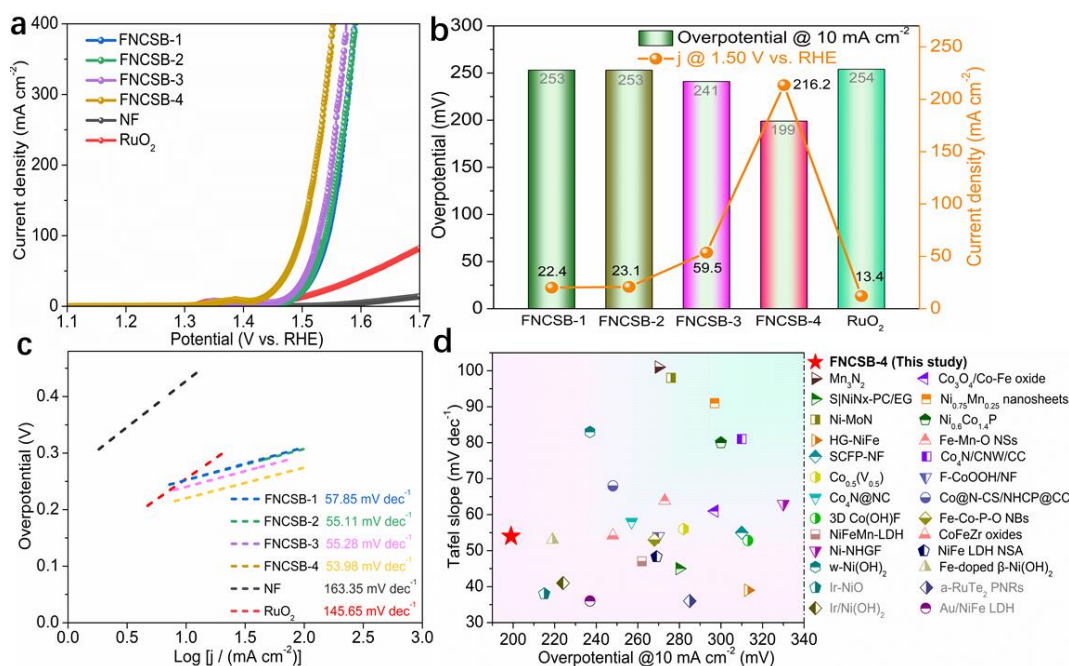


Figure 6.4. OER performance of FNCSBs. (a) LSV curves of FNCSBs, the RuO₂ catalyst, and bare NF. (b) η_{10} , and the current densities at 1.50 V vs. RHE of FNCSBs and the RuO₂ catalyst. (c) Tafel plots of FNCSBs and the RuO₂ catalyst. (d) OER activity comparison graph showing the Tafel slope with η_{10} for FNCSB-4 and reported state-of-the-art TM-based electrocatalysts, as well as noble metal-containing catalysts (listed in Table 6.3).

The OER electrocatalytic performance of as-obtained catalysts was tested in a 1.0 M KOH solution. For direct comparison, the OER activity of the commercial RuO₂ catalyst and NF was also measured. The LSV polarization curves in Fig. 6.4a disclose that FNCSB-4 outperforms its analogues, the RuO₂ catalyst, and NF for OER. Remarkably, to attain the j_{10} , FNCSB-4 only requires an η of 199 mV which is significantly lower than other investigated catalysts (Fig. 6.4b). Compared with other samples, FNCSB-4 exhibits the highest j of 216.2 mA cm⁻² at the η of 270 mV, 16 times higher than that of the RuO₂ catalyst. The oxidation peaks located at 1.3 - 1.4 V vs. RHE originate from the electrooxidation of Ni species from the Ni component in FNCSBs and the NF substrate (Chen et al., 2020e). Additionally, NF exhibits a low OER activity ($\eta_{10} = 428$ mV), revealing its minor contribution to the catalytic activity

of FNCSBs. The OER kinetics of FNCSBs and the RuO₂ catalyst are analyzed with the Tafel plots. Compared with NF (163.35 mV dec⁻¹), RuO₂ (145.65 mV dec⁻¹), FNCSB-1 (57.85 mV dec⁻¹), FNCSB-2 (55.11 mV dec⁻¹), and FNCSB-3 (55.28 mV dec⁻¹), FNCSB-4 displays the lowest Tafel slope (53.98 mV dec⁻¹) (Fig. 6.4c). These results insinuate that FNCSB-4 is the most kinetically favourable electrocatalyst among the studied materials. The major difference between FNCSB-4 and other materials is the higher content of Ni and Fe, suggesting that Ni and Fe may be the most active components in FNCSBs for OER, which is in line with previous reports (Gao and Yan, 2020; Liang et al., 2017; Zhao et al., 2020b). Furthermore, to the best of our knowledge, compared to other recently reported waste-derived OER catalysts, FNCSB-4 achieves a record-high activity (Table 6.3). In addition, FNCSB-4 exhibits a better OER activity (η_{10} , Tafel slope) than most of the state-of-the-art TM-based nanocatalysts, as well as a group of noble metal-contained catalysts (Fig. 6.4d, Table 6.4), such as Ni-MoN (276 mV, 98 mV dec⁻¹) (Zhu et al., 2018b), Fe-doped β -Ni(OH)₂ (219 mV, 53 mV dec⁻¹) (Kou et al., 2019), Fe-Mn-O NSs (273 mV, 63.9 mV dec⁻¹) (Teng et al., 2018), and Ir/Ni(OH)₂ (224 mV, 41 mV dec⁻¹) (Zhao et al., 2020a).

Table 6.3. A summary of the OER properties of FNCSB-4 and the recently documented waste-derived OER catalysts.

Waste	Catalyst	η (mV)	Reference
Scrap copper wires	NiCoP/SCW	$\eta_{10} = 220$	<i>Adv. Energy Mater.</i> 2018, 8, 1802615.
Biomass wastes	F-(1-5)/NF	$\eta_{50} = 293$	<i>Nat. Sustain.</i> 2020, 3, 556-563.
Spent eggshell membranes	ESM/CNT/NiCo ₂ O ₄	$\eta_{20} = 420$	<i>Nanoscale</i> 2015, 7, 14378-14384.

Scrap stainless steel wires	SSW Rs-12 h	$\eta_{100} = 257$	<i>Adv. Energy Mater.</i> 2020, 10, 1904020.
Spent Zn-C batteries	Mn ₃ O ₄	$\eta_{10} = 360$	<i>ChemElectroChem</i> 2020, 7, 2073-2080.
Spent Li-ions batteries	Ni _{0.5} Mn _{0.3} Co _{0.2} (OH) ₂	$\eta_{10} = 280$	<i>J. Clean. Prod.</i> 2019, 236, 117576.
Waste carrots	PC-Ni _{0.75}	$\eta_{10} = 368$	<i>Electrochim. Acta</i> 2019, 314, 49-60.
Biomass wastes	BRC _{AC} 850 ₂	$\eta_{10} = 450$	<i>ACS Sustainable Chem. Eng.</i> 2019, 7, 17039-17046.
Spent steel powder	HSSP	$\eta_{10} = 359$	<i>Electrochim. Acta</i> 2021, 371, 137848.
Biomass wastes	N-PC@Ni	$\eta_{10} = 314$	<i>Nanomaterials</i> 2020, 10, 76.
Diaper wastes	NiO@CFs	$\eta_{10} = 280$	<i>Fuel</i> 2021, 294, 120558.
Cotton textile wastes	Fe ₃ O ₄ /NiS@CC	$\eta_{10} = 310$	<i>J. Mater. Sci. Technol.</i> 2020, 59, 92-99.
Purchased Fe foam*	NiFe(OH) _x /FF	$\eta_{386.9} = 300$	<i>Small</i> 2020, 16, 2000663.
Spent tea leaves	Co@PC-8	$\eta_{10} = 327$	<i>Green Chem.</i> 2020, 22, 6967-6980.
WPCBs	FNCSB-4	$\eta_{10} = 199$ $\eta_{20} = 205$	This study

$$\eta_{100} = 251$$

$$\eta_{400} = 301$$

* The Fe foam reported in this study is directly purchased from a company, and actually it is not a kind of waste.

Table 6.4. A summary of the OER properties of the recently documented TM-based nanocatalysts, as well as a group of noble metal catalysts.

Catalyst	η_{10} (mV)	Tafel slope (mV dec ⁻¹)	Reference
NCNTFs	370	93	<i>Nat. Energy</i> 2016, 1, 15006.
Mn ₃ N ₂	270	101	<i>Angew. Chem. Int. Ed.</i> 2018,57, 698.
w-Ni(OH) ₂	237	83	<i>Nat. Commun.</i> 2019, 10, 1–10.
HG-NiFe	313	39	<i>Sci. Adv.</i> , 2018, 4, eaap7970.
Ni-NHGF	330	63	<i>Nat. Catal.</i> 2018, 1, 63.
Ni-MoN	276	98	<i>Adv. Energy Mater.</i> 2018, 8, 1802327.
S NiN _x -PC/EG	280	45	<i>Nat. Commun.</i> 2019, 10, 1392.
Fe-Mn-O NSs	273	63.9	<i>Adv. Funct. Mater.</i> 2018, 28, 1802463.
Co ₃ O ₄ /Co-Fe oxide	297	61	<i>Adv. Mater.</i> 2018, 30, 1801211.
Ni _{0.6} Co _{1.4} P	300	80	<i>Adv. Funct. Mater.</i> 2018, 28, 1706008.
Co ₄ N@NC	257	58	<i>ACS Energy Lett.</i> 2020, 5, 692.
Co ₄ N/CNW/CC	310	81	<i>J. Am. Chem. Soc.</i> 2016, 138, 10226.
NiFe LDH NSA	269	48.3	<i>Nat. Commun.</i> 2018, 9, 2609.
Co _{0.5} (V _{0.5})	282	56	<i>Adv. Energy Mater.</i> 2020, 10, 1903571.

FeOOH(Se)/IF	287	54	<i>J. Am. Chem. Soc.</i> 2019, 141, 7005-7013.
F-CoOOH/NF	270	54	<i>Angew. Chem. Int. Ed.</i> 2018, 57, 15471.
Co@N- CS/NHCP@CC	248	68	<i>Adv. Energy Mater.</i> 2019, 1803918.
3D Co(OH)F	313	52.8	<i>Adv. Mater.</i> 2017, 29, 1700286.
Fe-Co-P-O NBs	268	53	<i>Energy Environ. Sci.</i> 2019, 12, 3348.
SCFP-NF	310	55	<i>Adv. Mater.</i> 2018, 30, 1804333.
Ni _{0.75} Mn _{0.25} nanosheets	297	91	<i>ACS Energy Lett.</i> 2018, 3, 2150.
Fe/Fe ₃ C-MC	320	51	<i>Angew. Chem. Int. Ed.</i> 2021, 60, 2120.
Fe-Co-O/Co@NC- mNS/NF	257	41.56	<i>Small</i> 2021, 2101312.
NH ₄ CoPO ₄ H ₂ O	252	57	<i>Adv. Sci.</i> 2021, 2100498.
Fe-doped β - Ni(OH) ₂	219	53	<i>ACS Energy Lett.</i> 2019, 4, 622.
Co ₃ O ₄ -Ag@B	270	62	<i>Appl. Catal. B.</i> 2021, 120529.
NiFeMn-LDH	262	47	<i>Energy Environ. Sci.</i> 2017, 10, 121–128.
CoFeZr oxides	248	54.2	<i>Adv. Mater.</i> 2019, 1901439.
La _{0.33} SrCo _{0.5} Fe _{0.5} O _x	240	-	<i>Appl. Catal. B.</i> 2021, 297, 120484.
Ir-NiO	215	38	<i>J. Am. Chem. Soc.</i> , 2020, 142(16), 7425-7433.
a-RuTe ₂ PNRs	285	36	<i>Nat. Commun.</i> 2019, 10, 5692.
Ir/Ni(OH) ₂	224	41	<i>Adv. Mater.</i> , 2020, 2000872.

Au/NiFe LDH	237	36	<i>J. Am. Chem. Soc.</i> 2018, 140, 3876-3879.
FNCSB-4	199	53.98	This study

EIS analyses provide more information on the electrocatalytic kinetic characteristics of catalysts. The Nyquist plots are depicted in Fig. 6.5a and analyzed to measure the R_{ct} . As displayed in Table 6.5, FNCSBs exhibit similar R_{ct} , which are much smaller than that of NF (177.1 Ω), with FNCSB-4 possessing the smallest R_{ct} of 2.4 Ω . These results confirm the efficient charge transfer at the interface of FNCSB catalysts and electrolytes during the OER process.

Table 6.5. Calculated charge transfer resistance (R_{ct}) and solution resistance (R_s) (in Ohm, Ω) of the materials deposited on NF obtained from the Nyquist plot during the EIS experiments.

Catalyst	R_s	R_{ct}
FNCSB-1	1.112	4.939
FNCSB-2	1.191	5.147
FNCSB-3	1.268	3.628
FNCSB-4	1.325	2.415

To evaluate the active site density of various catalysts, the C_{dl} of FNCSBs are determined by conducting CV measurements in a narrow potential range (1.10 - 1.20 V vs. RHE) without redox process, with various scan rates. The calculated C_{dl} of FNCSB-4 is 4.68 mF cm^{-2} , outperforming FNCSB-1 (2.94 mF cm^{-2}), FNCSB-2 (3.08 mF cm^{-2}), and FNCSB-3 (3.13 mF cm^{-2}). Hence, FNCSB-4 with the highest ECSA (117.0 cm^2) can offer many more electrochemically active sites for OER and enhance the catalytic performance (Fig. 6.5b). To get a better understanding of the intrinsic catalytic activity of per active site, the LSV curves were normalized with ECSA (j_{ECSA}). As

illustrated in Fig. 6.5b, FNCSB-4 only takes an η of 317 mV to drive a ECSA normalized j_3 , outperforming FNCSB-1 (337 mV), FNCSB-2 (336 mV), and FNCSB-3 (325 mV). As a result, both the large active surface area and the high intrinsic catalytic activity benefit the OER performance of FNCSB-4. Interestingly, there is a linear relationship between the η at the ECSA normalized current density of 3 mA cm⁻² (η_3) and the (Fe + Ni) ratio ($r_{\text{Fe+Ni}}$) in FNCSBs of all the FNCSBs ($\eta_3 = -1.19 r_{\text{Fe+Ni}} + 365.76$ mV), revealing that the ratio of (Fe + Ni) in the multimetal borides plays a critical role in determining the intrinsic OER activity (Fig. 6.5c). This finding benefits further the design of high-performance OER catalysts via composition regulation.

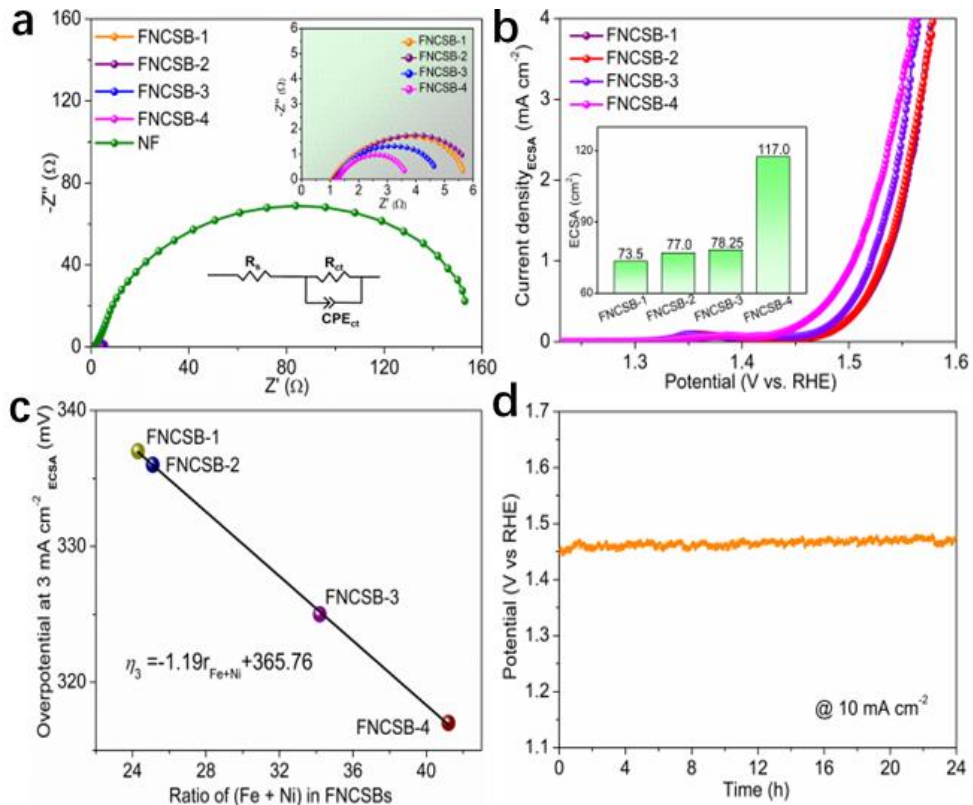


Figure 6.5. (a) Nyquist plots of FNCSBs and NF at 1.5 V vs. RHE, and the inset shows an enlarged part of the Nyquist plots. (b) ECSA normalized LSV curves for FNCSBs, and ECSA values of FNCSBs (inset). (c) Linear relationship between the η at the ECSA normalized current density of 3 mA

cm⁻² and the (Fe + Ni) ratio in FNCSBs of all FNCSBs. (d) Chronopotentiometry curve of FNCSB-4 at j_{10} for 24 h.

Stability is a critical parameter to evaluate the practical value of OER catalysts. Herein, the durability of FNCSB-4 toward OER was assessed by the chronopotentiometry test at j_{10} exhibits a negligible increase of η after 24 h operating in alkaline solution, further confirming the long-term stability of FNCSB-4 (Fig. 6.5d). Generally, the as-synthesized FNCSBs show excellent OER performance under alkaline conditions, suggesting that the WPCBs derived low-cost FNCSBs are enticing candidatures for anode catalysts in industrial water splitting systems.

6.3.3. Elucidation of the structure-activity correlations

Transition metal-based catalysts (e.g., sulfides, alloys, phosphides) will undergo surface reconstruction during the OER process, and the *in situ* generated metal (oxy)hydroxides (e.g., FeOOH, NiOOH) act as the real active sites (Hausmann et al., 2020; Li et al., 2020b; Li et al., 2019c; Sivanantham et al., 2020). In this study, to understand the structural evolution dynamics during the catalytic process and uncover the nature of the active species' structure-activity relationship, the post-CA FNCSB-4 was thoroughly characterized via microscopic, spectroscopic, and analytical techniques.

Unlike the as-prepared catalyst, TEM images tell that the morphology of FNCSB-4 undergoes profound variation during the OER process. It is clear that part of the aggregated nanocolumn-like particles on FNCSB-4 has been converted into cross-link nanofilm analogues during the OER test, and the thin nanosheets are composed of a reduced number of layers that are loosely overlapping with each other (Fig. 6.6a). The HRTEM image exhibits a hybrid amorphous/crystalline structure (Fig. 6.6b). Many lattice fringes are markedly presented, signifying the generation of stable species during the OER process.

The surface composition of FNCSB-4 after the OER process was further monitored by XPS. In the spectrum of Ni 2p (Fig. 6.6c), the peaks belonging to Ni⁰ are absent, while the peaks assigned to Ni²⁺ and Ni³⁺ (855.9 and 873.9 eV) (Qin et al., 2019) maintain during the OER stability test, implying the generation of nickel (oxy)hydroxide. Significantly different from the Fe 2p spectrum before OER, signals attribute to Fe⁰/Fe²⁺ are substituted by the trivalent Fe³⁺ (Fig. 6.6d), and two peaks located at 711.1 and 724.2 eV owing to the FeOOH phase (Liu et al., 2020; Zhong et al., 2016). Similarly, the peaks assigned to Cu^{0/1+} are absent in the spectrum of Cu 2p, while two peaks at 933.2 and 953.1 eV can be assigned to Cu²⁺ (Fig. 6.6e), implying the generation of Cu(OH)₂ on the catalyst surface. Combined with the XPS results and the HRTEM images, the abundant lattice fringes in Fig. 6.6b can be indexed to metal (oxy)hydroxides FeOOH, NiOOH/Ni(OH)₂, and Cu(OH)₂ (Zhang et al., 2019b; Zhang et al., 2019d). In the O 1s spectrum (Fig. 6.6f), the lattice oxygen species of the post-OER catalyst increase considerably than the as-prepared catalyst, which further verifies the formation of metal oxyhydroxides on the catalyst surface. Interestingly, the spectra of B and Sn exhibit noticeable different features. The signals of B and Sn elements almost disappeared in the post-OER spectra of FNCSB-4 (Fig. 6g-h), indicating that the surface of FNCSB-4 evolved into polyphase high-valent metal (oxy)hydroxides, which act as the catalytic active phase for OER (Zhang et al., 2020b).

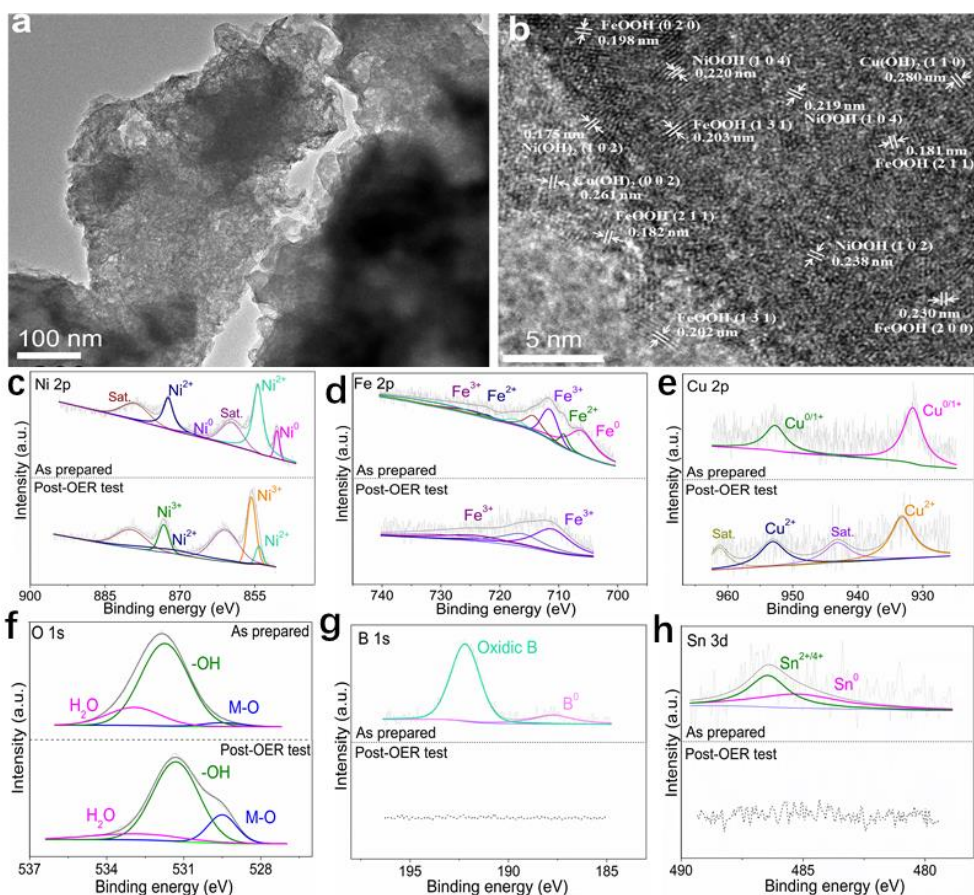


Figure 6.6. Post-OER characterizations of FNCSB-4. (a) TEM and (b) HRTEM images of FNCSB-4 after the OER test. High-resolution XPS scans in the (c) Ni 2p, (d) Fe 2p, (e) Cu 2p, (f) O 1s, (g) B 1s, and (h) Sn 3d regions of FNCSB-4 before and after the OER stability test.

The variation in the chemical composition of FNCSB-4 was also explored to verify the surface evolution during the OER test. Hereby, B and Sn on the catalyst surface are continuously dissolved into the electrolyte during the 12 h OER stability test, suggested by the ICP-MS measurement (Fig. 6.7a). The prominent etching of B and Sn results in abundant vacancies and regulated surface electron properties. This process not only enhances the charge/mass transfer and accelerates the surface self-reconstruction during the OER process, but also benefits the OER via assisting the adsorption of reaction intermediates on the catalyst surface.

The electrochemical properties of post-OER FNCSB-4 were also studied, and the results are presented in Fig. 6.7b-c. The LSV curves of FNCSB-4 before CV activation, FNCSB-4 after 20 CV cycles, and FNCSB-4 after the stability OER test provide some interesting information. First, the OER activity of FNCSB-4 can be significantly enhanced during the 20 CV cycles, and the η_{10} decreased from 257 mV to 199 mV. This activation process mainly refers to the oxidation of surface metal borides species. Second, the OER activity of FNCSB-4 is further improved under the long-term OER test, which is in line with the chronoamperometric *i-t* curve in Fig. 6.5d. As discussed above, the morphology/nanostructure of FNCSB-4 evolved from nanoparticles to nanosheets during the OER test, resulting in higher surface area and populated active sites. With this in mind, the OER activity enhancement during the durability test can be ascribed to the gradual generation of metal (oxy)hydroxides, and the increased catalytical active sites. The latter one is also verified via the ECSA results, as the ECSA value increased by 1.25 times during the OER test. Such a favourable increment implies the expansion of the electrochemical surface area, with the aid of morphology evolution and B/Sn etching during the OER process.

Last but not least, the amorphous feature of FNCSB-4 also benefits the surface reconstruction during OER. The abundant under coordinative and unsaturated sites/crystal defects in amorphous FNCSB-4 trigger anions' dissolution since electrochemical etching preferentially occurs at the crystal defects (Song et al., 2016), which will accelerate the surface self-reconstruction of active sites. Also, the rich unsaturated sites can help the adsorption/desorption of intermediates during the OER process and promote the overall OER process (Anantharaj and Noda, 2019; Chen et al., 2020d).

In general, the excellent OER activity of FNCSB-4 is chiefly due to the accelerated surface self-reconstruction by B/Sn etching, efficient mass/charge

transfer, and multiple active sites (Ni/Fe/Cu (oxy)hydroxides), as well as the hierarchical structure and amorphous feature, as schematized in Fig. 6.7d.

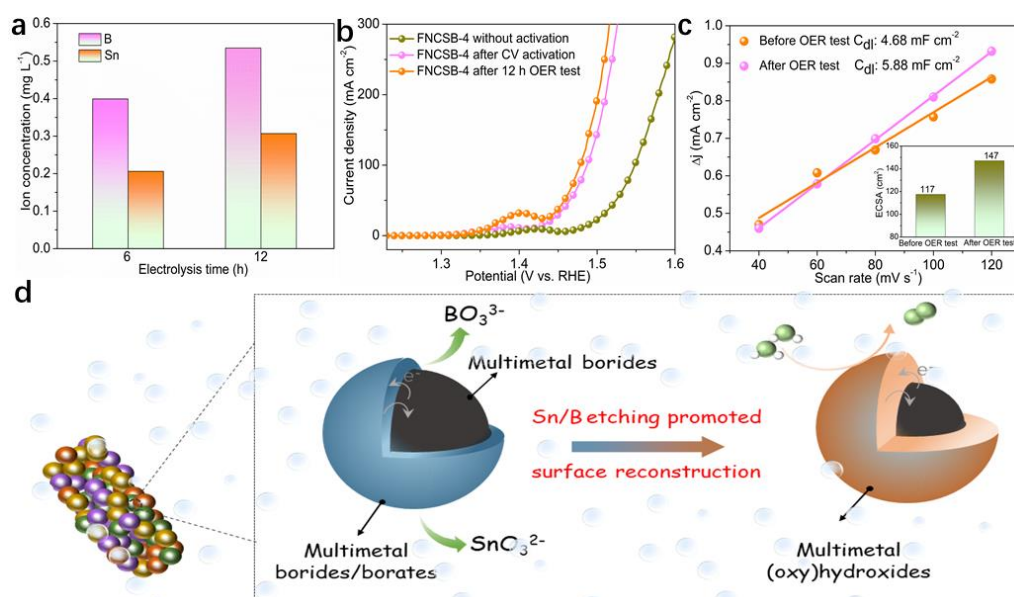


Figure 6.7. Surface evolution process of FNCSB-4 during OER. (a) B and Sn leaching in electrolytes during the 12 h OER test. (b) LSV curves of pristine FNCSB-4, CV activated FNCSB-4, and post-OER FNCSB-4 in 1.0 M KOH. (c) Difference in current density ($\Delta j = (j_a - j_c)/2$) plots against scan rate of FNCSB-4 before and after OER test, and the inset shows the ECSA values. (d) Illustration of the proposed surface evolution process and the mechanism for the enhanced OER activity of FNCSB-4.

6.4. Conclusions

In conclusion, we have developed a facile and efficient boriding strategy to directly convert the leachates of waste printed circuit boards (WPCBs) into magnetic mixed metal borides (FeNiCuSnBs) for OER for the first time. Fe, Ni, Cu, and Sn were efficiently recovered via the boriding reduction and magnetic separation process, with a metal cation recovery rate of 99.78%, 99.98%, 99.96%, and 99.49%, respectively. The optimized sample exhibit excellent catalytic performance for OER ($\eta_{10} = 199$ mV), outperforming the

most recently reported catalysts and all waste-derived OER catalysts. In-depth mechanism analyses suggest that the multimetal borides undergo surface reconstruction induced by B/Sn etching, and the *in situ* generated multimetal (oxy)hydroxides act as the active species to facilitate O₂ evolution. In addition, the efficient mass/charge transfer, the amorphous feature, and the hierarchical structure also contribute to superior electrocatalytic performance. This study gains an insight into the correlation between surface self-reconstruction and OER catalytic activity of multimetal boride-based catalysts. In addition, the boriding strategy reported here can be further applied to the efficient recycling and advanced energy-driven applications of valuable metals from other e-wastes for achieving a sustainable energy future.

CHAPTER 7

Recycling spent water treatment adsorbents for efficient electrocatalytic water oxidation reaction

This chapter has been derived from the published paper of *Resources, Conservation & Recycling*, 2022, 178, 106037.

7.1. Introduction

Heavy metal contaminated wastewater is one of the most critical environmental concerns because of its effects on public health and the ecosystem (Ji et al., 2021; Luo et al., 2021). Various techniques have been employed to control heavy metal pollutants in water, such as chemical precipitation, filtration, electrodeposition, neutralization, reverse osmosis, and adsorption (Xiong et al., 2021; Zou et al., 2021; Zuo et al., 2021). Among all these strategies, adsorption is an efficient and widely used one to remove and collect heavy metals ions from industrial wastewater (Chai et al., 2021; Luo et al., 2019; Ni et al., 2019a). Excellent adsorbents have been developed and shown good adsorption performance toward heavy metals adsorption, such as graphene, biochar, and metal oxides (Hao et al., 2019a; Huang et al., 2020). Among them, biochar derived from carbonization of different biomass has attracted enormous interest due to its low cost, conductive porous structure, large surface area, and tunable nanostructure (Alam et al., 2018; Chai et al., 2021). With the applications of the adsorption process, a large quantity of spent adsorbents also occurs in the industry (Singh and Singhal, 2013). After their end-use, the disposal of these massive waste adsorbents is a critical solid waste issue (Chai et al., 2021). In most cases, they have been incinerated or landfilled, and these practices exacerbate the solid waste treatment problem and are not facile in achieving the goal of carbon neutrality (He et al., 2018a; Vakili et al., 2019). In this respect, it is of great environmental significance and economic interest to reutilize these spent carbon-based adsorbents via a resource utilization strategy (Oldham et al., 2021; Sundriyal et al., 2021), for instance, converting them into valuable electroactive materials to achieve the industrial ecology philosophy.

With environmental issues apart, transition metals (TM, e.g., Cu, Ni, Co, Mn, and Fe) have gained growing attention in designing cost-effective

catalysts for emerging energy-related OER which plays a critical role in developing green hydrogen energy via water splitting (Suen et al., 2017; Yang et al., 2021; Zhou et al., 2021). Until now, a key issue in advancing sustainable hydrogen energy is the development of low-cost and efficient OER catalysts (Li et al., 2021; Wan et al., 2021). Recently, amorphous 3d TMBs have received much attention due to their remarkable electrochemical activity, flexible electronic properties, and earth abundance (Chunduri et al., 2019; Gupta et al., 2019b). To improve TMBs' electrocatalytic performance, anchoring electroactive nanoparticles onto porous substrates (e.g., carbon materials) with a large surface area is an advisable strategy because the porous scaffolds can limit the aggregation of boride nanoparticles and facilitate electrolyte diffusion during the electrochemical reaction (Mao et al., 2020). To this end, integrating metal borides with porous substrates to construct heterostructured electrocatalysts directly from industrial wastes (e.g., spent carbon-based adsorbents) would be of great environmental and economic significance.

Inspired by the "waste-to-wealth" principle on industrial ecology, for the first time, we developed a facile strategy to directly convert the multiple metal ions contaminated biochar adsorbents into heterostructured electrocatalysts. Via this one-step boriding strategy, the converted spent biochar adsorbent shows high efficiency in electrocatalytic OER. With a low manufacturing cost, the optimized heterostructured catalyst exhibits excellent OER performance ($\eta_{10} = 251$ mV). Furthermore, comprehensive analyses suggest the high catalytic efficiency mainly attributed to the porous biochar confined well-dispersed nano-sized metallic borides. The boriding method developed in this report can not only be applied to regenerate efficient catalysts from biochar-based spent carbon-based adsorbents, but can be further broadened to other types of spent heavy metal removal products, like membranes, metal

oxides/sulfides adsorbents, metal-organic frameworks, and polymeric nanocomposites, for other types of advanced applications.

7.2. Experimental section

7.2.1. Conversion of spent adsorbents to electrocatalysts

Preparation of biochar

The biochar was prepared from waste rice husk by a facile pyrolysis process. In a typical process, the waste rice husk collected from a rice processing plant in Guangdong, China was firstly air-dried and pulverized. Then, the obtained powders were soaked in the 3 M ZnCl₂ solution for 12 h, dried at 105 °C, and placed in a tube furnace. Nitrogen gas was introduced into the tube furnace for 20 min to ensure an inert atmosphere. After that, the pretreated waste rice husk was calcined at 600 °C under the pure nitrogen gas condition for a period of 2 h. Then, the collected sample was oxidized by a mixture of concentrated HNO₃ and H₂SO₄ (1:3 (v/v)) for 6 h at 80 °C. The acid treatment was used to oxidize the biochar, in order to improve its adsorption performance. Apart from acid treatment, alkali treatment, coating with carbonaceous materials, oxidizing-agents modification, metal salts or metal oxides modification are also widely employed to enhance the adsorption capacity of biochar. Subsequently, the resulting biochar was washed with DI water and dried in a vacuum oven, and then it was sealed and stored.

Heavy metal adsorption experiments

As the adsorption process in practical wastewater treatment plants typically applies adsorbents in a continuous mode (Rosales et al., 2017; Zhao et al., 2021; Zheng et al., 2019). A fixed-bed column packed with biochar was employed to conduct the adsorption tests in this study to simulate the industrial process. Typically, a certain amount of biochar was packed as an interlayer in

the homemade acrylic column with an internal diameter of 16 mm and a height of 100 mm. The two sides of the columns were filled with acid-cleaned high-purity quartz sands as supports. Two kinds of wastewater collected from Jiangxi, China, were used as the influent in this study, and the properties of industrial wastewater are listed in Table 7.1. Before using, the pH value of wastewater was regulated to 5-6 by 0.1 M HCl and 0.1 M NaOH solution. Then, the influent was continuously fed into the column in the bottom-to-top mode with a rate of 5 mL min⁻¹. In this study, to ensure sufficient adsorption of metal ions onto biochar, the adsorption process was running for 2 h. After the adsorption test, the used biochar was taken out for further use.

Table 7.1. Characters of industrial wastewater.

Property	Sample 1	Sample 2
pH	1	0.5
TOC*	0.26 mg L ⁻¹	0.51 mg L ⁻¹
Cu ²⁺	317.26 mg L ⁻¹	234.15 mg L ⁻¹
Ni ²⁺	759.25 mg L ⁻¹	631.65 mg L ⁻¹
Fe ³⁺	-	476.48 mg L ⁻¹

*TOC: Total organic carbon.

Conversion of waste adsorbents to catalysts

A facile boriding process realized the conversion of waste adsorbents to electrocatalysts. First, the waste adsorbents were placed in an empty container, and a freshly excessive NaBH₄ solution was dipped into the container by a syringe with vigorous magnetic stirring. After the reaction, a small amount of the reaction solution was collected to measure the concentration of metals, and the as-formed black particles were collected with magnets and washed with ethanol and DI water. Lastly, the samples were dried in a vacuum oven at 50 °C for 24 h.

The whole process is shown in Fig. 7.1.

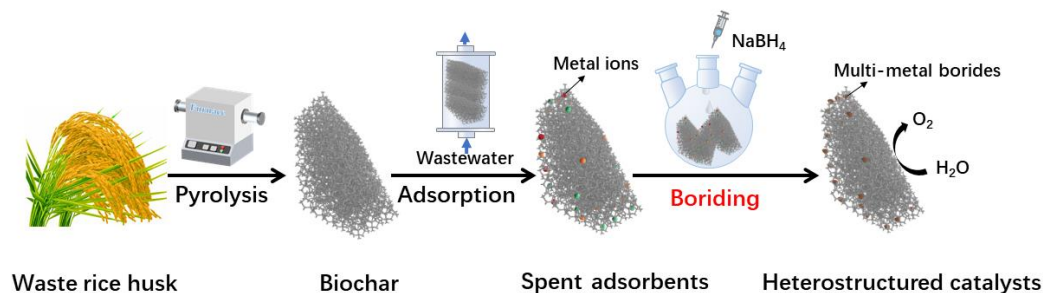


Figure 7.1. Schematic of the design of heterostructured OER electrocatalysts from spent biochar adsorbents.

7.2.2. Physical and chemical characterization

Methods for XRD, SEM, TEM, XPS, and ICP-MS measurements are described in Chapter 4, Section 4.2.2.

To investigate the surface chemistry of the biochar, FTIR was tested on a Bruker V80 machine at room temperature. The surface area and porosity of the biochar were obtained with a physical adsorption apparatus (ASAP2460), and the elemental analysis of the biochar was performed with a Thermo Scientific Flash 2000 Organic Elemental Analyzer, and the total organic carbon (TOC) of wastewater was tested with a TOC analyzer (Shimadzu). The magnetic properties of the sample were studied by a vibrating sample magnetometer (LakeShore 7404).

7.2.3. Electrochemical tests

Methods for electrochemical measurements are described in Chapter 4, Section 4.2.3.

7.3. Results and discussion

7.3.1. Conversion of spent adsorbents into borides/SA

Generally, spent adsorbents are incinerated or landfilled (Fig. 7.2a) and are turned into metal-laden solid wastes (He et al., 2018a; Vakili et al., 2019), which would exacerbate the solid waste treatment problem. In this study, our approach to convert spent biochar-based adsorbents (SA) into heterostructured catalysts is realized via a facile boriding strategy, as demonstrated in Fig. 7.2b. Specifically, a certain amount of metal ions-laden biochar was first placed in a three-necked flask, and freshly prepared excessive sodium borohydride solution was then dipped into the vessel using a syringe under vigorous stirring. After the reaction, the products were collected with magnets, then subjected to be washed and dried (see Experimental Section for details). The metal cations on the SA can be unselectively reduced within several minutes via the following chemical equations (Arivu et al., 2018). For the Ni²⁺ and Cu²⁺ laden SA: $2 \text{Ni}^{2+} + 2 \text{Cu}^{2+} + 8 \text{BH}_4^- + 18 \text{H}_2\text{O} \rightarrow 2 \text{NiCuB} + 9 \text{H}_2 + 6 \text{B}(\text{OH})_3$; for the Fe³⁺, Ni²⁺ and Cu²⁺ laden SA: $\text{Fe}^{3+} + \text{Ni}^{2+} + \text{Cu}^{2+} + 7 \text{BH}_4^- + 18 \text{H}_2\text{O} \rightarrow \text{FeNiCuB} + 9 \text{H}_2 + 6 \text{B}(\text{OH})_3$. It is worth noting that the generated metal boride/biochar heterostructures can be easily separated by a magnet (Fig. 7.3a), and the magnetic properties of NiCuFeB/SA were further investigated with a vibrating sample magnetometer. The magnetic hysteresis loop diagram of NiCuFeB/SA is shown in Fig. 7.3b, and its saturation magnetization is 14.11 emu g⁻¹. Hence, under the magnetic field, NiCuFeB/SA aggregates can be easily separated from the reaction solution, which could further facilitate the large-scale separation process.

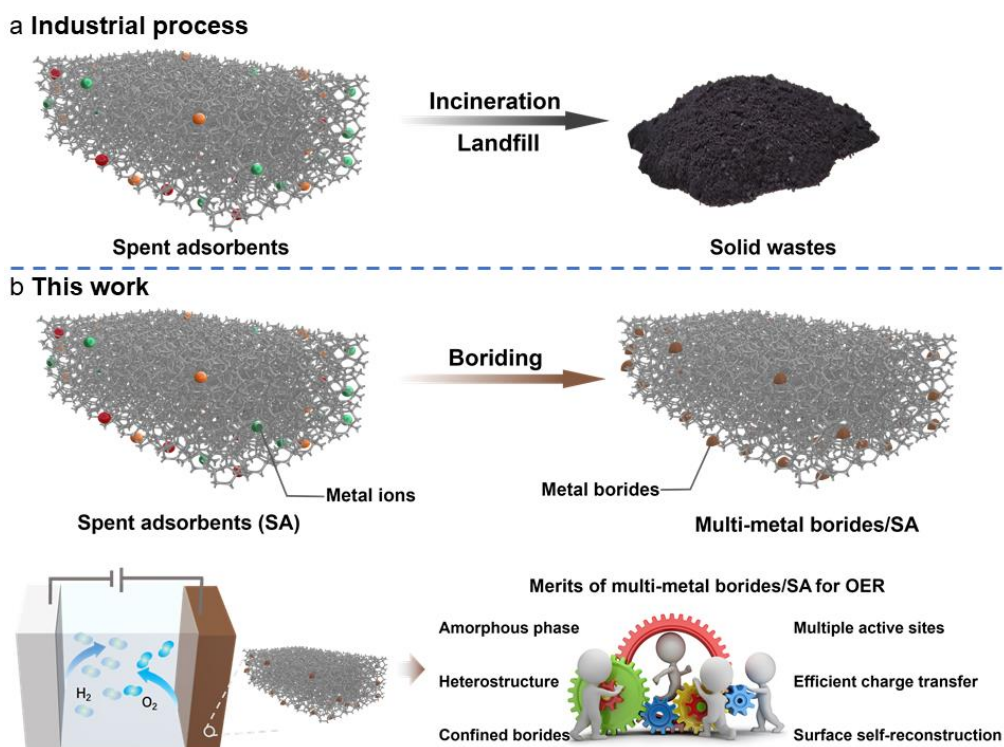


Figure 7.2. (a) Industrial process of spent adsorbents treatment. (b) General strategy of converting biochar based heavy metal contaminated spent adsorbents into OER electrocatalysts, and the multiple merits of multimetal borides/SA as electrocatalysts for OER.

Evaluating the conversion efficiency of SA to electrocatalysts is of great significance. In this study, the conversion efficiency is defined as the ratio of metal in obtained metal boride/biochar particles to the adsorbed metal by the biochar adsorbent, which was further calculated via calculating the metal concentrations in the reaction solution after the boriding process. As shown in Fig. 7.3c, the conversion efficiencies of Ni, Cu, and Fe reach 99.98%, 100.00%, and 99.99%, respectively, in the NiCuFeB/SA reaction system. To check the universal feature of the proposed eco-design principle, another catalyst (NiCuB/SA) based on the spent biochar was prepared by the same procedures, from a different wastewater precursor. Similarly, in the NiCuB/SA reaction system, the conversion efficiencies of Ni and Cu reach 100.00% and 99.99%, respectively. Therefore, it can be seen that all of the adsorbed metal ions on

the spent adsorbent have been totally converted into metal borides via the facile boriding process. In addition, the metal contents in NiCuFeB/SA and NiCuB/SA were further studied via ICP-MS. Compared with NiCuB/SA ($\text{Ni}_{51.1}\text{Cu}_{42.3}\text{B}_{6.6}/\text{SA}$), NiCuFeB/SA ($\text{Ni}_{43.6}\text{Cu}_{18.6}\text{Fe}_{32.1}\text{B}_{5.7}/\text{SA}$) contains a higher summation of 75.7 % Ni and Fe concentration, which might contribute to better OER performance.

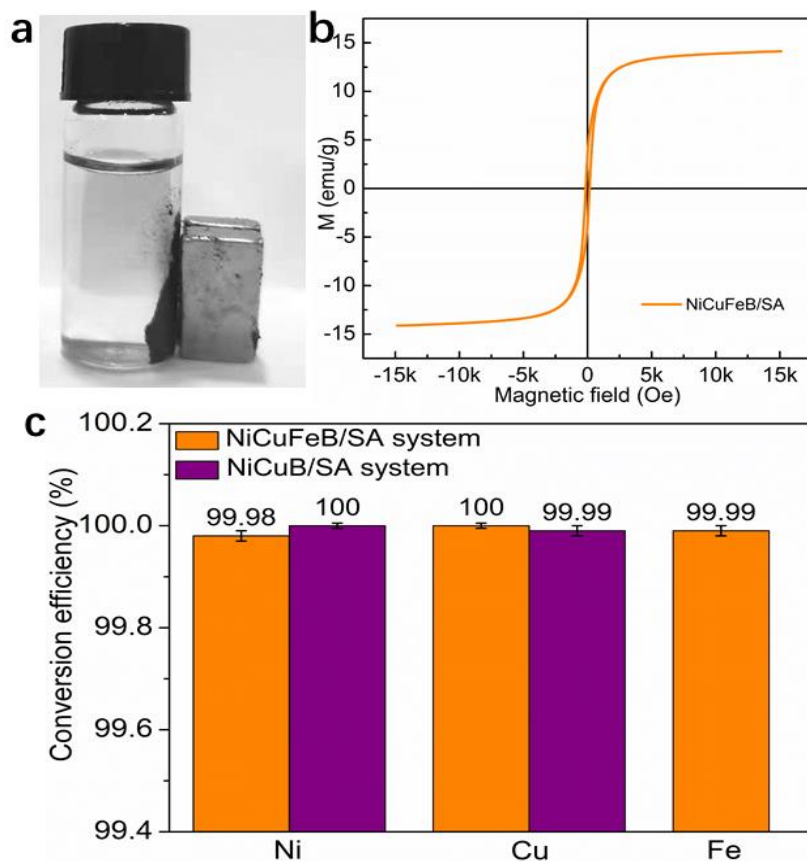


Figure 7.3. (a) An image of magnetic separation of metal boride/biochar heterostructures from reaction solution. (b) conversion efficiency of NiCuB/SA and NiCuFeB/SA reaction system.

Compared with the traditional industrial spent adsorbent treatment process (e.g., landfill, incineration), the direct conversion of spent adsorbents into highly efficient electrocatalysts could significantly avoid the loss of critical metals, minimize the negative environmental impact, and significantly

reduce the tremendous energy, economic and environmental costs for catalyst preparation.

7.3.2. Characterizations of synthesized borides/SA

The morphology and nanostructure of NiCuFeB/SA were first examined with TEM. The boride nanoparticles, with the particle size varies within the range of 30-50 nm, mainly gather at the pore and edge of biochar. The reason could be ascribed to that metal ions are more likely to react with the nitrogen/oxygen-containing groups at the surface of biochar. The adsorption mechanism of metal ions on biochar was further investigated via XPS. As shown in Fig. 7.4, peaks of C 1s, O 1s, N 1s, Ni 2p, Fe 2p, and Cu 2p appeared in biochar after adsorption, indicating the successful adsorption of metal ions onto biochar. Compared with the pre-adsorption biochar, the N 1s spectrum shows a new peak at 402.2 eV, which should be assigned to the NH₂-C in the coordination form, which confirms the fixation of metal ions onto the biochar. In addition, two specific peaks shifted to the lower binding energy after metal ions sorption, which is likely because the nitrogen atoms share electrons with metals, thereby reducing the electron densities of the nitrogen atoms (Yang and Jiang, 2014). Moreover, the C=O-N/C=O-C groups (532.8 eV) in the O 1s spectrum of the post-adsorption biochar show a significant shift, which should be chemical adsorption between metal ions and oxygen-containing groups (Chen et al., 2021a). No significant changes were observed in the C 1s spectra before and after the adsorption process. Therefore, the metal ions mainly react with the oxygen and nitrogen-containing groups of SA during the adsorption process.

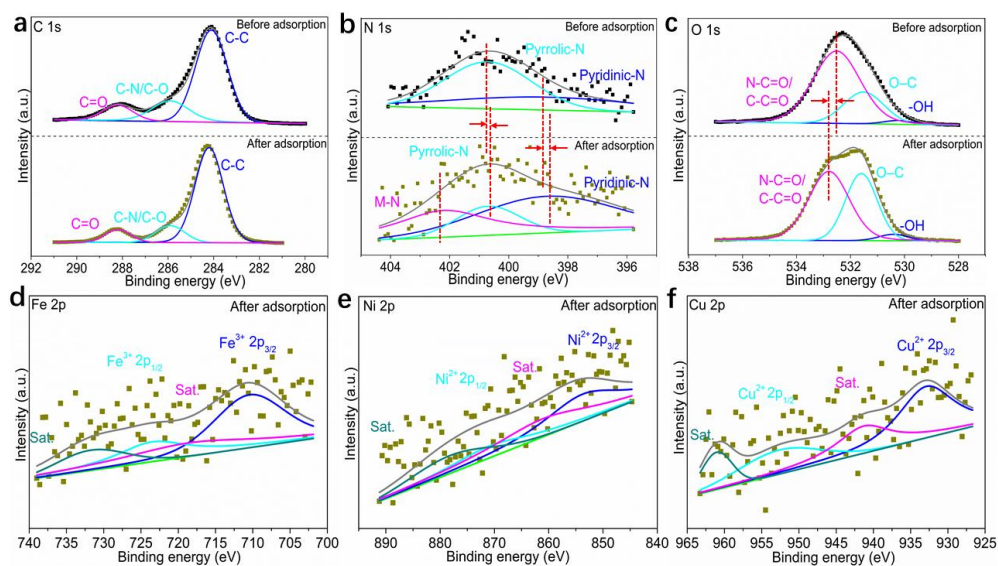


Figure 7.4. XPS spectra of (a) C 1s, (b) N1s and (c) O 1s for biochar before and after metal ions adsorption, (d) Fe 2p, (e) Ni 2p, and (f) Cu 2p spectra for post-adsorption biochar.

The N_2 adsorption-desorption experiment suggests that the spent biochar shows a surface area of $57.57 \text{ m}^2 \text{ g}^{-1}$ (Langmuir specific surface area) with abundant mesopores (Fig. 7.5), which would benefit the reactant diffusion and accelerate the catalytic process. Moreover, the pore confinement effect of biochar also facilitates the formation of small size and well-dispersed metal boride nanoparticles. Accordingly, the biochar could be an ideal nanoreactor for the synthesis of metal nanocatalysts, with the following merits: 1) the biochar surface with rich oxygen-containing groups and the pore confinement effect could reinforce the interaction between biochar and metal ions for better control the growth of metal boride nanoparticles during the following boriding process; 2) the porous structures with the large surface area ensures abundant electroactive sites for the catalytic reaction, facilitate the penetration and diffusion of electrolytes, and promote the transportation of produced oxygen gas during the OER process.

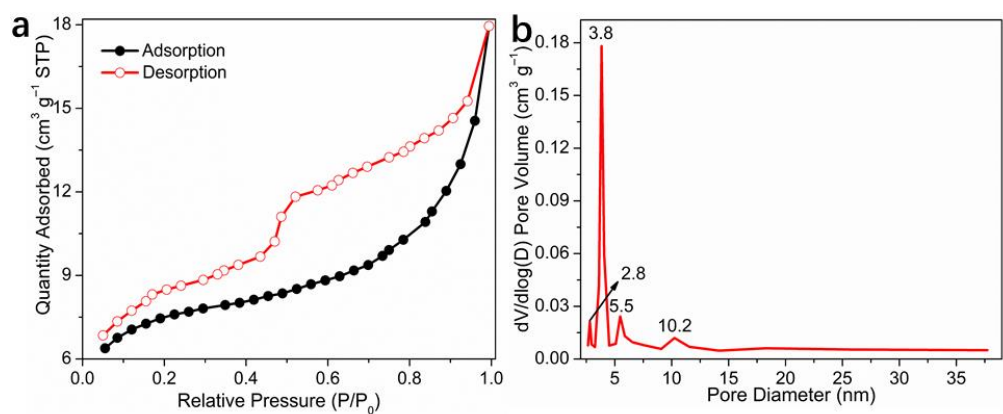


Figure 7.5. (a) N₂ adsorption-desorption isotherms of the biochar, (b) corresponding pore distribution of the biochar based on a method of Barrett-Joyner-Halenda (BJH).

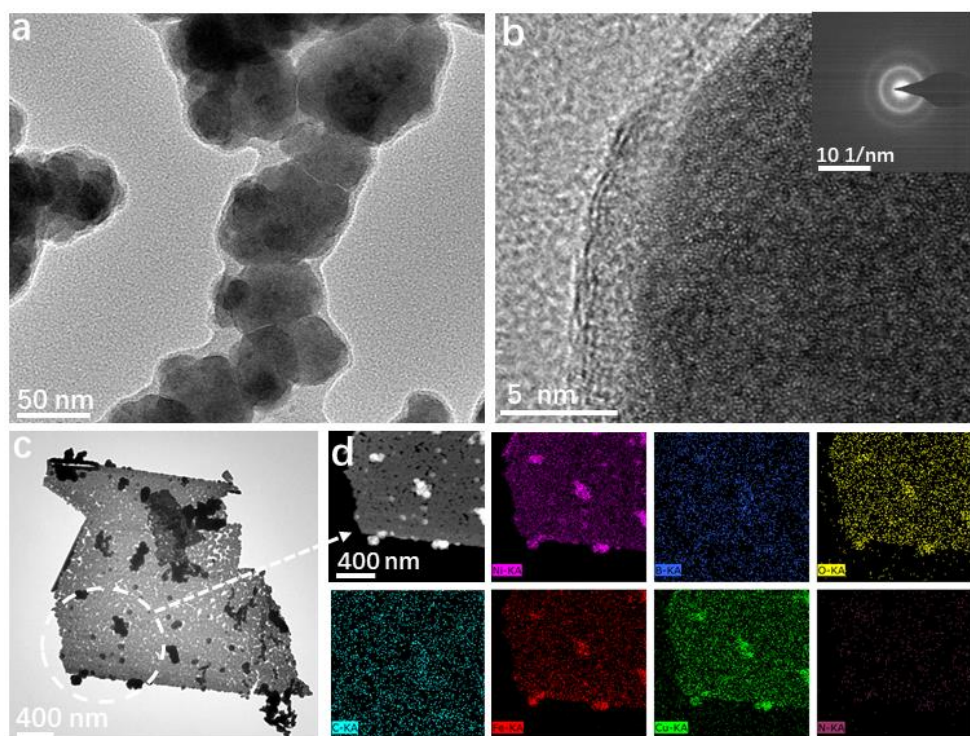


Figure 7.6. Microscopic characterization of the as-converted NiCuFeB/SA. (a) TEM image. (b) HRTEM image, and the inset is the corresponding SAED pattern. (c) EDS mapping.

The nanostructure of NiCuFeB/SA is further analyzed with the TEM and HRTEM. As depicted in Fig. 7.6a-b, a clear observation at the edge of the metal

boride nanoparticles shows an extension of the amorphous layer which might be ascribed to a metal borate/oxide layer on boride particles (Nsanzimana et al., 2018b). In addition, the SAED pattern (inset of Fig. 7.6b) indicates a low crystalline, pseudo-amorphous structure of NiCuFeB/SA because only a few broad distinct diffraction rings are observed. The biochar can enhance the electron conductivity within the electrode and the penetration and diffusion of electrolytes could also be accelerated by the as-observed rich nanopores within biochar (Fig. 7.6c) (Wei et al., 2019), which can further enhance the catalysis process. The EDS mapping analysis indicates the existence of B, Fe, C, N, Ni, O, and Cu elements in NiCuFeB/SA (Fig. 7.6d), and the evenly distributed C, N, and O elements suggests N, O co-doped in the porous carbon structure. The elemental analysis further supports this result. As shown in Table 7.2, the biochar mainly contains C, O, N, and H, as well as a small amount of S. Furthermore, it is clear that the surface oxidized boride particles (NiCuFeBO) are well isolated on large biochar, and the high dispersion of boride nanoparticles facilitates the exposure of rich catalytically active sites. In addition, the presence of oxygen in metal borides is mainly because of the unpreventable oxidation when borides are exposed to water/air (Masa et al., 2017), verifying the TEM results.

Table 7.2. Elemental composition of the biochar.

Element	C	O	N	H	S
Content (%)	51.18	39.29	5.46	3.98	0.09

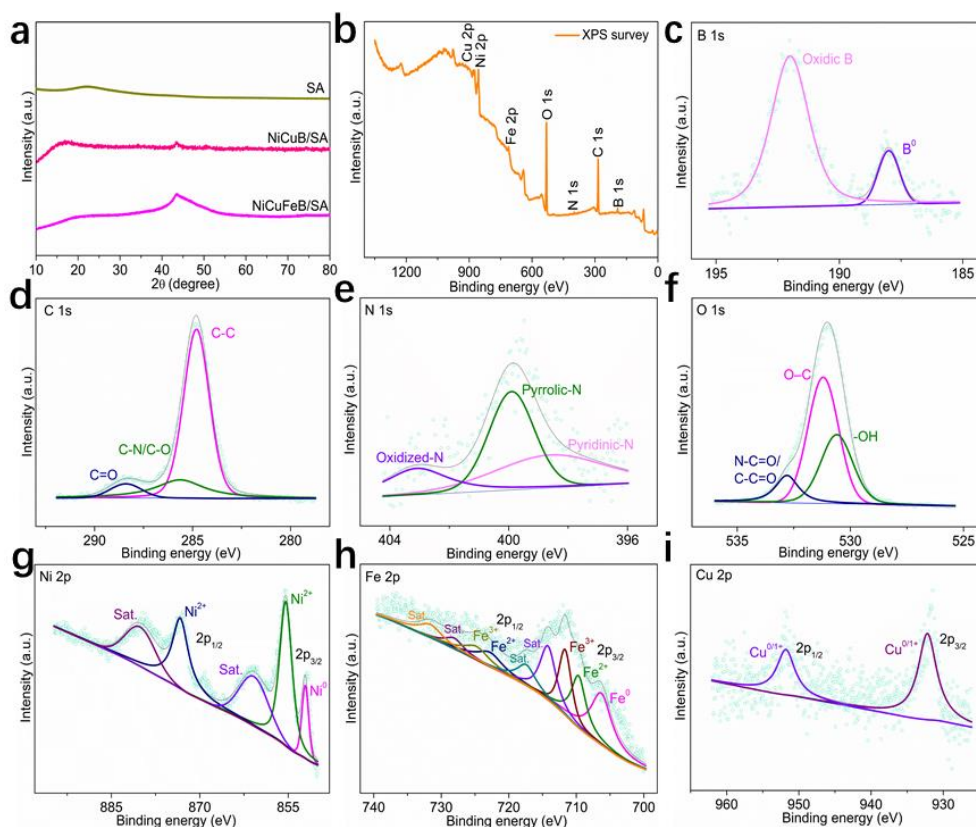


Figure 7.7. (a) XRD patterns of NiCuFeB/SA, NiCuB/SA, and SA. XPS spectra of NiCuFeB/SA: (b) survey (c) B 1s, (d) C 1s, (e) N 1s, (f) O 1s, (g) Ni 2p, (h) Fe 2p, and (i) Cu 2p.

Moreover, the crystal structure of NiCuFeB/SA was further characterized with XRD. For SA, there are no crystalline peaks, and only a broad hump in 2θ range of $20 - 30^\circ$ is observed, suggesting the amorphous feature of the as-obtained biochar (Fig. 7.7a). Similarly, NiCuFeB/SA and NiCuB/SA diffraction patterns also show an amorphous phase feature consistent with the TEM image observation results. XPS was further employed to probe the surface chemical states on NiCuFeB/SA. In the survey spectra of NiCuFeB/SA, the existence of B, C, N, O, Ni, Fe, and Cu elements is confirmed (Fig. 7.7b). In the spectrum of B 1s, two peaks at 187.9 and 192.0 eV are observed, which can be ascribed to metalloid boron and oxidized boron, respectively (Fig. 7.7c). It can be found that the metalloid B in NiCuFeB/SA shows higher binding energy than that of pure B element (187.0 eV), suggesting B atoms in

NiCuFeB/SA can donate electrons to metals (Chen et al., 2021c; Masa et al., 2019). Therefore, the presence of B can regulate the electronic structures of metals in NiCuFeB/SA. In Fig. 7.7d, the C 1s spectrum shows three peaks at 284.8, 285.6, and 288.4 eV, which can be attributed to C-C, C-N/C-O, and C=O, separately (Bano et al., 2018; Wang et al., 2017a). The N 1s spectrum of NiCuFeB/SA can be attributed to pyridinic N (398.7 eV), pyrrolic N (399.8 eV), and oxidized N (403.1 eV) (Fig. 7.7e). Figure 7.7f shows that NiCuFeB/SA shows three peaks at 530.6, 531.2, and 532.8 eV in the O 1s spectrum, which contribute to the binding energies of hydroxyl groups (-OH), O-C, and C=O-N/C=O-C, separately. The rich oxygen-containing groups (C=O, C-O, and C-OH) can regulate the adsorption of water and oxygenated intermediates on NiCuFeB/SA, resulting in enhanced electrocatalytic performance. The formation of N, O co-doped carbon is also verified by the FTIR spectrum of SA, as depicted in Fig. 7.8. The Ni 2p spectrum is resolved into five peaks in Fig. 7.7g. Two lower binding energies at 855.4 and 873.3 eV can be indexed to Ni²⁺ 2p_{3/2} and Ni²⁺ 2p_{1/2} with two satellite peaks at 860.8 and 880.1 eV, respectively. Additionally, the peak with a lower binding energy of 852.1 eV can be ascribed to Ni⁰, indicating the generation of Ni-B in NiCuFeB/SA. In Fig. 7.7h, the peak located at 706.3 eV is indexed to Fe⁰ in Fe-B, and the other two spin-orbit doublets are derived from Fe³⁺ (711.6 and 724.7 eV) and Fe²⁺ (709.7 and 722.8 eV). The presence of oxidized Fe species is because of the surface oxidation of iron borides (Li et al., 2019d). There are two peaks in the Cu 2p core-line spectrum (Fig. 7.7i). The binding energy at 932.2 eV can be indexed to the Cu 2p_{3/2} of metallic Cu or Cu⁺, and the higher binding energy at 951.8 eV is assigned to Cu^{0/1+} 2p_{1/2} (Ling et al., 2018). Overall, the XPS results confirm the N and O functionalized carbon and the surface oxidized metal borides, and the oxygen-containing group-rich surface would promote the OER process.

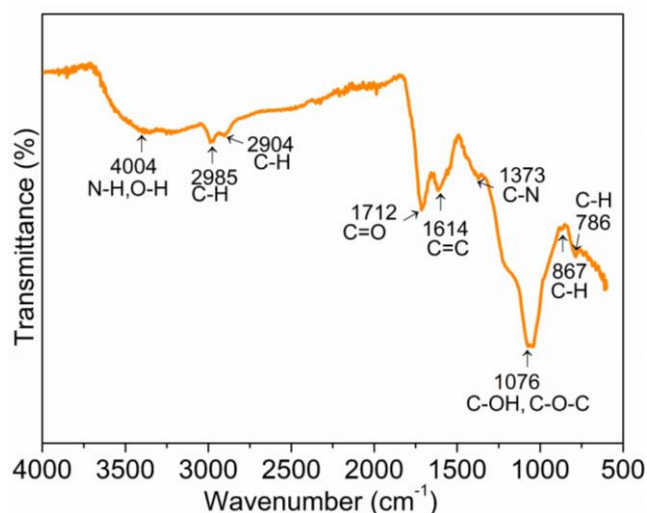


Figure 7.8. FTIR spectrum of SA.

7.3.3. Electrochemical properties of borides/SA

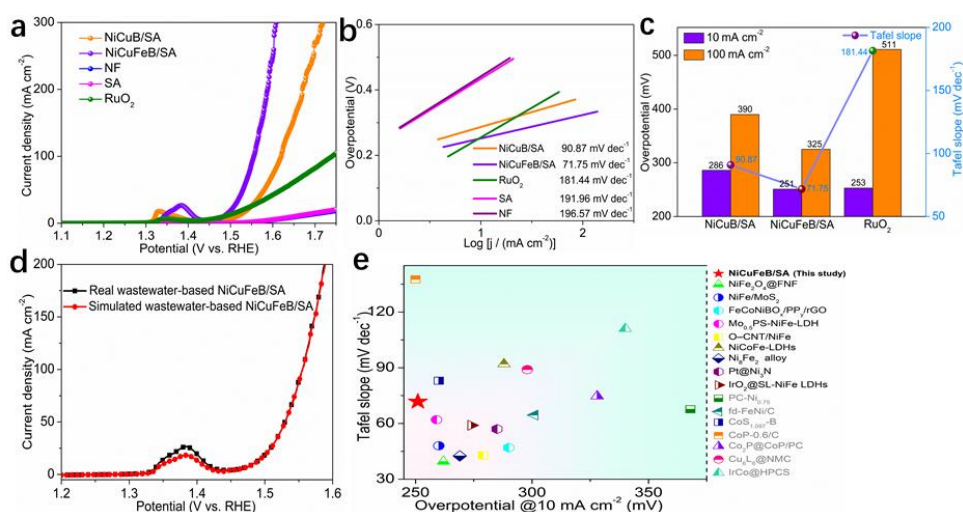


Figure 7.9. OER performance of catalysts. (a) LSV curves and (b) Tafel plots of the catalysts in 1.0 M KOH. (c) Comparison of η_{100} , η_{10} , and Tafel slopes of NiCuB/SA, NiCuFeB/SA, and the RuO₂ catalyst. (d) LSV curves real wastewater-based NiCuFeB/SA and simulated wastewater-based NiCuFeB/SA. (e) OER activity comparison graph showing the Tafel slope with η_{10} for NiCuFeB/SA and reported the state-of-the-art TM-based electrocatalysts, as well as biochar-based heterostructured catalysts.

The OER performance of as-designed catalysts was tested in alkaline solution (1.0 M KOH, pH = 13.6) with a typical three-electrode configuration. For direct comparison, OER performance of bare SA, NF, and the commercial RuO₂ catalyst were also measured. The η was calculated through η (V) = E_{RHE} - 1.23 V, and a lower η means a higher OER activity. As shown by the LSV polarization curves in Fig. 7.9a, both bare NF and SA exhibit negligible OER activity, while the RuO₂ catalyst shows an OER activity with an η of 253 mV to drive the benchmark j_{10} ($\eta_{10} = 253$ mV). The noticeable oxidation peaks located at 1.3 - 1.4 V vs. RHE stem from the electrooxidation of Ni species in the NF substrate and the metal borides (Wu et al., 2019b). In remarkable contrast, the spent adsorbent-derived heterostructured catalysts (NiCuB/SA and NiCuFeB/SA) demonstrate significantly improved OER activity, especially at high current densities. Typically, NiCuFeB/SA exhibits the best catalytic activity ($\eta_{100} = 325$ mV), surpassing the NiCuB/SA (390 mV) and the RuO₂ catalyst (511 mV). The electrochemical kinetics is further analyzed via the Tafel plots derived from the LSV curves. Compared with NF (196.57 mV dec⁻¹), SA (191.96 mV dec⁻¹), RuO₂ (181.44 mV dec⁻¹), and NiCuB/SA (90.87 mV dec⁻¹), NiCuFeB/SA exhibits the significantly accelerated OER kinetics with the smallest Tafel slope of 71.75 mV dec⁻¹ (Fig. 7.9b). As depicted in Fig. 7.9c, the lowest η and Tafel slope hint that NiCuFeB/SA is the most thermodynamically and kinetically favourable electrocatalyst among the studied materials. It is worth noting that NiCuFeB/SA shows much better OER activities than NiCuB/SA, suggesting that the presence of Fe enhances the catalytic performance. Such results are in line with previous studies (Feng et al., 2020; Han et al., 2016). Given the importance of chemical components on OER performance of catalysts, the OER performance of boride/SA could be further optimized by regulating metal concentrations in the original wastewater. Since the actual wastewater is complex, and the observed good electrocatalytic performance of NiCuFeB/SA may also come from other substances in the wastewater. To identify the real active components in the obtained catalysts,

simulated wastewater containing Ni, Cu, Fe metals, and the metal concentrations are the same as the real wastewater Sample 2 (Table 7.1) was prepared. The simulated wastewater-based NiCuFeB/SA was synthesized and its OER performance was tested. As shown in Fig. 7.9d, the simulated wastewater-based NiCuFeB/SA shows a similar OER activity to that of the real wastewater-based NiCuFeB/SA as the LSV curves are almost coincident in the OER region. Hence, it can be seen that the high OER performance of NiCuFeB/SA derives from the Ni, Cu, and Fe. Additionally, NiCuFeB/SA exhibits comparable OER activities (η_{10} , Tafel slope) to most of the recently reported TM-based catalysts, as well as a group of biochar-bearing heterostructured catalysts (Fig. 7.9e, Table 7.3), such as O-CNT/NiFe (279 mV, 42.8 mV dec⁻¹) (Lin et al., 2020), IrO₂@SL-NiFe LDHs (274 mV, 59 mV dec⁻¹) (Li et al., 2020a), FeSe/NC-PoFeSe (330 mV, 76 mV dec⁻¹) (Wang et al., 2018a), and IrCo@HPCS (340 mV, 111 mV dec⁻¹) (Shen et al., 2019).

Table 7.3. A summary of the recently documented TM-based and biochar-bearing OER catalysts.

Catalyst	η_{10} (mV)	Tafel slope (mV dec ⁻¹)	Reference
Ni _{0.6} Co _{1.4} P	300	80	<i>Adv. Funct. Mater.</i> 2018, 28, 1706008.
Mn ₃ N ₂	270	101	<i>Angew. Chem. Int. Ed.</i> 2018, 57, 698.
Ni _{0.75} Mn _{0.25} nanosheets	297	91	<i>ACS Energy Lett.</i> 2018, 3, 2150.
NiFeMn-LDH	262	47	<i>Energy Environ. Sci.</i> 2017, 10, 121–128.
MnGa ₄ /NF	293	98	<i>Angew. Chem. Int. Ed.</i> 2019, 58, 16569.

Ru-RuP _x -Co _x P	291	85.4	<i>Nano Energy</i> , 2018, 53, 270-276.
Co@NC-600	372	62.5	<i>Adv. Energy Mater.</i> 2018, 8, 1702838.
Ni-MoN	276	98	<i>Adv. Energy Mater.</i> 2018, 8, 1802327.
Co ₄ N/CNW/CC	310	81	<i>J. Am. Chem. Soc.</i> 2016, 138, 10226
Co _{0.5} (V _{0.5})	282	56	<i>Adv. Energy Mater.</i> 2020, 10, 1903571.
NiFe-LDH/FeSoy-CNSs-A	300	45	<i>Nano Res.</i> 2020, 1-12.
Fe-NSDC	410	59	<i>Small</i> 2019, 15, 1900307.
IrCo@HPCS	340	111	<i>J. Mater. Chem. A</i> 2019, 7(17), 10662-10671.
NiFeO _x /NP-C-800	320	59.03	<i>Energy Storage Mater.</i> 2018, 11: 134-143.
NiCuFeB/SA	251	71.75	This study

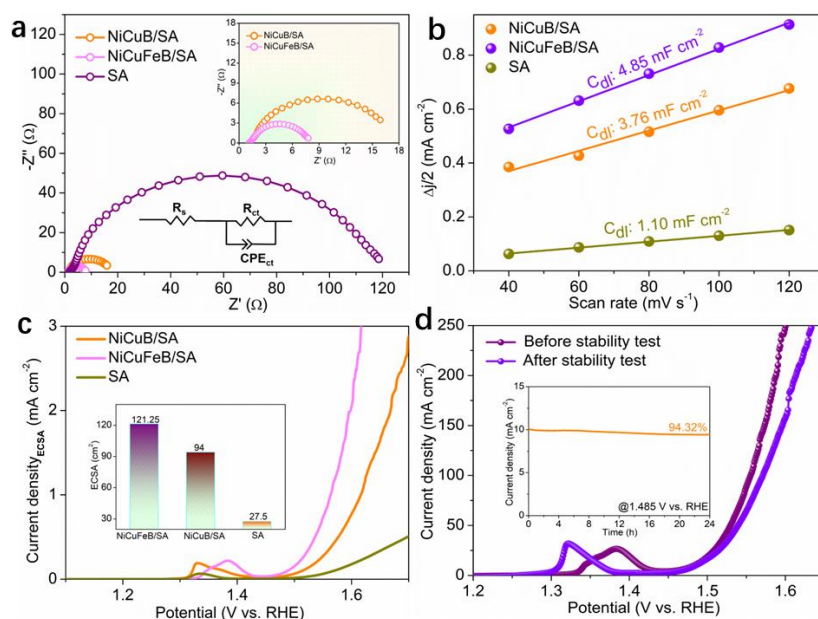


Figure 7.10. (a) Nyquist plots of NiCuB/SA, NiCuFeB/SA, and NF at 1.5 V vs. RHE, and the inset shows an enlarged part of the Nyquist plots. (b) The difference in current density ($\Delta j = (j_a - j_c)/2$) plots against scan rate of as-prepared catalysts. (c) LSV curves normalized with ECSA of NiCuB/SA, NiCuFeB/SA, and NF, and the inset shows ECSA values. (d) LSV curves of NiCuFeB/SA before and after the OER test, and the inset shows the chronoamperometric curve of NiCuFeB/SA at 1.485 V vs. RHE.

The charge transfer characteristics of catalysts were further investigated by EIS. The Nyquist plots in Fig. 7.10a were first fitted with an equivalent circuit. Based on the fitting results (Table 7.4), all of the three samples (i.e., NiCuB/SA, NiCuFeB/SA, and NF) show similar R_s , which is ascribed to the solution resistance. The kinetic performance of catalysts can be evaluated by their R_{ct} , where a lower R_{ct} value represents faster charge transportation. The R_{ct} of bare NF (121.6 Ω) is much larger than metal boride/SA heterostructures, indicating a sluggish OER process at the NF/electrolyte interface. Compared to NiCuB/SA (15.5 Ω), NiCuFeB/SA exhibits a lower R_{ct} (6.6 Ω), which may be attributed to the strong electron-interaction after Fe adding. These results confirm the high conductivity of metal borides and accelerated charge transfer

at the electrolyte and NiCuFeB/SA electrode interface during the OER process(Choi et al., 2020; Zhao et al., 2020c).

Table 7.4. Calculated charge transfer resistance (R_{ct}) and solution resistance (R_s) (in Ohm, Ω) of the materials deposited on NF obtained from the Nyquist plot during the EIS experiments.

Catalyst	R_s	R_{ct}
NiCuB/SA	1.156	15.54
NiCuFeB/SA	1.132	6.615
NF	1.742	121.6

To measure the active site density of various catalysts, the C_{dl} is obtained via conducting CV tests with various scan rates. The calculated C_{dl} of NiCuFeB/SA is 4.85 mF cm^{-2} , which is higher than those of NiCuB/SA (3.76 mF cm^{-2}) and NF (1.10 mF cm^{-2}) (Fig. 7.10b). Accordingly, NiCuFeB/SA with the highest ECSA (121.25 cm^2) can offer many more electrochemically active sites for OER and enhance the catalytic performance (Fig. 7.10c). Towards a deeper understanding of the intrinsic activity of each active site on the various catalyst surface, the LSV current curves were normalized against ECSA (j_{ECSA}) (Fig. 7.10c). The η required for NiCuFeB/SA to deliver an ECSA normalized $j_{0.5}$ is 306 mV, outperforming NiCuB/SA (347 mV) and NF (467 mV). Therefore, both the enlarged ECSA and the high intrinsic activity contribute to the excellent OER performance of NiCuFeB/SA.

Apart from the catalytic activity, the structural stability of the waste-derived catalyst was also tested via the CA measurement. Figure 7.10d shows a slight loss ($\sim 5\%$) of j after 24 h running, indicating that NiCuFeB/SA exhibits good performance stability in 1 M KOH solution. Additionally, the LSV curves before and after the 24 h test suggest that the OER performance decreased slightly, and the η_{10} only increased by 2 mV. The slight degradation

of the OER activity during the stability test should be originated from the detachment of catalyst particles induced by the continuous O₂ bubbles releasing or the lasting O₂ bubbles on the electrode surface that block the catalytic reaction. Generally, the as-synthesized boride/SA catalysts show excellent OER performance under alkaline conditions, suggesting that the spent adsorbents derived low-cost heterostructured electrocatalysts are alluring candidatures for OER catalysts.

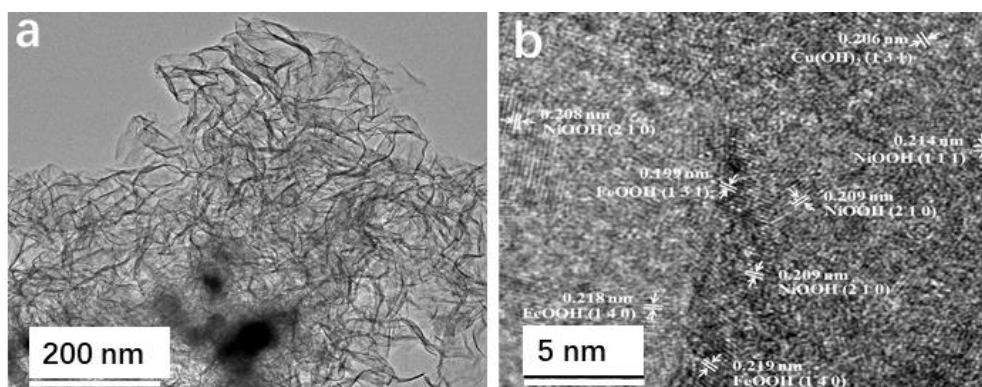


Figure 7.11. (a)TEM and (b) HRTEM images of NiCuFeB/SA after the OER test.

The post-OER NiCuFeB/SA was thoroughly characterized to understand its advantages for OER. The TEM images of post-OER NiCuFeB/SA show that the morphology undergoes a substantial structure and morphology evolution during the OER process. The *in situ* evolved numerous ultrathin nanosheet structures with irregular shapes gathered and formed the hierarchical structure (Fig. 7.11a). Moreover, the HRTEM images of post-OER NiCuFeB/SA showcases a mixed crystalline and amorphous phase (Fig. 7.11b), which is totally different from the amorphous feature of the pristine one. XPS analysis further suggests that all of the low valence species (Ni⁰, Fe^{0/2+}, Cu^{0/1+}) of metals in post-OER NiCuFeB/SA are wholly absent, while the high valence species (Ni^{2+/3+}, Fe³⁺, Cu²⁺) of metals become more prominent (Fig. 7.12), while B signals are almost missing. Such variations are due to the electrochemical oxidation of NiCuFeB/SA under OER conditions. Combined

the XPS results with HRTEM images. The abundant lattice fringes can be indexed to FeOOH, NiOOH/Ni(OH)₂, and Cu(OH)₂ which act as the active sites for OER, agreeing with a previous study (Liu et al., 2021).

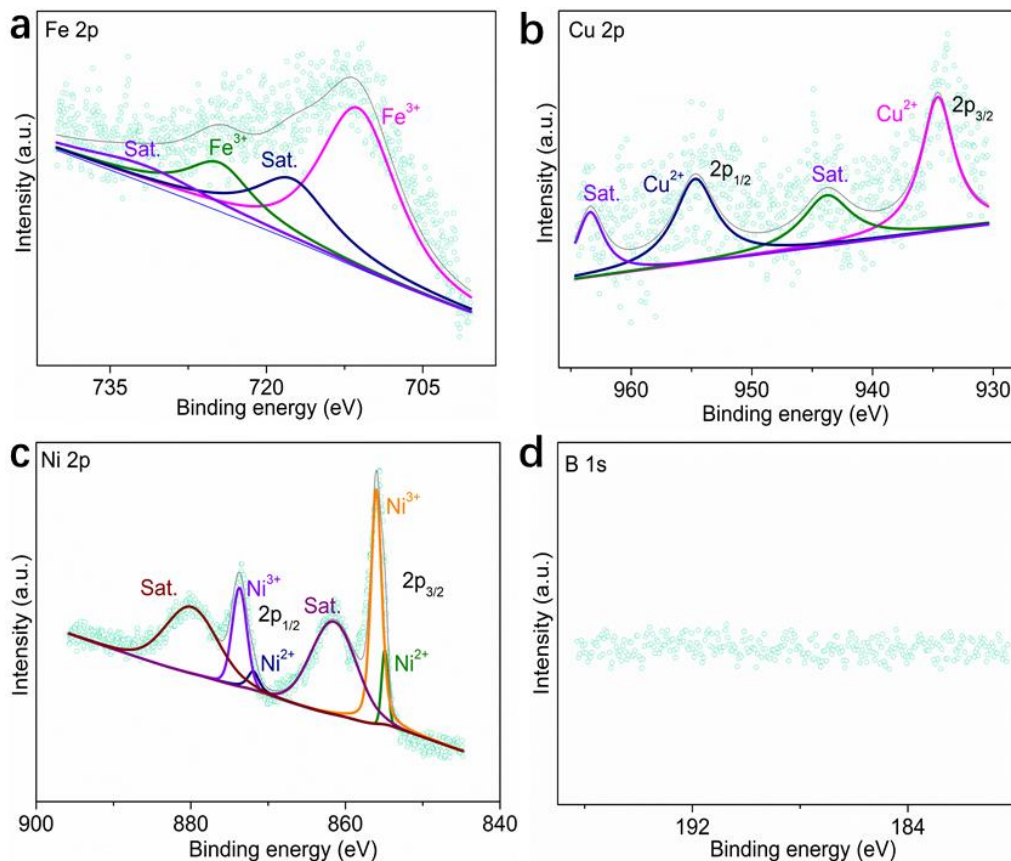


Figure 7.12. High-resolution XPS scans of NiCuFeB/SA in (a) Fe 2p, (b) Cu 2p, (c) Ni 2p, and (d) B 1s regions after the OER test.

In general, the excellent OER activity of NiCuFeB/SA principally attributes to the porous biochar confined highly-dispersed and small-sized metal borides, *in situ* generated multiple active sites (Fe/Ni/Cu (oxy)hydroxides), efficient mass/charge transfer, as well as the amorphous and heterostructure feature.

7.4. Conclusions

In conclusion, we have performed the facile boriding strategy to turn spent biochar-based water treatment adsorbents into heterostructured

electrocatalysts for efficient OER without metal loss, for the first time. The as-prepared magnetic metal boride/biochar heterostructures exhibit excellent OER performance, and the optimized one requires an η of 251 mV to attain 10 mA cm⁻² in 1 M KOH solution, with good durability. Further explorations indicate that the superior electrocatalytic performance is mainly attributed to the porous biochar confined well-dispersed and small-sized metal borides, the *in situ* evolved active multimetal (oxy)hydroxides, favourable charge-transfer kinetics, as well as the heterostructure and quasi-amorphous feature. This study provides a general strategy to engineer efficient electrocatalysts from industrial spent adsorbents, which also can be broadened to the low-cost and high-value reuse of other metal-contaminated solid wastes in an economically and environment-friendly way.

CHAPTER 8
Conclusions and
recommendations

8.1. Conclusions

This thesis aims to develop efficient catalyst design strategies for the construction of cost-effective TMS and TMB electrocatalysts for EWS. The conclusions of each experimental study are shown below:

A FeB-based OER pre-catalyst with accelerated surface reconstruction and upgraded intrinsic activity of evolved FeOOH by W and P co-doping has been developed. The amorphous W and P co-doped FeB exhibits great OER activity in alkaline media ($\eta_{10} = 209$ mV, Tafel slope = 39.87 mV dec⁻¹), as well as excellent long-term durability. Furthermore, the anion (borate and phosphate) etching during the OER process facilitates the surface reconstruction and accelerates the mass/charge transfer. Density functional theory calculations suggest W doping can enhance intrinsic catalytic activity by optimizing the adsorption free energy of reaction intermediates. What is more, the hierarchical structure and amorphous feature of W, P co-doped FeB also benefit the overall OER process. This study provides a general strategy to optimize metal borides (e.g., CoB_x, MoB_x, NiB_x) for OER pre-catalysts.

Beyond OER, a bifunctional nanoworm-like nickel sulfide nanostructure has been designed for OWS via a one-step solvothermal route. Benefiting from the smaller size, larger electrochemical surface area, and lower charge transfer resistance, the as-prepared nanoworm-like nickel sulfides (NiS-NW/NF) perform better than the nanoplate-like counterpart. The NiS-NW/NF only demands an η of 279 mV to acquire 100 mA cm⁻² for OER, exceeding most of reported nickel sulfide-based catalysts. In addition, when used as a bifunctional catalyst for OWS, the NiS-NW/NF achieves j_{10} at only 1.563 V with good long-term durability. This study provides a facile and effective strategy for the design and development of cost-effective catalysts for water electrolysis.

To further enhance the cost-effectiveness of catalysts, a facile and efficient boriding strategy has been developed to directly convert the leachates of WPCBs into magnetic mixed metal borides (FeNiCuSnBs) for OER for the first time. Fe, Ni, Cu, and Sn were efficiently recovered via the boriding reduction and magnetic separation process, with a metal cation recovery rate of 99.78%, 99.98%, 99.96%, and 99.49%, respectively. The as-obtained borides exhibit excellent catalytic performance for OER, and the optimized sample only requires a low η of 199 mV to attain 10 mA cm^{-2} , outperforming most recently reported catalysts and all of waste-derived OER catalysts. In-depth mechanism analyses suggest that the multimetal borides undergo surface reconstruction induced by B/Sn etching, and the *in situ* generated multimetal (oxy)hydroxides act as the active species to facilitate O_2 evolution. In addition, the efficient mass/charge transfer, the amorphous feature, and the hierarchical structure also contribute to superior electrocatalytic performance. This study gains an insight into the correlation between surface self-reconstruction and OER catalytic activity of multimetal boride-based catalysts. In addition, the boriding strategy enables efficient recycling and advanced energy-driven applications of valuable metals from e-waste for achieving a sustainable energy future.

The facile boriding strategy has been also employed to turn spent biochar-based water treatment adsorbents into heterostructured electrocatalysts for efficient OER without metal loss. The as-prepared magnetic metal boride/biochar heterostructures exhibit excellent OER performance, and the optimized one requires a low η of 251 mV to attain 10 mA cm^{-2} in 1 M KOH solution, with good durability. Further explorations indicate that the superior electrocatalytic performance is mainly attributed to the porous biochar confined well-dispersed and small-sized metal borides, the *in situ* evolved active multimetal (oxy)hydroxides, favourable charge-transfer kinetics, as well as the heterostructure and quasi-amorphous feature. This study provides a

general strategy to engineer efficient electrocatalysts from industrial spent adsorbents, which also can be broadened to the low-cost and high-value reuse of other metal-contaminated solid wastes in an economically and environment-friendly way.

Among the four typical catalysts reported in the thesis (i.e., W, P-FeB, NiS-NW/NF, FeNiCuSnB-4, NiCuFeB/SA), the WPCBs-derived FeNiCuSnB-4 exhibit the best OER performance with high cost-effectiveness and environmental significance. In addition, the bifunctional NiS-NW/NF shows good potential for overall water electrolysis.

8.2. Recommendations

In this thesis, although some efficient TMS and TMB electrocatalysts have been achieved for EWS, there are still some critical issues that deserve future explorations. Below are some recommendations for future study on this topic:

Firstly, the design of novel electrocatalysts requires novel strategies to increase the number of active sites and improve the conductivity, intrinsic activity, as well as durability. The "all-in-one" strategy can offer the pristine material impressive catalytic properties. However, logically assembling the related approaches remains a critical issue, which deserves more effort. In addition, computational methods can provide valuable guidelines to rapidly discover novel catalysts for EWS. Combining experimental tests and computational results will improve the research efficiency and avoid the time-consuming trial-and-error route. Another vital factor that should be considered is the catalyst preparation procedures, where the reaction time and temperature, safety issues, and environmental consequences should be carefully evaluated.

Secondly, to get a better view of the electrochemical process, it is necessary to adopt advanced *in situ*/operando techniques (e.g., XPS, XAS, Raman spectroscopy, infrared spectroscopy) to monitor the evolution of surface active sites and the reaction intermediates, as well as the surface reconstruction and dissolution of active compounds. Furthermore, integrating these experimental methods with the DFT calculations leads to a better understanding of the electrocatalytic mechanism. More efforts are encouraged to uncover the catalytic mechanism of different categories of catalysts with the aid of state-of-the-art experimental and theoretical tools.

Thirdly, parameters for catalysts evaluation should be further standardized. To date, η_{10} and Tafel slope are the most popular descriptors and used by almost all the reported papers. However, other factors are often documented randomly, such as the specific/mass activity, turnover frequency, stability, and onset potential. These issues result in unfair performance comparisons among different catalysts. Additionally, mass loading has a major influence on the evaluating parameters.

Finally, it is worth noticing that many OER/HER catalysts also exhibit good performances for the oxygen reduction reaction. These multifunctional catalysts are favorable to minimize the operation cost and to simplify the design of experimental devices in PEM water electrolyzers, batteries, and fuel cells. Consequently, it is of great value to examine the origins of functional versatility and to provide guidance for the design of on-demanding multifunctional electrocatalysts for practical energy storage/conversion devices.

REFERENCES

- Alam, M.S., Gorman-Lewis, D., Chen, N., Flynn, S.L., Ok, Y.S., Konhauser, K.O. and Alessi, D.S. 2018. Thermodynamic Analysis of Nickel(II) and Zinc(II) Adsorption to Biochar. *Environmental Science & Technology* 52(11), 6246-6255.
- An, L., Sun, Y., Zong, Y., Liu, Q., Guo, J. and Zhang, X. 2018. Nickel iron boride nanosheets on rGO for active electrochemical water oxidation. *Journal of Solid State Chemistry* 265, 135-139.
- Anantharaj, S., Ede, S.R., Karthick, K., Sam Sankar, S., Sangeetha, K., Karthik, P.E. and Kundu, S. 2018. Precision and correctness in the evaluation of electrocatalytic water splitting: revisiting activity parameters with a critical assessment. *Energy & Environmental Science* 11(4), 744-771.
- Anantharaj, S., Ede, S.R., Sakthikumar, K., Karthick, K., Mishra, S. and Kundu, S. 2016. Recent Trends and Perspectives in Electrochemical Water Splitting with an Emphasis on Sulfide, Selenide, and Phosphide Catalysts of Fe, Co, and Ni: A Review. *ACS Catalysis* 6(12), 8069-8097.
- Anantharaj, S., Karthick, K. and Kundu, S. 2017. Evolution of layered double hydroxides (LDH) as high performance water oxidation electrocatalysts: A review with insights on structure, activity and mechanism. *Materials Today Energy* 6, 1-26.
- Anantharaj, S. and Noda, S. 2019. Amorphous Catalysts and Electrochemical Water Splitting: An Untold Story of Harmony. *Small* 16(2), e1905779.
- Arivu, M., Masud, J., Umapathi, S. and Nath, M. 2018. Facile synthesis of Ni₃B/rGO nanocomposite as an efficient electrocatalyst for the oxygen evolution reaction in alkaline media. *Electrochemistry Communications* 86, 121-125.
- Assefi, M., Maroufi, S., Yamauchi, Y. and Sahajwalla, V. 2019. Core-Shell Nanocatalysts of Co₃O₄ and NiO Shells from New (Discarded) Resources: Sustainable Recovery of Cobalt and Nickel from Spent Lithium-Ion Batteries, Ni-Cd Batteries, and LCD Panel. *ACS Sustainable Chemistry & Engineering* 7(23), 19005-19014.
- Bano, D., Kumar, V., Singh, V.K. and Hasan, S.H. 2018. Green synthesis of fluorescent carbon quantum dots for the detection of mercury(ii) and glutathione. *New Journal of Chemistry* 42(8), 5814-5821.
- Basu, M. 2018. Nanotubes of NiCo₂S₄/Co₉S₈ Heterostructure: Efficient Hydrogen Evolution Catalyst in Alkaline Medium. *Chemistry – An Asian Journal* 13(21), 3204-3211.
- Bediako, D.K., Lassalle-Kaiser, B., Surendranath, Y., Yano, J., Yachandra, V.K. and Nocera, D.G. 2012. Structure-activity correlations in a nickel-borate oxygen evolution catalyst. *Journal of the American Chemical Society* 134(15), 6801-6809.
- Cao, G.-X., Xu, N., Chen, Z.-J., Kang, Q., Dai, H.-B. and Wang, P. 2017. Cobalt-Tungsten-Boron as an Active Electrocatalyst for Water Electrolysis. *ChemistrySelect* 2, 6187-6193.

- Carenco, S., Portehault, D., Boissiere, C., Mezailles, N. and Sanchez, C. 2013. Nanoscaled metal borides and phosphides: recent developments and perspectives. *Chemical Reviews* 113(10), 7981-8065.
- Chai, W.S., Cheun, J.Y., Kumar, P.S., Mubashir, M., Majeed, Z., Banat, F., Ho, S.-H. and Show, P.L. 2021. A review on conventional and novel materials towards heavy metal adsorption in wastewater treatment application. *Journal of Cleaner Production* 296, 126589.
- Chakraborty, B., Beltrán-Suito, R., Hausmann, J.N., Garai, S., Driess, M. and Menezes, P.W. 2020. Enabling Iron-Based Highly Effective Electrochemical Water-Splitting and Selective Oxygenation of Organic Substrates through In Situ Surface Modification of Intermetallic Iron Stannide Precatalyst. *Advanced Energy Materials* 10(30), 2001377.
- Chattopadhyay, J. and Srivastava, R. (2017) *Advanced Nanomaterials in Biomedical, Sensor and Energy Applications*, Springer.
- Chaudhari, N.K., Jin, H., Kim, B. and Lee, K. 2017. Nanostructured materials on 3D nickel foam as electrocatalysts for water splitting. *Nanoscale* 9(34), 12231-12247.
- Chen, H., Ouyang, S., Zhao, M., Li, Y. and Ye, J. 2017. Synergistic Activity of Co and Fe in Amorphous $\text{Co}_x\text{-Fe-B}$ Catalyst for Efficient Oxygen Evolution Reaction. *ACS Applied Materials & Interfaces* 9(46), 40333-40343.
- Chen, J., Ren, B., Cui, H. and Wang, C. 2020a. Constructing Pure Phase Tungsten-Based Bimetallic Carbide Nanosheet as an Efficient Bifunctional Electrocatalyst for Overall Water Splitting. *Small* 16(23), e1907556.
- Chen, P., Xu, K., Zhou, T., Tong, Y., Wu, J., Cheng, H., Lu, X., Ding, H., Wu, C. and Xie, Y. 2016. Strong-Coupled Cobalt Borate Nanosheets/Graphene Hybrid as Electrocatalyst for Water Oxidation Under Both Alkaline and Neutral Conditions. *Angewandte Chemie International Edition* 55(7), 2488-2492.
- Chen, X., Yu, Z., Wei, L., Zhou, Z., Zhai, S., Chen, J., Wang, Y., Huang, Q., Karahan, H.E., Liao, X. and Chen, Y. 2019a. Ultrathin nickel boride nanosheets anchored on functionalized carbon nanotubes as bifunctional electrocatalysts for overall water splitting. *Journal of Materials Chemistry A* 7(2), 764-774.
- Chen, Y., Li, M., Li, Y., Liu, Y., Chen, Y., Li, H., Li, L., Xu, F., Jiang, H. and Chen, L. 2021a. Hydroxyapatite modified sludge-based biochar for the adsorption of Cu^{2+} and Cd^{2+} : Adsorption behavior and mechanisms. *Bioresource Technology* 321, 124413.
- Chen, Z., Duan, X., Wei, W., Wang, S. and Ni, B.-J. 2019b. Recent advances in transition metal-based electrocatalysts for alkaline hydrogen evolution. *Journal of Materials Chemistry A* 7(25), 14971-15005.
- Chen, Z., Duan, X., Wei, W., Wang, S. and Ni, B.-J. 2020b. Electrocatalysts for acidic oxygen evolution reaction: Achievements and perspectives. *Nano Energy* 78, 105392.
- Chen, Z., Duan, X., Wei, W., Wang, S. and Ni, B.-J. 2020c. Iridium-based nanomaterials for electrochemical water splitting. *Nano Energy* 78, 105270.

- Chen, Z., Duan, X., Wei, W., Wang, S., Zhang, Z. and Ni, B.-J. 2020d. Boride-based electrocatalysts: Emerging candidates for water splitting. *Nano Research* 13(2), 293-314.
- Chen, Z., Ibrahim, I., Hao, D., Liu, X., Wu, L., Wei, W., Su, D. and Ni, B.-J. 2020e. Controllable design of nanoworm-like nickel sulfides for efficient electrochemical water splitting in alkaline media. *Materials Today Energy* 18, 100573.
- Chen, Z., Kang, Q., Cao, G., Xu, N., Dai, H. and Wang, P. 2018. Study of cobalt boride-derived electrocatalysts for overall water splitting. *International Journal of Hydrogen Energy* 43(12), 6076-6087.
- Chen, Z., Liu, Y., Wei, W. and Ni, B.-J. 2019c. Recent advances in electrocatalysts for halogenated organic pollutant degradation. *Environmental Science: Nano* 6(8), 2332-2366.
- Chen, Z., Wei, W. and Ni, B.-J. 2021b. Cost-effective catalysts for renewable hydrogen production via electrochemical water splitting: Recent advances. *Current Opinion in Green and Sustainable Chemistry* 27, 100398.
- Chen, Z., Zheng, R., Graś, M., Wei, W., Lota, G., Chen, H. and Ni, B.-J. 2021c. Tuning electronic property and surface reconstruction of amorphous iron borides via W-P co-doping for highly efficient oxygen evolution. *Applied Catalysis B: Environmental* 288, 120037.
- Choi, M.J., Kim, T.L., Kim, J.K., Lee, T.H., Lee, S.A., Kim, C., Hong, K., Bark, C.W., Ko, K.T. and Jang, H.W. 2020. Enhanced Oxygen Evolution Electrocatalysis in Strained A-Site Cation Deficient LaNiO₃ Perovskite Thin Films. *Nano Letters* 20(11), 8040-8045.
- Christopher, P., Jin, S., Sivula, K. and Kamat, P.V. 2021. Why Seeing Is Not Always Believing: Common Pitfalls in Photocatalysis and Electrocatalysis. *ACS Energy Letters* 6(2), 707-709.
- Chunduri, A., Gupta, S., Bapat, O., Bhide, A., Fernandes, R., Patel, M.K., Bambole, V., Miotello, A. and Patel, N. 2019. A unique amorphous cobalt-phosphide-boride bifunctional electrocatalyst for enhanced alkaline water-splitting. *Applied Catalysis B: Environmental* 259, 118051.
- Dang, S., Zhu, Q.-L. and Xu, Q. 2017. Nanomaterials derived from metal-organic frameworks. *Nature Reviews Materials* 3(1), 1-14.
- Dastafkan, K. and Zhao, C. 2020. Recent trends in alkaline hydrogen evolution using nonprecious multi-metallic electrocatalysts. *Current Opinion in Green and Sustainable Chemistry* 25, 100342.
- Ding, H., Liu, H., Chu, W., Wu, C. and Xie, Y. 2021. Structural Transformation of Heterogeneous Materials for Electrocatalytic Oxygen Evolution Reaction. *Chemical Reviews*. <https://doi.org/10.1021/acs.chemrev.1c00234>.
- Ding, Y., Li, H. and Hou, Y. 2018. Phosphorus-doped nickel sulfides/nickel foam as electrode materials for electrocatalytic water splitting. *International Journal of Hydrogen Energy* 43(41), 19002-19009.

- Dinh, K.N., Liang, Q., Du, C.-F., Zhao, J., Tok, A.I.Y., Mao, H. and Yan, Q. 2019. Nanostructured metallic transition metal carbides, nitrides, phosphides, and borides for energy storage and conversion. *Nano Today* 25, 99-121.
- Dionigi, F. and Strasser, P. 2016. NiFe-Based (Oxy)hydroxide Catalysts for Oxygen Evolution Reaction in Non-Acidic Electrolytes. *Advanced Energy Materials* 6(23), 1600621.
- Du, H., Kong, R., Qu, F. and Lu, L. 2018. Enhanced electrocatalysis for alkaline hydrogen evolution by Mn doping in a Ni₃S₂ nanosheet array. *Chemical Communications* 54(72), 10100-10103.
- Elumeeva, K., Masa, J., Medina, D., Ventosa, E., Seisel, S., Kayran, Y.U., Genç, A., Bobrowski, T., Weide, P., Arbiol, J., Muhler, M. and Schuhmann, W. 2017. Cobalt boride modified with N-doped carbon nanotubes as a high-performance bifunctional oxygen electrocatalyst. *Journal of Materials Chemistry A* 5(40), 21122-21129.
- Fan, K., Chen, H., Ji, Y., Huang, H., Claesson, P.M., Daniel, Q., Philippe, B., Rensmo, H., Li, F., Luo, Y. and Sun, L. 2016. Nickel-vanadium monolayer double hydroxide for efficient electrochemical water oxidation. *Nature Communications* 7, 11981.
- Fang, M., Dong, G., Wei, R. and Ho, J.C. 2017. Hierarchical Nanostructures: Design for Sustainable Water Splitting. *Advanced Energy Materials* 7(23), 1700559.
- Fang, Y.-H. and Liu, Z.-P. 2010. Mechanism and tafel lines of electro-oxidation of water to oxygen on RuO₂ (110). *Journal of the American Chemical Society* 132(51), 18214-18222.
- Feng, C., Faheem, M.B., Fu, J., Xiao, Y., Li, C. and Li, Y. 2020. Fe-Based Electrocatalysts for Oxygen Evolution Reaction: Progress and Perspectives. *ACS Catalysis* 10(7), 4019-4047.
- Feng, J.X., Wu, J.Q., Tong, Y.X. and Li, G.R. 2018. Efficient Hydrogen Evolution on Cu Nanodots-Decorated Ni₃S₂ Nanotubes by Optimizing Atomic Hydrogen Adsorption and Desorption. *Journal of the American Chemical Society* 140(2), 610-617.
- Gao, R. and Yan, D. 2020. Recent Development of Ni/Fe-Based Micro/Nanostructures toward Photo/Electrochemical Water Oxidation. *Advanced Energy Materials* 10(11), 1900954.
- Guan, Y., Xuan, H., Li, H. and Han, P. 2019. Synthesis of 3D flower-like nickel-molybdenum-sulfur microspheres as efficient and stable electrocatalyst for hydrogen and oxygen evolution reactions. *Electrochimica Acta* 320, 134614.
- Guo, F.-F., Wu, Y., Ai, X., Chen, H., Li, G., Chen, W. and Zou, X. 2019a. A class of metal diboride electrocatalysts synthesized by a molten salt-assisted reaction for the hydrogen evolution reaction. *Chemical Communications* 55(59), 8627-8630.
- Guo, M., Zhou, L., Li, Y., Zheng, Q., Xie, F. and Lin, D. 2019b. Unique nanosheet-nanowire structured CoMnFe layered triple hydroxide arrays as self-supporting

- electrodes for a high-efficiency oxygen evolution reaction. *Journal of Materials Chemistry A* 7(21), 13130-13141.
- Guo, R., Lai, X., Huang, J., Du, X., Yan, Y., Sun, Y., Zou, G. and Xiong, J. 2018. Phosphate-Based Electrocatalysts for Water Splitting: Recent Progress. *ChemElectroChem* 5(24), 3822-3834.
- Guo, Y., Hong, X., Wang, Y., Li, Q., Meng, J., Dai, R., Liu, X., He, L. and Mai, L. 2019c. Multicomponent Hierarchical Cu-Doped NiCo-LDH/CuO Double Arrays for Ultralong-Life Hybrid Fiber Supercapacitor. *Advanced Functional Materials* 29(24), 1809004.
- Guo, Y., Park, T., Yi, J.W., Henzie, J., Kim, J., Wang, Z., Jiang, B., Bando, Y., Sugahara, Y., Tang, J. and Yamauchi, Y. 2019d. Nanoarchitectonics for Transition-Metal-Sulfide-Based Electrocatalysts for Water Splitting. *Advanced Materials* 31(17), e1807134.
- Guo, Y., Yao, Z., Shang, C. and Wang, E. 2017. Amorphous Co₂B Grown on CoSe₂ Nanosheets as a Hybrid Catalyst for Efficient Overall Water Splitting in Alkaline Medium. *ACS Applied Materials & Interfaces* 9(45), 39312-39317.
- Guo, Y., Yuan, W., Zhao, X., Hao, W., Li, J., Wang, L. and Ma, X. 2019e. The performance of surface oxidized Ni₃B, Ni₂B and NiB₂ electrocatalysts for overall water splitting. *ChemElectroChem* 6(3), 764-770.
- Gupta, S., Jadhav, H., Sinha, S., Miotello, A., Patel, M.K., Sarkar, A. and Patel, N. 2019a. Cobalt-Boride Nanostructured Thin Films with High Performance and Stability for Alkaline Water Oxidation. *ACS Sustainable Chemistry & Engineering* 7(19), 16651-16658.
- Gupta, S., Patel, M.K., Miotello, A. and Patel, N. 2019b. Metal Boride-Based Catalysts for Electrochemical Water-Splitting: A Review. *Advanced Functional Materials* 30(1), 1906481.
- Han, H., Choi, H., Mhin, S., Hong, Y.-R., Kim, K.M., Kwon, J., Ali, G., Chung, K.Y., Je, M., Umh, H.N., Lim, D.-H., Davey, K., Qiao, S.-Z., Paik, U. and Song, T. 2019a. Advantageous crystalline–amorphous phase boundary for enhanced electrochemical water oxidation. *Energy & Environmental Science* 12(8), 2443-2454.
- Han, H., Hong, Y.R., Woo, J., Mhin, S., Kim, K.M., Kwon, J., Choi, H., Chung, Y.C. and Song, T. 2019b. Electronically Double-Layered Metal Boride Hollow Nanoprism as an Excellent and Robust Water Oxidation Electrocatalysts. *Advanced Energy Materials* 9(13), 1803799.
- Han, L., Dong, S. and Wang, E. 2016. Transition-Metal (Co, Ni, and Fe)-Based Electrocatalysts for the Water Oxidation Reaction. *Advanced Materials* 28(42), 9266-9291.
- Han, N., Liu, P., Jiang, J., Ai, L., Shao, Z. and Liu, S. 2018. Recent advances in nanostructured metal nitrides for water splitting. *Journal of Materials Chemistry A* 6(41), 19912-19933.
- Hao, Q., Jia, G., Wei, W., Vinu, A., Wang, Y., Arandiyani, H. and Ni, B.-J. 2019a. Graphitic carbon nitride with different dimensionalities for energy and environmental applications. *Nano Research* 13(1), 18-37.

- Hao, W., Wu, R., Yang, H. and Guo, Y. 2019b. Photothermal coupling electrolysis on Ni–W–B toward practical overall water splitting. *Journal of Materials Chemistry A* 7(20), 12440-12445.
- Hao, W., Wu, R., Zhang, R., Ha, Y., Chen, Z., Wang, L., Yang, Y., Ma, X., Sun, D., Fang, F. and Guo, Y. 2018. Electroless Plating of Highly Efficient Bifunctional Boride-Based Electrodes toward Practical Overall Water Splitting. *Advanced Energy Materials* 8(26), 1801372.
- Hausmann, J.N., Khalaniya, R.A., Das, C., Remy-Speckmann, I., Berendts, S., Shevelkov, A.V., Driess, M. and Menezes, P.W. 2021. Intermetallic Fe₆Ge₅ formation and decay of a core-shell structure during the oxygen evolution reaction. *Chemical Communications* 57(17), 2184-2187.
- Hausmann, J.N., Mebs, S., Laun, K., Zebger, I., Dau, H., Menezes, P.W. and Driess, M. 2020. Understanding the formation of bulk- and surface-active layered (oxy)hydroxides for water oxidation starting from a cobalt selenite precursor. *Energy & Environmental Science* 13(10), 3607-3619.
- He, D., Zhang, L., Zhao, Y., Mei, Y., Chen, D., He, S. and Luo, Y. 2018a. Recycling Spent Cr Adsorbents as Catalyst for Eliminating Methylmercaptan. *Environmental Science & Technology* 52(6), 3669-3675.
- He, T., Nsanzimana, J.M.V., Qi, R., Zhang, J.-Y., Miao, M., Yan, Y., Qi, K., Liu, H. and Xia, B.Y. 2018b. Synthesis of amorphous boride nanosheets by the chemical reduction of Prussian blue analogs for efficient water electrolysis. *Journal of Materials Chemistry A* 6(46), 23289-23294.
- He, W., Ren, G., Li, Y., Jia, D., Li, S., Cheng, J., Liu, C., Hao, Q., Zhang, J. and Liu, H. 2020. Amorphous nickel-iron hydroxide films on nickel sulfide nanoparticles for the oxygen evolution reaction. *Catalysis Science & Technology* 10(6), 1708-1713.
- Heard, C.J., Cejka, J., Opanasenko, M., Nachtigall, P., Centi, G. and Perathoner, S. 2019. 2D Oxide Nanomaterials to Address the Energy Transition and Catalysis. *Advanced Materials* 31(3), e1801712.
- Hou, J., Wu, Y., Zhang, B., Cao, S., Li, Z. and Sun, L. 2019. Rational Design of Nanoarray Architectures for Electrocatalytic Water Splitting. *Advanced Functional Materials* 29(20), 1808367.
- Hu, C. and Dai, L. 2019. Doping of Carbon Materials for Metal-Free Electrocatalysis. *Advanced Materials* 31(7), e1804672.
- Hu, F., Wang, H., Zhang, Y., Shen, X., Zhang, G., Pan, Y., Miller, J.T., Wang, K., Zhu, S., Yang, X., Wang, C., Wu, X., Xiong, Y. and Peng, Z. 2019a. Designing Highly Efficient and Long-Term Durable Electrocatalyst for Oxygen Evolution by Coupling B and P into Amorphous Porous NiFe-Based Material. *Small* 15(28), 1901020.
- Hu, Q., Li, G., Han, Z., Wang, Z., Huang, X., Chai, X., Zhang, Q., Liu, J. and He, C. 2019b. General Synthesis of Ultrathin Metal Borate Nanomeshes Enabled by 3D Bark-Like N-Doped Carbon for Electrocatalysis. *Advanced Energy Materials* 9(28), 1901130.

- Hu, X., Zhang, S., Sun, J., Yu, L., Qian, X., Hu, R., Wang, Y., Zhao, H. and Zhu, J. 2019c. 2D Fe-containing cobalt phosphide/cobalt oxide lateral heterostructure with enhanced activity for oxygen evolution reaction. *Nano Energy* 56, 109-117.
- Huang, Q.-S., Wu, W., Wei, W., Song, L., Sun, J. and Ni, B.-J. 2020. Highly-efficient Pb^{2+} removal from water by novel $\text{K}_2\text{W}_4\text{O}_{13}$ nanowires: Performance, mechanisms and DFT calculation. *Chemical Engineering Journal* 381, 122632.
- Huang, X., Leng, M., Xiao, W., Li, M., Ding, J., Tan, T.L., Lee, W.S.V. and Xue, J. 2017. Activating basal planes and S-terminated edges of MoS_2 toward more efficient hydrogen evolution. *Advanced Functional Materials* 27(6), 1604943.
- Ji, C., Wu, D., Lu, J., Shan, C., Ren, Y., Li, T., Lv, L., Pan, B. and Zhang, W. 2021. Temperature regulated adsorption and desorption of heavy metals to A-MIL-121: Mechanisms and the role of exchangeable protons. *Water Research* 189, 116599.
- Jia, Y., Chen, J. and Yao, X. 2018. Defect electrocatalytic mechanism: concept, topological structure and perspective. *Materials Chemistry Frontiers* 2(7), 1250-1268.
- Jian, J., Yuan, L., Qi, H., Sun, X., Zhang, L., Li, H., Yuan, H. and Feng, S. 2018. $\text{Sn-Ni}_3\text{S}_2$ Ultrathin Nanosheets as Efficient Bifunctional Water-Splitting Catalysts with a Large Current Density and Low Overpotential. *ACS Applied Materials & Interfaces* 10(47), 40568-40576.
- Jiang, J., Sun, F., Zhou, S., Hu, W., Zhang, H., Dong, J., Jiang, Z., Zhao, J., Li, J. and Yan, W. 2018. Atomic-level insight into super-efficient electrocatalytic oxygen evolution on iron and vanadium co-doped nickel (oxy) hydroxide. *Nature Communications* 9(1), 1-12.
- Jiang, J., Wang, M., Yan, W., Liu, X., Liu, J., Yang, J. and Sun, L. 2017a. Highly active and durable electrocatalytic water oxidation by a $\text{NiB}_{0.45}/\text{NiO}_x$ core-shell heterostructured nanoparticulate film. *Nano Energy* 38, 175-184.
- Jiang, W.-J., Tang, T., Zhang, Y. and Hu, J.-S. 2020. Synergistic Modulation of Non-Precious-Metal Electrocatalysts for Advanced Water Splitting. *Accounts of Chemical Research* 53(6), 1111-1123.
- Jiang, W.J., Niu, S., Tang, T., Zhang, Q.H., Liu, X.Z., Zhang, Y., Chen, Y.Y., Li, J.H., Gu, L., Wan, L.J. and Hu, J.S. 2017b. Crystallinity-Modulated Electrocatalytic Activity of a Nickel(II) Borate Thin Layer on Ni_3B for Efficient Water Oxidation. *Angewandte Chemie International Edition* 56(23), 6572-6577.
- Joo, J., Kim, T., Lee, J., Choi, S.I. and Lee, K. 2019. Morphology-Controlled Metal Sulfides and Phosphides for Electrochemical Water Splitting. *Advanced Materials* 31(14), e1806682.
- Jothi, P.R., Zhang, Y., Yubuta, K., Culver, D.B., Conley, M. and Fokwa, B.P.T. 2018. Abundant Vanadium Diboride with Graphene-like Boron layers for Hydrogen Evolution. *ACS Applied Energy Materials* 2(1), 176-181.
- Kim, J., Kim, H., Kim, S.-K. and Ahn, S.H. 2018. Electrodeposited amorphous Co-P-B ternary catalyst for hydrogen evolution reaction. *Journal of Materials Chemistry A* 6(15), 6282-6288.

- Klemenz, S., Schuch, J., Hawel, S., Zieschang, A.M., Kaiser, B., Jaegermann, W. and Albert, B. 2018. Synthesis of a Highly Efficient Oxygen-Evolution Electrocatalyst by Incorporation of Iron into Nanoscale Cobalt Borides. *ChemSusChem* 11(18), 3150-3156.
- Kong, F., Qiao, Y., Zhang, C., Fan, X., Kong, A. and Shan, Y. 2020. Unadulterated carbon as robust multifunctional electrocatalyst for overall water splitting and oxygen transformation. *Nano Research* 13(2), 401-411.
- Kou, T., Smart, T., Yao, B., Chen, I., Thota, D., Ping, Y. and Li, Y. 2018. Theoretical and Experimental Insight into the Effect of Nitrogen Doping on Hydrogen Evolution Activity of Ni₃S₂ in Alkaline Medium. *Advanced Energy Materials* 8(19), 1703538.
- Kou, T., Wang, S., Hauser, J.L., Chen, M., Oliver, S.R.J., Ye, Y., Guo, J. and Li, Y. 2019. Ni Foam-Supported Fe-Doped β -Ni(OH)₂ Nanosheets Show Ultralow Overpotential for Oxygen Evolution Reaction. *ACS Energy Letters* 4(3), 622-628.
- Li, B., Li, Z., He, F., Pang, Q. and Shen, P. 2019a. One-pot preparation of Ni₃S₂@3-D graphene free-standing electrode by simple Q-CVD method for efficient oxygen evolution reaction. *International Journal of Hydrogen Energy* 44(59), 30806-30819.
- Li, D., Li, T., Hao, G., Guo, W., Chen, S., Liu, G., Li, J. and Zhao, Q. 2020a. IrO₂ nanoparticle-decorated single-layer NiFe LDHs nanosheets with oxygen vacancies for the oxygen evolution reaction. *Chemical Engineering Journal* 399, 125738.
- Li, H., Wen, P., Li, Q., Dun, C., Xing, J., Lu, C., Adhikari, S., Jiang, L., Carroll, D.L. and Geyer, S.M. 2017. Earth-abundant iron diboride (FeB₂) nanoparticles as highly active bifunctional electrocatalysts for overall water splitting. *Advanced Energy Materials* 7(17), 1700513.
- Li, J., Chen, H., Liu, Y., Gao, R. and Zou, X. 2019b. In situ structural evolution of a nickel boride catalyst: synergistic geometric and electronic optimization for the oxygen evolution reaction. *Journal of Materials Chemistry A* 7(10), 5288-5294.
- Li, J., Luo, Z., He, F., Zuo, Y., Zhang, C., Liu, J., Yu, X., Du, R., Zhang, T., Infante-Carrió, M.F., Tang, P., Arbiol, J., Llorca, J. and Cabot, A. 2018a. Colloidal Ni-Co-Sn nanoparticles as efficient electrocatalysts for the methanol oxidation reaction. *Journal of Materials Chemistry A* 6(45), 22915-22924.
- Li, J. and Zheng, G. 2017. One-Dimensional Earth-Abundant Nanomaterials for Water-Splitting Electrocatalysts. *Advanced Science* 4(3), 1600380.
- Li, P., Jin, Z. and Xiao, D. 2014. A one-step synthesis of Co-P-B/rGO at room temperature with synergistically enhanced electrocatalytic activity in neutral solution. *Journal of Materials Chemistry A* 2(43), 18420-18427.
- Li, R., Hu, B., Yu, T., Chen, H., Wang, Y. and Song, S. 2020b. Insights into Correlation among Surface-Structure-Activity of Cobalt-Derived Pre-Catalyst for Oxygen Evolution Reaction. *Advanced Science* 7(5), 1902830.

- Li, S., Li, Z., Ma, R., Gao, C., Liu, L., Hu, L., Zhu, J., Sun, T., Tang, Y., Liu, D. and Wang, J. 2021. A Glass-Ceramic with Accelerated Surface Reconstruction toward the Efficient Oxygen Evolution Reaction. *Angewandte Chemie International Edition* 60(7), 3773-3780.
- Li, Y., Du, X., Huang, J., Wu, C., Sun, Y., Zou, G., Yang, C. and Xiong, J. 2019c. Recent Progress on Surface Reconstruction of Earth-Abundant Electrocatalysts for Water Oxidation. *Small* 15(35), e1901980.
- Li, Y., Huang, B., Sun, Y., Luo, M., Yang, Y., Qin, Y., Wang, L., Li, C., Lv, F., Zhang, W. and Guo, S. 2019d. Multimetal Borides Nanochains as Efficient Electrocatalysts for Overall Water Splitting. *Small* 15(1), e1804212.
- Li, Y., Xu, H., Huang, H., Gao, L., Zhao, Y. and Ma, T. 2018b. Synthesis of Co-B in porous carbon using a metal-organic framework (MOF) precursor: A highly efficient catalyst for the oxygen evolution reaction. *Electrochemistry Communications* 86, 140-144.
- Liang, D., Lian, C., Xu, Q., Liu, M., Liu, H., Jiang, H. and Li, C. 2020. Interfacial charge polarization in $\text{Co}_2\text{P}_2\text{O}_7@\text{N}$, P co-doped carbon nanocages as Mott-Schottky electrocatalysts for accelerating oxygen evolution reaction. *Applied Catalysis B: Environmental* 268, 118417.
- Liang, H., Gandi, A.N., Xia, C., Hedhili, M.N., Anjum, D.H., Schwingenschlögl, U. and Alshareef, H.N. 2017. Amorphous NiFe-OH/NiFeP Electrocatalyst Fabricated at Low Temperature for Water Oxidation Applications. *ACS Energy Letters* 2(5), 1035-1042.
- Liang, X., Dong, R., Li, D., Bu, X., Li, F., Shu, L., Wei, R. and Ho, J.C. 2018. Coupling of Nickel Boride and $\text{Ni}(\text{OH})_2$ Nanosheets with Hierarchical Interconnected Conductive Porous Structure Synergizes the Oxygen Evolution Reaction. *ChemCatChem* 10(20), 4555-4561.
- Lin, J., Wang, H., Zheng, X., Du, Y., Zhao, C., Qi, J., Cao, J., Fei, W. and Feng, J. 2018. Controllable synthesis of core-branch $\text{Ni}_3\text{S}_2/\text{Co}_9\text{S}_8$ directly on nickel foam as an efficient bifunctional electrocatalyst for overall water splitting. *Journal of Power Sources* 401, 329-335.
- Lin, Y.C., Chuang, C.H., Hsiao, L.Y., Yeh, M.H. and Ho, K.C. 2020. Oxygen Plasma Activation of Carbon Nanotubes-Interconnected Prussian Blue Analogue for Oxygen Evolution Reaction. *ACS Applied Materials & Interfaces* 12(38), 42634-42643.
- Ling, P., Zhang, Q., Cao, T. and Gao, F. 2018. Versatile Three-Dimensional Porous $\text{Cu}@\text{Cu}_2\text{O}$ Aerogel Networks as Electrocatalysts and Mimicking Peroxidases. *Angewandte Chemie International Edition* 57(23), 6819-6824.
- Liu, D., Dai, L., Lin, X., Chen, J.F., Zhang, J., Feng, X., Mullen, K., Zhu, X. and Dai, S. 2019. Chemical Approaches to Carbon-Based Metal-Free Catalysts. *Advanced Materials* 31(13), e1804863.
- Liu, G., He, D., Yao, R., Zhao, Y. and Li, J. 2018a. Amorphous NiFeB nanoparticles realizing highly active and stable oxygen evolving reaction for water splitting. *Nano Research* 11(3), 1664-1675.

- Liu, H., Ma, X., Rao, Y., Liu, Y., Liu, J., Wang, L. and Wu, M. 2018b. Heteromorphic NiCo₂S₄/Ni₃S₂/Ni Foam as a Self-Standing Electrode for Hydrogen Evolution Reaction in Alkaline Solution. *ACS Applied Materials & Interfaces* 10(13), 10890-10897.
- Liu, J., Zhu, D., Guo, C., Vasileff, A. and Qiao, S.-Z. 2017. Design Strategies toward Advanced MOF-Derived Electrocatalysts for Energy-Conversion Reactions. *Advanced Energy Materials* 7(23), 1700518.
- Liu, Q., Zhao, H., Jiang, M., Kang, Q., Zhou, W., Wang, P. and Zhou, F. 2020. Boron enhances oxygen evolution reaction activity over Ni foam-supported iron boride nanowires. *Journal of Materials Chemistry A* 8(27), 13638-13645.
- Liu, X. and Dai, L. 2016. Carbon-based metal-free catalysts. *Nature Reviews Materials* 1(11), 1-12.
- Liu, X., Meng, J., Zhu, J., Huang, M., Wen, B., Guo, R. and Mai, L. 2021. Comprehensive Understandings into Complete Reconstruction of Precatalysts: Synthesis, Applications, and Characterizations. *Advanced Materials* 33, 2007344.
- Long, X., Qiu, W., Wang, Z., Wang, Y. and Yang, S. 2019. Recent advances in transition metal-based catalysts with heterointerfaces for energy conversion and storage. *Materials Today Chemistry* 11, 16-28.
- Lu, Q., Yu, J., Zou, X., Liao, K., Tan, P., Zhou, W., Ni, M. and Shao, Z. 2019. Self-Catalyzed Growth of Co, N-Codoped CNTs on Carbon-Encased CoS_x Surface: A Noble-Metal-Free Bifunctional Oxygen Electrocatalyst for Flexible Solid Zn-Air Batteries. *Advanced Functional Materials*, 29(38), 1904481.
- Lu, W., Liu, T., Xie, L., Tang, C., Liu, D., Hao, S., Qu, F., Du, G., Ma, Y., Asiri, A.M. and Sun, X. 2017. In Situ Derived CoB Nanoarray: A High-Efficiency and Durable 3D Bifunctional Electrocatalyst for Overall Alkaline Water Splitting. *Small* 13(32), 1700805.
- Luo, J., Sun, M., Ritt, C.L., Liu, X., Pei, Y., Crittenden, J.C. and Elimelech, M. 2019. Tuning Pb(II) Adsorption from Aqueous Solutions on Ultrathin Iron Oxychloride (FeOCl) Nanosheets. *Environmental Science & Technology* 53(4), 2075-2085.
- Luo, J., Yu, D., Hristovski, K.D., Fu, K., Shen, Y., Westerhoff, P. and Crittenden, J.C. 2021. Critical Review of Advances in Engineering Nanomaterial Adsorbents for Metal Removal and Recovery from Water: Mechanism Identification and Engineering Design. *Environmental Science & Technology* 55(8), 4287-4304.
- Lv, L., Yang, Z., Chen, K., Wang, C. and Xiong, Y. 2019. 2D Layered Double Hydroxides for Oxygen Evolution Reaction: From Fundamental Design to Application. *Advanced Energy Materials* 9(17), 1803358.
- Lyu, F., Wang, Q., Choi, S.M. and Yin, Y. 2019. Noble-Metal-Free Electrocatalysts for Oxygen Evolution. *Small* 15(1), e1804201.
- Ma, M., Qu, F., Ji, X., Liu, D., Hao, S., Du, G., Asiri, A.M., Yao, Y., Chen, L. and Sun, X. 2017a. Bimetallic Nickel-Substituted Cobalt-Borate Nanowire Array: An Earth-Abundant Water Oxidation Electrocatalyst with Superior Activity and Durability at Near Neutral pH. *Small* 13(25), 1700394.

- Ma, X., Wen, J., Zhang, S., Yuan, H., Li, K., Yan, F., Zhang, X. and Chen, Y. 2017b. Crystal Co_xB ($x = 1-3$) Synthesized by a Ball-Milling Method as High-Performance Electrocatalysts for the Oxygen Evolution Reaction. *ACS Sustainable Chemistry & Engineering* 5(11), 10266-10274.
- Mann, D.K., Xu, J., Mordvinova, N.E., Yannello, V., Ziouani, Y., González-Ballesteros, N., Sousa, J.P.S., Lebedev, O.I., Kolen'ko, Y.V. and Shatruk, M. 2019. Electrocatalytic water oxidation over AlFe_2B_2 . *Chemical Science* 10(9), 2796-2804.
- Mao, H., Guo, X., Fu, Y., Yang, H., Zhang, Y., Zhang, R. and Song, X.-M. 2020. Enhanced electrolytic oxygen evolution by the synergistic effects of trimetallic FeCoNi boride oxides immobilized on polypyrrole/reduced graphene oxide. *Journal of Materials Chemistry A* 8(4), 1821-1828.
- Masa, J., Piontek, S., Wilde, P., Antoni, H., Eckhard, T., Chen, Y.T., Muhler, M., Apfel, U.P. and Schuhmann, W. 2019. Ni-Metalloid (B, Si, P, As, and Te) Alloys as Water Oxidation Electrocatalysts. *Advanced Energy Materials* 9(26), 1900796.
- Masa, J., Sinev, I., Mistry, H., Ventosa, E., de la Mata, M., Arbiol, J., Muhler, M., Roldan Cuenya, B. and Schuhmann, W. 2017. Ultrathin High Surface Area Nickel Boride (Ni_xB) Nanosheets as Highly Efficient Electrocatalyst for Oxygen Evolution. *Advanced Energy Materials* 7(17), 1700381.
- Masa, J., Weide, P., Peeters, D., Sinev, I., Xia, W., Sun, Z., Somsen, C., Muhler, M. and Schuhmann, W. 2016. Amorphous Cobalt Boride (Co_2B) as a Highly Efficient Nonprecious Catalyst for Electrochemical Water Splitting: Oxygen and Hydrogen Evolution. *Advanced Energy Materials* 6(6), 1502313.
- Natarajan, S. and Aravindan, V. 2018. Burgeoning Prospects of Spent Lithium-Ion Batteries in Multifarious Applications. *Advanced Energy Materials* 8(33), 1802303.
- Ni, B.J., Huang, Q.S., Wang, C., Ni, T.Y., Sun, J. and Wei, W. 2019a. Competitive adsorption of heavy metals in aqueous solution onto biochar derived from anaerobically digested sludge. *Chemosphere* 219, 351-357.
- Ni, Y., He, B., Luo, S., Wu, X., Feng, X., Luo, Y., Lin, J., Sun, J., Fan, K. and Ji, Y. 2019b. Microporous core-shell $\text{Co}_{11}(\text{HPO}_3)_8(\text{OH})_6/\text{Co}_{11}(\text{PO}_3)_8\text{O}_6$ nanowires for highly efficient electrocatalytic oxygen evolution reaction. *Applied Catalysis B: Environmental* 259, 118091.
- Niu, B. and Xu, Z. 2019. In-situ preparation of Nb-Pb codoped and Pd loaded TiO_2 photocatalyst from waste multi-layer ceramic capacitors by a chlorination-leaching process. *Green Chemistry* 21(4), 874-884.
- Nsanzimana, J.M.V., Dangol, R., Reddu, V., Dou, S., Peng, Y., Dinh, K.N., Huang, Z., Yan, Q. and Wang, X. 2018a. Facile Synthesis of Amorphous Ternary Metal Borides-Reduced Graphene Oxide Hybrid with Superior Oxygen Evolution Activity. *ACS Applied Materials & Interfaces* 11(1), 846-855.
- Nsanzimana, J.M.V., Gong, L., Dangol, R., Reddu, V., Jose, V., Xia, B.Y., Yan, Q., Lee, J.-M. and Wang, X. 2019. Tailoring of Metal Boride Morphology via

- Anion for Efficient Water Oxidation. *Advanced Energy Materials* 9(28), 1901503.
- Nsanzimana, J.M.V., Peng, Y., Xu, Y.Y., Thia, L., Wang, C., Xia, B.Y. and Wang, X. 2018b. An Efficient and Earth-Abundant Oxygen-Evolving Electrocatalyst Based on Amorphous Metal Borides. *Advanced Energy Materials* 8(1), 1701475.
- Oldham, D., Rajib, A., Dandamudi, K.P.R., Liu, Y., Deng, S. and Fini, E.H. 2021. Transesterification of Waste Cooking Oil to Produce A Sustainable Rejuvenator for Aged Asphalt. *Resources, Conservation and Recycling* 168, 105297.
- Park, H., Encinas, A., Scheifers, J.P., Zhang, Y. and Fokwa, B.P.T. 2017a. Boron-Dependency of Molybdenum Boride Electrocatalysts for the Hydrogen Evolution Reaction. *Angewandte Chemie International Edition* 56(20), 5575-5578.
- Park, H., Zhang, Y., Lee, E., Shankhari, P. and Fokwa, B.T.P. 2019. Designing highly active high current density HER electrocatalysts: Graphene-like boron layer and tungsten as key ingredients in metal diborides. *ChemSusChem* 12(16), 3726-3731.
- Park, H., Zhang, Y., Scheifers, J.P., Jothi, P.R., Encinas, A. and Fokwa, B.P.T. 2017b. Graphene- and Phosphorene-like Boron Layers with Contrasting Activities in Highly Active Mo_2B_4 for Hydrogen Evolution. *Journal of the American Chemical Society* 139(37), 12915-12918.
- Qin, C., Fan, A., Ren, D., Luan, C., Yang, J., Liu, Y., Zhang, X., Dai, X. and Wang, M. 2019. Amorphous NiMS (M: Co, Fe or Mn) holey nanosheets derived from crystal phase transition for enhanced oxygen evolution in water splitting. *Electrochimica Acta* 323, 134756.
- Qin, J.-F., Yang, M., Hou, S., Dong, B., Chen, T.-S., Ma, X., Xie, J.-Y., Zhou, Y.-N., Nan, J. and Chai, Y.-M. 2020. Copper and cobalt co-doped Ni_3S_2 grown on nickel foam for highly efficient oxygen evolution reaction. *Applied Surface Science* 502, 144172.
- Qu, Y., Yang, M., Chai, J., Tang, Z., Shao, M., Kwok, C.T., Yang, M., Wang, Z., Chua, D., Wang, S., Lu, Z. and Pan, H. 2017. Facile Synthesis of Vanadium-Doped Ni_3S_2 Nanowire Arrays as Active Electrocatalyst for Hydrogen Evolution Reaction. *ACS Applied Materials & Interfaces* 9(7), 5959-5967.
- Ren, H., Sun, X., Du, C., Zhao, J., Liu, D., Fang, W., Kumar, S., Chua, R., Meng, S., Kidkhunthod, P., Song, L., Li, S., Madhavi, S. and Yan, Q. 2019. Amorphous Fe-Ni-P-B-O Nanocages as Efficient Electrocatalysts for Oxygen Evolution Reaction. *ACS Nano* 13(11), 12969-12979.
- Rosales, E., Meijide, J., Pazos, M. and Sanroman, M.A. 2017. Challenges and recent advances in biochar as low-cost biosorbent: From batch assays to continuous-flow systems. *Bioresource Technology* 246, 176-192.
- S. Gupta, N.P., R. Fernandes, R. Kadrekar, Alpa Dashora, A.K. Yadav, D. Bhattacharyya, S.N. Jha, A. Miotello, D.C. Kothari 2016. Co-Ni-B nanocatalyst for efficient hydrogen evolution reaction in wide pH range. *Applied Catalysis B: Environmental* 192, 126-133.

- S. Gupta, N.P., R. Fernandes, S. Hanchate, A. Miotello, D.C. Kothari 2017. Co-Mo-B Nanoparticles as a Non-Precious and Efficient Bifunctional Electrocatalyst for Hydrogen and Oxygen Evolution. *Electrochimica Acta* 232, 64-71.
- Seh, Z.W., Kibsgaard, J., Dickens, C.F., Chorkendorff, I., Norskov, J.K. and Jaramillo, T.F. 2017. Combining theory and experiment in electrocatalysis: Insights into materials design. *Science* 355, 6321.
- Seitz, L.C., Dickens, C.F., Nishio, K., Hikita, Y., Montoya, J., Doyle, A., Kirk, C., Vojvodic, A., Hwang, H.Y., Norskov, J.K. and Jaramillo, T.F. 2016. A highly active and stable IrO_x/SrIrO₃ catalyst for the oxygen evolution reaction. *Science* 353(6303), 1011-1014.
- Selvam, N.C.S., Du, L., Xia, B.Y., Yoo, P.J. and You, B. 2020. Reconstructed Water Oxidation Electrocatalysts: The Impact of Surface Dynamics on Intrinsic Activities. *Advanced Functional Materials* 31(12), 2008190.
- Shan, J., Ling, T., Davey, K., Zheng, Y. and Qiao, S.Z. 2019. Transition-Metal-Doped RuIr Bifunctional Nanocrystals for Overall Water Splitting in Acidic Environments. *Advanced Materials* 31(17), 1900510.
- She, S., Zhu, Y., Chen, Y., Lu, Q., Zhou, W. and Shao, Z. 2019. Realizing Ultrafast Oxygen Evolution by Introducing Proton Acceptor into Perovskites. *Advanced Energy Materials* 9(20), 1900429.
- Shen, J., Wu, H., Sun, W., Wu, Q., Zhen, S., Wang, Z. and Sun, K. 2019. Biomass-derived hierarchically porous carbon skeletons with in situ decorated IrCo nanoparticles as high-performance cathode catalysts for Li-O₂ batteries. *Journal of Materials Chemistry A* 7(17), 10662-10671.
- Sheng, M., Wu, Q., Wang, Y., Liao, F., Zhou, Q., Hou, J. and Weng, W. 2018. Network-like porous Co-Ni-B grown on carbon cloth as efficient and stable catalytic electrodes for hydrogen evolution. *Electrochemistry Communications* 93, 104-108.
- Shi, Q., Fu, S., Zhu, C., Song, J., Du, D. and Lin, Y. 2019. Metal-organic frameworks-based catalysts for electrochemical oxygen evolution. *Materials Horizons* 6(4), 684-702.
- Shi, Y., Du, W., Zhou, W., Wang, C., Lu, S., Lu, S. and Zhang, B. 2020. Unveiling the Promotion of Surface-Adsorbed Chalcogenate on the Electrocatalytic Oxygen Evolution Reaction. *Angewandte Chemie International Edition* 59(50), 22470-22474.
- Shifa, T.A., Wang, F., Liu, Y. and He, J. 2018. Heterostructures Based on 2D Materials: A Versatile Platform for Efficient Catalysis. *Advanced Materials* 31(45), 1804828.
- Shit, S., Chhetri, S., Jang, W., Murmu, N.C., Koo, H., Samanta, P. and Kuila, T. 2018. Cobalt Sulfide/Nickel Sulfide Heterostructure Directly Grown on Nickel Foam: An Efficient and Durable Electrocatalyst for Overall Water Splitting Application. *ACS Applied Materials & Interfaces* 10(33), 27712-27722.
- Singh, T. and Singhal, R. 2013. Reuse of a waste adsorbent poly(AAc/AM/SH)-Cu superabsorbent hydrogel, for the potential phosphate ion removal from waste

- water: Matrix effects, adsorption kinetics, and thermodynamic studies. *Journal of Applied Polymer Science* 129(6), 3126-3139.
- Sivanantham, A., Ganesan, P., Vinu, A. and Shanmugam, S. 2020. Surface Activation and Reconstruction of Non-Oxide-Based Catalysts Through in Situ Electrochemical Tuning for Oxygen Evolution Reactions in Alkaline Media. *ACS Catalysis* 10(1), 463-493.
- Song, F., Schenk, K. and Hu, X. 2016. A nanoporous oxygen evolution catalyst synthesized by selective electrochemical etching of perovskite hydroxide $\text{CoSn}(\text{OH})_6$ nanocubes. *Energy & Environmental Science* 9(2), 473-477.
- Staszak-Jirkovský, J., Malliakas, C.D., Lopes, P.P., Danilovic, N., Kota, S.S., Chang, K.-C., Genorio, B., Strmcnik, D., Stamenkovic, V.R. and Kanatzidis, M.G. 2016. Design of active and stable Co-Mo-S_x chalcogels as pH-universal catalysts for the hydrogen evolution reaction. *Nature Materials* 15(2), 197.
- Suen, N.T., Hung, S.F., Quan, Q., Zhang, N., Xu, Y.J. and Chen, H.M. 2017. Electrocatalysis for the oxygen evolution reaction: recent development and future perspectives. *Chemical Society Reviews* 46(2), 337-365.
- Sun, G.L., Reynolds, E.E. and Belcher, A.M. 2020. Using yeast to sustainably remediate and extract heavy metals from waste waters. *Nature Sustainability* 3(4), 303-311.
- Sun, H., Xu, X., Chen, G., Zhou, Y., Lin, H.J., Chen, C.T., Ran, R., Zhou, W. and Shao, Z.J.C. 2019a. Smart Control of Composition for Double Perovskite Electrocatalysts toward Enhanced Oxygen Evolution Reaction. *ChemSusChem* 12(23), 5111-5116.
- Sun, H., Xu, X., Yan, Z., Chen, X., Jiao, L., Cheng, F. and Chen, J. 2018. Superhydrophilic amorphous Co-B-P nanosheet electrocatalysts with Pt-like activity and durability for the hydrogen evolution reaction. *Journal of Materials Chemistry A* 6(44), 22062-22069.
- Sun, J., Zhang, W., Wang, S., Ren, Y., Liu, Q., Sun, Y., Tang, L., Guo, J. and Zhang, X. 2019b. Ni-Co-B nanosheets coupled with reduced graphene oxide towards enhanced electrochemical oxygen evolution. *Journal of Alloys and Compounds* 776, 511-518.
- Sun, T., Zhang, G., Xu, D., Lian, X., Li, H., Chen, W. and Su, C. 2019c. Defect chemistry in 2D materials for electrocatalysis. *Materials Today Energy* 12, 215-238.
- Sundriyal, S., Shrivastav, V., Pham, H.D., Mishra, S., Deep, A. and Dubal, D.P. 2021. Advances in bio-waste derived activated carbon for supercapacitors: Trends, challenges and prospective. *Resources, Conservation and Recycling* 169, 105548.
- Tang, T., Jiang, W.-J., Niu, S., Yuan, L.-P., Hu, J.-S. and Wan, L.-J. 2019. Hetero-coupling of a carbonate hydroxide and sulfide for efficient and robust water oxidation. *Journal of Materials Chemistry A* 7(38), 21959-21965.
- Teng, Y., Wang, X.-D., Liao, J.-F., Li, W.-G., Chen, H.-Y., Dong, Y.-J. and Kuang, D.-B. 2018. Atomically Thin Defect-Rich Fe-Mn-O Hybrid Nanosheets as

- High Efficient Electrocatalyst for Water Oxidation. *Advanced Functional Materials* 28(34), 1802463.
- Tiwari, J.N., Dang, N.K., Sultan, S., Thangavel, P., Jeong, H.Y. and Kim, K.S. 2020. Multi-heteroatom-doped carbon from waste-yeast biomass for sustained water splitting. *Nature Sustainability* 3(7), 556-563.
- Vakili, M., Deng, S., Cagnetta, G., Wang, W., Meng, P., Liu, D. and Yu, G. 2019. Regeneration of chitosan-based adsorbents used in heavy metal adsorption: A review. *Separation and Purification Technology* 224, 373-387.
- Varun Vij, S.S., Ahmad M. Harzandi, Abhishek Meena, Jitendra N. Tiwari, Wang-Geun Lee, Taeseung Yoon, Kwang S. Kim 2017. Nickel-Based Electrocatalysts for Energy-Related Applications: Oxygen Reduction, Oxygen Evolution, and Hydrogen Evolution Reactions. *ACS Catalysis* 7(10), 7196-7225.
- Vrubel, H. and Hu, X. 2012. Molybdenum boride and carbide catalyze hydrogen evolution in both acidic and basic solutions. *Angewandte Chemie International Edition* 51(51), 12703-12706.
- Wan, G., Freeland, J.W., Kloppenburg, J., Petretto, G., Nelson, J.N., Kuo, D.Y., Sun, C.J., Wen, J.G., Diulus, J.T., Herman, G.S., Dong, Y.Q., Kou, R.H., Sun, J.Y., Chen, S., Shen, K.M., Schlom, D.G., Rignanese, G.M., Hautier, G., Fong, D.D., Feng, Z.X., Zhou, H. and Suntivich, J. 2021. Amorphization mechanism of SrIrO₃ electrocatalyst: How oxygen redox initiates ionic diffusion and structural reorganization. *Science Advances* 7(2), eabc7323.
- Wan, H., Liu, X., Wang, H., Ma, R. and Sasaki, T. 2019a. Recent advances in developing high-performance nanostructured electrocatalysts based on 3d transition metal elements. *Nanoscale Horizons* 4(4), 789-808.
- Wan, K., Luo, J., Zhou, C., Zhang, T., Arbiol, J., Lu, X., Mao, B.W., Zhang, X. and Fransaer, J. 2019b. Hierarchical Porous Ni₃S₄ with Enriched High-Valence Ni Sites as a Robust Electrocatalyst for Efficient Oxygen Evolution Reaction. *Advanced Functional Materials* 29(18), 1900315.
- Wang, G., Li, J., Liu, M., Du, L. and Liao, S. 2018a. Three-Dimensional Biocarbon Framework Coupled with Uniformly Distributed FeSe Nanoparticles Derived from Pollen as Bifunctional Electrocatalysts for Oxygen Electrode Reactions. *ACS Applied Materials & Interfaces* 10(38), 32133-32141.
- Wang, H., Li, C., Fang, P., Zhang, Z. and Zhang, J.Z. 2018b. Synthesis, properties, and optoelectronic applications of two-dimensional MoS₂ and MoS₂-based heterostructures. *Chemical Society Reviews* 47(16), 6101-6127.
- Wang, J., Zhong, H.X., Qin, Y.L. and Zhang, X.B. 2013. An efficient three-dimensional oxygen evolution electrode. *Angewandte Chemie International Edition* 52(20), 5248-5253.
- Wang, L., Li, J., Zhao, X., Hao, W., Ma, X., Li, S. and Guo, Y. 2019a. Surface-Activated Amorphous Iron Borides (Fe_xB) as Efficient Electrocatalysts for Oxygen Evolution Reaction. *Advanced Materials Interfaces* 6(6), 1801690.

- Wang, M., Han, J., Hu, Y. and Guo, R. 2017a. Mesoporous C, N-codoped TiO₂ hybrid shells with enhanced visible light photocatalytic performance. *RSC Advances* 7(25), 15513-15520.
- Wang, W., Liu, D., Hao, S., Qu, F., Ma, Y., Du, G., Asiri, A.M., Yao, Y. and Sun, X. 2017b. High-Efficiency and Durable Water Oxidation under Mild pH Conditions: An Iron Phosphate-Borate Nanosheet Array as a Non-Noble-Metal Catalyst Electrode. *Inorganic Chemistry* 56(6), 3131-3135.
- Wang, Y., Mayorga-Martinez, C.C., Chia, X., Sofer, Z., Mohamad Latiff, N. and Pumera, M. 2019b. Bipolar Electrochemistry as a Simple Synthetic Route toward Nanoscale Transition of Mo₂B₅ and W₂B₅ for Enhanced Hydrogen Evolution Reaction. *ACS Sustainable Chemistry & Engineering* 7(14), 12148-12159.
- Wang, Y., Yan, D., El Hankari, S., Zou, Y. and Wang, S. 2018c. Recent Progress on Layered Double Hydroxides and Their Derivatives for Electrocatalytic Water Splitting. *Advanced Science* 5(8), 1800064.
- Wang, Y., Zhu, Y., Zhao, S., She, S., Zhang, F., Chen, Y., Williams, T., Gengenbach, T., Zu, L., Mao, H., Zhou, W., Shao, Z., Wang, H., Tang, J., Zhao, D. and Selomulya, C. 2020. Anion Etching for Accessing Rapid and Deep Self-Reconstruction of Precatalysts for Water Oxidation. *Matter* 3(6), 2124-2137.
- Wei, H., Wang, H., Li, A., Li, H., Cui, D., Dong, M., Lin, J., Fan, J., Zhang, J., Hou, H., Shi, Y., Zhou, D. and Guo, Z. 2019. Advanced porous hierarchical activated carbon derived from agricultural wastes toward high performance supercapacitors. *Journal of Alloys and Compounds* 820, 153111.
- Wei, J., Zhou, M., Long, A., Xue, Y., Liao, H., Wei, C. and Xu, Z.J. 2018. Heterostructured Electrocatalysts for Hydrogen Evolution Reaction Under Alkaline Conditions. *Nano-Micro Letters* 10(4), 75.
- Wu, F., Guo, X., Hao, G., Hu, Y. and Jiang, W. 2019a. Synthesis of Iron–Nickel Sulfide Porous Nanosheets via a Chemical Etching/Anion Exchange Method for Efficient Oxygen Evolution Reaction in Alkaline Media. *Advanced Materials Interfaces* 6(18), 1900788.
- Wu, Q., Wang, S., Guo, J., Feng, X., Li, H., Lv, S., Zhou, Y. and Chen, Z. 2021. Insight into sulfur and iron effect of binary nickel-iron sulfide on oxygen evolution reaction. *Nano Research*. <https://doi.org/10.1007/s12274-021-3800-6>.
- Wu, X., Han, X., Ma, X., Zhang, W., Deng, Y., Zhong, C., Hu, W.J.A.a.m. and interfaces 2017a. Morphology-controllable synthesis of Zn-Co-mixed sulfide nanostructures on carbon fiber paper toward efficient rechargeable zinc-air batteries and water electrolysis. *ACS Applied Materials & Interfaces* 9(14), 12574-12583.
- Wu, X., Yang, Y., Zhang, T., Wang, B., Xu, H., Yan, X. and Tang, Y. 2019b. CeO_x-Decorated Hierarchical NiCo₂S₄ Hollow Nanotubes Arrays for Enhanced Oxygen Evolution Reaction Electrocatalysis. *ACS Applied Materials & Interfaces* 11(43), 39841-39847.
- Wu, Z., Guo, J., Wang, J., Liu, R., Xiao, W., Xuan, C., Xia, K. and Wang, D. 2017b. Hierarchically Porous Electrocatalyst with Vertically Aligned Defect-Rich

- CoMoS Nanosheets for the Hydrogen Evolution Reaction in an Alkaline Medium. *ACS Applied Materials & Interfaces* 9(6), 5288-5294.
- Wu, Z., Nie, D., Song, M., Jiao, T., Fu, G. and Liu, X. 2019c. Facile Synthesis of Co-Fe-B-P Nanochains as Efficient Bifunctional Electrocatalysts for Overall Water-splitting. *Nanoscale* 11(15), 7506-7512.
- Xin, W., Jiang, W.J., Lian, Y., Li, H., Hong, S., Xu, S., Yan, H. and Hu, J.S. 2019. NiS₂ nanodotted carnation-like CoS₂ for enhanced electrocatalytic water splitting. *Chemical Communications* 55(26), 3781-3784.
- Xing, C., Xue, Y., Huang, B., Yu, H., Hui, L., Fang, Y., Liu, Y., Zhao, Y., Li, Z. and Li, Y. 2019. Fluorographdiyne: A Metal-Free Catalyst for Applications in Water Reduction and Oxidation. *Angewandte Chemie International Edition* 58(39), 13897-13903.
- Xiong, C., Xue, C., Huang, L., Hu, P., Fan, P., Wang, S., Zhou, X., Yang, Z., Wang, Y. and Ji, H. 2021. Enhanced selective removal of Pb (II) by modification low-cost bio-sorbent: Experiment and theoretical calculations. *Journal of Cleaner Production* 316, 128372.
- Xu, H., Shang, H., Wang, C., Jin, L., Chen, C., Wang, C. and Du, Y. 2020. Three-dimensional open CoMoO_x/CoMoS_x/CoS_x nanobox electrocatalysts for efficient oxygen evolution reaction. *Applied Catalysis B: Environmental* 265, 118605.
- Xu, N., Cao, G., Chen, Z., Kang, Q., Dai, H. and Wang, P. 2017. Cobalt nickel boride as an active electrocatalyst for water splitting. *Journal of Materials Chemistry A* 5(24), 12379-12384.
- Xue, C., Li, G., Wang, J., Wang, Y. and Li, L. 2018. Fe³⁺ doped amorphous Co₂BO_y(OH)_z with enhanced activity for oxygen evolution reaction. *Electrochimica Acta* 280, 1-8.
- Yan, K.-L., Shang, X., Li, Z., Dong, B., Chi, J.-Q., Liu, Y.-R., Gao, W.-K., Chai, Y.-M. and Liu, C.-G. 2017. Facile synthesis of binary NiCoS nanorods supported on nickel foam as efficient electrocatalysts for oxygen evolution reaction. *International Journal of Hydrogen Energy* 42(27), 17129-17135.
- Yan, Y., He, T., Zhao, B., Qi, K., Liu, H. and Xia, B.Y. 2018. Metal/covalent-organic frameworks-based electrocatalysts for water splitting. *Journal of Materials Chemistry A* 6(33), 15905-15926.
- Yang, G.-X. and Jiang, H. 2014. Amino modification of biochar for enhanced adsorption of copper ions from synthetic wastewater. *Water Research* 48, 396-405.
- Yang, L., Liu, Z., Zhu, S., Feng, L. and Xing, W. 2021. Ni-based layered double hydroxide catalysts for oxygen evolution reaction. *Materials Today Physics* 16, 100292.
- Yang, M.Q., Wang, J., Wu, H. and Ho, G.W. 2018. Noble Metal-Free Nanocatalysts with Vacancies for Electrochemical Water Splitting. *Small* 14(15), e1703323.

- Yang, Y., Huang, G., Xie, M., Xu, S. and He, Y. 2016. Synthesis and performance of spherical $\text{LiNi}_x\text{Co}_y\text{Mn}_{1-x-y}\text{O}_2$ regenerated from nickel and cobalt scraps. *Hydrometallurgy* 165, 358-369.
- You, B., Jiang, N. and Sun, Y. *J.I.C.F.* 2016. Morphology–activity correlation in hydrogen evolution catalyzed by cobalt sulfides. *Inorganic Chemistry Frontiers* 3(2), 279-285.
- You, B. and Sun, Y. 2018. Innovative Strategies for Electrocatalytic Water Splitting. *Accounts of Chemical Research* 51(7), 1571-1580.
- Yu, F., Yao, H., Wang, B., Zhang, K., Zhang, Z., Xie, L., Hao, J., Mao, B., Shen, H. and Shi, W. 2018. Nickel foam derived nitrogen doped nickel sulfide nanowires as an efficient electrocatalyst for the hydrogen evolution reaction. *Dalton Transactions* 47(29), 9871-9876.
- Yu, N., Cao, W., Huttula, M., Kayser, Y., Hoenicke, P., Beckhoff, B., Lai, F., Dong, R., Sun, H. and Geng, B. 2020. Fabrication of FeNi hydroxides double-shell nanotube arrays with enhanced performance for oxygen evolution reaction. *Applied Catalysis B: Environmental* 261, 118193.
- Yu, P., Wang, F., Shifa, T.A., Zhan, X., Lou, X., Xia, F. and He, J. 2019. Earth abundant materials beyond transition metal dichalcogenides: A focus on electrocatalyzing hydrogen evolution reaction. *Nano Energy* 58, 244-276.
- Yu, X.Y. and Lou, X.W. 2018. Mixed metal sulfides for electrochemical energy storage and conversion. *Advanced Energy Materials* 8(3), 1701592.
- Yuan, W., Wang, S., Ma, Y., Qiu, Y., An, Y. and Cheng, L. 2020. Interfacial Engineering of Cobalt Nitrides and Mesoporous Nitrogen-Doped Carbon: Toward Efficient Overall Water-Splitting Activity with Enhanced Charge-Transfer Efficiency. *ACS Energy Letters* 5(3), 692-700.
- Zeng, M., Wang, H., Zhao, C., Wei, J., Qi, K., Wang, W. and Bai, X. 2016. Nanostructured Amorphous Nickel Boride for High-Efficiency Electrocatalytic Hydrogen Evolution over a Broad pH Range. *ChemCatChem* 8, 708-712.
- Zhang, B., Zheng, X., Voznyy, O., Comin, R., Bajdich, M., Garcia-Melchor, M., Han, L., Xu, J., Liu, M., Zheng, L., Garcia de Arquer, F.P., Dinh, C.T., Fan, F., Yuan, M., Yassitepe, E., Chen, N., Regier, T., Liu, P., Li, Y., De Luna, P., Janmohamed, A., Xin, H.L., Yang, H., Vojvodic, A. and Sargent, E.H. 2016a. Homogeneously dispersed multimetal oxygen-evolving catalysts. *Science* 352(6283), 333-337.
- Zhang, C., Shi, Y., Yu, Y., Du, Y. and Zhang, B. 2018a. Engineering Sulfur Defects, Atomic Thickness, and Porous Structures into Cobalt Sulfide Nanosheets for Efficient Electrocatalytic Alkaline Hydrogen Evolution. *ACS Catalysis* 8(9), 8077-8083.
- Zhang, D., Kong, X., Jiang, M., Lei, D. and Lei, X. 2019a. NiOOH-Decorated α -FeOOH Nanosheet Array on Stainless Steel for Applications in Oxygen Evolution Reactions and Supercapacitors. *ACS Sustainable Chemistry & Engineering* 7(4), 4420-4428.
- Zhang, F., Zhang, H., Salla, M., Qin, N., Gao, M., Ji, Y., Huang, S., Wu, S., Zhang, R., Lu, Z. and Wang, Q. 2021. Decoupled Redox Catalytic Hydrogen

- Production with a Robust Electrolyte-Borne Electron and Proton Carrier. *Journal of the American Chemical Society* 143(1), 223-231.
- Zhang, G., Feng, Y.-S., Lu, W.-T., He, D., Wang, C.-Y., Li, Y.-K., Wang, X.-Y. and Cao, F.-F. 2018b. Enhanced Catalysis of Electrochemical Overall Water Splitting in Alkaline Media by Fe Doping in Ni₃S₂ Nanosheet Arrays. *ACS Catalysis* 8(6), 5431-5441.
- Zhang, H., Jiang, H., Hu, Y., Li, Y., Xu, Q., Petr, S. and Li, C. 2019b. Tailorable surface sulfur chemistry of mesoporous Ni₃S₂ particles for efficient oxygen evolution. *Journal of Materials Chemistry A* 7(13), 7548-7552.
- Zhang, H. and Lv, R. 2018. Defect engineering of two-dimensional materials for efficient electrocatalysis. *Journal of Materiomics* 4(2), 95-107.
- Zhang, H., Maijenburg, A.W., Li, X., Schweizer, S.L. and Wehrspohn, R.B. 2020a. Bifunctional Heterostructured Transition Metal Phosphides for Efficient Electrochemical Water Splitting. *Advanced Functional Materials* 30(34), 2003261.
- Zhang, H., Tian, W., Duan, X., Sun, H., Liu, S. and Wang, S. 2019c. Catalysis of a Single Transition Metal Site for Water Oxidation: From Mononuclear Molecules to Single Atoms. *Advanced Materials* 32(18), 1904037.
- Zhang, J., Li, X., Liu, Y., Zeng, Z., Cheng, X., Wang, Y., Tu, W. and Pan, M. 2018c. Bi-metallic boride electrocatalysts with enhanced activity for the oxygen evolution reaction. *Nanoscale* 10(25), 11997-12002.
- Zhang, K., Xia, X., Deng, S., Zhong, Y., Xie, D., Pan, G., Wu, J., Liu, Q., Wang, X. and Tu, J. 2019d. Nitrogen-Doped Sponge Ni Fibers as Highly Efficient Electrocatalysts for Oxygen Evolution Reaction. *Nano-Micro Letters* 11(1), 1-11.
- Zhang, P., Wang, M., Yang, Y., Yao, T., Han, H. and Sun, L. 2016b. Electroless plated Ni-B_x films as highly active electrocatalysts for hydrogen production from water over a wide pH range. *Nano Energy* 19, 98-107.
- Zhang, Q., Li, X.L., Tao, B.X., Wang, X.H., Deng, Y.H., Gu, X.Y., Li, L.J., Xiao, W., Li, N.B. and Luo, H.Q. 2019e. CoNi based alloy/oxides@N-doped carbon core-shell dendrites as complementary water splitting electrocatalysts with significantly enhanced catalytic efficiency. *Applied Catalysis B: Environmental* 254, 634-646.
- Zhang, Q., Zhong, H., Meng, F., Bao, D., Zhang, X. and Wei, X. 2018d. Three-dimensional interconnected Ni (Fe)O_xH_y nanosheets on stainless steel mesh as a robust integrated oxygen evolution electrode. *Nano Research* 11(3), 1294-1300.
- Zhang, S.L., Guan, B.Y., Lu, X.F., Xi, S., Du, Y. and Lou, X.W.D. 2020b. Metal Atom-Doped Co₃O₄ Hierarchical Nanoplates for Electrocatalytic Oxygen Evolution. *Advanced Materials* 32(31), 2002235.
- Zhang, Y., Guo, L., Tao, L., Lu, Y. and Wang, S. 2018e. Defect-Based Single-Atom Electrocatalysts. *Small Methods* 3(9), 1800406.
- Zhao, G., Li, P., Cheng, N., Dou, S.X. and Sun, W. 2020a. An Ir/Ni(OH)₂ Heterostructured Electrocatalyst for the Oxygen Evolution Reaction: Breaking

- the Scaling Relation, Stabilizing Iridium(V), and Beyond. *Advanced Materials* 32(24), 2000872.
- Zhao, J., Su, A., Tian, P., Tang, X., Collins, R.N. and He, F. 2021. Arsenic (III) Removal by Mechanochemically Sulfidated Microscale Zero Valent Iron under Anoxic and Oxidic Conditions. *Water Research* 198, 117132.
- Zhao, J., Zhang, J.-J., Li, Z.-Y. and Bu, X.-H. 2020b. Recent Progress on NiFe-Based Electrocatalysts for the Oxygen Evolution Reaction. *Small* 16(51), 2003916.
- Zhao, P., Zhang, Z., He, H., Yu, Y., Li, X., Xie, W., Yang, Z. and Cai, J. 2019a. Cobalt-Tungsten Bimetallic Carbide Nanoparticles as Efficient Catalytic Material for High-Performance Lithium-Sulfur Batteries. *ChemSusChem* 12(21), 4866-4873.
- Zhao, S., Lu, X., Wang, L., Gale, J. and Amal, R. 2019b. Carbon-Based Metal-Free Catalysts for Electrocatalytic Reduction of Nitrogen for Synthesis of Ammonia at Ambient Conditions. *Advanced Materials* 31(13), 1805367.
- Zhao, S., Wang, D.W., Amal, R. and Dai, L. 2019c. Carbon-Based Metal-Free Catalysts for Key Reactions Involved in Energy Conversion and Storage. *Advanced Materials* 31(9), 1801526.
- Zhao, S., Wang, Y., Dong, J., He, C.-T., Yin, H., An, P., Zhao, K., Zhang, X., Gao, C. and Zhang, L. 2016. Ultrathin metal-organic framework nanosheets for electrocatalytic oxygen evolution. *Nature Energy* 1(12), 1-10.
- Zhao, Y., Jin, B., Vasileff, A., Jiao, Y. and Qiao, S.-Z. 2019d. Interfacial nickel nitride/sulfide as a bifunctional electrode for highly efficient overall water/seawater electrolysis. *Journal of Materials Chemistry A* 7(14), 8117-8121.
- Zhao, Y., Wan, W., Chen, Y., Erni, R., Triana, C.A., Li, J., Mavrokefalos, C.K., Zhou, Y. and Patzke, G.R. 2020c. Understanding and Optimizing Ultra-Thin Coordination Polymer Derivatives with High Oxygen Evolution Performance. *Advanced Energy Materials* 10(37), 2002228.
- Zheng, Y., Wang, B., Wester, A.E., Chen, J., He, F., Chen, H. and Gao, B. 2019. Reclaiming phosphorus from secondary treated municipal wastewater with engineered biochar. *Chemical Engineering Journal* 362, 460-468.
- Zhong, H.-X., Zhang, Q., Wang, J., Zhang, X.-B., Wei, X.-L., Wu, Z.-J., Li, K., Meng, F.-L., Bao, D. and Yan, J.-M. 2018a. Engineering ultrathin C₃N₄ quantum dots on graphene as a metal-free water reduction electrocatalyst. *ACS Catalysis* 8(5), 3965-3970.
- Zhong, H., Wang, J., Meng, F. and Zhang, X. 2016. In Situ Activating Ubiquitous Rust towards Low-Cost, Efficient, Free-Standing, and Recoverable Oxygen Evolution Electrodes. *Angewandte Chemie International Edition* 128(34), 10091-10095.
- Zhong, X., Tang, J., Wang, J., Shao, M., Chai, J., Wang, S., Yang, M., Yang, Y., Wang, N., Wang, S., Xu, B. and Pan, H. 2018b. 3D heterostructured pure and N-Doped Ni₃S₂/VS₂ nanosheets for high efficient overall water splitting. *Electrochimica Acta* 269, 55-61.

- Zhou, L., Xiu, F., Qiu, M., Xia, S. and Yu, L. 2017. The adsorption and dissociation of water molecule on goethite (010) surface: A DFT approach. *Applied Surface Science* 392, 760-767.
- Zhou, Y.-N., Yu, W.-L., Cao, Y.-N., Zhao, J., Dong, B., Ma, Y., Wang, F.-L., Fan, R.-Y., Zhou, Y.-L. and Chai, Y.-M. 2021. S-doped nickel-iron hydroxides synthesized by room-temperature electrochemical activation for efficient oxygen evolution. *Applied Catalysis B: Environmental* 292, 120150.
- Zhou, Y., Xi, S., Yang, X. and Wu, H. 2019. In situ hydrothermal growth of metallic $\text{Co}_9\text{S}_8\text{-Ni}_3\text{S}_2$ nanoarrays on nickel foam as bifunctional electrocatalysts for hydrogen and oxygen evolution reactions. *Journal of Solid State Chemistry* 270, 398-406.
- Zhu, B., Zou, R. and Xu, Q. 2018a. Metal-Organic Framework Based Catalysts for Hydrogen Evolution. *Advanced Energy Materials* 8(24), 1801193.
- Zhu, C., Yin, Z., Lai, W., Sun, Y., Liu, L., Zhang, X., Chen, Y. and Chou, S.-L. 2018b. Fe-Ni-Mo Nitride Porous Nanotubes for Full Water Splitting and Zn-Air Batteries. *Advanced Energy Materials* 8(36), 1802327.
- Zhu, J., Sun, M., Liu, S., Liu, X., Hu, K. and Wang, L. 2019a. Study of active sites on Se-MnS/NiS heterojunctions as highly efficient bifunctional electrocatalysts for overall water splitting. *Journal of Materials Chemistry A* 7(47), 26975-26983.
- Zhu, Y., Tahini, H.A., Hu, Z., Chen, Z.G., Zhou, W., Komarek, A.C., Lin, Q., Lin, H.J., Chen, C.T., Zhong, Y., Fernandez-Diaz, M.T., Smith, S.C., Wang, H., Liu, M. and Shao, Z. 2019b. Boosting Oxygen Evolution Reaction by Creating Both Metal Ion and Lattice-Oxygen Active Sites in a Complex Oxide. *Advanced Materials* 32(1), 1905025.
- Zou, W., Feng, X., Wang, R., Wei, W., Luo, S., Zheng, R., Yang, D., Mi, H. and Chen, H. 2021. High-efficiency core-shell magnetic heavy-metal absorbents derived from spent- LiFePO_4 Battery. *Journal of Hazardous Materials* 402, 123583.
- Zuo, W., Yu, Y. and Huang, H. 2021. Making waves: Microbe-photocatalyst hybrids may provide new opportunities for treating heavy metal polluted wastewater. *Water Research* 195, 116984.

APPENDIX

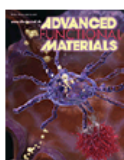
Permission of Reproduction from the Copyright Owner

Rightslink® by Copyright Clearance Center



?
Help ▾

Live Chat



Bifunctional Heterostructured Transition Metal Phosphides for Efficient Electrochemical Water Splitting

Author: Ralf B. Wehrspohn, Stefan L. Schweizer, Xiaopeng Li, et al

Publication: Advanced Functional Materials

Publisher: John Wiley and Sons

Date: Jun 29, 2020

© 2020 The Authors. Published by WILEY-VCH Verlag GmbH & Co. KGaA, Weinheim

Open Access Article

This is an open access article distributed under the terms of the [Creative Commons CC BY](#) license, which permits unrestricted use, distribution, and reproduction in any medium, provided the original work is properly cited.

You are not required to obtain permission to reuse this article.

For an understanding of what is meant by the terms of the Creative Commons License, please refer to [Wiley's Open Access Terms and Conditions](#).

Permission is not required for this type of reuse.

Wiley offers a professional reprint service for high quality reproduction of articles from over 1400 scientific and medical journals. Wiley's reprint service offers:

- Peer reviewed research or reviews
- Tailored collections of articles
- A professional high quality finish
- Glossy journal style color covers
- Company or brand customisation
- Language translations
- Prompt turnaround times and delivery directly to your office, warehouse or congress.

Please contact our Reprints department for a quotation. Email corporatesaleseurope@wiley.com or corporatesalesusa@wiley.com or corporatesalesDE@wiley.com.



Theoretical and Experimental Insight into the Effect of Nitrogen Doping on Hydrogen Evolution Activity of Ni3S2 in Alkaline Medium

Author: Yat Li, Yuan Ping, David Thota, et al
 Publication: Advanced Energy Materials
 Publisher: John Wiley and Sons
 Date: Mar 15, 2018

© 2018 WILEY-VCH Verlag GmbH & Co. KGaA, Weinheim

Order Completed

Thank you for your order.

This Agreement between Zhijie Chen ("You") and John Wiley and Sons ("John Wiley and Sons") consists of your license details and the terms and conditions provided by John Wiley and Sons and Copyright Clearance Center.

Your confirmation email will contain your order number for future reference.

License Number 5174070359688 [Printable Details](#)

License date Oct 22, 2021

Licensed Content

Licensed Content Publisher	John Wiley and Sons
Licensed Content Publication	Advanced Energy Materials
Licensed Content Title	Theoretical and Experimental Insight into the Effect of Nitrogen Doping on Hydrogen Evolution Activity of Ni3S2 in Alkaline Medium
Licensed Content Author	Yat Li, Yuan Ping, David Thota, et al
Licensed Content Date	Mar 15, 2018
Licensed Content Volume	8
Licensed Content Issue	19
Licensed Content Pages	8

Order Details

Type of use	Dissertation/Thesis
Requestor type	University/Academic
Format	Print and electronic
Portion	Figure/table
Number of figures/tables	3
Will you be translating?	No

About Your Work

Title	TRANSITION METAL-BASED CATALYSTS FOR ELECTROCHEMICAL WATER SPLITTING
Institution name	University of Technology Sydney
Expected presentation date	Jan 2022

Additional Data

Portions	Figures 1.2.3
----------	---------------

Requestor Location

Requestor Location	Zhijie Chen 15 Broadway Ultimo Sydney, NSW 2007 Australia Attrc
--------------------	--

Tax Details

Publisher Tax ID	EU826007151
------------------	-------------

\$ Price

Total	0.00 AUD
-------	----------

Would you like to purchase the full text of this article? If so, please continue on to the content ordering system located here: [Purchase PDF](#)
 If you click on the buttons below or close this window, you will not be able to return to the content ordering system.

Total: 0.00 AUD

[CLOSE WINDOW](#)

[ORDER MORE](#)

Engineering Sulfur Defects, Atomic Thickness, and Porous Structures into Cobalt Sulfide Nanosheets for Efficient Electrocatalytic Alkaline Hydrogen Evolution



Author: Chao Zhang, Yanmei Shi, Yifu Yu, et al

Publication: ACS Catalysis

Publisher: American Chemical Society

Date: Sep 1, 2018

Copyright © 2018, American Chemical Society

PERMISSION/LICENSE IS GRANTED FOR YOUR ORDER AT NO CHARGE

This type of permission/license, instead of the standard Terms and Conditions, is sent to you because no fee is being charged for your order. Please note the following:

- Permission is granted for your request in both print and electronic formats, and translations.
- If figures and/or tables were requested, they may be adapted or used in part.
- Please print this page for your records and send a copy of it to your publisher/graduate school.
- Appropriate credit for the requested material should be given as follows: "Reprinted (adapted) with permission from {COMPLETE REFERENCE CITATION}. Copyright {YEAR} American Chemical Society." Insert appropriate information in place of the capitalized words.
- One-time permission is granted only for the use specified in your RightsLink request. No additional uses are granted (such as derivative works or other editions). For any uses, please submit a new request.

If credit is given to another source for the material you requested from RightsLink, permission must be obtained from that source.

[BACK](#)

[CLOSE WINDOW](#)

Efficient Hydrogen Evolution on Cu Nanodots-Decorated Ni₃S₂ Nanotubes by Optimizing Atomic Hydrogen Adsorption and Desorption



Author: Jin-Xian Feng, Jin-Qi Wu, Ye-Xiang Tong, et al
 Publication: Journal of the American Chemical Society
 Publisher: American Chemical Society
 Date: Jan 1, 2018

Copyright © 2018, American Chemical Society

PERMISSION/LICENSE IS GRANTED FOR YOUR ORDER AT NO CHARGE

This type of permission/license, instead of the standard Terms and Conditions, is sent to you because no fee is being charged for your order. Please note the following:

- Permission is granted for your request in both print and electronic formats, and translations.
- If figures and/or tables were requested, they may be adapted or used in part.
- Please print this page for your records and send a copy of it to your publisher/graduate school.
- Appropriate credit for the requested material should be given as follows: "Reprinted (adapted) with permission from {COMPLETE REFERENCE CITATION}. Copyright {YEAR} American Chemical Society." Insert appropriate information in place of the capitalized words.
- One-time permission is granted only for the use specified in your RightsLink request. No additional uses are granted (such as derivative works or other editions). For any uses, please submit a new request.

If credit is given to another source for the material you requested from RightsLink, permission must be obtained from that source.

[BACK](#)

[CLOSE WINDOW](#)

Heteromorphic NiCo₂S₄/Ni₃S₂/Ni Foam as a Self-Standing Electrode for Hydrogen Evolution Reaction in Alkaline Solution



Author: Hui Liu, Xiao Ma, Yuan Rao, et al

Publication: Applied Materials

Publisher: American Chemical Society

Date: Apr 1, 2018

Copyright © 2018, American Chemical Society

PERMISSION/LICENSE IS GRANTED FOR YOUR ORDER AT NO CHARGE

This type of permission/license, instead of the standard Terms and Conditions, is sent to you because no fee is being charged for your order. Please note the following:

- Permission is granted for your request in both print and electronic formats, and translations.
- If figures and/or tables were requested, they may be adapted or used in part.
- Please print this page for your records and send a copy of it to your publisher/graduate school.
- Appropriate credit for the requested material should be given as follows: "Reprinted (adapted) with permission from (COMPLETE REFERENCE CITATION). Copyright (YEAR) American Chemical Society." Insert appropriate information in place of the capitalized words.
- One-time permission is granted only for the use specified in your RightsLink request. No additional uses are granted (such as derivative works or other editions). For any uses, please submit a new request.

If credit is given to another source for the material you requested from RightsLink, permission must be obtained from that source.

[BACK](#)

[CLOSE WINDOW](#)



Electronically Double-Layered Metal Boride Hollow Nanoprism as an Excellent and Robust Water Oxidation Electrocatalysts

Author: Taeseup Song, Yong-Chae Chung, Heechae Choi, et al
 Publication: Advanced Energy Materials
 Publisher: John Wiley and Sons
 Date: Feb 12, 2019

© 2019 WILEY-VCH Verlag GmbH & Co. KGaA, Weinheim

Order Completed

Thank you for your order.
 This Agreement between Zhijie Chen ("You") and John Wiley and Sons ("John Wiley and Sons") consists of your license details and the terms and conditions provided by John Wiley and Sons and Copyright Clearance Center.

Your confirmation email will contain your order number for future reference.

License Number: 5174071273796 [Printable Details](#)

License date: Oct 22, 2021

Licensed Content		Order Details	
Licensed Content Publisher	John Wiley and Sons	Type of use	Dissertation/Thesis
Licensed Content Publication	Advanced Energy Materials	Requestor type	University/Academic
Licensed Content Title	Electronically Double-Layered Metal Boride Hollow Nanoprism as an Excellent and Robust Water Oxidation Electrocatalysts	Format	Print and electronic
Licensed Content Author	Taeseup Song, Yong-Chae Chung, Heechae Choi, et al	Portion	Figure/table
Licensed Content Date	Feb 12, 2019	Number of figures/tables	3
Licensed Content Volume	9	Will you be translating?	No
Licensed Content Issue	13		
Licensed Content Pages	11		

About Your Work		Additional Data	
Title	TRANSITION METAL-BASED CATALYSTS FOR ELECTROCHEMICAL WATER SPLITTING	Portions	Figures 1.2.5
Institution name	University of Technology Sydney		
Expected presentation date	Jan 2022		

Requestor Location		Tax Details	
Requestor Location	Zhijie Chen 15 Broadway Ultimo Sydney, NSW 2007 Australia Attrn:	Publisher Tax ID	EU826007151

\$ Price	
Total	0.00 AUD

Would you like to purchase the full text of this article? If so, please continue on to the content ordering system located here: [Purchase PDF](#)
 If you click on the buttons below or close this window, you will not be able to return to the content ordering system.

Total: 0.00 AUD

[CLOSE WINDOW](#)

[ORDER MORE](#)

SHOPPING CART [Empty this cart](#)

Currency **AUD**

1. Journal of materials chemistry. A, Materials for energy and sustainability

Article: Synthesis of amorphous boride nanosheets by the chemical reduction of Prussian blue analogs for efficient water electrolysis

0.00 AUD

ISSN	2050-7488	Publisher	Royal Society of Chemistry
Type of Use	Republish in a thesis/dissertation	Portion	Chart/graph/table/figure

LICENSED CONTENT

Publication Title	Journal of materials chemistry. A, Materials for energy and sustainability	Rights holder	Royal Society of Chemistry
Article Title	Synthesis of amorphous boride nanosheets by the chemical reduction of Prussian blue analogs for efficient water electrolysis	Publication Type	Journal
Author/Editor	Royal Society of Chemistry (Great Britain)	Start Page	23289
Date	01/01/2012	End Page	23294
Language	English	Issue	46
Country	United Kingdom of Great Britain and Northern Ireland	Volume	6

REQUEST DETAILS

Portion Type	Chart/graph/table/figure	Distribution	Worldwide
Number of charts / graphs / tables / figures requested	3	Translation	Original language of publication
Format (select all that apply)	Print, Electronic	Copies for the disabled?	Yes
Who will republish the content?	Academic institution	Minor editing privileges?	Yes
Duration of Use	Life of current edition	Incidental promotional use?	Yes

Lifetime Unit Quantity	Up to 4,999	Currency	AUD
Rights Requested	Main product and any product related to main product		

NEW WORK DETAILS

Title	TRANSITION METAL-BASED CATALYSTS FOR ELECTROCHEMICAL WATER SPLITTING	Institution name	University of Technology Sydney
Instructor name	Zhijie Chen	Expected presentation date	2022-01-01

ADDITIONAL DETAILS

Order reference number	N/A	The requesting person / organization to appear on the license	Zhijie Chen
------------------------	-----	---	-------------

REUSE CONTENT DETAILS

Title, description or numeric reference of the portion(s)	Figure 1 and Figure s1	Title of the article/chapter the portion is from	Synthesis of amorphous boride nanosheets by the chemical reduction of Prussian blue analogs for efficient water electrolysis
Editor of portion(s)	He, Ting; Nsanzimana, Jean Marie Vianney; Qi, Ruijuan; Zhang, Jun-Ye; Miao, Mao; Yan, Ya; Qi, Kai; Liu, Hongfang; Xia, Bao Yu	Author of portion(s)	He, Ting; Nsanzimana, Jean Marie Vianney; Qi, Ruijuan; Zhang, Jun-Ye; Miao, Mao; Yan, Ya; Qi, Kai; Liu, Hongfang; Xia, Bao Yu
Volume of serial or monograph	6	Issue, if republishing an article from a serial	46
Page or page range of portion	23289-23294	Publication date of portion	2018-01-01

[Remove](#)

Total Items: 1

Cart Total: 0.00 AUD



Amorphous Cobalt Boride (Co₂B) as a Highly Efficient Nonprecious Catalyst for Electrochemical Water Splitting: Oxygen and Hydrogen Evolution

Author: Wolfgang Schuhmann, Martin Muhler, Christoph Somsen, et al
 Publication: Advanced Energy Materials
 Publisher: John Wiley and Sons
 Date: Jan 7, 2016

© 2016 WILEY-VCH Verlag GmbH & Co. KGaA, Weinheim

Order Completed

Thank you for your order.
 This Agreement between Zhijie Chen ("You") and John Wiley and Sons ("John Wiley and Sons") consists of your license details and the terms and conditions provided by John Wiley and Sons and Copyright Clearance Center.

Your confirmation email will contain your order number for future reference.

License Number 5174080501301 [Printable Details](#)

License date Oct 22, 2021

Licensed Content

Licensed Content Publisher	John Wiley and Sons
Licensed Content Publication	Advanced Energy Materials
Licensed Content Title	Amorphous Cobalt Boride (Co ₂ B) as a Highly Efficient Nonprecious Catalyst for Electrochemical Water Splitting: Oxygen and Hydrogen Evolution
Licensed Content Author	Wolfgang Schuhmann, Martin Muhler, Christoph Somsen, et al
Licensed Content Date	Jan 7, 2016
Licensed Content Volume	6
Licensed Content Issue	6
Licensed Content Pages	10

Order Details

Type of use	Dissertation/Thesis
Requestor type	University/Academic
Format	Print and electronic
Portion	Figure/table
Number of figures/tables	3
Will you be translating?	No

About Your Work

Title	TRANSITION METAL-BASED CATALYSTS FOR ELECTROCHEMICAL WATER SPLITTING
Institution name	University of Technology Sydney
Expected presentation date	Jan 2022

Additional Data

Portions	Figures 1.3-4
----------	---------------

Requestor Location

Requestor Location	Zhijie Chen 15 Broadway Ultimo Sydney, NSW 2007 Australia Attn:
--------------------	--

Tax Details

Publisher Tax ID	EU826007151
------------------	-------------

Price

Total	0.00 AUD
-------	----------

Would you like to purchase the full text of this article? If so, please continue on to the content ordering system located here: [Purchase PDF](#)
 If you click on the buttons below or close this window, you will not be able to return to the content ordering system.

Total: 0.00 AUD



Ultrathin High Surface Area Nickel Boride (Ni₃B) Nanosheets as Highly Efficient Electrocatalyst for Oxygen Evolution

Author: Justus Masa, Ilya Sinev, Hemma Mistry, et al
 Publication: Advanced Energy Materials
 Publisher: John Wiley and Sons
 Date: May 10, 2017

© 2017 WILEY-VCH Verlag GmbH & Co. KGaA, Weinheim

Order Completed

Thank you for your order.

This Agreement between Zhijie Chen ("You") and John Wiley and Sons ("John Wiley and Sons") consists of your license details and the terms and conditions provided by John Wiley and Sons and Copyright Clearance Center.

Your confirmation email will contain your order number for future reference.

License Number 5174080776584 [Printable Details](#)

License date Oct 22, 2021

Licensed Content

Licensed Content Publisher John Wiley and Sons
 Licensed Content Publication Advanced Energy Materials
 Licensed Content Title Ultrathin High Surface Area Nickel Boride (Ni₃B) Nanosheets as Highly Efficient Electrocatalyst for Oxygen Evolution
 Licensed Content Author Justus Masa, Ilya Sinev, Hemma Mistry, et al
 Licensed Content Date May 10, 2017
 Licensed Content Volume 7
 Licensed Content Issue 17
 Licensed Content Pages 8

Order Details

Type of use Dissertation/Thesis
 Requestor type University/Academic
 Format Print and electronic
 Portion Figure/table
 Number of figures/tables 1
 Will you be translating? No

About Your Work

Title TRANSITION METAL-BASED CATALYSTS FOR ELECTROCHEMICAL WATER SPLITTING
 Institution name University of Technology Sydney
 Expected presentation date Jan 2022

Additional Data

Portions Figure 2

Requestor Location

Requestor Location Zhijie Chen
 15 Broadway Ultimo
 Sydney, NSW 2007 Australia
 Attr:

Tax Details

Publisher Tax ID EU826007151

\$ Price

Total 0.00 AUD

Would you like to purchase the full text of this article? If so, please continue on to the content ordering system located here: [Purchase PDF](#)
 If you click on the buttons below or close this window, you will not be able to return to the content ordering system.

Total: 0.00 AUD



Highly active and durable electrocatalytic water oxidation by a Ni_{0.45}/NiO_x core-shell heterostructured nanoparticulate film

Author: Jian Jiang, Mei Wang, Wensheng Yan, Xiaofeng Liu, Jinxuan Liu, Jinlong Yang, Licheng Sun
 Publication: Nano Energy
 Publisher: Elsevier
 Date: August 2017

© 2017 Elsevier Ltd. All rights reserved.

Order Completed

Thank you for your order.

This Agreement between Zhijie Chen ("You") and Elsevier ("Elsevier") consists of your license details and the terms and conditions provided by Elsevier and Copyright Clearance Center.

Your confirmation email will contain your order number for future reference.

License Number 5174080998412 [Printable Details](#)
 License date Oct 22, 2021

Licensed Content

Licensed Content Publisher Elsevier
 Licensed Content Publication Nano Energy
 Licensed Content Title Highly active and durable electrocatalytic water oxidation by a Ni_{0.45}/NiO_x core-shell heterostructured nanoparticulate film
 Licensed Content Author Jian Jiang, Mei Wang, Wensheng Yan, Xiaofeng Liu, Jinxuan Liu, Jinlong Yang, Licheng Sun
 Licensed Content Date Aug 1, 2017
 Licensed Content Volume 38
 Licensed Content Issue n/a
 Licensed Content Pages 10

Order Details

Type of Use reuse in a thesis/dissertation
 Portion figures/tables/illustrations
 Number of figures/tables/illustrations 2
 Format both print and electronic
 Are you the author of this Elsevier article? No
 Will you be translating? No

About Your Work

Title TRANSITION METAL-BASED CATALYSTS FOR ELECTROCHEMICAL WATER SPLITTING
 Institution name University of Technology Sydney
 Expected presentation date Jan 2022

Additional Data

Portions Figures 2-6

Requestor Location

Requestor Location Zhijie Chen
 15 Broadway
 Ultimo
 Sydney, NSW 2007
 Australia
 Attr:

Tax Details

Publisher Tax ID GB 494 6272 12

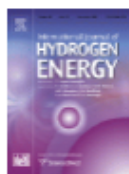
Price

Total 0.00 AUD

Total: 0.00 AUD

CLOSE WINDOW

ORDER MORE



Study of cobalt boride-derived electrocatalysts for overall water splitting

Author: Zhengjun Chen, Qing Kang, Guoxuan Cao, Ning Xu, Hongbin Dai, Ping Wang

Publication: International Journal of Hydrogen Energy

Publisher: Elsevier

Date: 22 March 2018

© 2018 Hydrogen Energy Publications LLC. Published by Elsevier Ltd. All rights reserved.

Order Completed

Thank you for your order.

This Agreement between Zhijie Chen ("You") and Elsevier ("Elsevier") consists of your license details and the terms and conditions provided by Elsevier and Copyright Clearance Center.

Your confirmation email will contain your order number for future reference.

License Number 5174090456856 [Printable Details](#)

License date Oct 22, 2021

Licensed Content

Licensed Content Publisher	Elsevier
Licensed Content Publication	International Journal of Hydrogen Energy
Licensed Content Title	Study of cobalt boride-derived electrocatalysts for overall water splitting
Licensed Content Author	Zhengjun Chen, Qing Kang, Guoxuan Cao, Ning Xu, Hongbin Dai, Ping Wang
Licensed Content Date	Mar 22, 2018
Licensed Content Volume	43
Licensed Content Issue	12
Licensed Content Pages	12

Order Details

Type of Use	reuse in a thesis/dissertation
Portion	figures/tables/illustrations
Number of figures/tables/illustrations	2
Format	both print and electronic
Are you the author of this Elsevier article?	No
Will you be translating?	No

About Your Work

Title	TRANSITION METAL-BASED CATALYSTS FOR ELECTROCHEMICAL WATER SPLITTING
Institution name	University of Technology Sydney
Expected presentation date	Jan 2022

Additional Data

Portions	Figures 4.7
----------	-------------

Requestor Location

Requestor Location	Zhijie Chen 15 Broadway Ultimo Sydney, NSW 2007 Australia Attr:
--------------------	--

Tax Details

Publisher Tax ID	GB 494 6272 12
------------------	----------------

Price

Total	0.00 AUD
-------	----------

Total: 0.00 AUD

CLOSE WINDOW

ORDER MORE